**PEOPLE'S DEMOCRATIC REPUBLIC OF ALGERIA**

**MINISTRY OF HIGHER EDUCATION AND SCIENTIFIC RESEARCH**

**FERHAT ABBAS UNIVERSITY – SETIF 1**

**FACULTY OF SCIENCE**

**DEPARTMENT OF CHEMISTRY**

Université Ferhat ABBAS Sétif 1

Faculty of Sciences

*Laboratory of Electrochemistry of Molecular and Complex Materials*

# LMD DOCTORAL THESIS

**Domain:** Materials Science

**Field**: Chemistry

**Option**: Pharmaceutical Chemistry

Presented by

**BOUCHAMA Anis**

In partial fulfillment of the requirements for the degree of

**Doctor in Pharmaceutical Chemistry**

Title:

## *"Synthesis, Biological Activities Evaluation, Density Functional Theory Investigation, and Molecular Docking studies of Hydroxybutyl and Hydroxypropyl Aminophosphonic Acids"*

**Examination Committee**

| | | |
|---|---|---|
| Pr. KAABOUB Lakhmissi | – Professor at Ferhat Abbas University Sétif 1 | – Chairperson |
| Pr. HELLAL Abdelkader | – Professor at Ferhat Abbas University Sétif 1 | – Supervisor |
| Dr. MESSASMA Zakia | – Doctor at Ferhat Abbas University Sétif 1 | – Examiner |
| Pr. HARAKATI Dalal | – Professor at University of Biskra | – Examiner |
| Dr. BENSOUICI Chawki | – Researcher at Biotechnology Research Center, Constantine | – Examiner |
| Dr. NOUAR Yacine | – Doctor at Ferhat Abbas University Sétif 1 | – Examiner |
| Dr. MADANI Abdelghani | – Doctor at Ferhat Abbas University Sétif 1 | – Guest |
| Dr. KITOUNI Siham | – Doctor at Ferhat Abbas University Sétif 1 | – Guest |

Academic Year

2025 – 2026

# *Dedication*

*To my beloved mother, whose boundless love, tireless sacrifices, and steadfast faith in me have illuminated every step of this journey. Your gentle wisdom and unwavering devotion have shaped the person I am today, and no words can fully express my gratitude for the countless nights you spent encouraging my dreams and comforting my doubts.*

*My family, whose unity and support gave me strength and solace through every challenge.*

*To my dear friends and brother in life, Abd El Errahman, Lotfi, Mohamed, and Bahaa, thank you for standing by me, for your laughter in moments of doubt, and for believing in my potential when I needed it most.*

*And to all who have encouraged me, shared my struggles, and inspired me to persevere, this work is lovingly dedicated to you.*

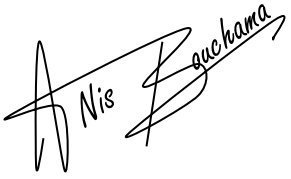

## *Acknowledgments*

I stand on the shoulders of giants—and it is with a heart full of gratitude that I acknowledge the extraordinary people who have made this voyage possible.

To my mentor and beacon, **Pr. HELLAL Abd El Kader**: your unwavering confidence and boundless curiosity have been the compass guiding my scientific odyssey. You breathed life into my ideas, turned obstacles into stepping-stones, and taught me that the greatest discoveries lie just beyond the horizon of our comfort zones. Thank you for lighting the way.

To **Dr. MADANI Abd El Ghani**: your insightful counsel and generous support were like refreshing rainfall on parched ground, reviving my motivation at every critical juncture.

To the two great harbors of my internship, **Pr. Pietro Matricardi** at Sapienza University of Rome, and **Pr. Annamaria Deagostino** at the University of Turin, thank you for opening your doors, sharing your expertise, and weaving me into the vibrant tapestry of international science. Your mentorship broadened my vision and enriched my craft.

To **Pr. CHAFAI Nadjib**, Director of the LEMMC laboratory, and the entire LEMMC family: your warmth, spirited discussions, and technical wizardry created a nurturing haven where my experiments could truly take flight.

To **Pr. Chawki Bensouisi**: Your generosity in providing reagents, equipment, and your deep expertise in biological assays made the critical experiments of this work possible. Your kindness was the elixir that kept this research alive.

To all the professors who have lit the flame of knowledge within me—your dedication and passion are the bedrock upon which my academic journey has been built.

To **Ferhat Abbas University – Setif 1**, Faculty of Science, and the Department of Chemistry: thank you for the facilities, the resources, and the spirit of inquiry you foster every day.

To the **Ministry of Higher Education and Scientific Research** and the various funding bodies: your generous support transformed aspirations into achievements.

Finally, I bow in deep appreciation before the members of my examination committee, whose discerning eyes and thoughtful critiques have refined this work: **Pr. KAABOUB Lakhmissi, Pr. MESSASMA Zakia, Pr. HARAKATI Dalal Dr. NOUAR Yacine, Dr. MADANI Abdelghani,** and **Dr. KITOUNI Siham**

# Table of contents

General Introduction ..... 1

I Bibliographic Review ..... 7

I.1 Introduction ..... 7

I.2 Historical Overview and Classification of Phosphonates ..... 8

I.2.1 Historical Development ..... 8

I.2.2 Structural Diversity and Nomenclature ..... 10

I.3 Synthetic Strategies for Organophosphonates ..... 11

I.3.1 Classical Reactions ..... 11

I.3.2 Modern Reactions ..... 13

I.3.3 Characterization and Purification ..... 20

I.4 Biological Activities ..... 20

I.4.1 Enzyme Inhibition ..... 20

I.4.2 Antimicrobial Properties ..... 20

I.4.3 Antiviral Activity ..... 23

I.4.4 Anticancer Potential ..... 25

I.4.5 Anti-inflammatory Effects ..... 27

I.4.6 Antioxidant Properties ..... 28

I.5 Agricultural Applications ..... 29

I.6 Density Functional Theory (DFT) and Computational Insights ..... 30

I.6.1 DFT Applications in Organophosphonates Research ..... 30

I.6.2 Docking Studies of Phosphonates ..... 30

I.6.3 Importance of Early ADME-T Assessment ..... 30

I.6.4 Integrating ADME-T with Design ..... 31

I.7 Nano Drug Delivery of Organophosphonates ..... 31

I.8 Somes of Nanodrug Delivery Systems Suitable for Organophosphonates ..... 32

I.8.1 Polymeric Nanoparticles ..... 32

I.8.2 Liposomes ..... 33
I.8.3 Nanohydrogels ..... 33
I.8.4 Hyaluronic Acid-Based Nanocarriers ..... 34
I.9 Challenges, Limitations, and Future Directions ..... 34
I.9.1 Synthetic Complexity and Cost ..... 34
I.9.2 Computational Accuracy and Validation ..... 34
I.9.3 Translating In Vitro to In Vivo ..... 35
I.9.4 Emerging Fields ..... 35
I.10 Conclusion ..... 35
II Materials and Methods ..... 38
II.1 Introduction ..... 38
II.2 Materials ..... 38
II.2.1 Chemicals and Reagents ..... 38
II.2.2 Equipment ..... 45
II.2.3 Software Tools : ..... 47
II.3 Experimental Methods ..... 51
II.3.1 Synthesis of Organophosphonates ..... 51
II.3.2 Density Functional Theory (DFT) Studies ..... 52
II.3.3 Molecular Docking ..... 54
II.3.4 ADME-T and Drug-likeness Predictions ..... 56
II.4 Nanoparticle investigation ..... 57
II.4.1 Nanohydrogel preparation ..... 57
II.4.2 Loading Efficiency (Drug Loading ) ..... 58
II.4.3 In Vitro Release Testing ..... 59
II.5 Bilogicals assay ..... 61
II.5.1 ABTS Scavenging Activity ..... 61
II.5.2 DPPH free radical ..... 62

II.5.3 Phenanthroline-Ferric Reducing Power Assay ..... 64
II.5.4 Ferric Reducing Power (FRP) Assay ..... 65
II.5.5 Antibacterial assay ..... 65
II.6 Conclusion ..... 66
III Synthesis and Evaluation of Organophosphonates ..... 71
III.1 Introduction ..... 71
III.2 Synthesis method ..... 71
III.2.1 Synthesis of α-Aminophosphonic Acids ($HAP_1$ and $HAP_2$) ..... 72
III.3 Preliminary Characterization: Solubility, Melting Points, and TLC ..... 75
III.3.1 Solubility Test ..... 75
III.3.2 Melting Points ..... 78
III.3.3 Thin-Layer Chromatography (TLC) Analysis ..... 78
III.4 Advanced Spectroscopic Analyses: IR, UV-Vis, and NMR ..... 79
III.4.1 Fourier Transform Infrared Spectroscopy (FT-IR) ..... 79
III.4.2 Ultraviolet-visible (UV-Vis) Spectrophotometry ..... 81
III.4.3 Nuclear Magnetic Resonance (NMR) ..... 82
III.4.4 Carbon$^{13}$ Nuclear Magnetic Resonance ($^{13}$C-NMR) ..... 84
III.5 Conclusion ..... 86
IV Computational Approach using DFT ..... 89
IV.1 Introduction ..... 89
IV.2 Integrative DFT Analysis ..... 89
IV.2.1 Geometric Optimization ..... 89
IV.2.2 Mulliken Atomic Charges Analysis ..... 91
IV.2.3 Dipole Moments ..... 95
IV.2.4 Frontier Molecular Orbital Analysis ..... 95
IV.2.5 Global Reactivity Descriptors ..... 96
IV.2.6 Molecular Electrostatic Potential Surface (MESP) ..... 98

IV.2.7 Vibrational Analysis ..... 100

IV.2.8 Thermodynamic characteristics ..... 104

IV.3 TD-DFT Analysis ..... 106

IV.3.1 Excited States & Transition Energies ..... 106

IV.3.2 Main Orbital Contributions to Excitations ..... 107

IV.3.3 Characterization of Transitions ..... 110

IV.4 Conclusion ..... 110

V Advancing Drug Discovery Docking & ADME-T ..... 112

V.1 Introduction ..... 112

V.2 Docking Simulations ..... 113

V.2.1 Interaction of $HAP_1$ and $HAP_2$ with Lipoxygenase (PDB: 1N8Q) ..... 113

V.2.2 Interaction of $HAP_1$ and $HAP_2$ with Superoxide Dismutase (SOD; PDB: 5YTO) 116

V.2.3 Interaction of $HAP_1$ and HAP2 with Catalase (CAT, PDB: 1DGF) ..... 119

V.2.4 Interaction of $HAP_1$ and $HAP_2$ with Glutathione Peroxidase (GPx, PDB: 2P31) 121

V.2.5 Ligand Preparation at Physiological pH for Molecular Docking ..... 124

V.2.6 Determining Predominant Ionic Species (pH 8) ..... 125

V.2.7 Interaction of the major microspecies with Lipoxygenase (PDB: 1N8Q). 126

V.3 ADME-T Predictions ..... 129

V.3.1 SwissADME Profiles of $HAP_1$ and $HAP_2$ ..... 129

V.3.2 pkCSM ADME-T Analysis ..... 132

V.3.3 StopTox Toxicological Profile Analysis ..... 135

V.3.4 ProTox Toxicological Profile Analysis ..... 136

V.4 Conclusion ..... 137

VI Biological Activities ..... 140

VI.1 INTRODUCTION ..... 140

VI.2 Antioxidant Activity Using Multiple Assays ..... 141

VI.2.1 Analysis of DPPH Assays ..... 141
VI.2.2 ABTS Radical Scavenging Activity ..... 143
VI.2.3 Phenanthroline Assay ..... 145
VI.2.4 FRAP Assay ..... 148
VI.3 Synergy Analysis of Antioxidant Combinations ..... 149
VI.3.1 Comparison of Synergy in DPPH and ABTS Assays ..... 149
VI.3.2 Interaction Effects: Synergy vs. Antagonism for Each Combination ..... 152
VI.3.3 Dose-Dependence of Synergy Effects ..... 153
VI.3.4 Statistical Significance of Synergy Scores ..... 156
VI.3.5 Synergy-Sensitivity Analysis of Antioxidant Combinations ..... 157
VI.4 antibacterial activity ..... 158
VI.5 Conclusion ..... 159
VII Nanodrug Delivery and Emerging Challenges ..... 162
VII.1 Introduction ..... 162
VII.2 Nanocarriers for Organophosphonate Drug Delivery ..... 162
VII.2.1 Drug Loading ..... 162
VII.2.2 Nanohydrogel Characterization: ..... 163
VII.2.3 *In Vitro* Drug-Release Analysis ..... 165
VII.3 Emerging Challenges ..... 170
VII.3.1 Novel Synthetic Methods ..... 170
VII.3.2 Computational Modeling ..... 171
VII.3.3 Biological Testing: Translational and Analytical Challenges ..... 174
VII.3.4 Nano-Drug Delivery : ..... 176
VII.4 Conclusion ..... 177
General Conclusion ..... 179
References ..... 187

## List Of Abbreviations

AChE – Acetylcholinesterase

ABTS – 2,2′-Azino-bis(3-ethylbenzothiazoline-6-sulfonic acid)

ADME-T – Absorption, Distribution, Metabolism, Excretion, and Toxicity

ATP – Adenosine Triphosphate

BChE – Butyrylcholinesterase

BHA – Butylated Hydroxyanisole

BHT – Butylated Hydroxytoluene

BBB – Blood–Brain Barrier

CAL-B – Candida antarctica Lipase B

CAT – Catalase

C–P – Carbon–Phosphorus bond

DNA – Deoxyribonucleic Acid

DFT – Density Functional Theory

DMSO – Dimethyl Sulfoxide

DTNB – 5,5′-Dithiobis(2-nitrobenzoic acid)

DPPH – 2,2-Diphenyl-1-picrylhydrazyl

EE – Encapsulation Efficiency

FT-IR – Fourier Transform Infrared Spectroscopy

FRAP – Ferric Reducing Antioxidant Power

GPx – Glutathione Peroxidase

HA – Hyaluronic Acid

HACH – Hyaluronan–Cholesterol

HAP1, HAP2 – The two α-aminophosphonic acids synthesized and studied (HAP1 derived from 3-aminopropanol; HAP2 from 4-aminobutanol)

HBA – Hydrogen Bond Acceptor

HBD – Hydrogen Bond Donor

HPLC – High-Performance Liquid Chromatography

$IC_{50}$ – Half-Maximal Inhibitory Concentration

$LD_{50}$ – Median Lethal Dose

LEMMC – Laboratory of Electrochemistry of Molecular Materials and Complexes

MD – Molecular Dynamics

MESP – Molecular Electrostatic Potential Surface

NMR – Nuclear Magnetic Resonance

NH, NHs – Nanohydrogel (singular, plural)

OPs – Organophosphonates

PEG – Polyethylene Glycol

PLGA – Poly(lactic-co-glycolic acid)

PDB – Protein Data Bank

PhD – Doctor of Philosophy

## *List Of Abbreviations*

PNP – p-Nitrophenol

PNPB – p-Nitrophenyl Butyrate

PNPCh – p-Nitrophenyl Choline

PNPGl – p-Nitrophenyl Glutamate

PDF – Portable Document Format

rpm – Revolutions per Minute

SOD – Superoxide Dismutase

TLC – Thin-Layer Chromatography

TD-DFT – Time-Dependent Density Functional Theory

$t_{50}$ – Time to 50 % cumulative release

USB – Universal Serial Bus

UV-Vis – Ultraviolet–Visible Spectroscopy

pkCSM – Pharmacokinetics prediction tool “pkCSM”

RMSD – Root-Mean-Square Deviation

RNA – Ribonucleic Acid

ROS – Reactive Oxygen Species

# List Of Figures

## Chapter I

Figure I. 1 The number of publications of organophosphorus compounds and α-Aminophosphonates synthesis in the last decade. (Source: Science Direct)..... 9
Figure I. 2 Timeline illustrating the history of organophosphonates. ..... 9
Figure I. 3 Phosphonate mono-di ester. ..... 10
Figure I. 4 Phosphonic acids..... 10
Figure I. 5 α-Aminophosphonates. ..... 10
Figure I. 6 α-Hydroxyphosphonates. ..... 11
Figure I. 7 Bisphosphonates. ..... 11
Figure I. 8 Michaelis–Arbuzov reaction. ..... 12
Figure I. 9 Kabachnik–Fields reaction. ..... 12
Figure I. 10 The Moedritzer-Irani reaction..... 13
Figure I. 11 Pudovik reaction. ..... 13
Figure I. 12 [bmim]AlCl4 system in Kabachnik–Fields reaction. ..... 14
Figure I. 13 Catalyst and solvent-free ultrasound promoted a rapid protocol for the one-pot synthesis of organophosphonates at room temperature. ..... 17
Figure I. 14 Screening of the catalysts (from BINOL) and the reaction conditions for the three-component reaction. ..... 18
Figure I. 15 Some examples of stereo-controlled synthesis of tetra-substituted organophosphonates. ..... 18
Figure I. 16 The enzymatic kinetic resolution of racemic mixtures of α-aminoalkylphosphonic acids and α-aminophosphonates..... 19
Figure I. 17 Lipase-Catalyzed Kabachnik–Fields reaction ..... 19
Figure I. 18 Structures of phosphonate inhibitors of the protein-tyrosine phosphatase 1B (PTP-1B) (compounds 1-2) and acetylcholinesterase (AChE) and butyrylcholinesterase (BChE) inhibitor (compounds 3). ..... 20
Figure I. 19 Structure of Fosfomycin. ..... 21
Figure I. 20 Structures of Tenofovir and Cidofovir..... 23
Figure I. 21 Some examples of organophosphonates as anti-inflammatory agents [76]..... 27
Figure I. 22 Some of the case studies and commercial products..... 29
Figure I. 23 Structure of PLGA. x= number of lactic acid units; y= number of glycolic acid units, and PEG. ..... 32

Figure I. 24 Schematic representation of Phosphonates encapsulated in PLGA nanoparticles. ..... 32
Figure I. 25 Illustrating the structure of liposomes. ..... 33
Figure I. 26 The CD44 antigen and HA structures. ..... 34

**Chapter II**

Figure II. 1 DPPH chemical structure ..... 42
Figure II. 2 ABTS chemical structure ..... 42
Figure II. 3 1,10-phenanthroline chemical structure ..... 43
Figure II. 4 Hyaluronan-cholesterol (HACH) ..... 57

**Chapter III**

Figure III. 1 IR spectrum of synthesis α-aminophosphonic acids (HAP1) ..... 80
Figure III. 2 IR spectrum of synthesis α-aminophosphonic acids (HAP2) ..... 80
Figure III. 3 UV–Vis absorption spectra of HAP1 and HAP in water ..... 82
Figure III. 4 $^{1}$H NMR spectrum for $HAP_1$ ..... 83
Figure III. 5 $^{1}$H NMR spectrum for $HAP_2$ ..... 84
Figure III. 6 $^{13}$C-NMR spectrum for $HAP_1$ ..... 85
Figure III. 7 $^{13}$C-NMR spectrum for $HAP_2$ ..... 86

**Chapter IV**

Figure IV. 1 Optimized structures of HAP1 and HAP2 at the B3LYP/6-31++G(d,p) level of theory. ..... 90
Figure IV. 2 Mulliken Atomic charges distribution of HAP1 and HAP2 calculated at ..... 94
Figure IV. 3 HOMO and LUMO orbitals of $HAP_1$ and $HAP_2$ calculated at B3LYP/6..... 96
Figure IV. 4 Molecular electrostatic potential surface (MESP) of $HAP_1$ and $HAP_2$ calculated at B3LYP/6-31G(d,p) level. ..... 99
Figure IV. 5 Experimental (Red) and Theoretical FTIR (Black) spectrums of $HAP_1$ and $HAP_2$ calculated at B3LYP/6-31G(d,p) level. ..... 103
Figure IV. 6 Calculated UV–Vis spectrum of $HAP_1$ and $HAP_2$ using TD-DFT at the B3LYP/6-31++G(d,p) level..... 106
Figure IV. 7 Molecular orbital (MO) of $HAP_1$ promotions contributing to each transition state. ..... 108
Figure IV. 8 Molecular orbital (MO) of $HAP_2$ promotions contributing to each transition state. ..... 109

**Chapter V**

Figure V. 1 Interactions for $HAP_1$ within the Lipoxygenase ..... 114
Figure V. 2 3D Interactions for $HAP_2$ within the Lipoxygenase..... 115
Figure V. 3 3D Interactions for $HAP_1$ within the Superoxide Dismutase ..... 117
Figure V. 4 3D Interactions for $HAP_2$ within the Superoxide Dismutase ..... 118
Figure V. 5 3D Interactions for $HAP_1$ within the Catalase ..... 120
Figure V. 6 3D Interactions for $HAP_2$ within the Catalase ..... 121
Figure V. 7 3D Interactions for $HAP_1$ within the Glutathione Peroxidase..... 122
Figure V. 8 3D Interactions for $HAP_2$ within the Glutathione Peroxidase..... 124
Figure V. 9 The major microspecies output from Marvin represents the dominant protonation states of $HAP_2$ at pH 8 (physiological pH). ..... 125
Figure V. 10 The major microspecies output from Marvin represents the dominant protonation states of $HAP_1$ at pH 8 (physiological pH). ..... 125
Figure V. 11 Interactions of $HAP_2$ microspecie (pH 8) within the Lipoxygenase ..... 127
Figure V. 12 Interactions of $HAP_1$ microspecie (pH 8) within the Lipoxygenase ..... 127

**Chapter VI**

Figure VI. 1 DPPH Antioxidant activity of selected single antioxidant compounds ($HAP_1$, $HAP_2$, BAH, and BHT in methanol 100 %) (n = 3). ..... 141
Figure VI. 2 ABTS Antioxidant activity of selected single antioxidant compounds ($HAP_1$, $HAP_2$, BAH, and BHT in methanol 100 %) (n = 3). ..... 144
Figure VI. 3 Absorbance vs. concentration dose-response curves for $HAP_1$, $HAP_2$, BHA, and BHT in the phenanthroline assay..... 146
Figure VI. 4 FRAP dose-response curves for $HAP_1$, $HAP_2$, and ascorbic acid (absorbance at 593 nm vs. concentration) ..... 148
Figure VI. 5 DPPH Antioxidant activity synergy scores models of selected single antioxidant compounds (BHA,BHT) by Synergie Finder ..... 150
Figure VI. 6 DPPH Antioxidant activity synergy scores models of selected single antioxidant compounds ($HAP_1$, $HAP_2$) by Synergie Finder ..... 150
Figure VI. 7 ABTS Antioxidant activity synergy scores models of selected single antioxidant compounds ($HAP_1$,$HAP_2$) by Synergie Finder ..... 151
Figure VI. 8 ABTS Antioxidant activity synergy scores models of selected single antioxidant compounds (BHA, BHT) by Synergie Finder ..... 151

Figure VI. 9 2D synergy heatmaps of DPPH antioxidant assay combination $HAP_1$ and $HAP_2$ using ZIP and HAS model generated by SynergyFinder ..... 154
Figure VI. 10 2D synergy heatmaps of ABTS antioxidant assay combination HAP1 and HAP2 using ZIP and HAS model generated by SynergyFinder ..... 155
Figure VI. 11 synergy heatmaps of DPPH antioxidant assay combination to standard BHA and BHT using the ZIP and HAS model generated by SynergyFinder..... 156
Figure VI. 12 2D synergy heatmaps of ABTS antioxidant assay combination to standard BHA and BHT using the ZIP and HAS model generated by SynergyFinder ..... 156

**Chapter VII**

Figure VII. 1 Comparative Encapsulation Efficiency and Drug Loading of HAP1 and HAP2 at Different Drug Amounts..... 163
Figure VII. 2 Distribution of Nanohydrogel Particle Size in Hap1 and Hap2 with Different Drug Loadings ..... 165
Figure VII. 3 In-vitro drug release profile of $HAP_1$ and $HAP_2$ at PH = 7.5 ..... 165
Figure VII. 4 Early-phase (0–4h) release kinetics of HAP1 (blue) and HAP2 (orange), showing experimental model fits (Higuchi – A; Korsmeyer–Peppas – B..... 167
Figure VII. 5 Late-phase (4–28h) release kinetics of HAP1 (blue) and HAP2 (orange), showing experimental model fits (Higuchi – A; Korsmeyer–Peppas – B). ..... 168

# List Of Tables

## Chapter I

Table I. 1 Comparative Overview of Catalysts, Reaction Times, and Yields in Organophosphonate Synthesis. ..... 15
Table I. 2 Synthesis of organophosphonates via Kabachnik–Fields Protocol under Microwave Irradiation under Neat Conditions ..... 16
Table I. 3Antimicrobial and Antifungal Activities of Compounds with Mechanistic Insights ..... 22
Table I. 4 Organohosphonate Analogs as Valuable Candidates for Antiviral Drug Development. ..... 24
Table I. 5 Examples of organophosphonate derivatives and their anticancer potential ..... 26
Table I. 6 Mechanistic Insights of Organophosphonates in Anti-Inflammatory Activity... 27
Table I. 7 Mechanisms of Organophosphonates Phosphonates in Antioxidant Activity. ... 28
Table I. 8 Structural Features Enhancing Antioxidant Efficacy of organophosphonates. .. 29

## Chapter II

Table II. 1 List of Organophosphorus Compounds and Their Specifications. ..... 39
Table II. 2 Commonly used solvents, their sources, and purity levels in this research. ..... 40
Table II. 3 Common additives used in this research, along with their sources, purity levels, and typical applications. ..... 41
Table II. 4 Principal Aspects of the Bacterial Strains Used in Antibacterial Screening ..... 44

## Chapter III

Table III. 1 Comparison of Reaction Time and Yields for $HAP_1$ and $HAP_2$ ..... 73
Table III. 2 Qualitative Solubility of Synthesized α-amino phosphonic acids HAP1 and HAP2 vs. Starting Reagent ..... 77
Table III. 3 Melting Points of the Synthesized α-amino phosphonic acids $HAP_1$ and $HAP_2$ ..... 78
Table III. 4 frontal ratios of synthesis α-amino phosphonic acids $HAP_1$ and $HAP_2$ ..... 78
Table III. 5 IR Absorption Bands for $HAP_1$ and $HAP_2$ ..... 81

## Chapter IV

Table IV. 1 Optimized geometric parameters (bond lengths (A°)/bond Angles (°)) of $HAP_1$ and $HAP_2$ calculated at B3LYP/6-31G(d,p) level. ..... 91

Table IV. 2 Distribution of Mulliken atomic charges of HAP1 and HAP2 calculated at B3LYP/6-31G++(d,p) level. 93
Table IV. 3 Electrical dipole moments of HAP1 and HAP2 calculated at B3LYP/6-31G(d,p) level 95
Table IV. 4 Energies of HOMO, LUMO, energy gap, and global chemical reactivity indices of synthesized HAP1 and HAP2. 98
Table IV. 5 Selected comparison of some theoretical and experimental wavenumbers (cm−1) of the HAP1 and HAP2 molecules. 102
Table IV. 6 Calculated thermodynamic parameters of $HAP_1$ and $HAP_2$ employing the B3LYP/6-311++G(d,p)level. 105
Table IV. 7 TD-DFT predicted Transition states energies, wavelengths, and oscillator strengths. 107

**Chapter V**

Table V. 1 Interactions Predicted for $HAP_1$ within the Lipoxygenase 1n8Q Active Site. 113
Table V. 2 Key Interactions Predicted for $HAP_2$ in the Lipoxygenase 1n8Q Active Site 114
Table V. 3 Comparison of Docking Parameters and Key Interactions for $HAP_1$ and $HAP_2$ in Lipoxygenase 1n8Q 116
Table V. 4 Interactions Predicted for $HAP_1$ within the SOD (5YTO) Active Site 117
Table V. 5 Interactions Predicted for $HAP_2$ within the SOD (5YTO) Active Site 118
Table V. 6 Interactions Predicted for $HAP_1$ with Catalase (1DGF) 119
Table V. 7 Interactions Predicted for HAP2 with Catalase (1DGF) 120
Table V. 8 Interactions Predicted for $HAP_1$ within Glutathione Peroxidase 122
Table V. 9 Interactions Predicted for $HAP_2$ with the Glutathione Peroxidase 123
Table V. 10 Interactions Predicted for $HAP_1$ (pH 8) within Lipoxygenase (1N8Q) 126
Table V. 11 Interactions Predicted for $HAP_2$ (pH 8) within Lipoxygenase (1N8Q) 128
Table V. 12 Lipophilicity & Water Solubility of $HAP_1$ and $HAP_2$ predicted by SwissADME 129
Table V. 13 Pharmacokinetics of $HAP_1$ and $HAP_2$ Predicted by SwissADME 130
Table V. 14 drug-likeness of $HAP_1$ and $HAP_2$ predicted by SwissADME 131
Table V. 15 Medicinal Chemistry Alerts of $HAP_1$ and $HAP_2$ predicted by SwissADME 131
Table V. 16 Absorption Profile of $HAP_1$ and $HAP_2$ predicted by pkCSM 132
Table V. 17 Distribution Profile of $HAP_1$ and $HAP_2$ predicted by pkCSM 133
Table V. 18 Metabolism Profile of $HAP_1$ and $HAP_2$ predicted by pkCSM 133

Table V. 19 Excretion Profile of $HAP_1$ and $HAP_2$ predicted by pkCSM..... 134
Table V. 20 Toxicity Profile of $HAP_1$ and $HAP_2$ Predicted by pkCSM ..... 135
Table V. 21 StopTox Toxicity Predictions Summary ..... 136

**Chapter VI**

Table VI. 1 DPPH $IC_{50}$ Values of Antioxidant Compounds ..... 141
Table VI. 2 ABTS $IC_{50}$ Values of Antioxidant Compounds ..... 144
Table VI. 3 $A_{50}$ Values of Antioxidant Compounds in the Phenanthroline Assay ..... 146
Table VI. 4 $A_{0.5}$ Values of Antioxidant Compounds in the FRAP Assay ..... 148
Table VI. 5 Synergy Scores for HAP1 and HAP2 Combination (α-amino phosphonic acids) in DPPH and ABTS assays..... 152
Table VI. 6 Synergy Scores for BHA and BHT Combination in DPPH and ABTS Assays ..... 153
Table VI. 7 The $HAP_1$ and $HAP_2$ antibacterial activity was evaluated by the disc diffusion method (Mean ± SD, n=3)..... 159

**Chapter VII**

Table VII. 1 Kinetic parameters for $HAP_1$ drug release derived from model fitting. ..... 169
Table VII. 2 Kinetic parameters for $HAP_2$ drug release derived from model fitting. ..... 169

**List of Schemes**

**Chapter II**

**Scheme II.1** Synthesis of (HAP1) and (HAP2) aminophosphonic acids via modified Irani-Moedritzer reaction..... 52

**Chapter III**

**Scheme III.1**Synthesis of α-Aminophosphonic Acids HAP1 and HAP2 via Conventional method ..... 72

**Scheme III.2** Synthesis of α-Aminophosphonic Acids HAP1 and HAP2 via microwave method ..... 73

**Scheme III.3** Proposed reaction mechanism for the α-aminophosphonic acid formation reaction (Pathway 1)..... 74

**Scheme III.4** Proposed reaction mechanism for the α-aminophosphonic acid formation reaction (Pathway 2)..... 75

# General introduction

# General Introduction

Organophosphonates (OPs) are a broad class of organophosphorus compounds characterized by the presence of a direct carbon–phosphorus (C–P) bond. This C–P linkage is exceptionally stable and hard to cleave, conferring resistance to chemical and enzymatic degradation and endowing organophosphonates with unique chemical properties such as strong metal-chelating ability [1]. Due to their stability and versatility, organophosphonates have wide-ranging applications in agriculture, industry, and medicine [2-4]. For instance, massive quantities of OPs are used as agrochemicals. The herbicide glyphosate [5], one of the most recognized organophosphonates worldwide, owes its efficacy to the robust C–P bond in its structure. In industrial settings, due to their durability, organophosphonates serve as flame retardants, corrosion inhibitors, and plasticizers [3]. Most notably, in the biomedical arena, organophosphonates have garnered significant interest for their medicinal chemistry applications, given their high biological activity and capacity to mimic natural phosphate [6].

Indeed, many organophosphonates exhibit potent biological activity and have been developed as therapeutic agents. Several phosphonate-based drugs are already in clinical use for the treatment of various diseases: for example, the antiviral nucleotide analogues adefovir and cidofovir contain a phosphonate group to resist cleavage by cellular enzymes [7].

Furthermore, organophosphonates have shown broad-spectrum pharmacological profiles. Owing to such successes, organophosphonate motifs are now ubiquitous in pharmaceutical research, appearing in drug candidates across antiviral, anticancer, and antimicrobial areas [8-10]. underscores the importance of advancing our understanding of their chemistry and biology.

A rich variety of synthetic approaches has been developed to incorporate the phosphonate group into organic molecules, reflecting the synthetic versatility of the C–P bond. Classic methods such as the Michaelis–Arbuzov [11-12] reaction and the Horner–Wadsworth–Emmons olefination [13-14] have long provided chemists with reliable routes to construct phosphonate-containing frameworks. These traditional reactions, together with others like the Kabachnik–Fields [15-16] condensation for α-aminophosphonates, and Irani-

Moedritzer [17] for amino phosphonic acids, established the foundational toolkit for phosphonate synthesis.

In recent years, modern catalytic and radical-based strategies have further expanded this toolkit. Transition-metal catalysis, in particular, has enabled milder and more flexible C–P bond-forming processes: for example, palladium-catalyzed cross-coupling methods [18] now permit the efficient assembly of complex organophosphonates with broad functional group tolerance. Such innovations have made Pd-catalyzed [19] C–P coupling an "inevitable" and powerful tool for generating diverse phosphonate architectures under relatively mild conditions. Likewise, emerging photochemical and radical-mediated phosphonylation techniques [20] allow the introduction of phosphonate groups into aliphatic frameworks that were previously challenging to functionalize, further demonstrating the adaptability of organophosphonate chemistry.

Through these advances, researchers can synthesize a wide array of organophosphonates with varied structures, tailoring their molecular frameworks for desired properties. This synthetic flexibility is crucial for exploring structure–activity relationships in medicinally active phosphonates and for accessing new compounds that could serve as enzyme inhibitors, prodrugs, or even catalysts. At the same time, the profusion of synthetic methodologies speaks to the continuing need for innovation: each new reaction broadens the chemical space of accessible phosphonates, opening opportunities to discover novel compounds with improved biological profiles.

Despite this progress, there remain significant challenges in the chemistry and application of organophosphonates. In synthesis, one enduring hurdle is the creation of chiral organophosphonates with precise stereochemical control [21]. Chiral phosphonate compounds are highly sought after in pharmaceuticals and even as ligands or catalysts, yet their preparation often requires laborious routes and chiral auxiliaries or catalysts.

Organophosphonate drugs often exhibit low cell membrane permeability and poor oral absorption because the phosphonate group is ionized at physiological pH [22], hindering passive diffusion. For example, potent phosphonate-based enzyme inhibitors like 2-PMPA show minimal cellular uptake and require prodrug derivatization to mask the charged

phosphonate and enable transport [23]. Medicinal chemists have responded by devising various prodrug strategies to temporarily neutralize the phosphonate's charge, but ensuring efficient activation and distribution of such prodrugs is an additional layer of complexity. These considerations

mean that when designing organophosphonates as drug candidates, one must strike a careful balance between stability, potency, and pharmacokinetic properties. Overall, the challenges associated with stereochemistry, reactivity, and drug delivery of phosphonates provide a clear motivation for continued research. By addressing these issues, chemists can unlock the full potential of organophosphonates and expand their applicability even further.

In light of the above context, this PhD thesis is therefore structured like

Chapter I: Bibliographic Review

In this chapter, I will provide an in-depth review of the current state of knowledge surrounding organophosphonates, including their synthesis, biological activities, and applications. The chapter will also discuss their significance in drug design, enzyme inhibition, and their use in agriculture. A detailed exploration of the synthesis methods and challenges of organophosphonates, including classical and modern synthetic strategies, will be presented. Furthermore, the relevance of computational tools like Density Functional Theory (DFT) and molecular docking in enhancing organophosphonate design will be explored. The chapter will conclude with a discussion on nanodrug delivery systems, focusing on how organophosphonates can be delivered efficiently using nanocarriers such as nanohydrogels and liposomes.

Chapter II: Materials and Methods

This chapter will outline the materials, chemicals, and equipment used in my research, alongside a detailed description of the experimental methods employed. I will detail the synthetic methods used for the preparation of organophosphonates, followed by the characterization techniques (e.g., IR, NMR, UV-Vis) for determining the purity and structure of synthesized compounds. Computational studies using Density Functional Theory (DFT) will be discussed, along with molecular docking simulations for predicting the binding affinity of synthesized compounds with target enzymes. The methodology for evaluating the

drug-likeness properties and ADME-T predictions will also be described, as well as the synthesis of nanocarriers and in vitro release testing of encapsulated organophosphonates.

Chapter III: Synthesis and Evaluation of Organophosphonates

In this chapter, I will focus on the synthetic procedures for preparing the α-aminophosphonic acids (HAP1 and HAP2). I will discuss the reaction conditions, reagents used, and optimization strategies for maximizing yield and purity. After synthesis, I will present preliminary and advanced characterization of these compounds, including solubility tests, melting points, TLC, and spectroscopic analyses (FT-IR, UV-Vis, NMR). This chapter aims to validate the synthetic process and provide a comprehensive profile of the synthesized compounds, setting the stage for their biological and computational evaluation.

Chapter IV: Computational Approach Using DFT

This chapter will explore the computational methods used to analyze the electronic structure of the synthesized organophosphonates, specifically using Density Functional Theory (DFT). I will discuss the key parameters, such as geometric optimization, Mulliken charges, dipole moments, and frontier molecular orbital analysis, which provide insight into the stability and reactivity of the compounds. The use of TD-DFT to investigate excited states and transition energies will be covered in depth, alongside the characterization of vibrational modes and thermodynamic properties. This computational data will aid in understanding the molecular behavior of HAP1 and HAP2 and predict their interactions with biological targets.

Chapter V: Advancing Drug Discovery: Docking & ADME-T

This chapter will focus on the use of molecular docking simulations to investigate the interaction of HAP1 and HAP2 with several antioxidant enzymes and drug targets such as lipoxygenase (1N8Q), superoxide dismutase (5YTO), catalase (1DGF), and glutathione peroxidase (2P31). I will describe how the synthesized organophosphonates bind to these enzymes and explore their potential as enzyme inhibitors. I will also present ADME-T predictions, assessing their absorption, distribution, metabolism, excretion, and toxicity profiles using SwissADME, pkCSM, and ProTox software tools. This chapter will demonstrate how computational approaches can enhance the design and selection of promising drug candidates.

Chapter VI: Biological Activities

In this chapter, I will present the biological evaluation of HAP1 and HAP2, including their antioxidant activity using multiple assays like DPPH, ABTS, and FRAP. I will also examine the antibacterial activity of the compounds against a range of Gram-positive and Gram-negative bacteria, as well as their anticholinesterase activity. The chapter will further explore the synergy between the organophosphonates and other antioxidant agents to assess the combinatory effects in these biological systems. This section aims to correlate the computational findings with experimental data and to evaluate the overall pharmacological potential of the synthesized organophosphonates.

Chapter VII: Nanodrug Delivery and Emerging Challenges

This chapter will explore the development of nanodrug delivery systems for efficiently transporting HAP1 and HAP2 to target tissues. I will discuss the formulation of nanohydrogels to encapsulate the organophosphonates, ensuring enhanced solubility and stability. I will also investigate the in vitro release kinetics of the encapsulated drugs, analyzing the drug loading and encapsulation efficiency. This chapter aims to explore the feasibility of using nanotechnology to improve the pharmacokinetics and bioavailability of the organophosphonates, facilitating their application in therapeutic settings.

I

# Bibliographic Review

# I Bibliographic Review

## I.1 Introduction

Organophosphonates, which contain a strong carbon–phosphorus (C–P) bond, are a remarkably versatile and helpful group of compounds. Their stability sets them apart from regular phosphate esters. As a result, they have found roles in a wide range of fields from designing new medicines to creating effective agricultural chemicals and advanced materials. Because they don't break down as easily in water, organophosphonates can be robust building blocks in drug discovery, enzyme inhibitors, antiviral and antibacterial treatments, and herbicides [1–3]. Outside of medicine, they are also valuable in materials science, where they help prevent corrosion, control mineral deposits (scaling), and can even be used to build metal-organic frameworks [4,5].

Organophosphonates are crucial to medicinal chemistry because their structure resembles the natural phosphate groups in many biological molecules and processes. These phosphates are essential to energy transfer (such as in ATP), sending signals inside cells (through protein phosphorylation), and forming the backbone of DNA and RNA [2,6]. By imitating these natural phosphate groups, organophosphonates can interact with proteins, enzymes, and nucleic acids in ways that either inhibit or adjust their activity.

The field has also benefited greatly from modern research tools and techniques. Advances in synthetic chemistry methods make it easier to create new organophosphonates, while computational approaches, like Density Functional Theory (DFT) and molecular docking, help predict how these compounds will behave. Early assessments of their drug-like properties, including how they are absorbed, distributed, metabolized, and eliminated from the body and their potential toxicity (ADME-T), make it possible to identify promising drug candidates before investing heavily in development. Together, these improvements have made the design of organophosphonate-based treatments more rational, efficient, and successful than ever.

This chapter takes a comprehensive look at the literature on organophosphonates. It explores their historical background, the variety of structures, how they're made, how they're characterized, and their many biological activities. It also delves into computational studies and the details of predicting their ADME-T properties. This broad overview sets the

stage for the new organophosphonate derivatives designed, synthesized, and tested in this PhD project.

## I.2 Historical Overview and Classification of Phosphonates

### I.2.1 Historical Development

The history of organophosphonate chemistry spans over a century, with its roots in the late 19th century during the early exploration of phosphorus-containing compounds such as phosphites and phosphates [7]. By the 1930s, the synthesis of phosphonic acids and esters laid a foundational framework for subsequent developments in amino phosphonate research [8]. In the mid-20th century, significant breakthroughs occurred, including the first synthesis of α-amino phosphonates in 1945, where these compounds were reported as analogs of α-amino acids [9]. The cornerstone of α-amino phosphonate synthesis was established in 1952 with the introduction of the Kabachnik–Fields reaction, a three-component condensation of an aldehyde, an amine, and a phosphite, which remains a widely used method in the field [10-11].

During the 1960s and 1970s, efforts focused on elucidating the reaction mechanisms of the Kabachnik–Fields reaction and diversifying α-amino phosphonates through variations in aldehydes, amines, and phosphites [12]. The 1980s marked a significant shift towards their medicinal applications, as α-amino phosphonates were recognized as enzyme inhibitors and structural analogs of amino acids [13]. This period also saw the introduction of asymmetric catalysts, enabling the synthesis of chiral α-amino phosphonates, which have profound implications in pharmaceutical development, particularly in the study of proteases and phosphatases [14].

The 1990s brought advancements in green chemistry and catalytic methodologies. The hydrophosphonylation of imines, involving the direct addition of phosphites to imines under mild conditions, emerged as an alternative to the Kabachnik–Fields reaction [15]. The use of Lewis acids such as $TiCl_4$ and $AlCl_3$ catalyzed these reactions, while solvent-free and microwave-assisted approaches enhanced efficiency and sustainability [16]. Building on these innovations, the 2000s introduced advanced catalysis, including the use of chiral organocatalysts and metal complexes for asymmetric synthesis [17]. Ionic liquids and

heterogeneous catalysts gained prominence, enabling environmentally friendly reactions and expanding the range of substrates to include ketones and heterocyclic compounds [18].

In the 2010s, synthetic strategies became even more diverse with the development of one-pot multicomponent reactions and bio-inspired enzymatic synthesis [19]. Applications expanded beyond pharmaceuticals to include material sciences, agriculture, and advanced medicinal chemistry. The 2020s have seen the rise of modern innovations like photocatalysis and electrocatalysis, utilizing visible light and electric currents for efficient synthesis [20]. A focus on green and sustainable chemistry has driven the adoption of solvent-free, aqueous, and recyclable catalytic systems, along with bio-based aldehydes and amines [21]. Current research highlights the potential of α-amino phosphonates in antiviral drug development, nanomaterials, and biocompatible coatings, while enzymatic and biomimetic approaches continue to expand their functional diversity for use in pharmaceuticals, agriculture, and functional materials [22].

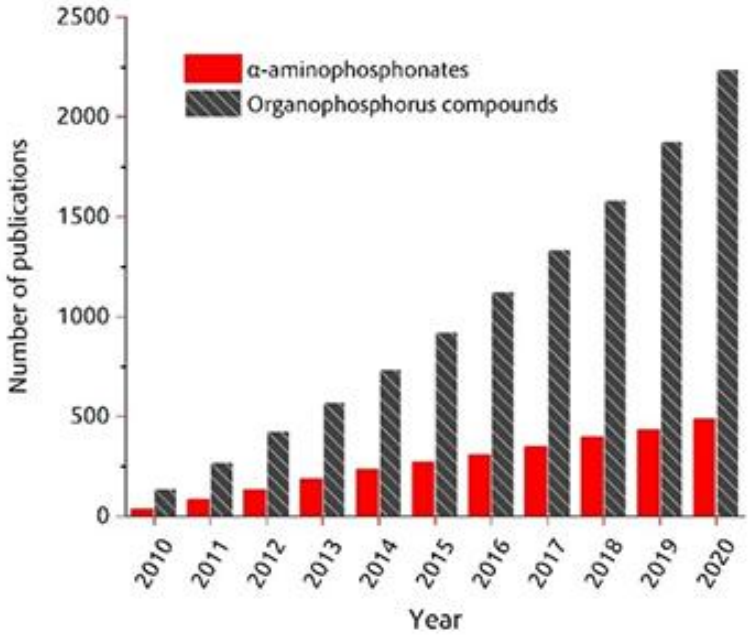


**Figure I. 1** The number of publications of organophosphorus compounds and α-Aminophosphonates synthesis in the last decade. (Source: Science Direct)

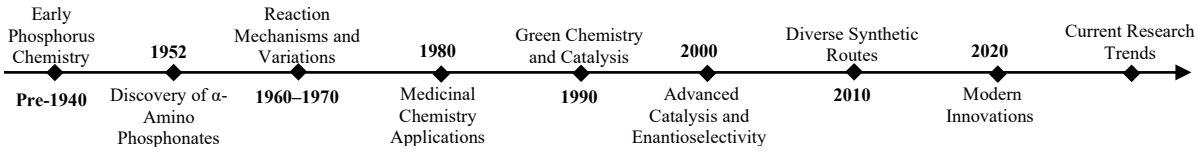


**Figure I. 2** Timeline illustrating the history of organophosphonates.

### I.2.2 Structural Diversity and Nomenclature

Phosphonates can be classified based on various criteria, including the oxidation state of phosphorus, the nature of substituents, the presence of heterocycles, and their functional group patterns. Common subtypes include:

- Phosphonate monoesters and diesters: $R–P(=O)(OR_1)_2$

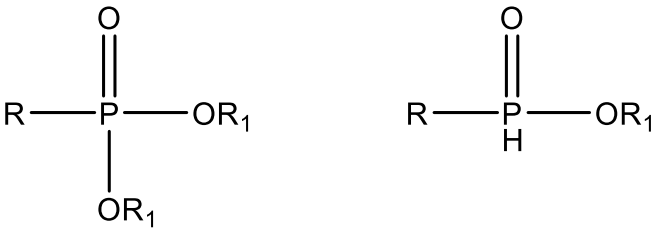


**Figure I. 3** Phosphonate mono-di ester.

- Phosphonic acids: $R–P(=O)(OH)_2$

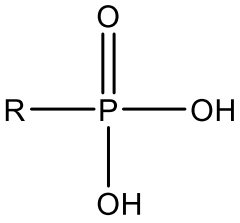


**Figure I. 4** Phosphonic acids.

- α-Aminophosphonates: Compounds with a P–C–N motif, often generated from the Kabachnik–Fields reaction [10-11].

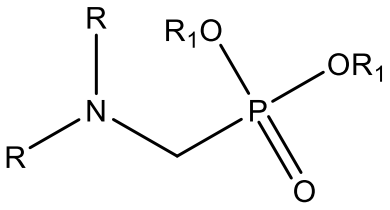


R= H , alkyle or alyle

$R_1$= H , alkyle or alyle

**Figure I. 5** α-Aminophosphonates.

α-Hydroxyphosphonates: Compounds with a P–C–O motif

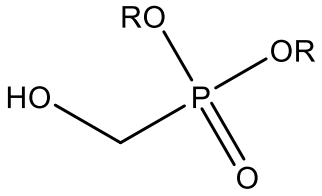


R= H , alkyle or alyle

**Figure I. 6** α-Hydroxyphosphonates.

Bisphosphonates: Compounds bearing two phosphonate groups on a single carbon, widely used in bone disease treatments [23–25].

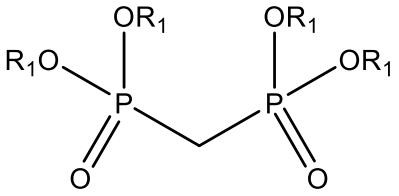


$R_1$= H , alkyle or alyle

**Figure I. 7** Bisphosphonates.

Phosphonates with heterocyclic frameworks: Bridging phosphonate groups onto heteroaromatic rings or fused systems to achieve novel bioactivities [26,27].

The structural diversity of organophosphonates is a key advantage, enabling the rational design of compounds tuned for specific biochemical targets or materials applications.

## I.3 Synthetic Strategies for Organophosphonates

### I.3.1 Classical Reactions

#### I.3.1.1 Michaelis–Arbuzov Reaction :

A cornerstone of phosphonate synthesis involves the rearrangement of trialkyl phosphites with alkyl halides to yield phosphonate esters [28–30]. This reaction provides a clean and versatile route to a wide range of substituted phosphonates, setting the stage for subsequent functionalization.

Hydrolysis of the resulting phosphonate ester can afford the corresponding phosphonic acid, expanding the accessible structural space.

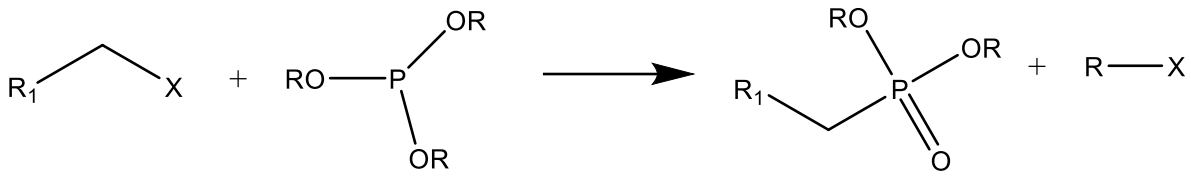


X= Cl, Br,I

R and $R_1$ = alkyl or aryl

**Figure I. 8** Michaelis–Arbuzov reaction**.**

### I.3.1.2 Kabachnik–Fields Reaction:

The three-component condensation of an aldehyde, an amine, and a phosphorus (III) reagent (e.g., dialkyl phosphite) yields α-aminophosphonates [10,11]. This one-pot synthesis is highly attractive for producing biologically relevant intermediates, including potential enzyme inhibitors and amino acid mimics.

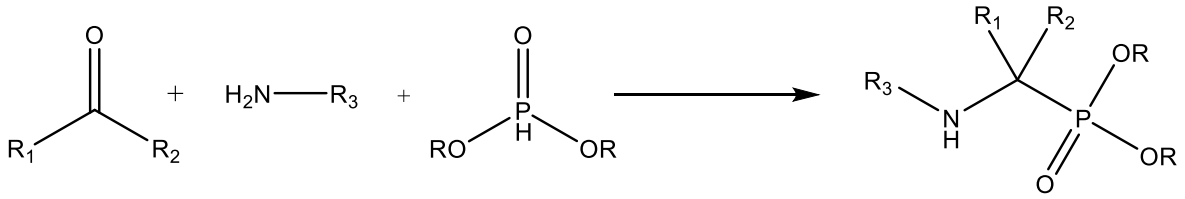


with : R,$R_1$,$R_2$,$R_3$ = H ; alkyles or aryles ....

**Figure I. 9** Kabachnik–Fields reaction.

### I.3.1.3 Moedritzer-Irani Reaction

The Moedritzer-Irani reaction is a classic and efficient method for the synthesis of α-amino phosphonates, a functional group of significant importance in organic and medicinal chemistry. First described in 1966, [31] this reaction involves the interaction of an aldehyde, ammonia or a primary amine, and a dialkyl phosphite under mild conditions. The mechanism includes the initial condensation of the aldehyde and ammonia to form an imine (Schiff base), followed by a nucleophilic addition of the phosphite to the imine, leading directly to the α-amino phosphonate product. This method is particularly attractive due to its simplicity, mild reaction conditions, and the frequent absence of catalysts. Typically performed in polar solvents such as water or methanol and at room temperature or with gentle heating, it is compatible with a wide range of substrates. The α-amino phosphonates synthesized via this reaction find critical applications in developing bioactive molecules, particularly as amino acid analogs, enzyme inhibitors, and antimicrobial agents [32]. The Moedritzer-Irani

reaction remains an essential approach for phosphonate functionalization, combining practicality and versatility for research in organic chemistry.

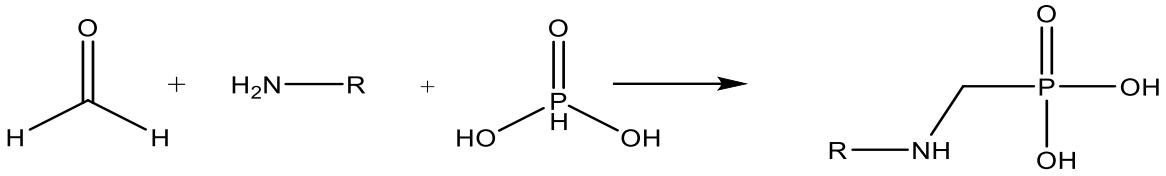


R= H , alkyles or aryles ....

**Figure I. 10** The Moedritzer-Irani reaction

### I.3.1.4 Pudovik Reaction

The Pudovik reaction, a cornerstone in organophosphorus chemistry, enables the formation of C–P bonds through the nucleophilic addition of phosphites to electrophilic carbon centers, such as aldehydes or imines, to afford α-hydroxyphosphonates and α-amino phosphonates. [33–34]. Advances in catalytic strategies, including asymmetric approaches, have further broadened the utility of the Pudovik reaction, allowing access to chiral phosphorus-containing compounds with tailored properties. As a result, this transformation remains an indispensable tool, continually expanding its role in complex molecule construction and sustainable chemical synthesis [35–36].

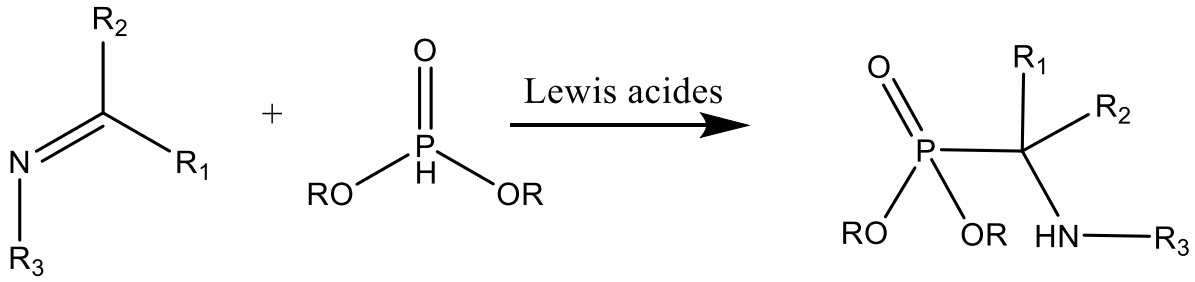


**Figure I. 11** Pudovik reaction.

## I.3.2 Modern Reactions

### I.3.2.1 Green Chemistry Initiatives:

Use of Water or Ionic Liquids as Solvents: Employing water or ionic liquids as reaction media has been explored to minimize environmental impact. For instance, certain studies have utilized ionic liquids like [bmim]$AlCl_4$ in the Kabachnik–Fields reaction, offering an eco-friendlier approach [37]

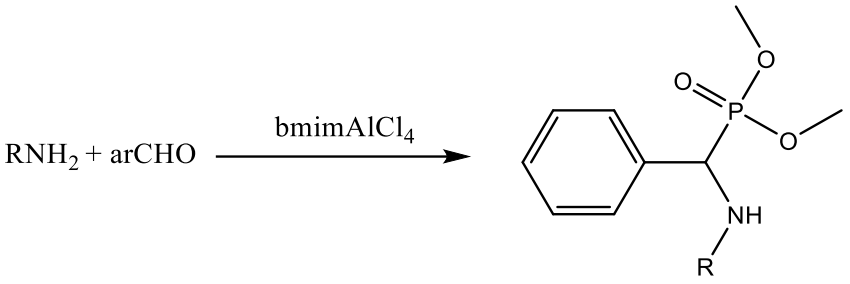


**Figure I. 12 [**bmim]AlCl4 system in Kabachnik–Fields reaction.

### I.3.2.2 Catalytic Enhancements :

Acid Catalysts: Brønsted acids such as p-toluenesulfonic acid (p-TsOH) and phosphoric acid ($H_3PO_4$) have been used to improve reaction yields. These catalysts facilitate the condensation process, leading to higher efficiency. [38]

Metal Catalysts: Lewis acids like titanium tetrachloride ($TiCl_4$) and zinc chloride ($ZnCl_2$) have effectively controlled the reaction. For example, zinc chloride has been utilized as a catalyst in the Kabachnik–Fields reaction, resulting in good yields under mild conditions. [39]

**Table I. 1** Comparative overview of catalysts, reaction times, and yields in organophosphonate synthesis.

| Compounds | Catalysts | Reaction Time (min) | Yield % | Ref |
|---|---|---|---|---|
| 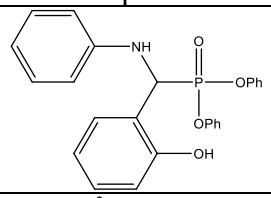 | $ZnCl_2$ | 42 | 70 | [39[a]] |
| 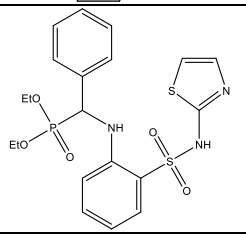 | $FeCl_3$ | 180 | 95 | [39[b]] |
| 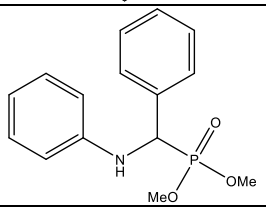 | $TiCl_4$ | 10 | 93 | [39[c]] |
| 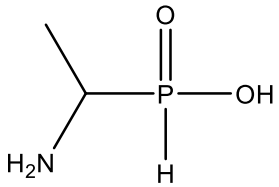 | $H_3PO_4$ | 60 | 91 | [39[d]] |
| 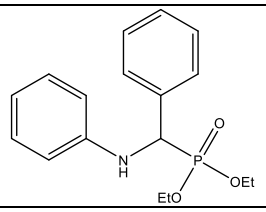 | $LnCl_3$ | 60 | 99 | [39[e]] |

### I.3.2.3 Microwave and Ultrasound-Assisted Synthesis:

Microwave irradiation is a powerful technique for speeding up reactions and boosting yields. In particular, microwave-assisted Kabachnik–Fields reactions carried out without solvents have proven highly effective for synthesizing organophosphonates. Using microwave heating instead of traditional methods offers significant advantages, especially under neat conditions. This method supports green chemistry principles by eliminating the use of solvents, making it both efficient and environmentally friendly. Additionally, microwave irradiation makes it possible to carry out reactions that would normally require harsh conditions or take too long to be practical, making it a valuable tool for modern synthetic chemistry [40].

**Table I. 2** Synthesis of organophosphonates via Kabachnik–Fields protocol under microwave irradiation under neat conditions

| Compounds | Microwave irradiation | | Conventional heating | |
|---|---|---|---|---|
| | Time (min) | Yield (%) | Time (h) | Yield (%) |
| 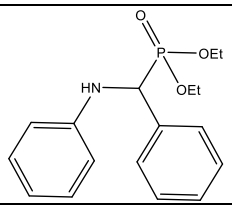 | 3 | 85 | 6 | 70 |
| 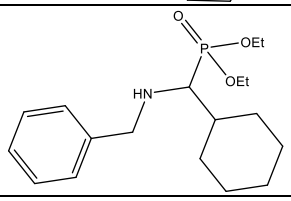 | 4 | 85 | 6 | 78 |
| 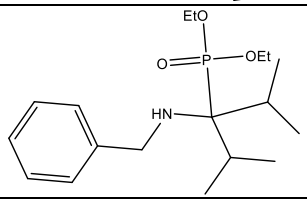 | 20 | 73 | 72 | 0 |
| 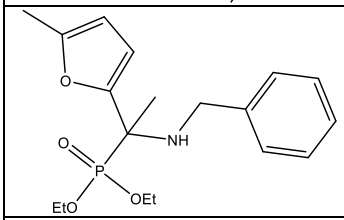 | 19 | 84 | 20 | 50 |
| 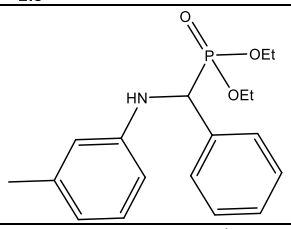 | 4-8 | 92 | 4 | 75 |
| 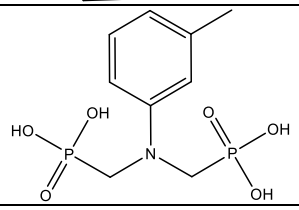 | 4-8 | 87 | 6 | 68 |
| 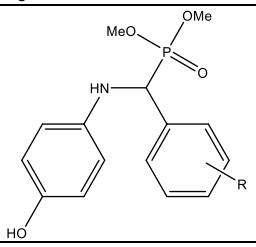 | 4-6 | 87-96 | 6-4 | 80-64 |

A recent study highlights a quick and efficient method for synthesizing aromatic organophosphonates using ultrasound. The reaction combines carbonyl compounds, amines, and triethyl phosphite without any solvent or catalyst and works at room temperature. Impressively, the products were obtained in excellent yields (81–99%) within just 20–45 seconds. However, when the same reactions were carried out in organic solvents, the yields dropped significantly. While this method is considered versatile, it struggles with ketones, producing only trace amounts or no product at all, even with extended reaction times [41].

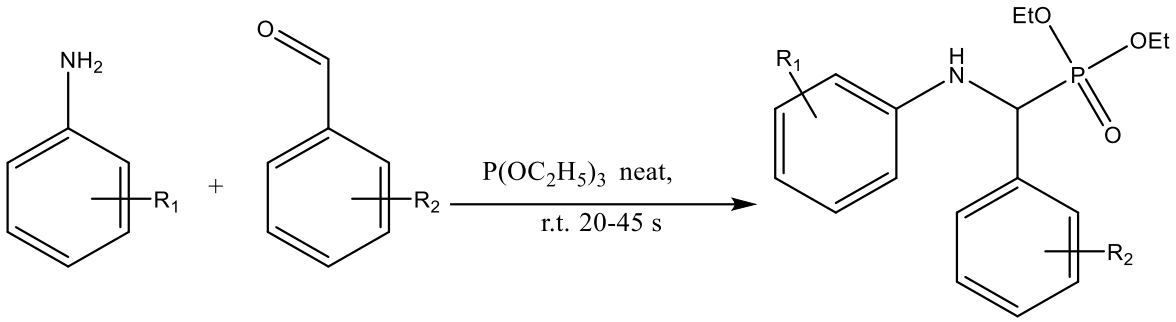


**Figure I. 13** Catalyst and solvent-free ultrasound promoted a rapid protocol for the one-pot synthesis of organophosphonates at room temperature.

### I.3.2.4 Asymmetric approaches

These methodologies highlight the diverse strategies employed in the asymmetric synthesis of organophosphonates, each offering unique advantages regarding enantioselectivity and applicability.

**Asymmetric Hydrophosphonylation of Imines:**

The addition of dialkyl phosphites to imines, known as the aza-Pudovik reaction, is a common approach for synthesizing organophosphonates. Chiral catalysts, including chiral Brønsted acids and chiral phosphoric acids, have been employed to induce enantioselectivity in this reaction. For instance, the use of a chiral Brønsted acid derived from BINOL has facilitated the enantioselective three-component hydrophosphorylation of aldehydes, amines, and phosphites [42-43].

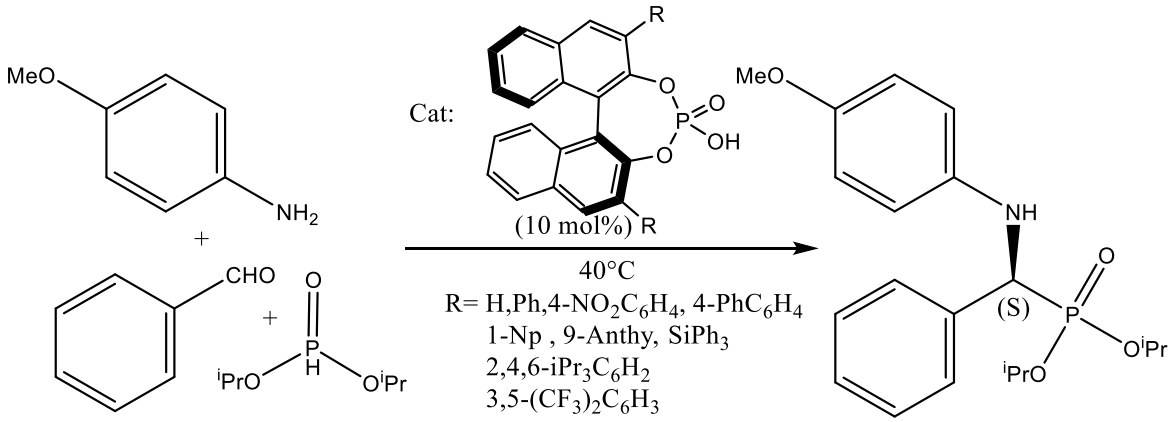


**Figure I. 14** Screening of the catalysts (from BINOL) and the reaction conditions for the three-component reaction.

**Diastereoselective Synthesis:**

Approaches involving the addition of nucleophiles to phosphorylated imines or the hydrophosphorylation of imines have been developed for the diastereoselective synthesis of tetrasubstituted organophosphonates. These methods enable the formation of multiple stereocenters with high selectivity [44].

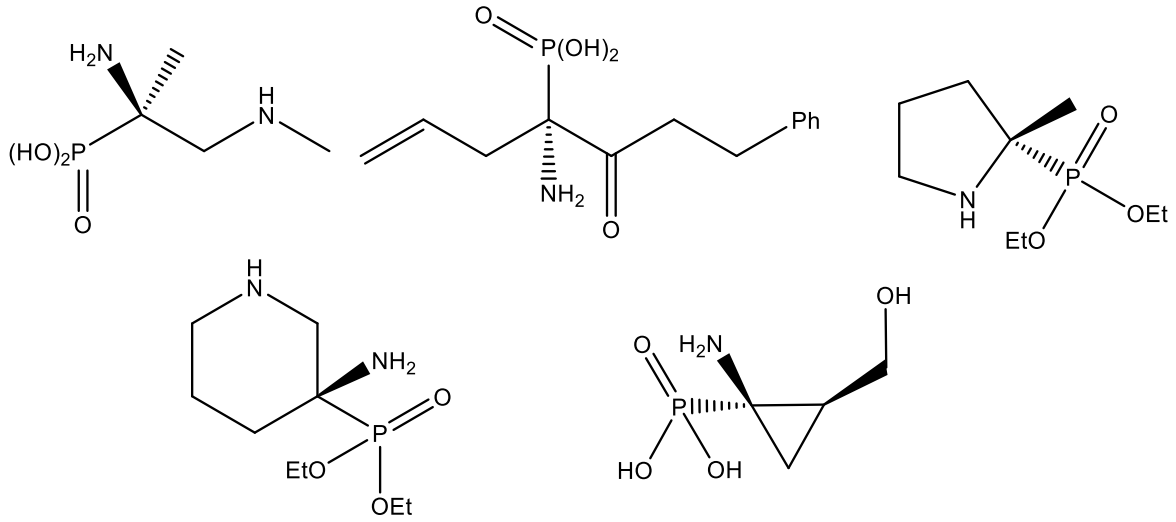


**Figure I. 15** Some examples of stereo-controlled synthesis of tetra-substituted organophosphonates.

### I.3.2.5 Biocatalytic and Enzymatic Methods :

Biocatalytic and enzymatic methods have emerged as sustainable approaches for the synthesis of organophosphonates, offering high selectivity under mild conditions. Notable methodologies include:

Enzymatic Kinetic Resolution: Penicillin G acylase has been employed to resolve racemic mixtures of α-aminoalkylphosphonic acids and α-aminophosphonates, yielding enantiomerically enriched products. This method achieves high enantiomeric excess but is limited to a maximum yield of 50% due to its kinetic resolution nature [45].

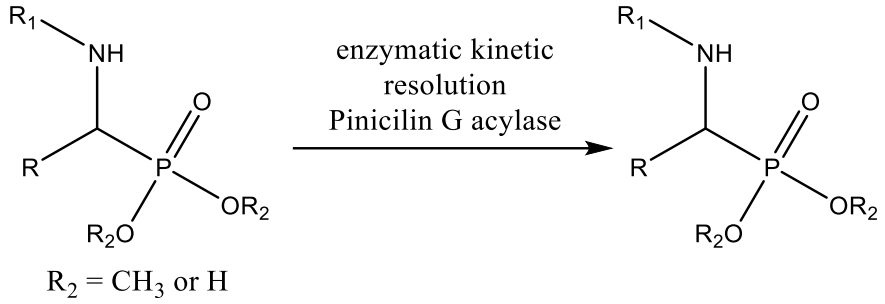


**Figure I. 16** The enzymatic kinetic resolution of racemic mixtures of α-aminoalkylphosphonic acids and α-aminophosphonates.

Lipase-Catalyzed Kabachnik–Fields Reaction: Candida antarctica lipase B (CAL-B) has been utilized to catalyze the Kabachnik–Fields reaction, facilitating the formation of organophosphonates from aniline derivatives. This biocatalytic approach operates under mild conditions and exemplifies the integration of enzymatic catalysis in multicomponent reactions [46].

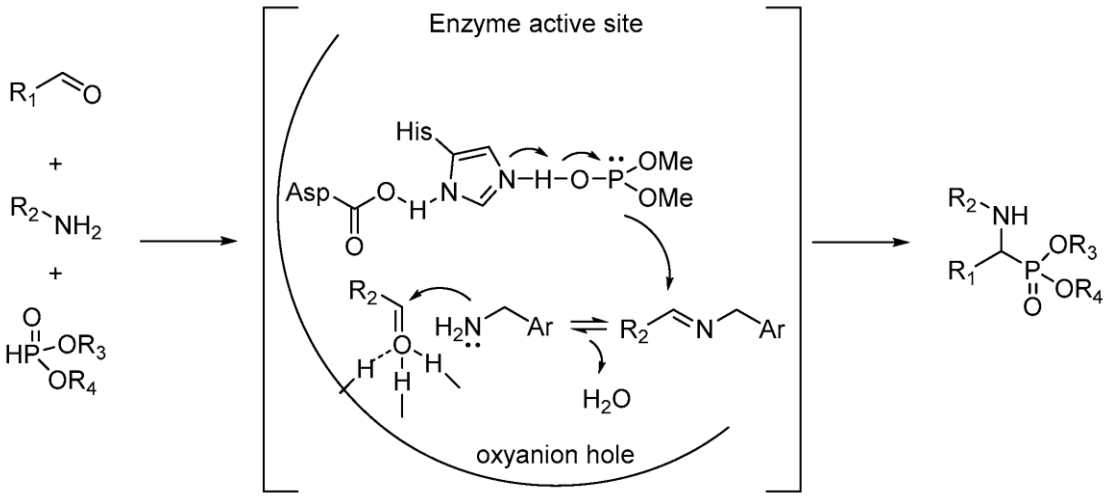


**Figure I. 17** Lipase-Catalyzed Kabachnik–Fields reaction

These modern strategies underscore the potential in synthesizing α-aminophosphonates, aligning with green chemistry principles by reducing the need for harsh reagents and conditions.

### I.3.3 Characterization and Purification

Typical characterization involves $^{1}H$, $^{13}C$, and $^{31}P$ NMR spectroscopy to confirm the presence and environment of the phosphonate group [47]. Infrared (IR) spectroscopy detects P=O stretching frequencies, while mass spectrometry (MS) and elemental analysis confirm molecular weight and purity. X-ray crystallography, where applicable, provides three-dimensional structural insight [48,49].

## I.4 Biological Activities

Organophosphonates exhibit a broad spectrum of biological activities.

### I.4.1 Enzyme Inhibition

The stable C–P bond in organophosphonates mimics the tetrahedral intermediates of phosphate ester hydrolysis. This property is exploited in the design of transition-state analog inhibitors targeting enzymes such as proteases, phosphatases, acetylcholinesterase (AChE), and butyrylcholinesterase (BChE) [50,52]. These inhibitors provide valuable biochemical tools and potential therapeutic leads in treating cancer, inflammation, and metabolic disorders.

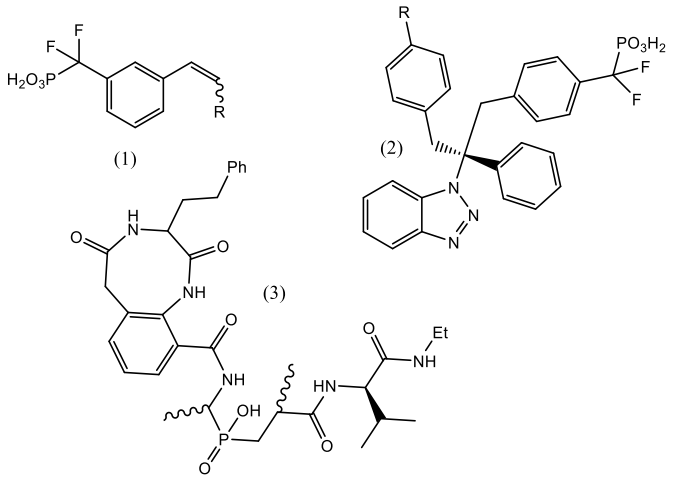


**Figure I. 18** Structures of phosphonate inhibitors of the protein-tyrosine phosphatase 1B (PTP-1B) (compounds 1-2) and acetylcholinesterase (AChE) and butyrylcholinesterase (BChE) inhibitor (compounds 3).

### I.4.2 Antimicrobial Properties

The antimicrobial efficacy of organophosphonates has been reported against Gram-positive and Gram-negative bacteria [53-54] and fungi [55]. These compounds often inhibit microbial growth enzymes or disrupt membrane integrity.

Fosfomycin is a prime example of an organophosphonate antibiotic that irreversibly inactivates the bacterial enzyme MurA, essential for cell wall biosynthesis [56,57].

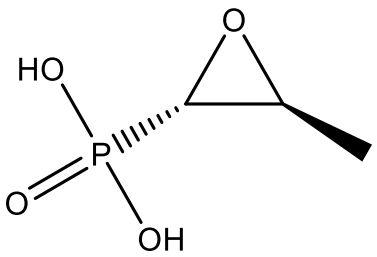


**Figure I. 19** Structure of Fosfomycin.

Beyond fosfomycin, scientists have developed phosphonate analogs to fight antibiotic resistance by targeting how bacteria survive. These innovative compounds disrupt biofilm formation, interfere with quorum sensing, and block other essential pathways bacteria use to thrive and resist traditional antibiotics [58,59;60].

Phosphonate analogs are a versatile and powerful tool in the battle against antibiotic-resistant bacteria. By attacking multiple survival mechanisms simultaneously, they enhance existing treatments and open the door to new therapeutic strategies. As research advances, phosphonate-based therapies are expected to play a crucial role in addressing the global challenge of antibiotic resistance [61].

**Table I.3** Antimicrobial and antifungal activities of compounds with mechanistic insights

| Compounds | Microorganism | Mechanism | Effect | Ref |
|---|---|---|---|---|
| 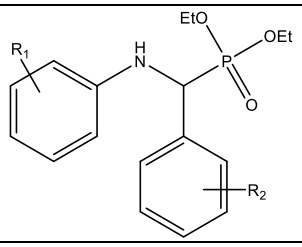 | Gram-Positive Bacteria | Enzyme Inhibition | Suppress bacterial growth | [61[a]] |
| 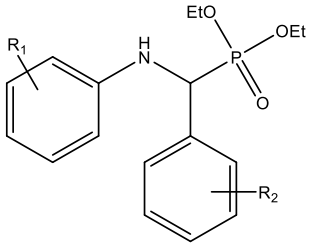 | Gram-Negative Bacteria | Membrane Disruption | Induce cell lysis | |
| 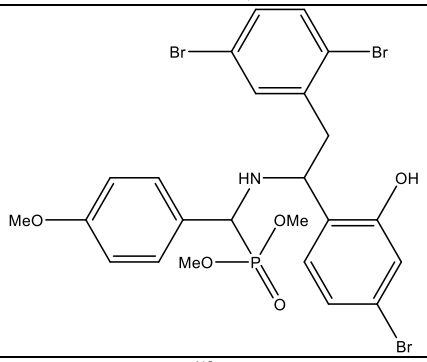 | Gram-positive bacteria and Gram-Negative Bacteria | Growth Inhibition | Suppress bacterial growth | [61[b]] |
| 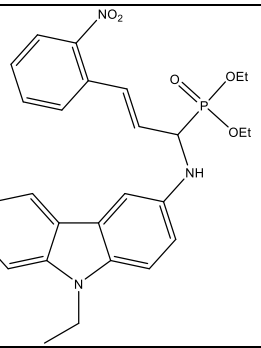 | Fungi | Growth Inhibition | Prevent fungal proliferation | [61[c]] |
| 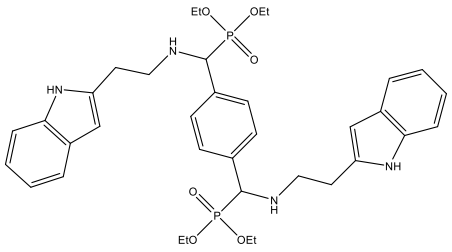 | Fungi | Growth Inhibition | Prevent fungal proliferation | [61[d]] |

### I.4.3 Antiviral Activity

Organophosphonates offer a promising approach to antiviral treatment, demonstrating strong effectiveness against several viruses, including HIV, hepatitis B and C (HBV and HCV), and herpes simplex virus (HSV). These innovative compounds block key viral enzymes like reverse transcriptase and integrase, which are essential for the virus to replicate and integrate into host cells.

Additionally, to organophosphonates, phosphonate nucleotide analogs such as tenofovir and cidofovir are highly effective antivirals. They act as chain terminators during viral DNA or RNA replication, stopping the virus from multiplying. This makes them invaluable in managing HIV and cytomegalovirus (CMV) infections [62–67].

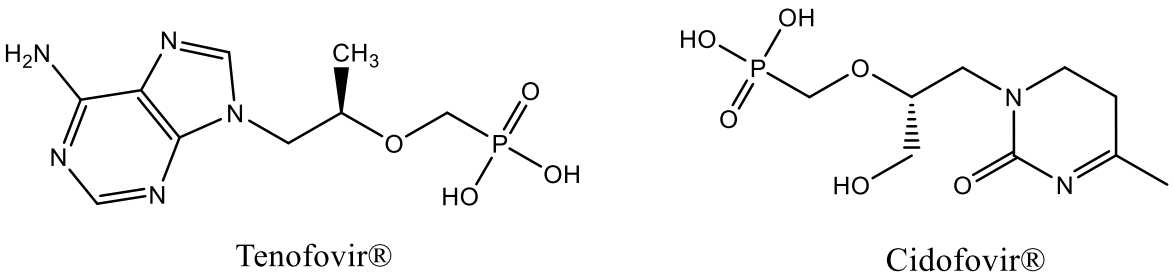


Tenofovir® Cidofovir®

**Figure I.** 20 Structures of Tenofovir and Cidofovir.

Research focuses on developing new phosphonate analogs to combat emerging viral threats like hepatitis C, various herpes viruses, and even SARS-CoV-2. The goal is to enhance their effectiveness and expand their therapeutic potential, offering broader protection against a wider range of viral infections [68–69,70]. The following table gives some results of organophosphonate Analogs as Valuable Candidates for Antiviral Drug Development.

**Table I. 3** Organohosphonate analogs are valuable candidates for antiviral drug development.

| Compounds | Virus | Target Enzyme | Activity | Ref |
|---|---|---|---|---|
| 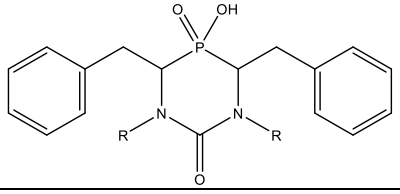 | HIV | Reverse Transcriptase , Integrase | Block viral replication | [70[a]] |
| 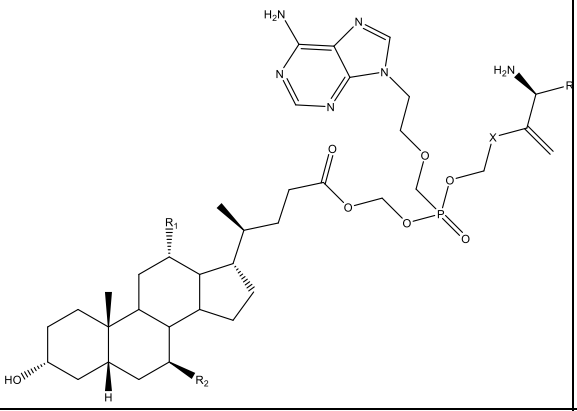 | HBV, HCV | Polymerases | Inhibit viral RNA synthesis | [70[b]] |
| 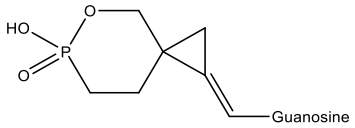 | HSV | DNA Polymerase | Impede viral DNA replication | [70[c]] |
| 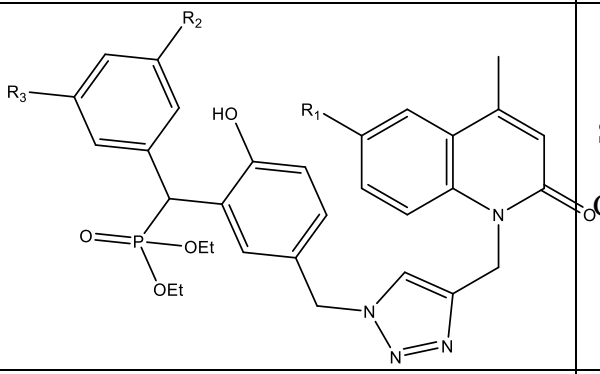 | SARS-CoV-2 | Viral Protease | Inhibit viral replication | [70[d]] |
| 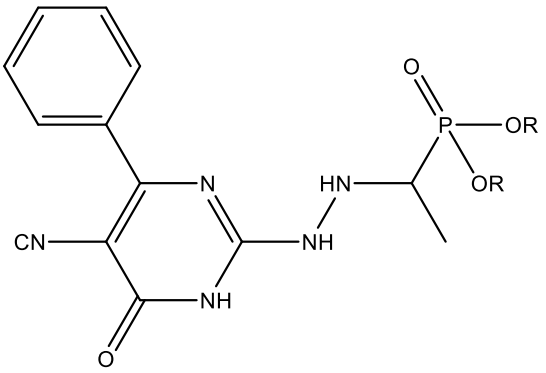 | Influenza | Neuraminidase Inhibition | Prevent viral spread | [70[e]] |

### I.4.4 Anticancer Potential

Several organophosphonates have shown strong potential as anticancer agents due to their significant cytotoxic effects on various cancer cell lines. These compounds work through diverse mechanisms, including stopping cell growth, triggering programmed cell death (apoptosis), and interfering with key metabolic pathways that cancer cells rely on to survive and grow [71].

One of the key strengths of organophosphonates lies in their structural flexibility. This allows scientists to tweak their structure, such as modifying some group or adjusting the phosphonate part to fine-tune their biological activity and improve their selectivity for specific cancer-related targets. These targets often include critical enzymes like kinases, proteases, and glycosyltransferases, which play vital roles in the survival of cancer cells [72].

The effectiveness of organophosphonates can vary between different types of cancer and cell lines. However, they tend to be especially potent against cancers that heavily depend on certain metabolic pathways targeted by these compounds. Another advantage is their selective action on cancer cells, which helps reduce unwanted side effects on normal, healthy cells, making them safer and more effective [73].

In summary, organophosphonates are a versatile and promising group of compounds with notable potential in anticancer therapy. Their ability to target multiple processes essential for tumor growth and survival, combined with their adaptable structure, makes them valuable candidates in the search for new cancer treatments. Ongoing research into their design, synthesis, and biological effects is crucial to maximizing their potential and turning laboratory findings into real benefits for cancer patients.

Below is a table with some examples of organophosphonate derivatives, their generalized structures, proposed targets, tested cancer cell lines, cytotoxic activities, and references.

**Table I. 4** Examples of organophosphonate derivatives and their anticancer potential

| Chemical Structure | Proposed Target/Mechanism | Cancer Cell Line(s) | Cytotoxic Activity ($IC_{50}$) | Ref |
|---|---|---|---|---|
| 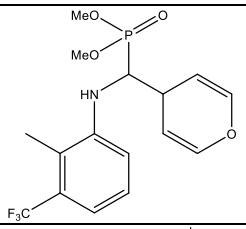 | Aminopeptidase N Inhibition, Blocking Tumor Invasion | MCF-7 (Breast) | 5.90 µM | [73[a]] |
| 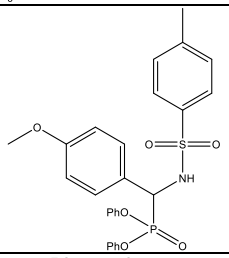 | Mitochondrial Apoptotic Pathway Activation | HL-60 (Leukemia) | ~11 µM | [73[b]] |
| 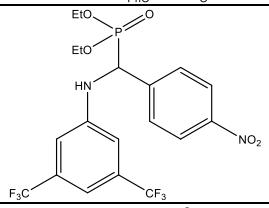 | Glycosyltransferase Inhibition, Altered Cell Surface Glycosylation | A549 (Lung) | ~7.5 µM | [73[c]] |
| 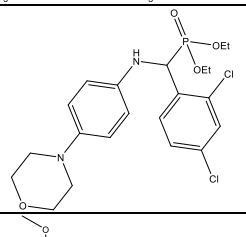 | Rotein Kinase Inhibition, Cell Cycle Arrest | MDA-MB-231 (Breast) | ~12 µM | [73[d]] |
| 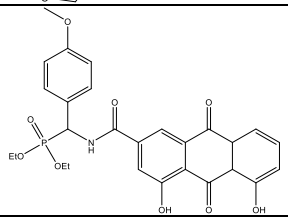 | GSK-3β Inhibition, Disruption of Wnt Signaling | HCT116 (Colon) | 5.32 µM | [73[e]] |
| 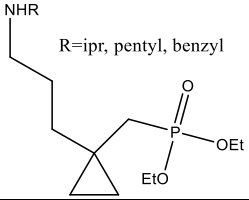  | Dipeptidyl Peptidase IV Inhibition, Impeding Tumor Cell Metabolism | PC-3 (Prostate) | ~8 µM | [73[f]] |
| 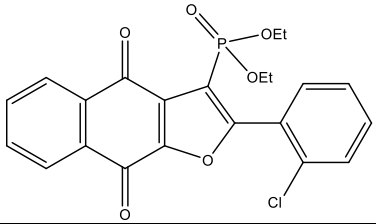 | proteasome Inhibition, Interference with Protein Turnover | HepG2 (Liver) | below 10 µM | [73[e]] |

### I.4.5 Anti-inflammatory Effects

By modulating enzymatic targets involved in inflammation, organophosphonates have shown potential as anti-inflammatory agents [74,75]. Inhibiting specific phosphatases or kinases can reduce cytokine release, offering new strategies to treat autoimmune disorders and inflammatory diseases.

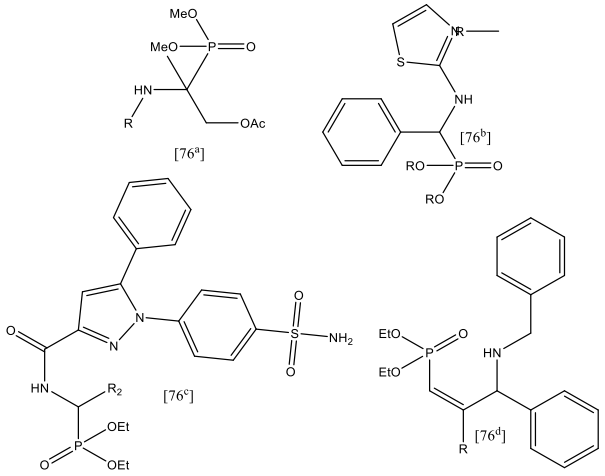


**Figure I. 21** Some examples of organophosphonates as anti-inflammatory agents [76].

#### I.4.5.1 Mechanistic Notes:

Organophosphonates exert their anti-inflammatory effects through multiple mechanisms that target key pathways involved in the inflammatory response. The tables below can give us these mechanistic pathways, highlighting the versatility of organo-phosphonates as promising scaffolds for developing effective anti-inflammatory agents.

**Table I. 5** Mechanistic Insights of Organophosphonates in Anti-Inflammatory Activity.

| Mechanism | Description |
|---|---|
| COX Inhibition | - Inhibition of cyclooxygenase enzymes (COX-1 and/or COX-2), which are essential for prostaglandin biosynthesis, involved in inflammation. |
| Downregulation of Pro-Inflammatory Cytokines | - Reduction in the production of cytokines such as TNF-$\alpha$, IL-1$\beta$, and IL-6, which are key signaling molecules in the inflammatory cascade. |
| Dual or Multi-target Action | - Some derivatives exhibit both anti-inflammatory and additional activities like antioxidant or antimicrobial effects, indicating multi-target potential. |

### I.4.6 Antioxidant Properties

Organophosphonates exhibit significant antioxidant properties because they neutralize reactive oxygen species (ROS) and prevent oxidative damage in biological systems. Their antioxidant activity is attributed to the presence of functional groups capable of donating electrons or hydrogen atoms, stabilizing free radicals, and chelating metal ions involved in ROS generation. [77-79]. Their antioxidant activity further protects neuronal cells from oxidative stress, a critical factor in AD progression. Moreover, these compounds chelate metal ions like $Cu^{2+}$ and $Fe^{2+}$, reducing metal-induced Aβ aggregation and oxidative damage [80]—such multifunctional roles position Organophosphonates as valuable scaffolds in developing novel AD therapeutics.

**Table I. 6** Mechanisms of organophosphonates in Antioxidant Activity.

| Mechanism | Description |
|---|---|
| Free Radical Scavenging | It donates electrons or hydrogen atoms to neutralize reactive oxygen species (ROS) such as DPPH radicals, hydroxyl radicals, and superoxide anions. |
| Chelation of Transition Metal Ions | Binds to metal ions like $Fe^{2+}$ and $Cu^{2+}$, preventing the generation of highly reactive hydroxyl radicals via Fenton and Haber-Weiss reactions. |
| Enhancement of Endogenous Antioxidant Enzymes | Increases the activity of enzymes such as superoxide dismutase (SOD) and glutathione peroxidase (GPx), bolstering the body's antioxidant defense system. |
| Structural Versatility | Incorporates functional groups (e.g., catechol, thiazole, fluorine, sulfonyl) that enhance antioxidant efficacy through various structural modifications. |

The antioxidant activity of Organophosphonates is intricately linked to their structural attributes. Key factors influencing this activity include the presence and positioning of hydroxyl groups, electronic properties of substituents, chelation capabilities, steric factors, and overall molecular conformation. Researchers can design Organophosphonates with enhanced antioxidant properties tailored for specific therapeutic applications by meticulously modifying these structural elements. The following table shows us the Structural Features Enhancing Antioxidant Efficacy in organophosphonates.

**Table I. 7** Structural features that enhance the antioxidant efficacy of organophosphonates.

| Structural Feature | Impact on Antioxidant Activity |
|---|---|
| Electron-donating groups (e.g., Catechol, Thiazole) | Facilitates free radical scavenging by stabilizing radicals through resonance stabilization, enhancing the compound's ability to neutralize ROS. |
| Fluorination | Improves lipophilicity, facilitating better cellular uptake, and provides additional sites for electron delocalization, thereby increasing radical scavenging efficiency. |
| Sulfonyl-Linkages | It enhances hydrogen bonding capabilities, stabilizes antioxidant radicals, and improves solubility in diverse biological environments, boosting overall antioxidant performance. |

## I.5 Agricultural Applications

Organophosphonates represent a versatile and potent class of compounds with significant applications in agriculture. Their roles as fungicides [81], herbicides [82], plant growth regulators [83], and nutrient sources contribute to enhanced crop protection and productivity [84]. The unique structural features of organophosphonates, such as the stable C-P bond and functional versatility, underpin their efficacy and broad applicability. The following figure contains some of the Case Studies and Commercial Products.

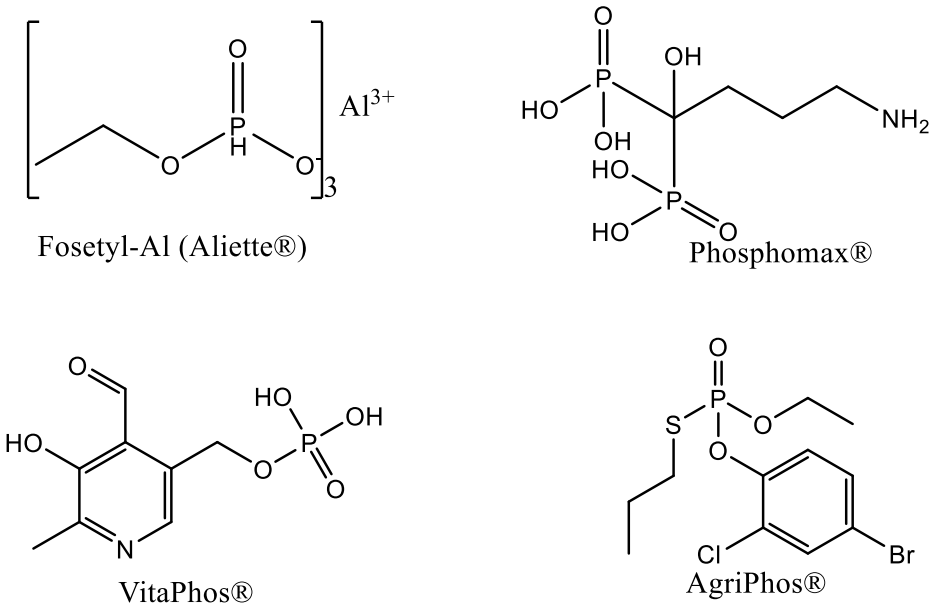


**Figure I. 22** Some of the case studies and commercial products

However, the benefits must be balanced against environmental and safety considerations. Ongoing research and development efforts focus on optimizing efficacy,

reducing the ecological footprint, and ensuring the sustainable use of organophosphonates in agricultural settings. As the global demand for sustainable and efficient farming practices grows, organophosphonates are poised to play an increasingly important role in meeting these challenges.

## I.6 Density Functional Theory (DFT) and Computational Insights

### I.6.1 DFT Applications in Organophosphonates Research

DFT calculations help predict conformations, electronic distributions, orbital energies, and reactivity trends of organophosphonates [85–87]. By correlating theoretical descriptors (e.g., HOMO-LUMO gaps, charge density, molecular electrostatic potential) with experimentally observed activities, researchers can rationalize structure-activity relationships (SARs) and guide the design of new derivatives.

DFT also assists in interpreting spectroscopic data (NMR, IR, Raman) and provides insight into reaction mechanisms underlying phosphonate formation or degradation [88–90]. As computational power and functionals improve, DFT-driven predictions become more reliable, accelerating the discovery pipeline.

### I.6.2 Docking Studies of Phosphonates

Docking has proved invaluable in identifying which organophosphonate derivatives are most likely to bind crucial biological targets (e.g., HIV reverse transcriptase, kinases, or phosphatases) [91–93]. By revealing key amino acid interactions, hydrogen bonding patterns, and hydrophobic pockets, molecular docking guides rational modifications that improve potency, selectivity, and pharmacological profiles. Integrating docking with DFT can refine the predicted binding poses and highlight electronic factors influencing affinity [94–96].

### I.6.3 Importance of Early ADME-T Assessment

A potent compound is not necessarily a good drug. To succeed clinically, a molecule must exhibit favorable pharmacokinetic and safety profiles. Early-stage in silico ADME-T predictions—covering absorption, distribution, metabolism, excretion, and toxicity are crucial to filter out candidates likely to fail later in development [97–99].

### I.6.4 Integrating ADME-T with Design

A multi-criteria optimization approach emerges by iterating between design, synthesis, docking, DFT calculations, and ADME-T predictions. Compounds that meet potency benchmarks have favorable binding modes and pass advanced ADME-T filters, reducing costly late-stage attrition [100–102].

## I.7 Nano Drug Delivery of Organophosphonates

Incorporating nanotechnology into drug delivery systems has significantly transformed the pharmaceutical industry, providing cutting-edge solutions to improve therapeutic agents' effectiveness, precision, and safety. organophosphonates, in particular, have attracted considerable interest due to their wide range of biological activities, which include antimicrobial, antiviral, anticancer, and enzyme-inhibitory effects we have seen before. Despite their potential, the clinical application of phosphonates is often limited by poor solubility, low bioavailability, and non-specific distribution within the body [103-105].

Nano Drug Delivery Systems (NDDS) offer a promising strategy to address these challenges. By utilizing nanoparticles and other nanoscale carriers, NDDS can enhance the solubility of phosphonate-based drugs [106], improve their bioavailability, and ensure more targeted delivery to specific tissues or cells. This targeted approach increases the therapeutic efficacy of the medicines and minimizes potential side effects by reducing off-target interactions [107].

Moreover, NDDS enable controlled release of organophosphonates, allowing for sustained drug levels over extended periods, enhancing treatment outcomes and patient compliance [108-109]. The versatility of nanotechnology also provides for the functionalization of drug carriers with various ligands, antibodies, or other targeting molecules, further improving the specificity of drug delivery [110].

In summary, integrating nanotechnology into the delivery of organophosphonate-based drugs holds great promise for overcoming existing limitations and unlocking the full therapeutic potential of organophosphonates. Ongoing research and development in this field will lead to more effective and safer treatments for various diseases, ultimately advancing healthcare outcomes.

## I.8 Somes of Nanodrug Delivery Systems Suitable for Organophosphonates

### I.8.1 Polymeric Nanoparticles

Polymeric nanoparticles, utilizing biodegradable polymers like poly(lactic-co-glycolic acid) (PLGA) and polyethylene glycol (PEG), are prominent nano-drug delivery systems for phosphonates. These polymers enable the encapsulation of phosphonates, allowing for controlled release and targeted delivery. The biodegradability of PLGA and PEG ensures the nanoparticles break down into non-toxic byproducts, minimizing adverse effects. Additionally, surface modifications with targeting ligands enhance the specificity of drug delivery to desired tissues or cells [111-112].

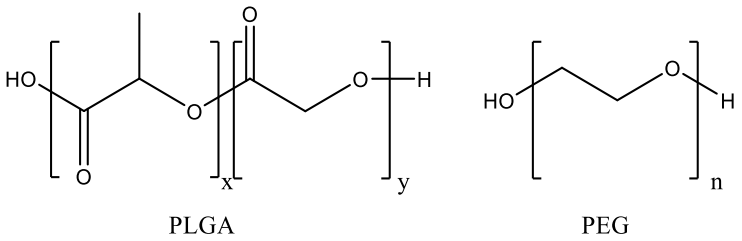


**Figure I. 23** Structure of PLGA. x= number of lactic acid units; y= number of glycolic acid units, and PEG.

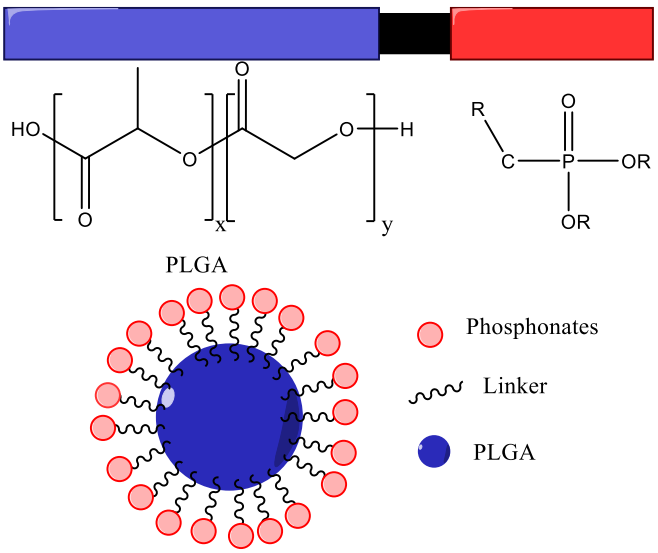


**Figure I. 24** Schematic representation of Phosphonates encapsulated in PLGA nanoparticles.

### I.8.2 Liposomes

Liposomes are versatile nano-drug delivery systems encapsulating hydrophilic and hydrophobic phosphonates within lipid-based vesicles. This dual encapsulation improves the solubility and stability of the drugs, protecting them from degradation before reaching target sites [113]. Surface modification with targeting ligands, such as antibodies or peptides, enhances delivery specificity. The biocompatible nature of liposomes also reduces the likelihood of immune responses, making them safe and effective phosphonate carriers [114-116].

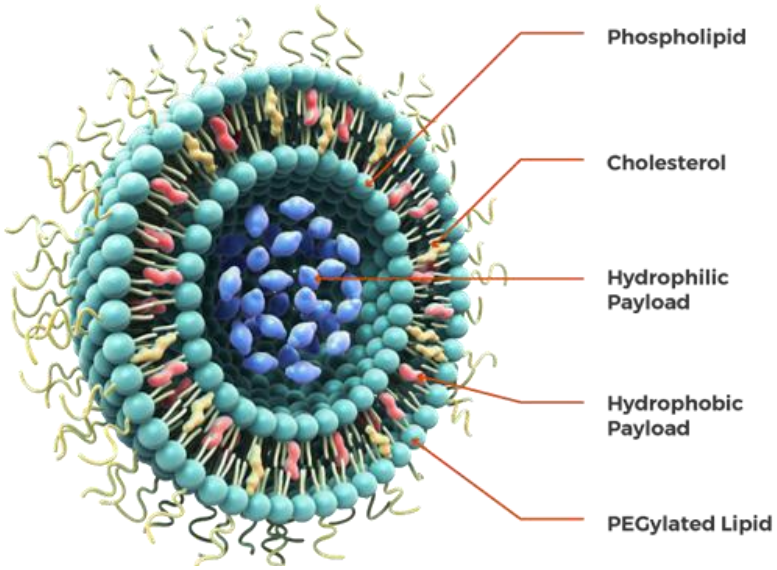


**Figure I. 25** Illustrating the structure of liposomes.

### I.8.3 Nanohydrogels

Nanogels (NGs), crosslinked polymer networks at the nanoscale, offer a versatile platform for next-generation drug delivery. Their engineered responsiveness enables on-demand release, reduced toxicity, and crossing biological barriers [117]. Due to their porous structure, they offer high loading capacities for phosphonates and are made from biocompatible, biodegradable materials, reducing immune responses [118]. Nanohydrogels exhibit stimuli-responsive behavior, allowing controlled drug release in response to pH, temperature, or enzymatic triggers [119]. Their network structure protects phosphonates from premature degradation, enhancing stability and therapeutic efficacy [120-121].

### I.8.4 Hyaluronic Acid-Based Nanocarriers

Hyaluronic acid-based nanocarriers are highly effective for delivering Organophosphonates due to the biocompatibility and bioactivity of hyaluronic acid (HA). HA binds explicitly to CD44 receptors, which are overexpressed in various cancer cells and inflamed tissues, enabling targeted delivery to pathological sites [122]. These nanocarriers can be engineered into nanoparticles, micelles, or hydrogels to enhance drug solubility and stability [123]. Additionally, HA can be modified with stimuli-responsive elements for controlled release, improving targeting, reducing immunogenicity, and enhancing overall therapeutic efficacy [124-125].

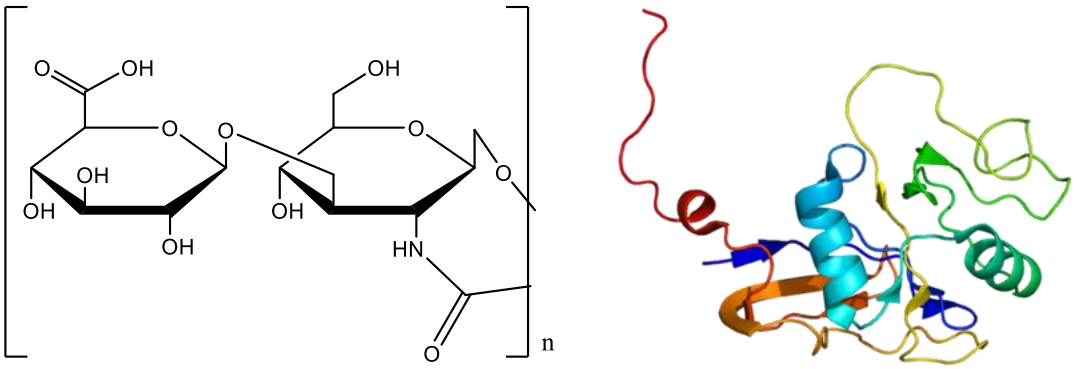


Hyaluronic acid CD44

**Figure I.** 26 The CD44 antigen and HA structures**.**

## I.9 Challenges, Limitations, and Future Directions

### I.9.1 Synthetic Complexity and Cost

Some organophosphonates require multi-step syntheses with low overall yields and challenging purifications. Scalability and cost remain concerns, motivating research into more robust catalytic methods, green chemistry approaches, and flow reactors to streamline production [28-31].

### I.9.2 Computational Accuracy and Validation

While DFT and docking tools have improved, their accuracy depends on parameter choices, functionals, and force fields. Cross-validation with experimental data is essential. Machine learning and artificial intelligence methods promise to enhance predictive power, enabling rapid screening of vast chemical spaces [87-90].

### I.9.3 Translating In Vitro to In Vivo

Many organophosphonates show potent activity in vitro but face challenges in reaching the target site in vivo due to poor ADME-T profiles, off-target toxicity, or instability. Addressing these issues requires iterative optimization and, in some cases, the design of prodrugs or formulation strategies that improve bioavailability and reduce toxicity [126-127].

### I.9.4 Emerging Fields

Integrating organophosphonates into nanomedicine, targeting carriers, and biodegradable polymers is an emerging trend. Using phosphonate ligands in metal-organic frameworks or as chelators for imaging agents expands the scope of biomedical applications [4-5]. Meanwhile, CRISPR-Cas9-based gene editing and high-throughput screening platforms could identify new therapeutic targets for organophosphonate intervention.[128].

## I.10 Conclusion

This chapter has surveyed the multifaceted landscape of organophosphonate research. From their historical foundations to their synthetic diversity, and from their broad biological activities to the adoption of Density Functional Theory (DFT), molecular docking, and ADME-T predictions in their development, organophosphonates exemplify the power of an integrated approach in drug discovery and medicinal chemistry. Additionally, the detailed examination of nano-drug delivery systems, including polymeric nanoparticles, liposomes, and hyaluronic acid-based nanocarriers, showcases innovative approaches to enhance the utility and efficacy of these compounds.

The synergy between experimental and computational methodologies has revolutionized how scientists approach the design and optimization of organophosphonates. The ability to predict properties before synthesis, rationalize observed activities, and eliminate non-viable candidates early in the pipeline accelerates progress. As computational techniques grow more sophisticated and experimental tools more refined, the potential for organophosphonates in addressing unmet medical needs and improving existing therapies continues to expand.

This knowledge sets the stage for the current dissertation's objectives: to design, synthesize, and biologically evaluate new organophosphonate derivatives guided by

theoretical (DFT) and in silico (docking, ADME-T) insights. The following chapters will delve into the methodologies, experimental work, results, and discussions that arise from this integrated approach, emphasizing the role of advanced drug delivery systems in maximizing the therapeutic potential of organophosphonates.

II

# Materials and Methods

# II Materials and Methods

## II.1 Introduction

This chapter presents a comprehensive and detailed examination of the materials, instruments, and methodologies utilized in the synthesis, characterization, computational modeling, and biological evaluation of the organophosphonate compounds studied in this investigation. The design and selection of each method were driven by the necessity for accuracy, consistency, and a comprehensive grasp of the chemical and biological characteristics of the target molecules. Initially, a comprehensive overview of all chemicals, reagents, and equipment is provided, highlighting their purity and essential handling guidelines in a manner that ensures you are well-informed and prepared.

The synthetic pathways for organophosphonates are outlined in a detailed, sequential manner, accompanied by analytical methods for verifying product identity and elucidating structure.

This chapter also highlights the crucial role of computational strategies in investigating the synthesized compounds' electronic, structural, and pharmacokinetic characteristics. These strategies, including DFT calculations, molecular docking, and drug-likeness assessments, are paramount. The increasing relevance of nanotechnology in drug delivery and various biomedical applications further underscores the importance of detailing nanoparticle preparation and characterization procedures. Lastly, the biological testing methodologies—covering antimicrobial and antioxidant assays are detailed, establishing the protocols for assessing the therapeutic potential of the synthesized organophosphonates.

This chapter is of utmost importance in ensuring the reproducibility and scientific soundness of the investigation. It establishes the essential framework for the results and discussions that will follow in the subsequent chapters, providing a solid foundation for future research and scientific advancement.

## II.2 Materials

### II.2.1 Chemicals and Reagents

#### II.2.1.1 Organophosphonate Precursors

All the chemicals utilized in this study were sourced from Sigma-Aldrich. The table below outlines the organophosphorus precursors used, including their sources, purity levels, and other pertinent information.

**Table II. 1** List of Organophosphorus Compounds and Their Specifications.

| Precursor | Chemical structure | Supplier | Purity | Comments |
|---|---|---|---|---|
| Diethyl Phosphite ($C_4H_{10}O_3P$) | 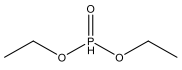 | Sigma-Aldrich | 98% | Used as a phosphorylation agent; sensitive to moisture. |
| Phosphorous Acid ($H_3PO_3$) | 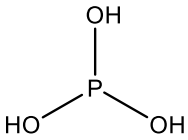 | Sigma-Aldrich | ≥98% | Precursor for organophosphonates; hygroscopic, stored in inert conditions. |
| 3-Aminopropanol ($H_2N$-$CH_2$-$CH_2$-$CH_2OH$) | 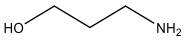 | Sigma-Aldrich | ≥98% | Bifunctional reagent; store at 2–8 °C, sensitive to oxidation. |
| 4-Aminobutanol ($H_2N$-$CH_2$-$CH_2$-$CH_2$-$CH_2OH$) | 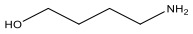 | Sigma-Aldrich | 98% | Bifunctional reagents, handled with care, can be hygroscopic. |
| Acetaldehyde ($CH_3CHO$) | 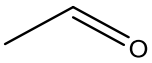 | Sigma-Aldrich | ≥99% | Volatile liquid; store cold and minimize exposure to air (polymerization). |

### II.2.1.2 Solvents

Solvents are essential in synthesizing and purifying organophosphonates, affecting reaction yields and selectivity. To achieve the best possible conditions, solvents of high purity were chosen. The table below summarizes the primary solvents utilized in this study, detailing their suppliers, purity levels, and relevant handling or storage considerations.

**Table II. 2** Commonly used solvents, their sources, and purity levels in this research.

| Solvent | Source | Purity/Grade | Comments |
|---|---|---|---|
| Dichloromethane (DCM) | Sigma-Aldrich | Analytic Grade, ≥99.8% | Stored over molecular sieves to maintain dryness; handled in a fume hood due to volatility. |
| Tetrahydrofuran (THF) | Sigma-Aldrich | Anhydrous, ≥99.9% | Typically stored under an inert atmosphere, it may require distillation before sensitive syntheses. |
| Methanol (MeOH) | Sigma-Aldrich | Analytic Grade, ≥99.9% | Used frequently for reaction workups. |
| Ethanol (EtOH) | Sigma-Aldrich | Absolute, ≥99.9% | Denatured or non-denatured varieties; ensure the correct type for the desired application. |
| Acetone | Sigma-Aldrich | Analytic Grade, ≥99.8% | Common solvent for cleaning and extraction; keep container well-sealed to minimize moisture uptake. |
| Diethyl Ether ($Et_2O$) | Sigma-Aldrich | Anhydrous, ≥99% | Highly volatile and flammable; store over sodium or molecular sieves if absolute dryness is needed. |
| n-Hexane | Merck | ≥95% | Used in thin layer chromatography TLC; stored at room temperature in a well-ventilated area. |
| Diethyl Acetate | Sigma-Aldrich | ≥99% | Medium boiling point is commonly used in extraction processes and as a mild solvent in specific reactions. |
| Dimethyl Sulfoxide (DMSO) | Merck | ≥99.9%, Anhydrous | Hygroscopic; widely used for difficult-to-dissolve compounds; stored tightly closed to prevent moisture uptake. |
| Acetonitrile (MeCN) | Merck | Analytic, ≥99.9% | The key solvent for recrystallization has a low boiling point, so it is handled in a fume hood due to toxicity concerns. |
| Water ($H_2O$) | In-laboratory | Bidistillated | Used for all aqueous solutions and final rinses; filtered and deionized on-site. |

### II.2.1.3 Additives

Our research uses various inorganic salts and mild reagents to optimize reaction conditions and improve product quality. Drying agents promote the elimination of residual moisture, whereas bisulfite functions as a mild reducing agent or scavenger for undesirable byproducts in biological activity, such as buffer phosphate solution.

The subsequent table delineates the principal additives employed in this study, encompassing their origins, purity grades, and customary applications.

**Table II. 3** Common additives used in this research, along with their sources, purity levels, and typical applications.

| Additive | Chemical Formula | Supplier | Purity | Usage | Comments |
|---|---|---|---|---|---|
| Sodium Sulfate | $Na_2SO_4$ | Sigma-Aldrich | ≥99% | Drying agent for organic phases | Anhydrous form is typically used and stored in a desiccator to maintain dryness. |
| Magnesium Sulfate | $MgSO_4$ | Sigma-Aldrich | ≥98% | Drying agent for organic phases | Often added after an extraction step, filter off the hydrated salt before solvent removal. |
| Sodium Bisulfite | $NaHSO_3$ | Sigma-Aldrich | ≥97% | Mild reducing agent, aldehyde scavenger | Used in specific reaction quenching procedures or to remove dissolved chlorine or aldehydes in situ [1]. |
| Disodium hydrogen phosphate | $Na_2HPO_4$ | Merck | ≥99% (ACS Reagent Grade) | - Preparation of phosphate buffers<br>- Nutrient source of phosphate | - Store in a cool, dry place<br>- Account for a water of crystallization when weighing |
| Sodium dihydrogen phosphate dihydrate | $NaH_2PO_4 \cdot$ | Merck | ≥98% (Lab Grade) | - pH adjustment | Used to set acidic range of phosphate buffers<br>- Store tightly sealed to prevent moisture absorption |
| Potassium Persulfate | $K_2S_2O_8$ | Merck | ≥99% | Strong oxidizing agent; initiator | Usually stored in a cool, dry place, decomposes |

| | | | | | |
|---|---|---|---|---|---|
| | | | | in polymerization reactions | upon prolonged exposure to heat or moisture |
| Iron(III) Chloride (anhydrous) | $FeCl_3$ | Merck | ≥98% | Oxidizing agent; used in etching solutions and as a catalyst in various organic reactions | Highly hygroscopic; store in sealed containers; handle with care due to corrosive nature |
| Trichloroacetic Acid (TCA) | $CCl_3COOH$ | Merck | ≥99% (Reagent Grade) | Protein precipitation, biochemical assays (e.g., nucleic acid and protein determination), pH modifier | Corrosive; handle with appropriate protective equipment; avoid inhalation and contact with skin |

### II.2.1.4 Biological Reagents

DPPH (2,2-diphenyl-1-picrylhydrazyl) is a stable free radical frequently used to determine antioxidant compounds' electron—or hydrogen-donating properties. It is generally obtained from Sigma-Aldrich with a minimum purity of 95%.

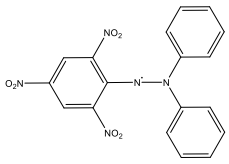

**Figure II. 1** DPPH chemical structure

$ABTS^{\bullet+}$ (2,2'-Azino-bis(3-ethylbenzothiazoline-6-sulfonic acid) Radical Cation) is a prevalent technique for evaluating antioxidant capacity by decolorizing the $ABTS^{\bullet+}$ radical cation, often obtained from Sigma-Aldrich (≥98% purity).

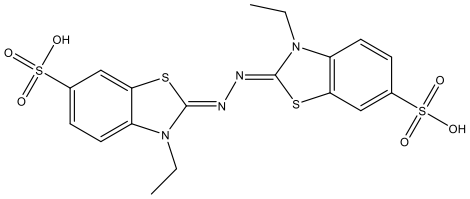

**Figure II. 2** $ABTS^{\bullet+}$ chemical structure

Phenanthroline (1,10-phenanthroline) is another reagent commonly employed in antioxidant assays, particularly those involving metal ion reduction or complexation. It

forms a highly colored complex with Fe(II), which can be monitored spectrophotometrically (commonly at 510 nm) to gauge the reducing power of antioxidant compounds. This chelating property makes phenanthroline-based assays helpful in determining a sample's capacity to reduce Fe(III) to Fe(II) or to inhibit metal-catalyzed oxidation processes. phenanthroline obtained from Sigma-Aldrich at high purity (≥99% is typical),

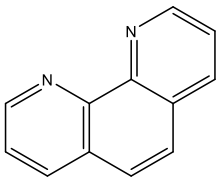


**Figure II. 3** 1,10-phenanthroline chemical structure

. Gram-positive *Streptococcus pyogenes, Staphylococcus aureus*, Gram-negative *Escherichia coli,* and *Pseudomonas aeruginosa* are among the bacterial strains used; they can be acquired from a microbiology lab of Hospital Center, Saadna Abdenour University Hospital—SETIF. These represent a variety of clinically relevant pathogens with distinct cell wall characteristics that offer a vast evaluation of antibacterial potential.

**Table II. 4** Principal Aspects of the Bacterial Strains Used in Antibacterial Screening

| Bacterial Strain | Gram Reaction | Morphology | Common Infections / Clinical Relevance [2-3]. | Additional Notes |
|---|---|---|---|---|
| *Streptococcus pyogenes (Group A Strep)* | Gram-positive | Spherical (cocci) in chains | Causes pharyngitis (strep throat), scarlet fever, rheumatic fever, and skin infections (impetigo). | Beta-hemolytic on blood agar produces various virulence factors (streptolysin). |
| *Staphylococcus aureus* | Gram-positive | Spherical (cocci) in clusters | Responsible for skin and soft tissue infections, pneumonia, toxic shock syndrome (TSS), and food poisoning. | It can be methicillin-resistant (MRSA) and grows in golden-yellow colonies on agar. |
| *Escherichia coli* | Gram-negative | Rod-shaped (bacilli) | Commonly associated with urinary tract infections (UTIs), gastroenteritis, and neonatal meningitis. | Part of normal intestinal flora, but certain strains (E. coli O157:H7) are pathogenic. |
| *Pseudomonas aeruginosa* | Gram-negative | Rod-shaped (bacilli) | Causes opportunistic infections in immunocompromised individuals, including pneumonia, UTIs, and wound infections. | It is notable for its multidrug resistance and produces a characteristic greenish pigment (pyocyanin). |

### II.2.1.5 Standards and Reference Compounds

BHT (Butylated Hydroxytoluene) and BHA (Butylated Hydroxyanisole) were used as standard reference compounds in antioxidant experiments, creating a benchmark for comparing test samples' free radical scavenging capacity.

Galantamine is an isoquinoline alkaloid that is a potent, reversible, and competitive acetylcholinesterase inhibitor. It also allosterically modifies nicotinic acetylcholine receptors. Galantamine is clinically indicated for the management of mild to moderate Alzheimer’s disease to mitigate cognitive deterioration. It is commonly utilized as a reference standard in cholinesterase inhibition experiments (including Ellman’s method) inside laboratory environments. Galantamine is often sourced from Sigma-Aldrich and has a purity of at least 98%.

Penicillin (pharmaceutical grade) also functioned as the standard for antibacterial evaluation, demonstrating its well-documented effectiveness against various bacterial infections.

### II.2.2 Equipment

#### II.2.2.1 Glassware and Reaction Apparatus

Glassware and reaction apparatus for organophosphate reactions usually contain round-bottom flasks, reflux condensers, heating flasks, magnetic stirrers, and thermometers to ensure an equal distribution of heat and consistent reaction kinetics.

All equipment must be carefully cleaned and dried to eliminate any liquids or impurities that could impair reaction efficiency, leading to accurate and high-yield results.

Rotary evaporator (Büchi Rotavapor) for solvent removal.

Thin-layer chromatography (TLC) was used to track the reaction's progress and finishing (0.25mm E Merck silica gel plates (60F–254)).

UV light (254 nm).

The microwave-irradiated synthesis was performed in a microwave oven (operating between 100 and 1000 W).

Stuart Scientific SMP3 for determining melting points

#### II.2.2.2 Spectroscopic Equipment:

**Fourier Transform Infrared Spectroscopy (FT-IR)**

Fourier Transform Infrared (FT-IR) analysis was conducted at our laboratory, the Laboratory of Electrochemical and Molecular Materials and Complexes (LEMMC). A Perkin Elmer FT-IR JASCO-4200 spectrometer with a double-beam setup in attenuated total reflectance (ATR) mode was utilized to get the IR spectra. The instrument resolution was established at 4 $cm^{-1}$, and the transmission results are presented in wavenumbers ($cm^{-1}$). Measurements were performed in the spectral range of 4000 to 600 $cm^{-1}$. Before analysis, the ATR crystal was meticulously cleaned to avert contamination, and each sample was positioned in direct contact with the crystal to guarantee excellent signal quality.

**Ultraviolet-visible (UV-Vis) Spectrophotometry**

The optical characteristics of the produced products were examined utilizing UV-Vis spectrophotometry. Under ambient circumstances, UV-Vis absorption spectra were obtained

using a JASCO V-650 spectrophotometer in the same laboratory (LEMMC). Measurements were conducted from 200 to 800 nm utilizing quartz cuvettes with a 1 cm optical path length. The samples were produced as ethanolic solutions at concentrations selected to prevent detector saturation, and baseline corrections were conducted using pure ethanol as the reference. This method yielded accurate and consistent absorbance measurements.

**Nuclear Magnetic Resonance (NMR)**

Nuclear Magnetic Resonance (NMR) analysis was performed at the Scientific and Technical Research Center in Physico-Chemical Analysis (CRAPC) with a Bruker spectrometer running at 400 MHz or 300 MHz for $^{1}H$ NMR and at 161.1 MHz for $^{31}P$ NMR. All measurements were conducted at ambient temperature. Chemical shifts (δ) are expressed in parts per million (ppm), relative to tetramethylsilane (TMS) as an internal standard, and referred to the residual signals of deuterated solvents ($CDCl_3$ or DMSO). Signal multiplicities are designated as singlet (s), doublet (d), double doublet (dd), triplet (t), quartet (q), or multiplet (m). The raw data were processed and analyzed with MestReNova software (V 14.3.2-32681, Mestrelab Research, Santiago de Compostela, Spain), which offered sophisticated tools for peak selecting, integration, coupling constant determination, and

### II.2.2.3 Biological Assay Equipment :

**Microplate Reader**

A 96-well microplate reader (at biotechnology researcher center CRBT) was utilized for high-throughput spectrophotometric analysis in biological experiments. This device employs a tungsten and deuterium lamp to encompass a wide wavelength range (190–850 nm), facilitating precise absorbance measurements throughout the UV-visible spectrum. The integrated temperature control system guarantees stable conditions for kinetic experiments. At the same time, the SoftMax Pro software facilitates user-friendly data capture, real-time monitoring, and thorough post-run analysis for calculating $IC_{50}$ or inhibitory percentages. The 96-well plate format facilitates concurrent analysis of numerous samples and controls, improving reproducibility and throughput. Data is automatically captured and exported in multiple formats for additional statistical analysis. This design provides a strong and dependable platform for evaluating the effectiveness of compounds in DPPH, ABTS, and other colorimetric or turbidimetric assays associated with antioxidant and antibacterial activities.

### II.2.2.4 Nanoparticle Synthesis and Characterization Tools

#### Autoclave for Nanoparticle Synthesis

This research utilized a Teflon-lined stainless-steel autoclave (Parr Instruments) for the hydrothermal production of nanoparticles. This configuration enables meticulously regulated high-temperature (often 120 °C to 220 °C) and high-pressure (usually up to 10–20 bar) conditions, essential for aiding particular crystallization pathways and fostering uniform particle development. The reactants, either dissolved or dispersed in suitable water, were placed into the Teflon liner, sealed within the stainless-steel casing, and underwent programmed heating and cooling cycles. Reaction periods typically ranged from 2 to 24 hours, contingent upon the targeted phase and particle size. The autoclave atmosphere was consistently sealed to avert solvent evaporation and sustain the necessary pressure, assuring the reproducible and regulated synthesis of nanoparticles. After the reaction, the autoclave was permitted to cool to ambient temperature before the meticulous product extraction.

#### Dynamic Light Scattering (DLS)

Dynamic Light Scattering measurements were performed with a Zetasizer Nano ZS at CRAPC. This apparatus assesses particle size by analyzing the variations in the intensity of scattered light, which correlate with the Brownian motion of nanoparticles in suspension. Analyses were conducted at a constant backscattering angle of 173°, with temperature regulation maintained at 25 °C to achieve stable measurement conditions. Before each measurement, samples were meticulously diluted with the suitable solvent (buffer solution) to mitigate various scattering effects and enhance data accuracy. Disposable or quartz cuvettes were utilized, with each sample often measured in triplicate to guarantee repeatability. The Zetasizer software generated the correlation functions and provided essential parameters, including the Z-average hydrodynamic diameter, polydispersity index (PDI), and, when applicable, zeta potential values, facilitating a thorough characterization of the synthesized nanoparticles.

### II.2.3 Software Tools :

### II.2.3.1 Quantum Chemical Software

#### Gaussian 09W

Gaussian 09W is a powerful package of computational chemistry software intended to model and predict various molecular characteristics. It accommodates multiple quantum mechanical methodologies, including Hartree-Fock (HF), post-HF, and Density Functional

Theory (DFT), enabling researchers to do geometry optimizations, frequency studies, reaction pathway investigations, and solvent modeling. The software is extensively utilized to precisely forecast electronic structures, thermochemical data, and molecular orbital characteristics, establishing it as a fundamental tool for in silico investigations of organic and inorganic systems [4].

**GaussView**

GaussView is an additional graphical user interface (GUI) for Gaussian 09W, enabling molecular structure construction, modification, and display. It streamlines the configuration of input files for Gaussian computations and offers visual representations of optimal geometries, molecular orbitals, and vibrational modes [5-6].

### II.2.3.2 Molecular Docking Software

**AutoDock**

AutoDock is a prevalent molecular docking software that utilizes a Lamarckian Genetic Algorithm to investigate potential binding conformations of tiny ligands within the active site of a macromolecular receptor. It computes binding energies and prioritizes binding conformations, facilitating the prediction of ligand-receptor interactions. He has also impacted structure-based drug design, virtual screening, and lead optimization research [7].

**AutoDock Vina**

AutoDock Vina employs a gradient-based search technique to efficiently dock ligands into a receptor, frequently resulting in quicker computations than AutoDock 4 while preserving substantial accuracy. The scoring function forecasts binding affinities, allowing researchers to prioritize prospective medication candidates by grading their docking configurations [8].

**PyMOL**

It is an open-source molecular visualization platform widely utilized in structural biology, biochemistry, and related disciplines for viewing and analyzing macromolecular structures, including proteins, nucleic acids, and small molecules. It provides extensive functionalities for producing high-quality 3D images and animations and conducting comprehensive molecular studies. The comprehensive features of PyMOL and its vibrant community support render it essential for numerous scientific workflows.[9].

### II.2.3.3 ADME-T Prediction Tools

**SwissADME**

SwissADME is a complimentary online service offering an extensive array of in silico predictions for chemical compounds' absorption, distribution, metabolism, excretion, and toxicity (ADME-T) profiles. It computes multiple physicochemical descriptors (for example, lipophilicity and solubility), assesses drug-likeness parameters (such as Lipinski's rule of five), and provides an overview of a molecule's probable pharmacokinetic properties [10].

**pkCSM**

pkCSM is a digital platform that utilizes graph-based signatures to forecast several ADME-T features, such as human intestinal absorption, clearance, and multiple toxicity endpoints (including hERG inhibition and Ames mutagenicity). It facilitates swift evaluation of chemical libraries, assisting in lead selection by identifying potential pharmacokinetic or toxicity concerns [11].

**Molinspiration**

Molinspiration is an online cheminformatics application that computes several molecular descriptors, including logP, molecular weight, topological polar surface area (TPSA), and hydrogen bond donors/acceptors. It also delivers rapid bioactivity forecasts for prevalent target classes, furnishing a preliminary evaluation of drug-likeness and biological promise [12].

**ADMET.AI**

ADMET.ai, developed by Green Stone Bio, is an AI-based online platform that provides an extensive array of in silico predictions for chemical substances' ADME-T (absorption, distribution, metabolism, excretion, and toxicity) profiles. It calculates several physicochemical descriptors (e.g., lipophilicity and solubility), assesses drug-likeness criteria (such as Lipinski's rule of five), and provides a comprehensive analysis of a molecule's pharmacokinetic and toxicological characteristics, facilitating the initial phases of drug discovery[13].

### II.2.3.4 Biological Synergy Tools

**Synergy finder**

SynergyFinder is an accessible, web-based platform intended to systematically assess the synergy or antagonism of medication combinations. The program utilizes established synergy scoring models—namely Bliss Independence, Loewe Additivity, and Zero

Interaction Potency (ZIP)—to expedite the detection of synergistic drug combinations or multi-drug therapies. SynergyFinder facilitates high-throughput combinatorial screenings, provides clear data visualization, and assists in the logical design of combination medicines to enhance therapeutic outcomes [14,15].

**CompuSyn**

CompuSyn is a prevalent software application utilized for evaluating the impacts of medication combinations, grounded in the median-effect concept and the Chou–Talalay methodology [16]. CompuSyn assists researchers in assessing drug interactions as synergistic, additive, or antagonistic by computing the Combination Index (CI) and producing dose-effect curves. Its intuitive interface and strong computational framework render it an essential tool for designing and analyzing combination trials in drug discovery and development [17].

### II.2.3.5 Data Analysis Tools

**ChemDraw Professional 16.0**

It is an advanced software created by PerkinElmer Informatics (previously CambridgeSoft) that enables users to illustrate and visualize intricate chemical structures, reaction processes, and biological pathways. It has an extensive array of drawing tools and a substantial collection of chemical templates, rendering it optimal for producing publication-quality chemical diagrams.

In addition to its drawing functionalities, it can forecast $^{1}H$ and $^{13}C$ NMR spectra, compute fundamental physicochemical parameters, and execute name-to-structure or structure-to-name transformations. It connects with other applications in the ChemOffice suite, ensuring interoperability with software such as Chem3D and ChemFinder for a comprehensive chemical information management solution.

**Origin**

Origin is a specialized software platform for data analysis, curve fitting, and graphical representation. It offers advanced statistical tools, batch processing capabilities, and customizable graphing options, making it suitable for handling complex datasets standard in chemical, biological, and engineering research [18].

**GraphPad Prism**

GraphPad Prism is an intuitive tool extensively utilized in the biomedical and pharmaceutical sectors for statistical analysis, curve fitting (such as dose-response curves), and generating high-quality visuals. It incorporates standard statistical tests and provides understandable visual representations of experimental data [19].

**Notepad++**

Notepad++ is a complimentary, open-source text and source code editor designed for Windows. It accommodates several programming languages and offers functionalities such as syntax highlighting, code folding, and customizable macros. This research used it to examine and modify text-based input/output files for the aforementioned computational software, facilitating rapid alterations and error verification without necessitating a complete integrated development environment (IDE) [20].

## II.3 Experimental Methods

### II.3.1 Synthesis of Organophosphonates

#### II.3.1.1 Conventional method

To synthesize two new α-amino phosphonic acids (HAP1 and HAP2), we employed the Moedritzer–Irani reaction [21], accurately measuring 0.01 mol of 3-aminopropanol or 4-aminobutanol using a high-precision analytical balance. Then, we transferred the amino alcohol to a 100 mL three-necked flask and solubilized it in distilled water. After that, we introduce 0.02 mol of phosphorus acid ($H_3PO_3$) and 0.02 mol of acetaldehyde, stirring continuously to ensure homogeneous distribution. The flask was on a heating mantle or oil bath with a temperature controller set to 100 °C, and the magnetic stirrer was used to ensure comprehensive mixing. The reaction was monitored with Thin Layer Chromatography (TLC) by extracting tiny samples hourly and transferring them to TLC plates pre-coated with silica gel. The reaction was rested for 6 to 7 hours, confirming its completion through the absence of starting materials and the majority of the target product. We use a rotary evaporator to remove solvent and isolate the crude product, which may require further purification. Recrystallization techniques involve dissolving the crude product in a small volume of hot solvent and permitting it to recrystallize throughout the cooling process. The following scheme shows the summary of this reaction. (Scheme II.1).

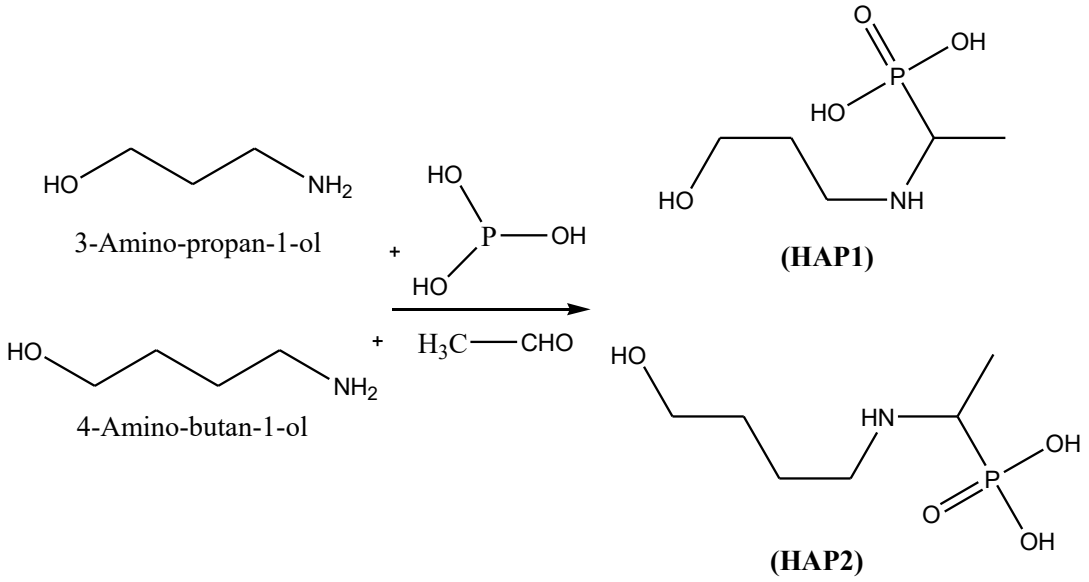


**Scheme II.1** Synthesis of (HAP1) and (HAP2) aminophosphonic acids via modified Irani-Moedritzer reaction.

### II.3.1.2 Microwave method

The process commenced by measuring 1.0 mmol of either 3-aminopropanol or 4-aminobutanol with a high-precision analytical balance. The selected amino alcohol was placed into a 10 mL quartz reaction tube, maintaining cleanliness to avoid contamination. 0.5 mL of distilled water was introduced to enhance dissolution and ensure uniform mixing. 2.0 mmol of phosphorous acid was added to the reaction mixture, initiating the condensation reaction essential to the Moedritzer-Irani approach. The mixture underwent microwave irradiation at a power level of 100 watts for 2 minutes, facilitating quick and uniform energy distribution, accelerating reaction kinetics, and perhaps increasing yields. After the initial irradiation phase, 4.0 mmol of acetaldehyde was meticulously introduced dropwise to regulate the exothermic characteristics of the condensation reaction and mitigate the potential for side reactions that can jeopardize the purity of the intended α-amino phosphonic acids. The sealed quartz tube was reinserted into the microwave reactor for an extra 6 minutes of irradiation, enabling the synthesis of HAP1 or HAP2 through condensing amino alcohol, phosphorous acid, and acetaldehyde.

### II.3.2 Density Functional Theory (DFT) Studies

We applied Density Functional Theory (DFT) for quantum chemistry computational using the 6-31G(d,p) basis set, which integrates Becke's three-parameter exchange function [22-23]. The selection of the 6-31G(d,p) basis set offers a judicious compromise between computational efficiency and precision, facilitating dependable optimization of molecular

geometries and ensuing property assessments. The DFT method is well-suited for analyzing the electronic structure of molecules, providing an effective balance between computing expense and the capacity to account for electron correlation effects crucial for precise predictions of molecular characteristics.

The molecular geometries were first tuned in the gas phase to confirm that the structures represent genuine minima on the potential energy surface. Geometry optimization entails the iterative adjustment of molecular coordinates until the stresses on each atom are minimized, yielding a stable conformation devoid of imaginary frequencies. This process is essential for acquiring precise structural data that underpin subsequent electrical and vibrational studies [24].

After the geometry optimization, vibrational frequency calculations confirmed that the optimized structures are at an energy minimum rather than a saddle point. These computations entail determining the second energy derivatives about atomic displacements, yielding a collection of vibrational modes and their associated frequencies. The lack of imaginary frequencies verifies that the structures represent genuine minima. Furthermore, the vibrational spectra offer theoretical insights into molecular vibrations, which can be juxtaposed with experimental infrared (IR) data for validation [25].

Alongside confirming the vibrational frequencies to ascertain the absence of imaginary frequencies and validate a genuine local minimum, we calculated numerous critical chemical parameters that affect the reactivity and stability of the compounds. In particular, these encompass:

- Determination of HOMO–LUMO energies and gap
- Dipole moment
- Mulliken charges
- Molecular electrostatic potential surface (MESP)
- Total energy (E_total) and thermochemical parameters (enthalpy, Gibbs free energy)

We additionally computed specific essential chemical parameters that affect the reactivity and stability of the compounds. The following properties are included:

**Ionization Potential (I):** Determined as the negative of the energy of the Highest Occupied Molecular Orbital (HOMO), $I = -E_{HOMO}$. It represents the energy required to remove an electron from the molecule.

**Electron Affinity (A):** Calculated as the negative of the energy of the Lowest Unoccupied Molecular Orbital (LUMO), $A = -E_{LUMO}$. It indicates the energy change when an electron is added to the molecule.

**Energy Gap (ΔE_GAP):** Defined as the difference between the HOMO and LUMO energies, $\Delta E_{GAP} = E_{HOMO} - E_{LUMO}$. This gap is critical in determining the molecule's electronic properties and chemical reactivity.

**Electronegativity (χ):** Calculated using the formula $\chi = (I + A)/2$, it quantifies a molecule's tendency to attract electrons.

**Chemical Potential (μ):** Given by $\mu = -\chi$, it reflects the escaping tendency of electrons from the molecule.

**Molecular Hardness (η):** Defined as $\eta = (E_{LUMO}—E_{HOMO})/2$, it measures a molecule's resistance to charge transfer.

**Molecular Softness (S):** Inversely related to hardness $S = 1/\eta$, it indicates the ease with which a molecule can be polarized.

**Electrophilicity Index (ω):** Calculated using $\omega = \mu^2/2\eta$., it quantifies a molecule's ability to accept electrons.

### II.3.3 Molecular Docking

#### II.3.3.1 Proteins Preparation

The target protein's three-dimensional (3D) structure was acquired from the Protein Data Bank (https://www.rcsb.org/) with PDB ID [26], opting for a structure with the highest resolution and fewest missing residues. Irrelevant heteroatoms (for example, crystallographic water molecules and ions) were eliminated unless necessary for protein function or structural integrity. Depending on their significance to the binding site and supporting literature, missing loops or side chains were either modeled or retained in their original state. The protonation states of ionizable residues (Asp, Glu, Lys, Arg, His) were modified to reflect physiological pH (~7.4) [27] via computational methods (such as PropKa through PyMOL plug-ins), and histidine residues were analyzed to identify the most likely tautomeric form. The purified protein structure was preserved in PDB format. Docking with

AutoDock or AutoDock Vina was transformed into PDBQT format utilizing AutoDockTools while assigning Gasteiger charges [28] and appropriate atom types.

### II.3.3.2 Ligands Preparation

Ligands were obtained from our organic synthesis, and the initial 2D structure of each ligand was constructed and validated for accuracy. The structures were further transformed into 3D if required. They underwent quantum chemical optimization utilizing Gaussian at a suitable theoretical level (e.g., B3LYP/6-31G(d)) to guarantee precise geometry and partial charge distribution. The optimized structures were extracted from the Gaussian output (including the .log or .chk formats) and saved as .mol2 or .pdb files. For instances requiring enhanced accuracy, RESP or ESP charges obtained via Gaussian calculations were utilized; otherwise, Gasteiger charges were allocated with AutoDockTools. Ultimately, all ligands were transformed into PDBQT format (utilizing AutoDockTools), guaranteeing appropriate protonation, atom types, and charges before docking.

### II.3.3.3 Docking Protocol:

The active site was determined by analyzing the location of the co-crystallized ligand (if present), consulting established functional or catalytic residues from the literature, and assessing accessible cavities in PyMOL. Docking simulations were conducted using AutoDock 4.2 and/or AutoDock Vina, with the grid box configured to encompass the critical active-site residues, providing an adequate area for ligand translation and rotation. In AutoDock 4.2, the Lamarckian Genetic Algorithm (LGA) [29] was selected, with the number of algorithm iterations (for instance, 50–100) and the maximum evaluations modified for thorough conformational sampling [30]. A configuration file for AutoDock Vina was utilized, detailing the receptor and ligand PDBQT files, grid box coordinates, exhaustiveness (typically 8–16) [31], and the number of binding modes (including 10 or more) [32]. Subsequently, each ligand was docked into the generated protein structure, yielding output files that included anticipated binding poses and estimated binding energies or scores.

### II.3.3.4 Post-Docking Analysis

The docking poses were initially prioritized according to estimated binding energies (AutoDock) or scores (AutoDock Vina), preserving the top 5–10 poses for each ligand for thorough examination. PyMOL was further employed to visualize the docked complexes and

delineate critical interactions, such as hydrogen bonds, hydrophobic contacts, π–π stacking, and salt bridges correlated with the corresponding protein residues [33]. In the presence of a co-crystallized ligand, redocking acted as a validation procedure by assessing the root-mean-square deviation (RMSD) between the experimentally obtained and predicted ligand orientations; an RMSD of less than 2.0 Å was considered indicative of a dependable docking approach [34]. In instances of docking several ligands, a comparative examination of their binding modes, energies, and residue interactions yielded additional insights into structure-activity correlations.

### II.3.4 ADME-T and Drug-likeness Predictions

SwissADME (online) was utilized to compute molecular descriptors, including molecular weight (MW), LogP, hydrogen-bond donors (HBD), and hydrogen-bond acceptors (HBA), as well as to assess Lipinski's Rule of Five [35]. Concurrently, pkCSM offered predictions for pharmacokinetic and toxicity parameters, encompassing oral absorption, blood-brain barrier permeability, and Ames toxicity. The evaluated key metrics encompassed drug-likeness (utilizing Lipinski's criteria: MW < 500, LogP < 5, HBD ≤ 5, HBA ≤ 10), pharmacokinetics (human intestinal absorption, Caco-2 permeability, plasma protein binding), and toxicity (Ames test, hepatotoxicity predictions, LD50). The resultant ADME-T profiles were juxtaposed with those of reference pharmaceuticals and established phosphonate compounds, revealing shortcomings that indicated potential structural alterations to improve drug likeness, absorption, and safety.

In the meantime, three complementary tools, pkCSM, Molinspiration, and ADMET.AI, were utilized to enhance the analysis of pharmacokinetic and toxicity parameters. pkCSM, utilizing graph-based signatures, produced predictions for oral absorption (human intestinal absorption), Caco-2 cell permeability (a measure of intestinal epithelial permeability), blood-brain barrier (BBB) penetration, and plasma protein binding (PPB). Furthermore, pkCSM offered toxicity predictions, including Ames mutagenicity, an essential indicator of potential carcinogenic risk. Molinspiration provided additional descriptor calculations and a drug-likeness assessment, facilitating the cross-verification of physicochemical attributes acquired through SwissADME. Furthermore, ADMET.ai utilized machine-learning techniques to assess a wide range of toxicity endpoints, including hepatotoxicity and LD50 (lethal dose) estimations. These interconnected yet separate platforms collectively provided an extensive perspective on how the structural characteristics of each molecule could affect both efficacy and safety.

## II.4 Nanoparticle investigation

Hyaluronan-cholesterol (HA Figure II.1) is a semi-synthetic hyaluronic acid (HA) derivative characterized by cholesterol groups' covalent attachment to the HA backbone [36-38]. This alteration confers amphiphilic characteristics, enabling HA to self-assemble in aquatic conditions and generate stable nanoparticles or micelles [39]. Consequently, HACH demonstrates the potential for applications like targeted drug delivery [40-42], wherein its hydrophobic cholesterol moieties encapsulate therapeutic compounds. At the same time, the hydrophilic HA segments enhance biocompatibility and targeting through HA receptor contacts.

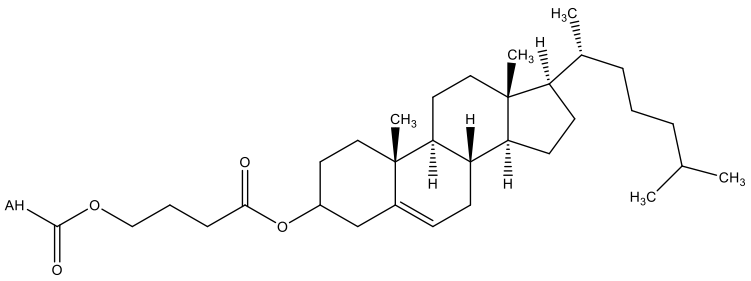


**Figure II. 4** Hyaluronan-cholesterol (HACH)

HA-CH exhibits limited solubility in water due to its cholesterol segments' hydrophobic characteristics. Nonetheless, HA-CH can autonomously generate nanohydrogels (NHs) or nanogels through self-assembly, wherein the cholesterol segments cluster to reduce water exposure while the hydrophilic hyaluronan backbone remains accessible. The amphiphilic nature is essential for producing stable nanocarriers, which can transport many therapeutic substances or be further modified for particular biomedical uses [43].

### II.4.1 Nanohydrogel preparation

To enhance HA's exposure to the following reaction mixes and optimize its processability, HA NHs are often synthesized before any further changes. In a standardized protocol, 50 mg of HACH is dissolved in distilled water to achieve a 2 mg/mL concentration and agitated overnight at room temperature (RT). This extended agitation guarantees sufficient hydration and partial self-assembly of the HACH molecules. The resultant suspension undergoes a typical autoclave sterilization cycle (121 °C, 1.1 bar, 20 min), which sterilizes the formulation and promotes the final creation of stable nanogels. Increased temperature and pressure conditions can facilitate self-assembly, encouraging denser aggregation of the hydrophobic cholesterol domains within the nanogel core. The final

product is a sterile dispersion of HACH nanohydrogels suitable for immediate use or subsequent functionalization for drug administration, tissue engineering, or other sophisticated biomedical applications.

### II.4.2 Loading Efficiency (Drug Loading )

#### II.4.2.1 Prepare the Drug Film

Organophosphonate was dissolved in acetone (or another organic solvent) at a concentration of 2 mg/mL, ensuring thorough dissolution through gentle vortexing or stirring if needed. Then, 0.5 mL of this stock solution into a clean glass vial and a rotary evaporator—set at a water bath temperature of about 30–40 °C, under moderate vacuum, and a rotational speed of 50–100 rpm—to remove the solvent and form a thin drug layer on the vial's interior surface. The evaporation was continued until no discernible solvent was present, and the film appeared desiccated. Finally, we verified that no residual solvent remained, as any residual traces could have compromised nanogel stability and encapsulation efficacy.

#### II.4.2.2 Hydrate the Film with Nanogels

The film was Hydrating with nanogels by meticulously introducing 3 mL of the nanogel suspension in water into the vial containing the desiccated organophosphonate film, with the nanogel concentration and composition previously established through earlier synthesis and characterization. The mixture was agitated to commence the rehydration of the drug film while the organophosphonate began to disperse into the nanogel phase. Subsequently, the vial is positioned on a magnetic stirrer and agitated at about 25 °C overnight (12–24 hours), facilitating the diffusion of drug molecules from the film into the nanogels, hence improving loading efficiency. Maintaining the vial with a loose cover to avert contamination and prevent evaporation of the aqueous phase. Subsequently, the agitated mixture is transferred to an ultrasonic bath sonicator and subjected to sonication for 20 minutes while maintaining the bath temperature at around 25 °C to avert excessive heating. This sonication facilitated the disaggregation of aggregates and enhanced the uniform distribution of the organophosphonate within the nanogels.

#### II.4.2.3 Nanogel Recovery

The nanogels were recovered by centrifuging the sonicated mixture at 4000 rpm for 15 minutes at 25 °C. This facilitated the sedimentation of drug-loaded nanogels and the separation from any unencapsulated or loosely bound drug in the supernatant. Subsequently, meticulously extracting the supernatant, with the ability to quantify its residual drug

concentration to assess encapsulation efficiency. To eliminate excess free drugs or impurities, the nanogel pellet was resuspended in a new buffer or water, and the centrifugation step was repeated until the desired purity was attained.

#### II.4.2.4 Encapsulation Efficiency:

The quantity of Organophosphonates effectively loaded was assessed by quantifying the drug concentration in the supernatant post-centrifugation, for instance, via UV-Vis spectroscopy. This facilitated the calculation of encapsulation efficiency (%) using the subsequent formula:

$$\text{Encapsulation efficiency (EE\%)} = \frac{Amount\ of\ drug\ in\ nanogels}{Total\ drug\ added} \times 100\%.$$

The quantity of drug in nanogels was determined by subtracting the measured drug content in the supernatant from the total drug initially introduced.

### II.4.3 In Vitro Release Testing

In vitro release testing was performed to analyze the temporal release of the drug from nanohydrogels under conditions that simulate physiological or application-specific environments. An appropriate release medium, specifically phosphate-buffered saline (PBS) at pH 7.4, was employed at 37 °C to replicate human body temperature. Sink conditions have been maintained by maintaining a low drug concentration, either by utilizing a sufficiently large amount of release medium or by routinely replacing it to facilitate continuous drug release. Samples were collected at predetermined intervals (for example, 0.5 hours, 1 hour, 2 hours, 4 hours, 8 hours, 24 hours, etc.) based on the anticipated release profile. Many experimental configurations, such as dialysis bag techniques or direct dispersion methods, were employed, in which the nanogels were placed in a vial or well, and the supernatant was collected at predetermined intervals to assess release kinetics.

#### II.4.3.1 Dialysis Bag Method

In the dialysis bag approach, a specified volume of drug-loaded nanohydrogels, which are 2 mL of dispersion, is introduced into a dialysis bag with a suitable molecular weight cutoff (MWCO of 10 kDa) that inhibits the release of nanohydrogels while permitting the diffusion of free Organophosphonates. The bag is immediately shut and inspected for leaks. The sealed bag is submerged in a beaker or flask containing a specified volume of release medium (PBS at pH 7.4), maintained at 37 °C with mild agitation (about 50–100

rpm), or positioned on a shaking platform to guarantee equal distribution. At specified intervals, 1 mL aliquots of the release media are extracted, substituted with fresh, pre-warmed medium to preserve consistent volume and sink conditions, and assessed for drug content utilizing appropriate analytical methods such as UV-Vis spectroscopy. The total drug release at each time point is determined using the known volume and measured concentration, and the data are shown as the cumulative release (%) against time.

### II.4.3.2 Direct Dispersion Method

In the traditional dispersion approach, drug-encapsulated nanohydrogels are placed into a vial or test tube containing a suitable volume of release medium (e.g., 3 mL of PBS), maintaining a ratio that facilitates sink conditions. The mixture is subsequently maintained at 37 °C with mild agitation or stirring. At certain intervals, the sample is centrifuged (e.g., at 10,000 rpm for 5–10 minutes) to segregate the free medication in the supernatant from the nanogels in the pellet. A tiny aliquot of the supernatant is meticulously obtained for pharmacological examination, usually via UV-Vis. The discarded supernatant is substituted, if required, with an equivalent volume of fresh buffer to preserve sink conditions. The cumulative release profile is established by graphing the percentage of medication released over time, allowing for comparison among different formulations or experimental settings.

### II.4.3.3 Additional Considerations

Additionally, variables related to in vitro release studies encompass the regulation of parameters such as pH (to replicate various physiological environments, including the acidic tumor microenvironment), ionic strength (since salinity and the presence of other ions can affect nanogel swelling and drug release), and enzyme exposure (e.g., hyaluronidase for hyaluronic acid-based systems) to emulate in vivo degradation. Measurement techniques vary from UV-Vis spectroscopy, which is straightforward and economical for drugs with distinct absorbance, to more advanced methods such as HPLC, which offers enhanced specificity and sensitivity, and LC-MS, utilized for comprehensive analyses, including identifying potential degradation products. Determining encapsulation efficiency (EE%) before the release study is crucial for precisely calculating the proportion of encapsulated medication released over time. Kinetic modeling helps clarify if the release is governed by diffusion, erosion, or a more intricate mechanism. Ultimately, performing experiments in triplicate or more, utilizing blank nanogels to assess assay interference, and incorporating a free drug control for comparison all contribute to the robustness and dependability of the data.

## II.5 Bilogicals assay

### II.5.1 ABTS Scavenging Activity

#### II.5.1.1 Preparation of the ABTS•+ Stock Solution

To create the ABTS solution, weigh 19.2 mg of ABTS to achieve a final concentration of 7 mM and dissolve it in 5 mL of ultrapure water. In a separate container, measure 3.3 mg of potassium persulfate ($K_2S_2O_8$), yielding a final concentration of 2.45 mM, and dissolve it in 5 mL of ultrapure water.

Subsequently, the ABTS solution was combined with the potassium persulfate solution, achieving a total volume of roughly 10 mL. Allow this mixture to rest in darkness either by encasing the container in aluminum foil or situating it in a dark chamber at ambient temperature for 12 to 16 hours. This incubation phase promotes the generation of the ABTS radical cation ($ABTS^{\bullet+}$).

After the incubation period, assess the absorbance of the $ABTS^{\bullet+}$ solution at 734 nm. Dilute the solution with ethanol (or water) until the absorbance attains 0.700 ± 0.020 at 734 nm. The modified $ABTS^{\bullet+}$ solution is now prepared for application in the assay [44].

#### II.5.1.2 Antioxidant Assay Procedure

Start the test by prepping the wells of your microplate. Transfer 160 µL of the $ABTS^{\bullet+}$ solution, measured to an absorbance of 0.700 ± 0.020 at 734 nm, into the container. Then, introduce 40 µL of your sample or extract, which contains the probable antioxidant compound that will be studied.

After combining the solutions, gently mix them and permit the reaction to occur for approximately 10 minutes at ambient temperature. If feasible, shield the mixture from direct light to preserve the integrity of the $ABTS^{\bullet+}$ radical throughout the incubation time.

In the end, quantify the solution's absorbance at 734 nm. Utilize an appropriate blank for comparison, which can be created by substituting the 40 µL of the sample or extract with an equivalent volume of the corresponding solvent. The disparity in absorbance between the control and the test mixture signifies the percentage of $ABTS^{\bullet+}$ decolorization, demonstrating the antioxidant ability of the examined material [44].

#### II.5.1.3 Data Analysis

A decrease in the absorbance at 734 nm reflects the tested sample's scavenging activity or antioxidant capacity. To quantify this activity, results can be presented either as a

percentage inhibition or with a standard antioxidant, such as Trolox, by generating a standard curve. The formula for calculating the percentage inhibition is:

$$\%\boldsymbol{Inhibition} = \frac{(A_0 - A_s)}{A_0} * 100$$

In this formula, $A_0$represents the absorbance of the $ABTS^{\bullet+}$ solution without the sample (the blank) while $A_s$Is the absorbance of the $ABTS^{\bullet+}$ solution after adding the sample? When a quantitative measure of antioxidant capacity is desired.

#### II.5.1.4 Notes and Tips

ABTS and its radical form ($ABTS^{\bullet+}$) are known for being highly sensitive to light, so we should keep the solutions protected from light whenever possible. Ethanol was commonly used to dilute $ABTS^{\bullet+}$, confirming that the final test solvent was compatible with every sample.

A standard reaction duration of 10 minutes was utilized, but some samples needed modifications if their radical-scavenging kinetics showed considerable variations. Moreover, we always ran tests in triplicate to guarantee dependability, using suitable controls—such as a solvent blank and a positive control to enable comprehensive data validation.

### II.5.2 DPPH free radical

#### II.5.2.1 Preparation of the DPPH Stock Solution

To create the DPPH stock solution, weigh 4 mg of DPPH (2,2-diphenyl-1-picrylhydrazyl) powder. Completely dissolve it in 100 mL of methanol, ensuring the powder is entirely solubilized. Upon dissolution, put the solution in an opaque container such as an amber bottle or one encased in aluminum foil and store it at 20 °C to preserve the radical's stability.

Before utilizing the stock solution, assess its absorbance at 517 nm with a spectrophotometer. If required, dilute with methanol until the absorbance approximates 0.50 at 517 nm. Upon completion of this correction, the DPPH solution is prepared for application in the assay [45].

#### II.5.2.2 Antioxidant Assay Procedure

Start by injecting 160 µL of the DPPH solution (previously adjusted to an absorbance of approximately 0.50 at 517 nm) into an appropriate test tube, microplate well, or cuvette. After that, add 40 µL of the sample containing the antioxidant for evaluation.

After combining the solutions, gently stir them to ensure complete dispersion. Allow the combination to rest for a suitable reaction duration, typically between 15 and 30 minutes at ambient temperature, protecting it from direct light to maintain the integrity of the DPPH radical.

Finally, the incubation period will be assessed using a spectrophotometer to determine the solution's absorbance at 517 nm ($A_{517}$). Evaluate this reading against a control (comprising the DPPH solution devoid of the sample) and a blank (containing solely the solvent) to ascertain the antioxidant activity of the examined sample [45].

### II.5.2.3 Data Analysis

The reduction of DPPH's deep violet color at 517 nm signifies radical scavenging by the tested antioxidant. The percentage of Radical Scavenging Activity (RSA) is calculated using the following equation:

$$\%\boldsymbol{Inhibition} = \frac{(A_{control} - A_{simpel})}{A_{control}} * 100$$

Where $A_{control}$ Is the absorbance of the DPPH solution without the sample and $A_{simpel}$ It is the absorbance of the solution containing the sample. A calibration curve can be constructed using a standard antioxidant for more quantitative comparisons. The results may be expressed as the $IC_{50}$ value (the concentration required to reduce the initial DPPH absorbance by 50%) or in terms of standard antioxidant equivalents.

### II.5.2.4 Notes and Tips

The selection of solvent is crucial in conducting the DPPH assay. While methanol is the predominant choice, alternative solvents like ethanol may be favored if the sample exhibits more solubility. It is essential to verify that the selected solvent does not compromise the stability of DPPH or disrupt the absorbance measurements.

The standard reaction time for the DPPH test typically ranges from 15 to 30 minutes, though this may fluctuate depending on the kinetics of the studied antioxidant. Certain antioxidants may necessitate extended durations for complete reaction; thus, it is prudent to tailor the incubation period to the unique attributes of each sample.

Due to DPPH's sensitivity to light, its preparation and measurement should be conducted in low-light circumstances, or the solutions should be protected from direct light exposure. This measure aids in averting the premature destruction of the DPPH radical.

Conduct all measures in triplicate to guarantee dependable outcomes. Furthermore, consistently incorporate a solvent control where 40 µL of the solvent substitutes the sample and a recognized standard antioxidant for technique validation. These controls mitigate solvent effects and validate the assay's accuracy.

### II.5.3 Phenanthroline-Ferric Reducing Power Assay

#### II.5.3.1 Reagent Preparation

To create a 0.5% w/v phenanthroline solution, measure 0.05 g of 1,10-phenanthroline and dissolve it in 10 mL of methanol (MeOH). Transfer the solution into an opaque container (amber bottle) and store it at ambient temperature to avert deterioration by light.

To prepare a 0.2% w/v ferric chloride solution, weigh 0.02 g of $FeCl_3$ and dissolve it in 10 mL of distilled water. If feasible, shield this solution from light to preserve its stability.

#### II.5.3.2 Assay Procedure

Commence the assay by formulating your reaction mixture in an appropriate microplate well. Incrementally introduce 10 µL of the sample, succeeded by 50 µL of the 0.2% $FeCl_3$ solution and 30 µL of the 0.5% phenanthroline solution. Subsequently, add 110 µL of methanol to the mixture, resulting in 200 µL for each reaction.

Upon assembling the reaction mixture, gently agitate the contents and incubate in the absence of light at 30 °C for 20 minutes. Upon completion of the incubation period, assess the absorbance at 510 nm utilizing a spectrophotometer or microplate reader. Incorporate a blank or reference control by substituting the sample with an equivalent volume of solvent; this mitigates background absorbance and enhances the accuracy of data interpretation [46].

#### II.5.3.3 Data Interpretation

A higher absorbance at 510 nm generally corresponds to a more substantial reducing power and higher antioxidant capacity of the tested sample.

Results can be expressed as an increase in absorbance compared to a control reagent or as equivalents of a standard antioxidant.

#### II.5.3.4 Controls and Standard

Butylated hydroxytoluene (BHT) is commonly employed as a positive control or standard for this assay. To establish a standard curve, prepare a series of BHT solutions with varying known concentrations and run them in parallel under the same conditions. By plotting the resulting absorbances against the corresponding concentrations, you can

compare your sample's reducing power to the BHT standard. When setting up the assay, include a blank control using the solvent (methanol) instead of the extract to account for any baseline absorbance or background interference.

### II.5.4 Ferric Reducing Power (FRP) Assay

#### II.5.4.1 Reagent Preparation

Begin by preparing the 1% potassium ferricyanide solution: weigh out 1 g of potassium ferricyanide ($K_3[Fe(CN)_6]$) and dissolve it thoroughly in 100 mL of distilled water. Next, create a 10% tri-chloroacetic acid (TCA) solution by weighing 1 g of TCA and dissolving it in 10 mL of distilled water.

For the 0.1% ferric chloride solution, weigh 0.1 g of $FeCl_3$ dissolve it in 100 mL of distilled water, ensuring the solution is well-mixed. Finally, prepare a phosphate buffer at pH 6.6 by combining suitable amounts of sodium dihydrogen phosphate ($NaH_2PO_4$) and disodium hydrogen phosphate ($Na_2HPO_4$). Use a pH meter to confirm that the solution is accurately adjusted to pH 6.6 [47].

#### II.5.4.2 Assay Procedure

For the start of the reaction, introduce 10 µL of the sample (extract) into an appropriate test tube or microplate well, then add 40 µL of phosphate buffer (pH 6.6) and 50 µL of the 1% potassium ferricyanide ($K_3[Fe(CN)_6]$) solution. Carefully combine these components and incubate the mixture at 50 °C for 20 minutes, utilizing a water bath or incubator.

Following incubation, incorporate 50 µL of the 10% TCA solution and 40 µL of distilled water to acidify the mixture. Subsequently, add 10 µL of the 0.1% ferric chloride ($FeCl_3$) solution, which triggers color development that signifies the sample's reducing capacity. Ultimately, the absorbance at 700 nm was assessed using a spectrophotometer or microplate reader. Ensure the inclusion of a blank that contains solely the solvent, devoid of any sample, to provide a baseline for absorbance correction [47].

### II.5.5 Antibacterial assay

In the disk diffusion assay, we inoculated plates by dipping a sterile cotton swab into a standardized bacterial suspension and then evenly spreading it over the surface of a pre-dried Mueller-Hinton Agar plate. Simultaneously, we prepared the test samples by impregnating sterile paper disks with the test extract at the desired concentrations or by creating wells in the agar and filling them with the test solution.

At the same time, the disks or the test solutions were carefully placed onto the inoculated agar surface to ensure proper contact for diffusion. The plates were then incubated at 35–37 °C for 18–24 hours, during which the bacteria were growing, and the active compounds were diffusing through the agar medium.

After incubation, we measured the diameter of the inhibition zones in millimeters. We then compared these results with those obtained from standard antibiotic controls and interpreted the data according to established clinical breakpoints, thereby assessing the antibacterial potency of the test extract.

## II.6 Conclusion

This chapter established a comprehensive framework to facilitate the synthesis, characterization, computational analysis, and biological evaluation of organophosphonate chemicals. Extensive descriptions of the chemicals, reagents, and specialized apparatus underscore the rigorous focus on purity, storage, and handling conditions vital for reproducible results. The synthesis methodologies, including traditional and microwave-assisted approaches, have been detailed, ensuring the reliable replication of α-amino phosphonic acid production.

Advanced analytical techniques, including TLC, FT-IR, UV-Vis spectrophotometry, and NMR, were utilized to verify the identity and structural integrity of the synthesized compounds. Incorporating computational methods, including DFT investigations and molecular docking, offers profound insights into these molecules' electrical characteristics, reactivity, and potential biological interactions. The chapter outlines the synthesis and characterization of nanohydrogels for drug delivery, as well as a series of biological experiments (antioxidant, antibacterial, and anticholinesterase properties) that collectively support the therapeutic potential of organophosphonates.

The meticulous selection and articulation of each methodology guarantee elevated experimental rigor and reproducibility standards while providing a robust basis for the ensuing analysis and discussion of outcomes. This integrated methodological approach is essential for enhancing our comprehension of these novel compounds' chemical and biological features. It establishes a foundation for future study and possible applications in biomedical science.

III

# Synthesis and Evaluation of Organophosphonates

# III Synthesis and Evaluation of Organophosphonates

## III.1 Introduction

This chapter analyzes the principal objectives of this investigation: the synthesis and characterization of novel organic phosphonic acids, particularly α-amino phosphonic acids. These molecules have been engineered to leverage their unique structural and functional characteristics, isolating them from traditional phosphonic acids. The difference between them stems from the addition of the α-amino group, which is expected to confer specific reactivity and prospective uses in catalysis, biological activity, and nanomaterials research.

In the following parts, we shall Summarize the synthetic results obtained during the investigation, specifying the approaches utilized. We shall deliver an exhaustive data analysis, including spectroscopic and analytical methodologies. We shall examine the findings of the contemporary literature, contrasting the efficacy and prospects of these α-amino phosphonic acids with recognized analogs. This approach provides a comprehensive understanding of the synthesized compounds' chemical behavior and structural characteristics, facilitating future research and practical applications.

## III.2 Synthesis method

The application of microwaves to accelerate reactions has emerged as a crucial instrument for achieving the objectives of green chemistry, particularly in waste reduction and energy conservation. Microwave irradiation provides swift and homogeneous heating, enabling reactions to attain optimal conditions quickly, a notable benefit compared to traditional approaches that can necessitate severe temperatures or extended reaction durations.

Microwave-assisted approaches are increasingly used in organic synthesis, mainly when conventional methods are ineffective or require high reaction conditions. The phosphonates examined in this work were easily synthesized utilizing a straightforward and efficient methodology, showcasing elevated yields, enhanced selectivity, and reaction efficacy. This method highlights the possibility of creating environmentally sustainable synthetic processes that may be scaled for industrial use, where sustainability and minimized energy use are essential considerations.

### III.2.1 Synthesis of α-Aminophosphonic Acids ($HAP_1$ and $HAP_2$)

#### III.2.1.1 By Conventional method

A solution containing 0.01 mol of 3-aminopropanol (or 4-aminobutanol) in 10 mL of water was mixed with 0.02 mol of $H_3PO_3$ and 0.02 mol of acetaldehyde in a three-necked flask. The reaction mixture was further heated to 100°C with continuous stirring for 6 to 7 hours. The reaction's progress was meticulously observed by thin-layer chromatography (TLC) to confirm the complete transformation of the reactants into the target α-aminophosphonic acid. After completion of the reaction, the solvent was eliminated via a rotary evaporator, thereby concentrating the crude product. Recrystallization was conducted using acetonitrile as the solvent to enhance the purity of the obtained α-aminophosphonic acid. This recrystallization process effectively removed impurities and produced a high-purity crystalline product appropriate for further analysis and applications. Scheme III.1 delineates the comprehensive reaction route, highlighting the conversion of the first substrates into the ultimate α-aminophosphonic acid product.

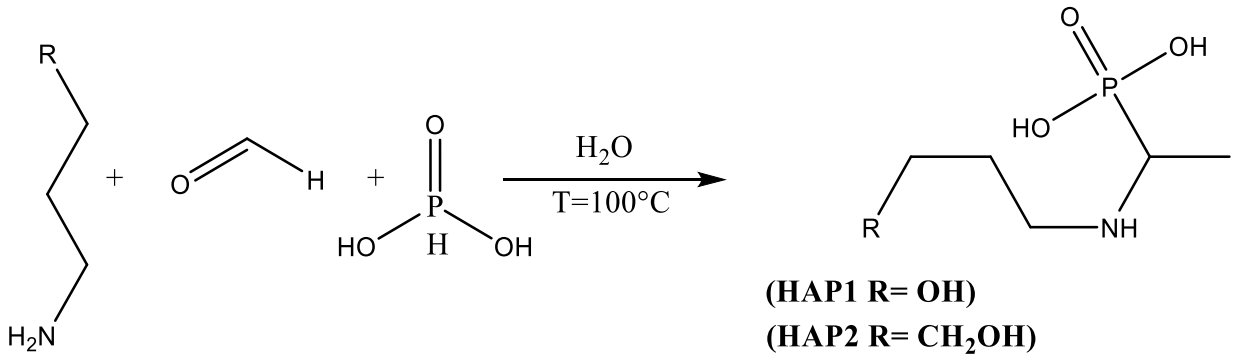


**Scheme III.1** Synthesis of α-Aminophosphonic Acids HAP1 and HAP2 via Conventional method

#### III.2.1.2 By Microwave method

In a 10 mL quartz tube, 1.0 mmol of 3-aminopropanol (or 4-aminobutanol) was dissolved in 0.5 mL of water, and 2.0 mmol of phosphorous acid was added ($H_3PO_3$). The reaction mixture was first irradiated in the microwave at 100 watts for 2 minutes to achieve comprehensive mixing and beginning activation of the reactants. Subsequently, four mmol of acetaldehyde was introduced dropwise via a pipette to maintain regulated reaction conditions. After incorporating acetaldehyde, the mixture underwent further microwave irradiation for 6 minutes. The solvent volume progressively diminished throughout this interval, and the synthesis of the target α-aminophosphonic acid was assessed via TLC. The

regulated microwave irradiation expedited the process and improved product yield through effective energy transfer. Upon finalization, the crude α-aminophosphonic acid was recrystallized from acetonitrile for further purification. The recrystallization procedure eliminated residual impurities, yielding a pure crystalline product. Scheme III.2 below illustrates the schematic depiction of the microwave-assisted synthesis and ensuing purification processes.

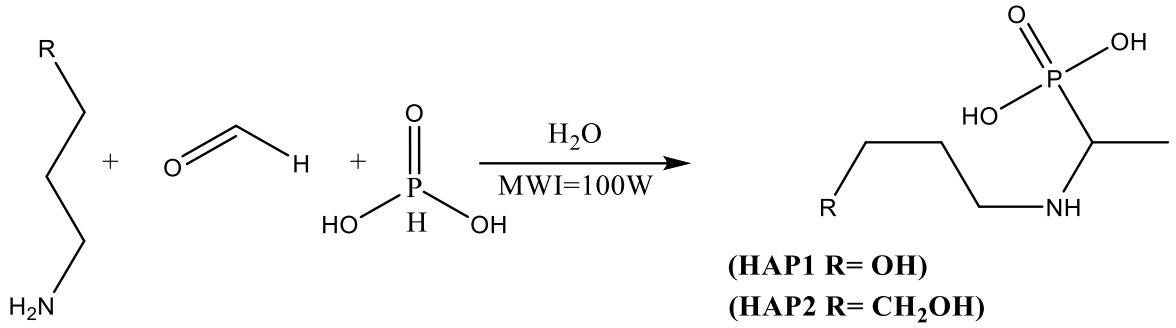


**Scheme III.2** Synthesis of α-Aminophosphonic Acids HAP1 and HAP2 via microwave method

### III.2.1.3 Analysis of Reaction Time and Yield

The α-aminophosphonic acids ($HAP_1$ and $HAP_2$) were prepared by both conventional and microwave-assisted organic synthesis (MAOS), as shown before

The results obtained from the two methods are summarized in Table III.1

**Table III. 1** Comparison of Reaction Time and Yields for $HAP_1$ and $HAP_2$

| Compound | Method | Reaction Time | Yield (%) |
|---|---|---|---|
| $HAP_1$ | Conventional | ~5–8 hours | 44% |
| $HAP_1$ | Microwave-Assisted | ~10 minutes | 90% |
| $HAP_2$ | Conventional | ~5–8 hours | 66% |
| $HAP_2$ | Microwave-Assisted | ~8 minutes | 92% |

The data show that microwave-assisted methods are superior to traditional heating for synthesizing α-aminophosphonic acids.

The microwave method nearly doubled the yield from 44% (conventional) to 90%. Similarly, $HAP_2$ significantly increased, with yields rising from 66% to 92%. For that, we can say that microwave irradiation promotes a more efficient reaction pathway, possibly by ensuring more uniform heating and rapid energy transfer, which enhances the reaction

kinetics also The microwave-assisted synthesis dramatically reduced the reaction time from several hours (~5–8 hours) to a few minutes (approximately 10 minutes for $HAP_1$ and 8 minutes for $HAP_2$) this differences in yield and time are so pronounced that they underscore a statistically and practically significant improvement when adopting microwave-assisted methods.

The integration of microwave-assisted organic synthesis to prepare α-aminophosphonic acids ($HAP_1$ and $HAP_2$) has shown a clear advantage over conventional methods. The significant improvements in yield and reaction time, along with environmental and economic benefits, highlight the potential for microwaves to become a mainstay in modern synthetic organic chemistry. The statistical chart and discussion presented here reinforce the transformative impact of microwave technology on reaction efficiency and sustainability.

### III.2.1.4 Reaction Mechanism

For the modified Irani-Moedritzer reaction, two general pathways have been proposed:

**Pathway 1**

In this route, an imine is initially formed through the nucleophilic attack of the lone pair on the nitrogen atom on the carbonyl group of acetaldehyde. The resulting alkoxide undergoes an intramolecular proton transfer, leading to the formation of an unstable amino-alcohol. This intermediate dehydrates by adding phosphorous acid, yielding the α-aminophosphonic acid ($HAP_1$ and $HAP_2$). The detailed mechanism is illustrated in the sequence of reactions presented in Scheme III.3.

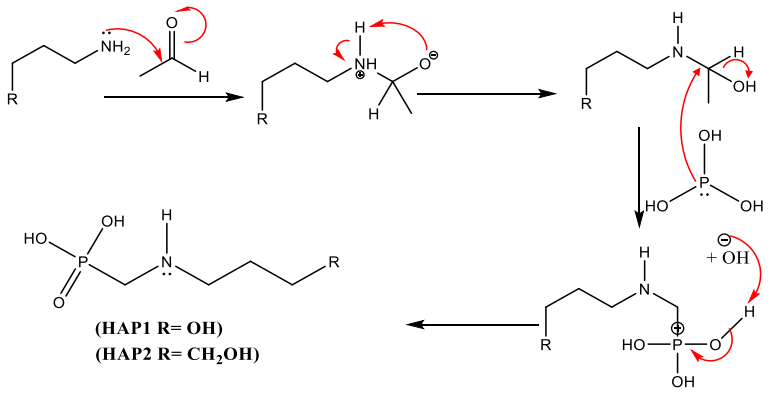


**Scheme III.3** Proposed reaction mechanism for the α-aminophosphonic acid formation reaction (Pathway 1)

**Pathway 2**

Another possibility consists of the nucleophilic attack of the lone pair on the phosphorus atom at the carbonyl group of acetaldehyde, creating an α-hydroxyphosphonic acid. The intermediate subsequently undergoes a second-order nucleophilic substitution ($SN_2$), wherein the hydroxyl group is substituted by an amino group derived from 3-aminopropanol (or 4-aminobutanol). In the next phase, the lone pair on the hydroxyl attached to the hydrogene to form the final product, α-aminophosphonic acid ($HAP_1$ and $HAP_2$) scheme III.4.

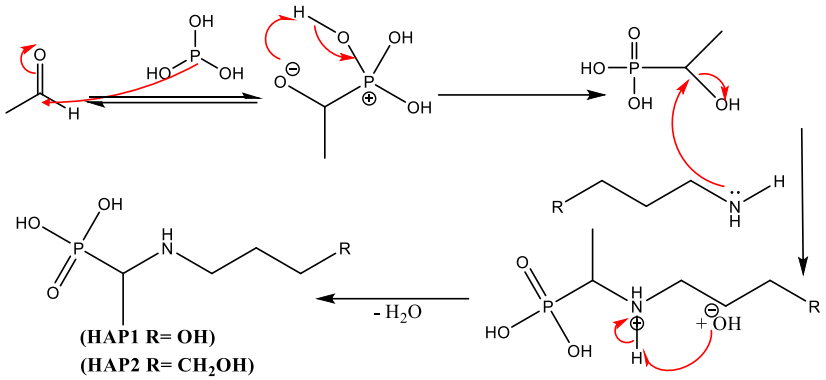


**Scheme III.4** Proposed reaction mechanism for the α-aminophosphonic acid formation reaction (Pathway 2)

Both pathways highlight the flexibility of the modified Irani-Moedritzer reaction, showing how several nucleophilic sites (nitrogen and phosphorus) can be utilized to synthesize α-aminophosphonic acids. The choice between these paths may be influenced by reaction conditions, reagent concentrations, and the particular substrates employed, as the mechanistic insights derived from these pathways not only deepen our comprehension of reaction dynamics but also present prospective opportunities for optimization. By regulating parameters such as temperature, solvent, and microwave irradiation, it may be feasible to preferentially promote one pathway over another, thus enhancing yield and selectivity in the synthesis of $HAP_1$ and $HAP_2$.

## III.3 Preliminary Characterization: Solubility, Melting Points, and TLC

### III.3.1 Solubility Test

Qualitative solubility evaluations were performed for the initial reagent and the newly generated compounds. The experiments entailed introducing minimal quantities of each compound into several solvents (including water, ethanol, chloroform, acetone, and

diethyl ether) at ambient temperature and subsequently under mild heating. The solutions were evaluated for complete, partial, or insolubility (including turbidity, clarity, and precipitation).

The solubility profiles of the synthesized products and the initial reagent show significant disparities (Table III.2). The initial reagent demonstrates intermediate solubility in polar solvents like ethanol at ambient temperature. In contrast, the newly produced compounds are predominantly insoluble under identical conditions. Conversely, the products dissolve more easily when heated, indicating possible alterations in molecular configuration or intermolecular interactions. These differences highlight the structural and physicochemical alterations that occurred during synthesis.

**Table III. 2** Qualitative Solubility of Synthesized α-amino phosphonic acids HAP1 and HAP2 vs. Starting Reagent

| Solvent | Temperature | 3-Aminopropanol | 4-Aminobutanol | HAP1 | HAP2 |
|---|---|---|---|---|---|
| (DCM) | Cold | HS | HS | PS | PS |
| | Hot | HS | HS | CS | CS |
| (THF) | Cold | HS | HS | PS | PS |
| | Hot | HS | HS | CS | CS |
| (MeOH) | Cold | HS | HS | CS | CS |
| | Hot | HS | HS | HS | HS |
| (EtOH) | Cold | CS | CS | PS | PS |
| | Hot | HS | HS | HS | HS |
| Acetone | Cold | HS | HS | HS | HS |
| | Hot | HS | HS | HS | HS |
| ($Et_2O$) | Cold | CS | CS | PS | PS |
| | Hot | CS | CS | CS | CS |
| n-Hexane | Cold | SS | SS | INS | INS |
| | Hot | PS | PS | INS | INS |
| (DMSO) | Cold | HS | HS | HS | HS |
| | Hot | HS | HS | HS | HS |
| (MeCN) | Cold | HS | HS. | CS | CS |
| | Hot | HS | HS | HS | HS |
| Water | Cold | INS | INS | HS | HS |
| | Hot | INS | INS | HS | HS |

HS=Highly soluble, CS=Completely soluble, PS= Partially soluble, INS=Insoluble SS=Slightly soluble

These results show that the synthetic procedures induced structural modifications (such as supplementary functional groups or increased molecular weight) that influenced solubility. These qualitative evaluations offer preliminary insights into potential polarity shifts and can inform the choice of suitable solvents for later purification or analysis, such as recrystallization or chromatography. Additional quantitative solubility assessments or further spectroscopic tests (including IR, and NMR) would validate these initial discoveries.

### III.3.2 Melting Points

Melting point analysis is a straightforward and commonly used method to assess the identity and purity of solid samples.

The melting points of the synthesized compounds have been determined using Stuart Scientific SMP3 melting point equipment and are presented in Table III.3. Each number represents the mean of three measurements, showing a standard deviation of ±2 °C.

**Table III. 3** Melting Points of the Synthesized α-amino phosphonic acids $HAP_1$ and $HAP_2$

| Compound | Observed Melting Point (°C) | Remarks |
|---|---|---|
| HAP1 | 122-124 | The narrow range suggests high purity |
| HAP2 | 128-130 | The narrow range suggests high purity |

All compounds exhibit relatively narrow melting ranges (1–2 °C), This range, combined with its reproducible measurements, hints at a high degree of purity following purification.

### III.3.3 Thin-Layer Chromatography (TLC) Analysis

We conducted thin-layer chromatography with silica gel plates. For the synthesis of amino phosphonic acid, a system of ethyl acetate/hexane was utilized as the solvent. Following development, the spots were observed under ultraviolet (UV) light, demonstrating that the resultant product exhibits absorption at a maximum wavelength ($\lambda_{max}$) of approximately 230 nm.

We determined the compounds' characteristics by calculating the frontal ratios ($R_f$) in Table III.4, which is defined as the ratio of the distance traveled by the compound (from the origin line to the spot) to the distance traveled by the solvent front (from the same origin line to the point where the solvent ceases). The $R_f$ value varies from 0 to 1 and is indicative of the compound, the type of stationary phase employed, and the selected solvent system (mobile phase).

**Table III. 4** frontal ratios of synthesis α-amino phosphonic acids $HAP_1$ and $HAP_2$

| Compound | $HAP_1$ | $HAP_2$ |
|---|---|---|
| **$R_f$** | 0.74 | 0.52 |

$HAP_1$ has an $R_f$ of 0.74, indicating that it travels farther up the plate in the given solvent system compared to $HAP_2$ ($R_f$ = 0.52). This suggests that $HAP_1$ is less polar or

interacts less strongly with the silica gel surface. By contrast, $HAP_2$'s lower $R_f$ implies stronger binding to the stationary phase, which could be due to higher polarity or more hydrogen-bonding capability.

The fact that both spots were visible under UV light at around 230 nm confirms the presence of chromophoric or conjugated moieties, which aligns with the structural characteristics of amino phosphonic acids.

These TLC results validate that $HAP_1$ and $HAP_2$ are distinct compounds, displaying different migration behaviors under the chosen conditions. The efficient separation on TLC also indicates that the reaction and subsequent purification steps were successful in producing discrete products, which is further confirmed by their distinct $R_f$ values.

## III.4 Advanced Spectroscopic Analyses: IR, UV-Vis, and NMR

### III.4.1 Fourier Transform Infrared Spectroscopy (FT-IR)

The FTIR spectra of $HAP_1$ and $HAP_2$ (FigIII.1 and Fig III.2) have been collected in the mid-infrared range (4000−400 $cm^{-1}$). The spectra displayed a broad band of moderate strength at 3800−3820 $cm^{-1}$, attributable to (O–H) stretching vibrations. The vibrations probably come from both phosphonic acid hydroxyl groups (P–OH) and any accessible alcoholic hydroxyl (C–OH) functions. The width of this band indicates hydrogen-bonding interactions, typically observed in phosphonic acids and organic molecules containing hydroxyl groups.

Further in the spectrum, two separate peaks at 3100 and 2970 $cm^{-1}$ were seen, indicating asymmetric stretching vibrations of $C_{sp2}$−H and $C_{sp3}$−H, respectively. In α-aminophosphonic acids, the alkyl region frequently exhibits minor absorptions attributable to methylene ($CH_2$) or methyl ($CH_3$) groups, which may overlap with NH stretching if the aminophosphonic structure contains free amine protons.

A clear peak is observed between 1600 and 1640 $cm^{-1}$, corresponding to stretching the –P(O)–OH group. This signal may occasionally be expanded or slightly shifted due to hydrogen bonding or intramolecular interactions. A pronounced, sharp band centered at 1230−1240 $cm^{-1}$ is attributed to the conjugated phosphoryl (P=O) stretching vibration, a critical diagnostic absorption in phosphonic acid derivatives.

A strong band in the area of 990−950 $cm^{-1}$ is ascribed to the P–O stretching vibration, commonly suggestive of phosphonate or phosphonic acid functionality. Extra bands

observed between 1273−1250 $cm^{-1}$ and 1150−1100 $cm^{-1}$ are attributed to C–O stretching vibrations ($C_{sp3}$–O), commonly present in α-aminophosphonic acid systems when ether linkages or alcoholic groups are proximate to the phosphorus center.

The presence of these distinctive bands verifies the efficient incorporation of the phosphonic acid group (P–OH, P=O) and the preservation of the α-amino substituent environment (such as $C_{sp3}$–H stretches, and possible NH bending overlaps). Minor fluctuations and variations in intensity between $HAP_1$ and $HAP_2$ may result from substituent effects, variances in hydrogen bonding, or subtle structural discrepancies in their respective side chains.

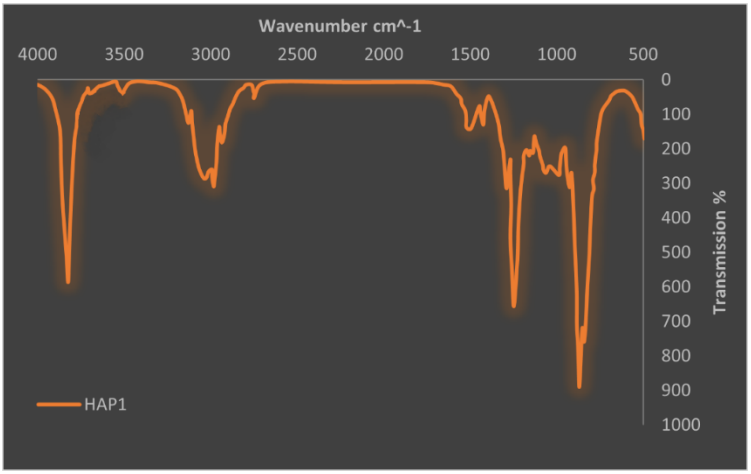


**Figure III. 1** IR spectrum of synthesis α-aminophosphonic acids (HAP1)

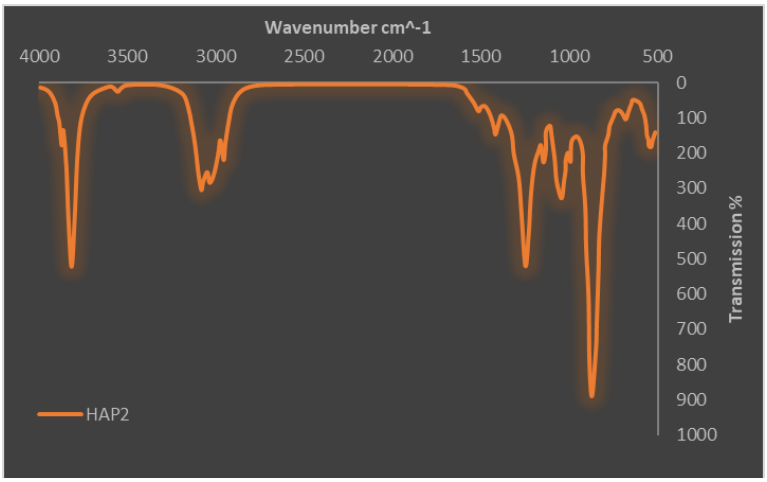


**Figure III. 2** IR spectrum of synthesis α-aminophosphonic acids (HAP2)

In summary, the FTIR spectra of these phosphonic acids show several important properties. The most characteristic absorption for phosphonic acids is the P=O stretch in the 1230–1240 $cm^{-1}$ range, while the signals at 990–950 $cm^{-1}$ (P–O) and 1600–1640 $cm^{-1}$ (P(O)–OH) further validate the existence of the phosphonic group. A wide O–H band

between 3800–3820 $cm^{-1}$ indicates free or hydrogen-bonded hydroxyl groups, with its width significantly affected by hydrogen-bonding networks in the molecular and solid state. The existence of both saturated and unsaturated carbon–hydrogen habitats is signified by the $C_{sp3}$–H stretching vibrations at roughly 3100 $cm^{-1}$ and 2970 $cm^{-1}$, respectively. Potential NH absorptions, generally observed between 3200 and 3400 $cm^{-1}$, may manifest if NH groups are unbound; however, these signals can be obscured or conflated with the extensive O–H band (Table III.5)

**Table III. 5** IR Absorption Bands for $HAP_1$ and $HAP_2$

| **Frequency ($cm^{-1}$) ($HAP_1$)** | **Assignment** | **Frequency ($cm^{-1}$) ($HAP_2$)** | **Assignment** |
|---|---|---|---|
| 3820–3800 | P–O–H stretching | 3823–3810 | P–O–H bending |
| 1600–1621 | P(O)–OH stretching | 1620–1633 | P(O)–OH bending |
| 1244 | P=O stretching | 1234–1240 | P=O bending |
| 990 | P–O–H stretching | 954 | P–O–H bending |

### III.4.2 Ultraviolet-visible (UV-Vis) Spectrophotometry

The UV-Vis spectra of the synthesis αamino phosphonic acids derivatives ($HAP_1$ and $HAP_2$ FigIII.3) indicate characteristic transitions linked to the >P=O chromophore, specifically n→σ* (shorter wavelength, higher energy) and n→π* (longer wavelength, lower energy) excitations that result from the non-bonding electron pairs on oxygen (FigIII.3). In $HAP_1$, the two different peak absorption wavelengths are observed at 236.52 nm (n→σ*) and 275.11 nm (n→π*), while in $HAP_2$, the analogous bands are located at 265.29 nm and 345.82 nm, the latter displaying a significant a larger profile. Such shifts and broadening are typically linked to electronic effects induced by various substituents, leading to modified orbital energies and perhaps improved intermolecular or intramolecular interactions. The existence of these unique and extensive bands in $HAP_2$ indicates that the >P=O group undergoes stronger conjugation and/or polar interactions compared to $HAP_1$, resulting in the stabilization of the excited state and therefore a bathochromic shift. The UV-Vis findings confirm the presence and electronic nature of the >P=O moiety, highlighting how variations

in substituents and molecular environments influence the position and shape of n→σ* and n→π* absorptions in phosphine oxide complexes.

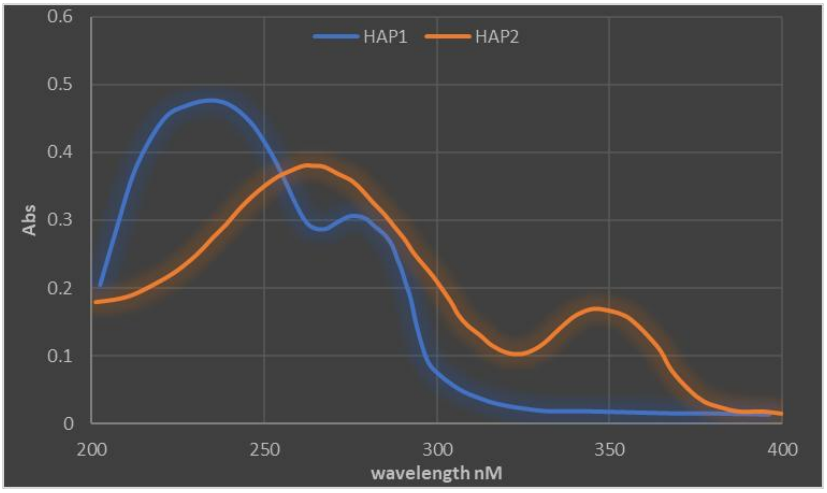


**Figure III. 3** UV–Vis absorption spectra of HAP1 and HAP in water

### III.4.3 Nuclear Magnetic Resonance (NMR)

#### III.4.3.1 Proton Nuclear Magnetic Resonance ($^1$H-NMR)

The detailed $^1$H NMR data for $HAP_1$(FigIII.4) in $D_2O$ indicate several resonances suggestive of a molecule with various functionalized alkyl chains and exchangeable protons (NH, OH, and P–OH). The initial signals at δ 1.2 ppm (d, C–$CH_3$) and δ 1.6 ppm (d, C–OH) suggest hydroxyl-bearing methine environments, whereas δ 2.0 ppm (s, P–OH) corresponds to the phosphor-hydroxyl proton. The quartet at δ 2.4 ppm (q, C–NH) indicates coupling with three equivalent protons (from $CH_2$ and CH), aligning with an NH-containing methylene group. Further resonances including δ 2.8 ppm (q, $CH_2$–$CH_2$–NH), indicating a methylene group interacting with another pair of methylene protons adjacent to an NH, and δ 1.8 ppm (m, $CH_2$–$CH_2$–$CH_2$), aligning with a more elongated methylene chain environment. The multiplet at δ 3.3 ppm (m, NH–CH($CH_3$)–P) indicates a methine proton neighboring both an NH and a phosphorus atom, while the quartet at δ 3.6 ppm (q, OH–$CH_2$–$CH_2$) implies a methylene group connected to another methylene near to an OH group. Collectively, these resonances delineate an intricate alkyl framework featuring numerous functional groups, with the specific chemical shifts and coupling patterns corroborating the existence of P–OH, NH, and OH functionalities, alongside discrete methine and methylene segments within $HAP_1$'s structure.

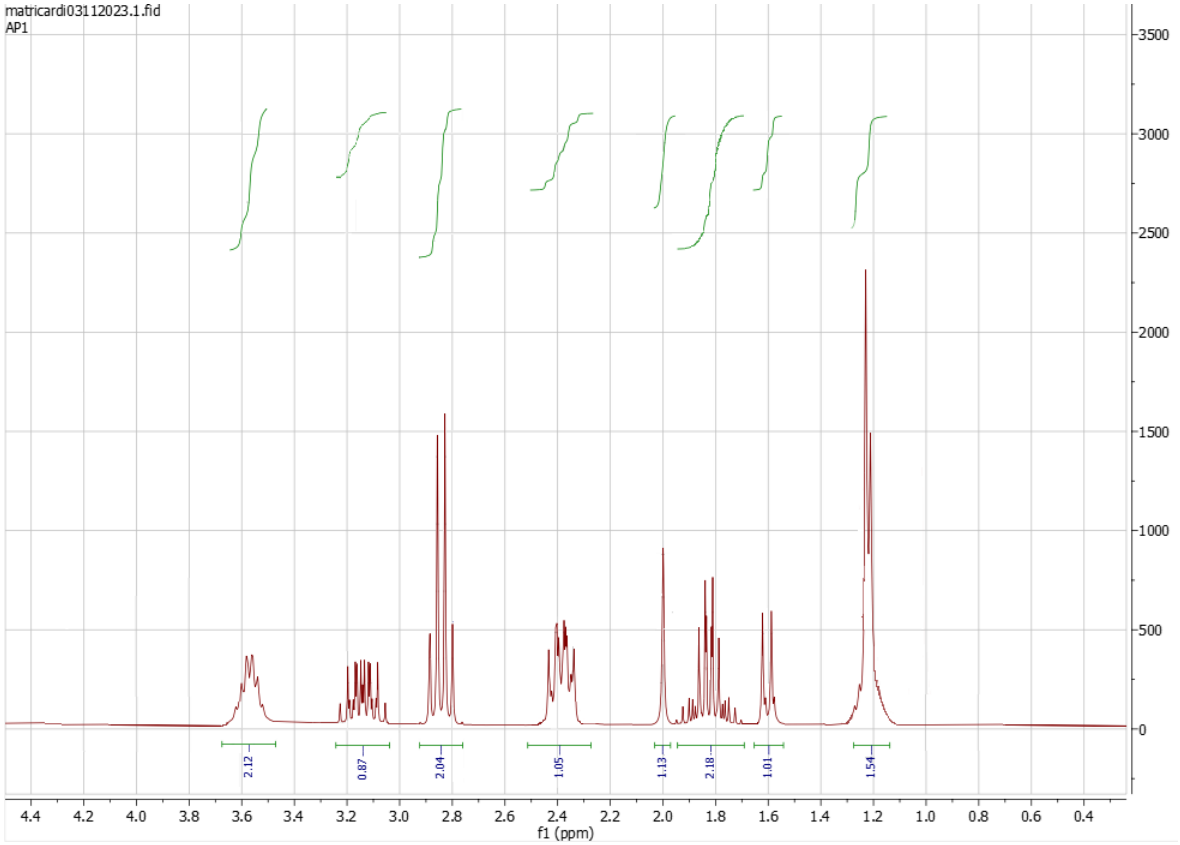


**Figure III. 4** $^{1}$H NMR spectrum for $HAP_1$

The $^{1}$H NMR spectrum (400 MHz, $D_2O$) of $HAP_2$(Fig III.5) shows a doublet at δ 1.4 ppm assigned to the methyl group (C–$CH_3$), while the doublet at δ 1.86 ppm corresponds to the proton of hydroxyl substituent (C–OH). A singlet at δ 2.12 ppm appears for the phosphor-hydroxyl proton (P–OH), and a quartet at δ 2.57 ppm arises from a C–NH environment that couples with three neighboring protons. Between δ 1.5 and 1.8 ppm, overlapping resonances indicate aliphatic methylene chains ($CH_2$–$CH_2$). The quartet at δ 2.9 ppm is attributed to a $CH_2$ group adjacent to NH (–$CH_2$–NH), whereas the multiplet at δ 3.9 ppm reflects methylene bearing an OH group ($CH_2$–OH). Finally, the multiplet at δ 4.2 ppm is assigned to a methine proton between NH and the phosphine oxide moiety (NH–CH($CH_3$)–P). These chemical shifts and coupling patterns collectively support the presence of multiple functional groups, including P–OH, NH, and OH units, as well as several aliphatic segments in the $HAP_2$ structure.

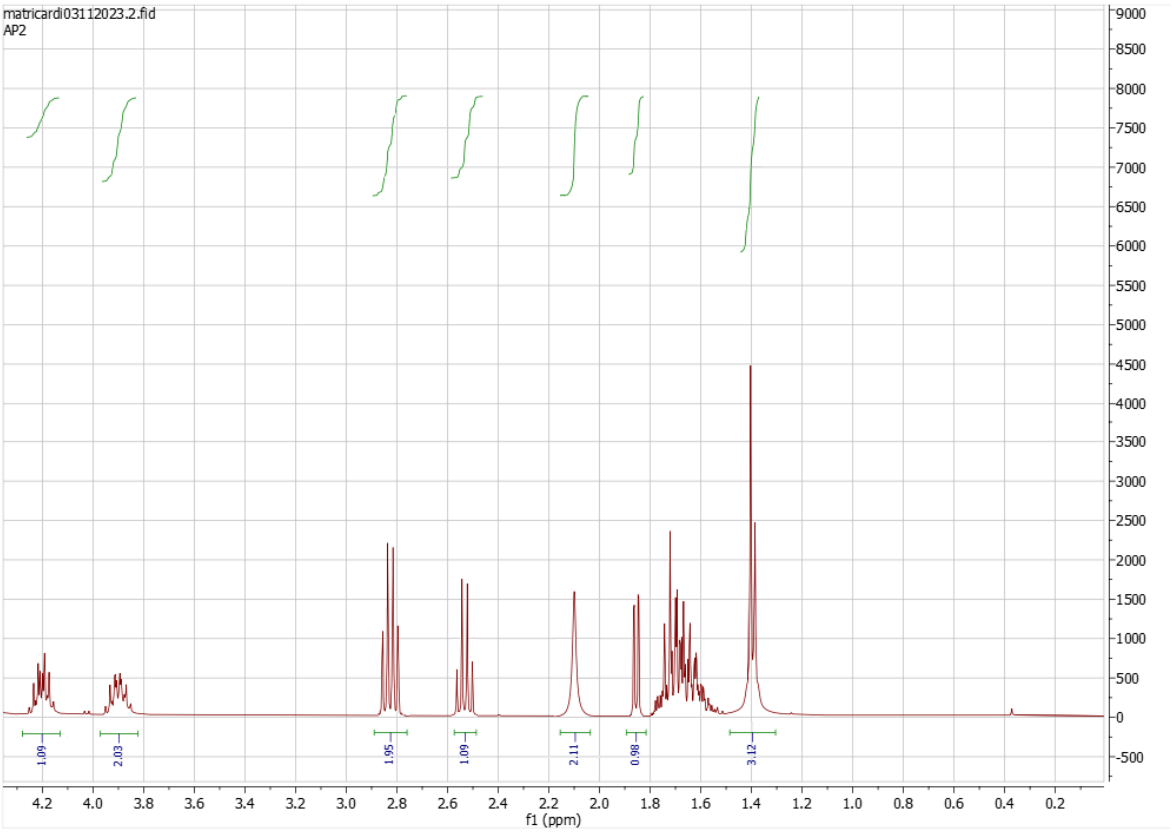


**Figure III. 5** $^{1}$H NMR spectrum for $HAP_2$

### III.4.4 Carbon$^{13}$ Nuclear Magnetic Resonance ($^{13}$C-NMR)

The $^{13}$C NMR spectrum (Fig III.6) of $HAP_1$ displays five different carbon resonances in addition to the solvent peak, each correlating with various functional groups and $^{31}$P-coupling effects. The low-field signal at δ 15 ppm (designated for CH–$CH_3$) indicates a methyl-bearing carbon in an aliphatic context. In contrast, the peak at δ 29.9 ppm represents a methylene ($CH_2$) unit in a comparatively protected area characteristic of saturated chains. Progressing forward, the resonance at δ 45.5 ppm ($CH_2$–NH) signifies a methylene group close to electronegative nitrogen, typically resulting in a larger frequency shift of the carbon signal. Two closely spaced signals at δ 49 and 50 ppm appear as a doublet due to $^{13}$C–$^{31}$P coupling (d, NH–CH($CH_3$)–P), emphasizing the intimate connection between this carbon and the phosphine oxide core. The peak at δ 61 ppm corresponds to a C–OH molecule, indicating a carbon linked to a hydroxyl group. The chemical shift values and the distinct splitting patterns substantiate the suggested molecular structure, affirming that the aliphatic carbons are near nitrogen-, oxygen-, and phosphorus-containing functional groups.

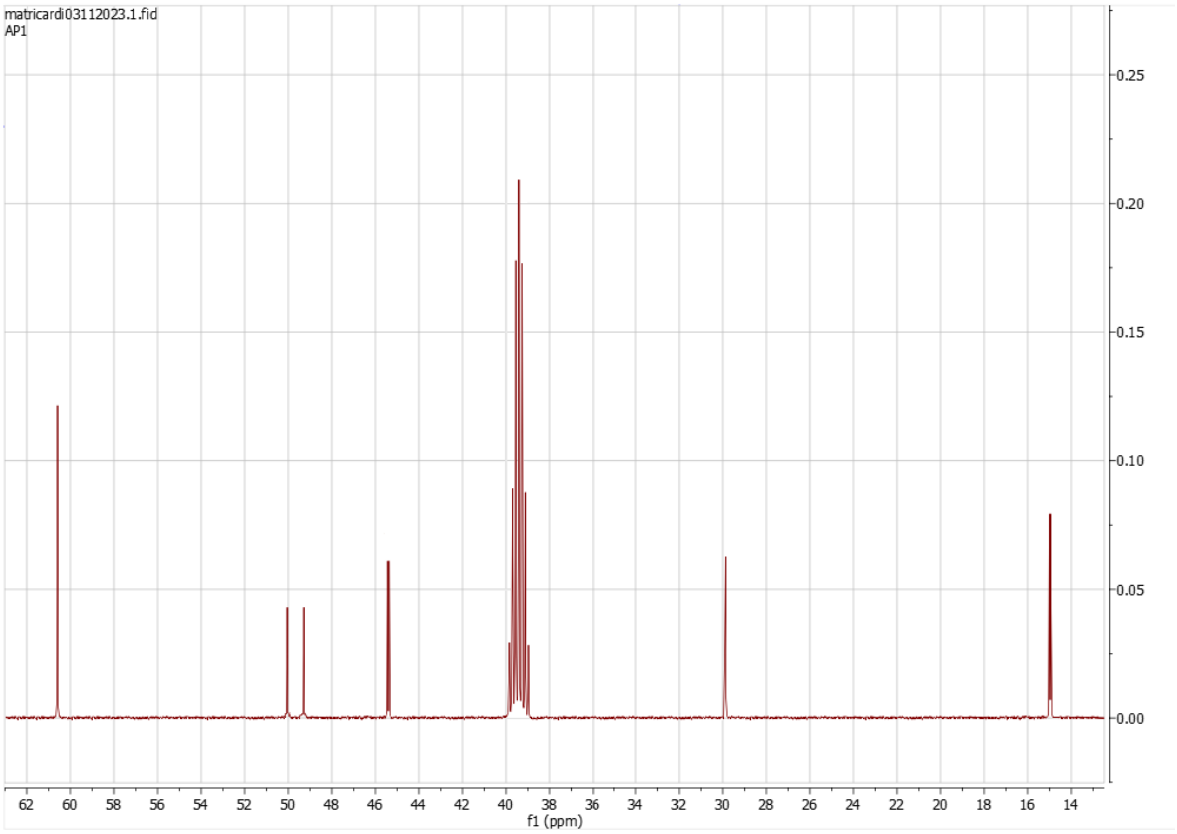


**Figure III. 6** $^{13}$C-NMR spectrum for $HAP_1$

The $^{13}$C NMR spectrum of $HAP_2$ (Figure III.7) displays six different carbon resonances, each elucidating the carbon atoms' molecular structure and electronic environment. The signal at δ 16.4 ppm corresponds to a methyl carbon ($CH_3$), indicative of an aliphatic environment where the methyl is attached to a methine. The two peaks at δ 26.7 and 28.9 ppm signify methylene groups (-$CH_2$-$CH_2$-), suggesting the existence of an elongated aliphatic chain. The resonance at δ 44.6 ppm belongs to a $CH_2$ group close to nitrogen ($CH_2$–NH), which is weakly deshielded because of the electron-withdrawing influence of the nitrogen atom. Two signals at δ 47.2 and 47.5 ppm manifest as a doublet caused by $^{13}$C–$^{31}$P coupling, indicative of the NH–CH($CH_3$)–P environment, so further substantiating the existence of the phosphine oxide core. The signal at δ 58.6 ppm is ascribed to a hydroxyl-bearing carbon (C–OH), indicating the effect of the electronegative oxygen atom on the chemical shift.

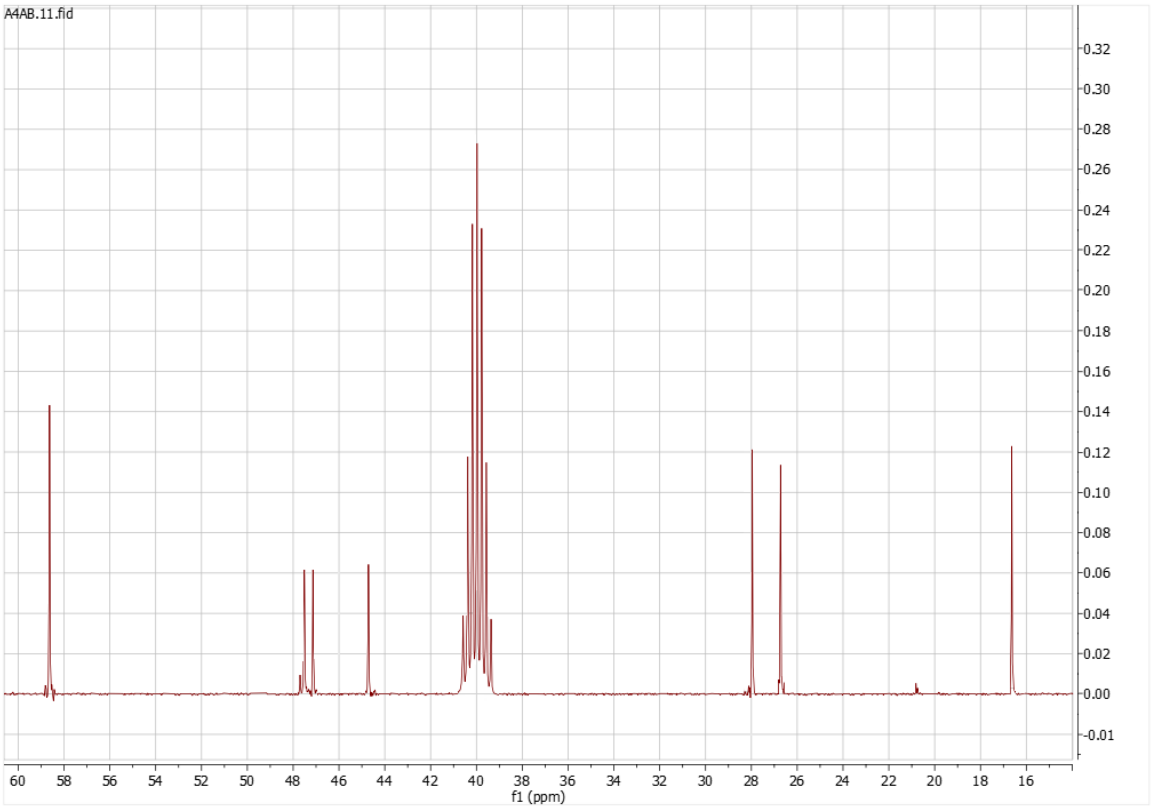


**Figure III. 7** $^{13}$C-NMR spectrum for $HAP_2$

Both spectra exhibit characteristic resonances for $CH_3$, $CH_2$, $CH_2$–NH, NH–$CH(CH_3)$–P, and C–OH, but shifts in the methylene and methine regions suggest that the electronic environment and steric interactions differ between the two compounds. The downfield shift of the $CH_2$–NH carbon in $HAP_2$ compared to $HAP_1$ suggests a slightly stronger deshielding effect, possibly due to conformational differences or altered hydrogen bonding. Additionally, the small difference in chemical shifts for the NH–$CH(CH_3)$–P doublet indicates subtle variations in the phosphorus environment, which may be influenced by neighboring functional groups. Overall, these spectral features confirm the expected structural similarities between $HAP_1$ and $HAP_2$ while highlighting differences in electronic distribution and molecular conformation.

## III.5 Conclusion

This chapter presents the effective synthesis and initial assessment of organophosphonate molecules, specifically the α-aminophosphonic acids $HAP_1$ and $HAP_2$. The synthesis process demonstrated efficacy, producing compounds appropriate for subsequent investigation and future application. Preliminary characterization methods (solubility assessment, melting point analysis, and TLC) demonstrated the synthesis of

comparatively pure compounds exhibiting consistent physical properties. Detailed spectroscopic investigations (FT-IR, UV-Vis, and both $^{1}$H- and $^{13}$C-NMR) validated the chemical structures and offered in-depth insights into the functional groups and molecular architectures. The findings provide a robust basis for subsequent evaluations of the biological activities and other uses of these organophosphonates. This work emphasizes the importance of methodical synthesis pathways and rigorous characterization methodologies, which collectively support the advancement of novel phosphonate-based compounds with potential applications in various scientific and industrial fields.

IV

# Computational Approach using DFT

# IV Computational Approach using DFT

## IV.1 Introduction

This chapter presents an extensive quantum chemistry and molecular modeling analysis of α-aminophosphonic acids (HAP1 and HAP2). Initially, we conduct a detailed study of their structural characteristics and vibrational assignments, coupled with an analysis of essential electrical properties namely, the HOMO and LUMO energies in the ground state utilizing DFT at the B3LYP/6-31G(d,p) [1] level with Gaussian 09 software [2] and Gauss view 6.0 [3]. Also, the molecular electrostatic potential (MESP) and partial atomic charges on carbon, nitrogen, oxygen, phosphorus, and hydrogen are calculated, elucidating the significance of charge distribution in reactivity. Thermodynamic characteristics, including heat capacities, enthalpies, and entropies, are obtained and analyzed, offering a comprehensive reference (including vibrational spectra) that enables swift and precise structural characterization.

Additionally, Time-Dependent Density Functional Theory (TD-DFT) analysis investigates the molecule's excited-state properties. Here, we compute excited-state transition energies, corresponding oscillator strengths, and the nature of electronic excitations. The main orbital contributions to excitations are explored to identify the dominant molecular orbitals involved in the transitions. Finally, the characterization of these transitions, distinguishing between n→π*, π→π*, or charge-transfer nature, provides essential insights into the optical and electronic properties of the studied molecule.

Using this integrated DFT and TD-DFT methodology, we aim to provide a comprehensive theoretical comprehension of the molecule's electrical configuration, stability, and spectroscopic characteristics, thereby enabling a direct correlation with experimental findings.

## IV.2 Integrative DFT Analysis

### IV.2.1 Geometric Optimization

DFT has become an effective tool for determining the structure, electronic, and thermodynamic properties of molecules. The molecular geometries of $HAP_1$ and $HAP_2$ were optimized employing DFT with hybrid exchange-correlation B3LYP functional with the average account of the exchange interactions contribution and with basis set 6-31G++(d,p), which is enough for good correlation of the theory and the experiment for molecules of such

size. The energy minima geometries of $HAP_1$ and $HAP_2$ were optimized using the Gaussian 09 program at the B3LYP/6-31G(d,p) level of DFT.

The optimized structures of $HAP_1$ and $HAP_2$ at B3LYP/6-31G(d,p) level with the atom numbering schemes are shown in Fig VI.1.

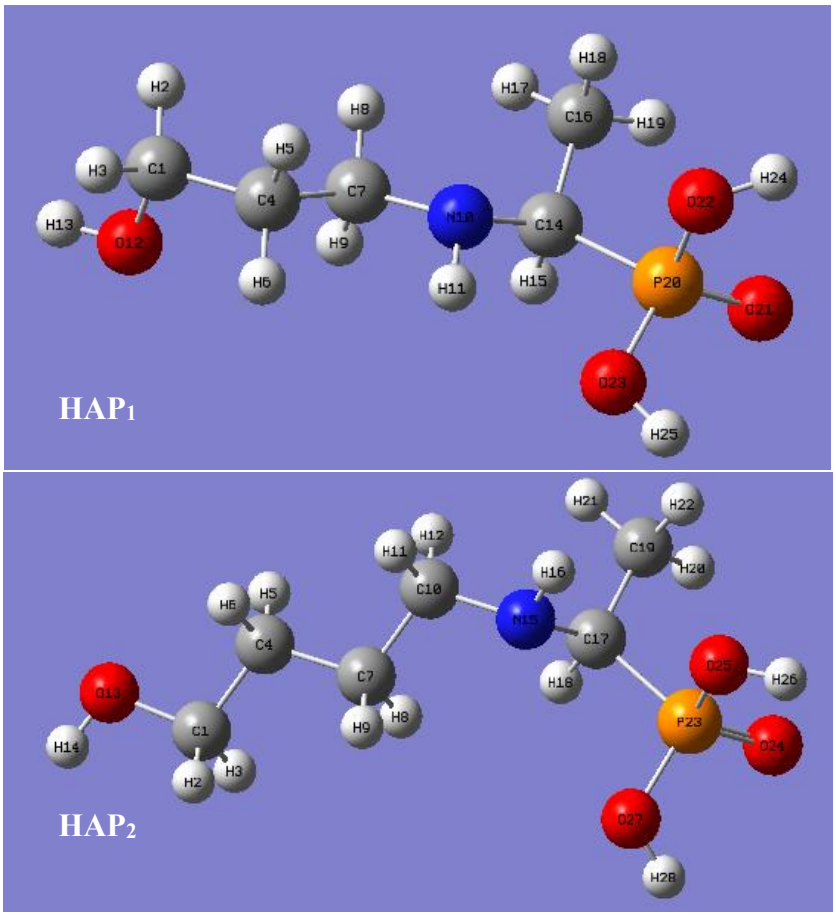


**Figure IV. 1** Optimized structures of HAP1 and HAP2 at the B3LYP/6-31++G(d,p) level of theory.

After the optimization of the molecular geometry, we have made a comparative study of some geometric parameters. Geometry parameters of $HAP_1$ and $HAP_2$ molecules (such as bond lengths and angles) are given in Table VI.1. Results indicate that the bond lengths of P23=O24/($HAP_2$) and P20=O21/($HAP_1$) have the same length value (nearly equal to 1.493A°). The bond distance of C–N is shorter in the case of $HAP_2$ (1.460A°) than that of $HAP_1$ (1.464A°). These results show good agreement with experimental data (P=O: 1.4993A°[5], C–N: 1.453 [6]). Aminophosphonic acid function possesses P–O bonds(≈1.63A°) which are longer than the same in literature (P–O ≈ 1.5441A° [5-8]). The values strongly depend on the electronic properties induced by the nature of substituents.

These results argue that theoretical results coincide well with the experimental

characteristics. The P23–O27 (1.629A°), P23–C17 (1.837A°), O13–H14(0.965A°) and C1–C19(1.541A°) bonds of $HAP_2$ are longer than those of $HAP_2$. The major differences in the bond angles are (O25–P23–O27) $HAP_2$(105.0°)>(O22–P20-O23) $HAP_1$(103.4°)

and (O25–P23–O24) $HAP_2$(114.1°)>(O22–P20–O21) $HAP_1$(112.4°).

It is noteworthy that the significant difference is between the (N10–C14–P20) $HAP_1$(110.7°) angle (N15–C17–P23) $HAP_2$(108.96°).

**Table IV. 1** Optimized geometric parameters (bond lengths (A°)/bond Angles (°)) of $HAP_1$ and $HAP_2$ calculated at B3LYP/6-31G(d,p) level.

| **$HPA_2$** | | **$HAP_1$** | |
|---|---|---|---|
| **Bond** | **Length (A °)** | **Bond** | **Length (A °)** |
| P23=O24 | **1.493** | P20=O21 | 1.490 |
| P23-O25 | **1.632** | P20-O22 | 1.631 |
| P23-O27 | **1.629** | P20-O23 | 1.628 |
| P23-C17 | **1.837** | P20-C14 | 1.836 |
| C17-N15 | 1.461 | C14-N10 | **1.464** |
| C1-O13 | 1.431 | C1-O12 | **1.432** |
| O13-H14 | **0.965** | O12-H13 | 0.965 |
| C1-C19 | **1.541** | C14-C16 | 1.537 |
| N15-C10 | 1.468 | N10-C7 | **1.469** |
| **Bond** | **Angle (°)** | **Bond** | **Angle (°)** |
| O25-P23-O27 | **105.0** | O22-P20-O23 | 103.4 |
| O25-P23-O24 | **114.1** | O22-P20-O21 | 112.4 |
| O27-P23-O24 | 112.7 | O23-P20-O21 | **115.9** |
| O24-P23-C17 | **117.8** | O21-P20-C14 | 116.4 |
| N15-C17-P23 | 108.9 | N10-C14-P20 | **110.7** |
| O13-C1-C4 | 108.0 | O12-C1-C4 | **108.6** |

### IV.2.2 Mulliken Atomic Charges Analysis

Mulliken atomic charge has an important role in the application of quantum chemical calculation to molecular systems. The Mulliken charge quantifies how the electronic structure changes under atomic displacement; it is, therefore, related directly to the chemical

bonds present in the molecule. It affects dipole moment, polarizability, electronic structure, and more properties of molecular systems [9,10]. The distribution of charges for the atoms suggests the formation of donor and acceptor involving the transfer of charge in the molecule and a chemical reaction [9]. The Mulliken atomic charges for both molecules are calculated byB3LYP/6-31G(d,p) method and collected in Table VI.2 and FigVI.2. From the obtained results, we have observed that the phosphorus atoms are all electropositive in both molecules. As well, all hydrogen atoms cover the positive charges. Generally, the heteroatoms (N, P, and O) can share their pairs of electrons with acceptor molecules. These results indicated that these atoms are the most reactive sites toward reactions. The presence of a significant negative charge on the oxygen atoms and a net positive charge on the hydrogen atoms suggested the formation of an intermolecular interaction in solid forms. The analysis of the results indicates that the O and N atoms are electronegative in both cases and constitute strong nucleophilic sites due to molecular relaxation.

**Table IV. 2** Distribution of Mulliken atomic charges of HAP1 and HAP2 calculated at B3LYP/6-31G++(d,p) level.

| **Atoms** | **Atomic charges** | **Atoms** | **Atomic charges** |
|---|---|---|---|
| C1 | -0.22 | C1 | -0.12 |
| H2 | 0.13 | H2 | 0.13 |
| H3 | 0.14 | H3 | 0.14 |
| C4 | -0.34 | C4 | -0.60 |
| H5 | 0.17 | H5 | 0.14 |
| H6 | 0.15 | H6 | 0.15 |
| C7 | -0.41 | C7 | 0.13 |
| H8 | 0.11 | H8 | 0.13 |
| H9 | 0.19 | H9 | 0.17 |
| **N10** | **-0.15** | C10 | -0.45 |
| H11 | 0.32 | H11 | 0.14 |
| O12 | -0.51 | H12 | 0.17 |
| H13 | 0.37 | O13 | -0.48 |
| C14 | -0.62 | H14 | 0.36 |
| H15 | 0.18 | **N15** | **-0.19** |
| C16 | -0.41 | H16 | 0.34 |
| H17 | 0.15 | C17 | -0.62 |
| H18 | 0.19 | H18 | 0.16 |
| H19 | 0.19 | C19 | -0.54 |
| **P20** | **1.54** | H20 | 0.18 |
| O21 | -0.70 | H21 | 0.15 |
| O22 | -0.64 | H22 | 0.17 |
| O23 | -0.66 | **P23** | **1.63** |
| H25 | 0.40 | O24 | -0.71 |
| H25 | 0.39 | O25 | -0.73 |
| | | H26 | 0.43 |
| | | O27 | -0.67 |
| | | H28 | 0.41 |

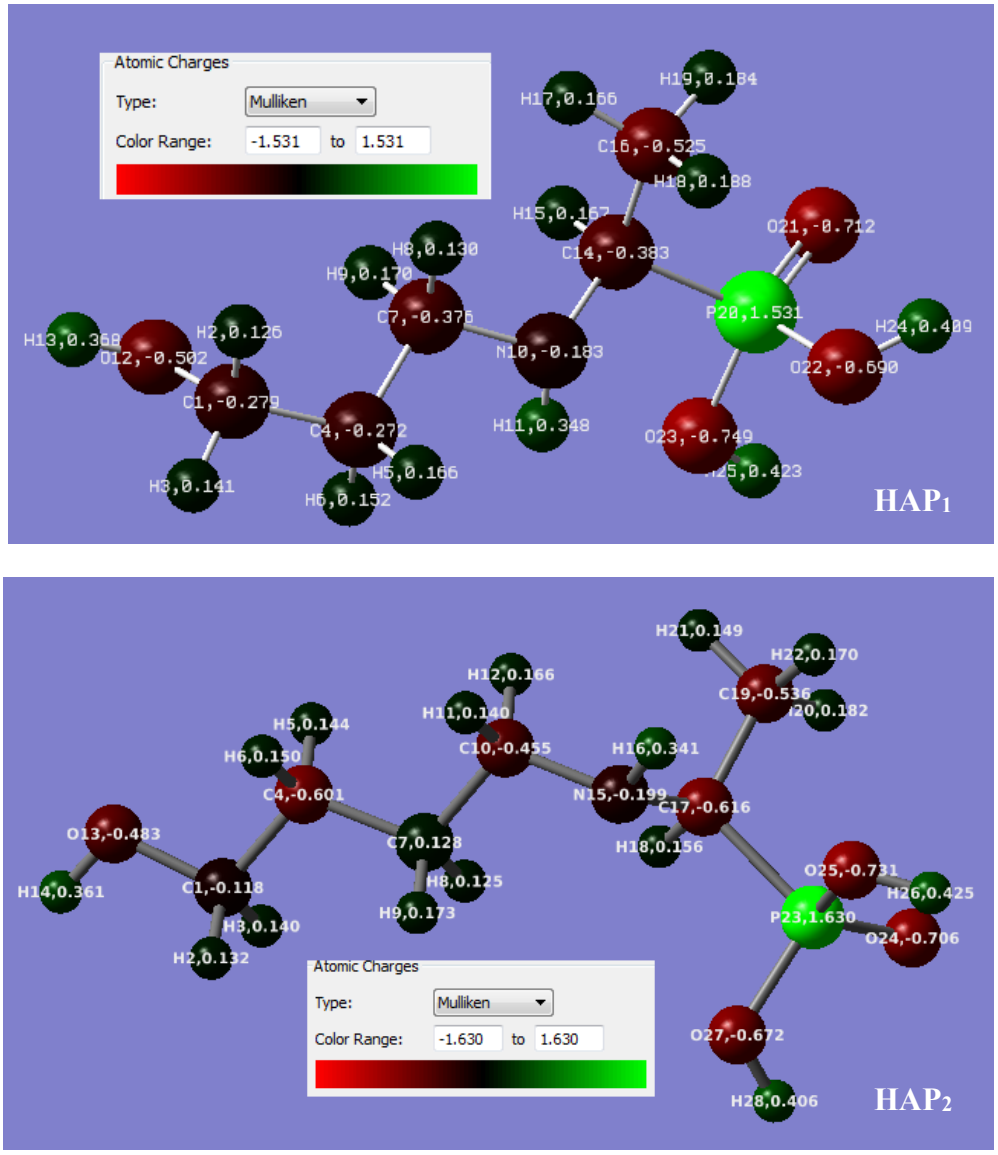


**Figure IV. 2** Mulliken Atomic charges distribution of HAP1 and HAP2 calculated at B3LYP/6-31G(d,p) level.

### IV.2.3 Dipole Moments

A molecule's dipole moment (μ) is another important molecular parameter that can be used to evaluate the chemical reactivity indicator and the polarity of molecules. It is used primarily μ designates the polarity of drug molecules, which is correlated to the fractional electric charge distribution in these molecules [11]. The total dipole moment in a Cartesian coordinate system can be calculated using the following equation:

$\mu = (\mu 2x + \mu 2y + \mu 2z)½(2)$

Table VI.3 presents the components of the moment {μi (i = x, y, z)} and the total dipole moment $\mu_{tot}$ for the two compounds $HAP_1$ and $HAP_2$. As can be seen from Table VI.3, the calculations showed that compound $HAP_1$ (3.09D) has higher dipole moment values than $HAP_2$ (1.09D). The dipole moment is greater in $HAP_1$can be explained by the difference in electronegativity caused by oxygen, nitrogen, and phosphorus atoms, which indicates a high reactivity of the $HAP_1$ to interact with the surrounding media.

**Table IV. 3** Electrical dipole moments of HAP1 and HAP2 calculated at B3LYP/6-31G(d,p) level

| Parameters | LPA | CPA |
|---|---|---|
| $\mu x$ | | |
| $\mu y$ | | |
| $\mu z$ | | |
| $\mu_{total}$ | **3.09** | **1.09** |

### IV.2.4 Frontier Molecular Orbital Analysis

The energies of the highest occupied molecular orbital (HOMO) and lowest occupied molecular orbital (LUMO) are very beneficial for physicists and chemists and are very significant terms in quantum chemistry, which play a role in determining the way the molecule interacts with another molecule, and take part in chemical stability and help to characterize the chemical reactivity and kinetic stability of the molecule [12]. The HOMO and LUMO plots of $HAP_1$ and $HAP_2$, are calculated using B3LYP level 6-31++(d,p) of DFT and are shown in FigVI.3. The green and red regions show MO with opposite phases. The red color indicates the positive phase, whereas the green color indicates the negative phase. In $HAP_1$ and $HAP_2$ molecules, it was found that the HOMO is mainly localized over the

carbonic chain and non-binding doublets of the nitrogen atom, while the LUMO is localized at the atoms of the phosphonic moiety.

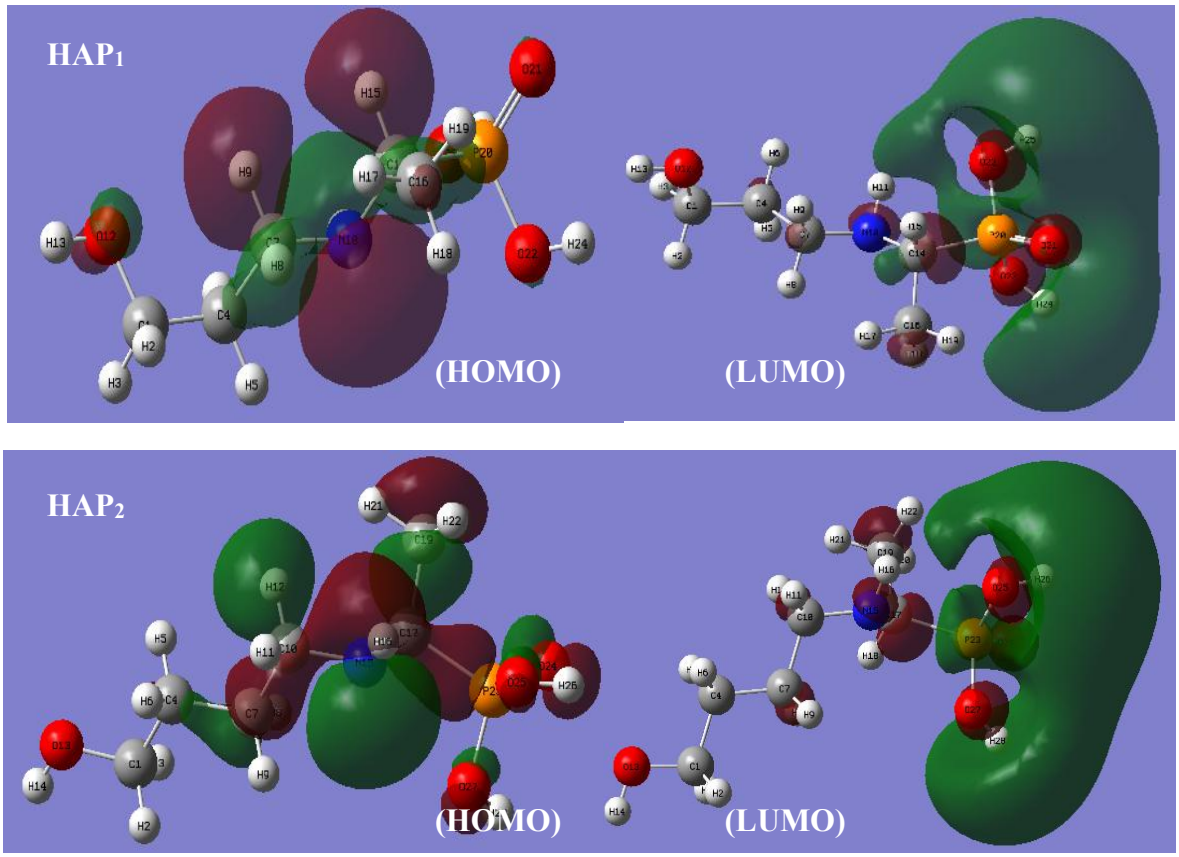


**Figure IV. 3** HOMO and LUMO orbitals of $HAP_1$ and $HAP_2$ calculated at B3LYP/6

### IV.2.5 Global Reactivity Descriptors

The frontier molecular orbital energies help to characterize the chemical reactivity and kinetic stability of the molecule. A high HOMO energy corresponds to a more reactive molecule and therefore to a high capacity to lose an electron. Conversely, a lower LUMO energy indicates a greater affinity for electrons, and higher values of $E_{LUMO}$ indicate a better electron donation tendency. On the other hand, it should be remembered that the studied molecules will accept more electrons if it has a lower LUMO energy value. The LUMO–HOMO energy gap (ΔEgap) is the most important parameter for the chemical reactivity and stability. The low value of the energy gap is generally associated with a high chemical reactivity or less stability [13]. Useful theoretical insights into chemical reactivity and selectivity parameters may be obtained by determining global qualitative chemical concepts that are frequently associated with the electron-donating ability of the molecule. The energy of the HOMO is directly proportional to the ionization potential ($IP = -E_{HOMO}$) whereas the energy of the LUMO is directly proportional to the electron affinity ($EA = -E_{LUMO}$) [13].

The Ionization Potential (IP) of a molecule is the energy that must be supplied to a neutral atom to pull out an electron and form a positive ion. While electron affinity (EA) refers to the ability of a neutral atom or molecule to capture an extra electron [14]. The molecule with a low (IP) value has a better electron donor character, and those with a high (AE) value have a good electron acceptor character. The global hardness (η) of a molecule corresponds to the gap between the HOMO and LUMO orbital energies ($\eta=1/2(E_{LUMO}-E_{HOMO})$). The larger the HOMO–LUMO energy gap the harder (or less softness ($S=1/\eta$)) the molecule whereas the smaller energy gap represents the high reactivity and low stability of the molecule. The hardness has been related to the stability of the chemical system. Electrophilicity index ($\omega=\mu 2/2\eta$) measures the capacity of a molecule to accept electrons. It is a measure of the stabilization in energy after a system has accepted an additional amount of electronic charge from the environment [15-17]. The chemical potential ($\mu = (E_{HOMO} + E_{LUMO})/2$) is used to describe the escaping tendency of electrons from an equilibrium system. The greater the electronic chemical potential, the less stable or more reactive the compound [14]. Electronegativity ($\chi=-\mu =(IP+EA)/2$) is the measure of an atom, molecule, or solid substance to attract electrons to itself [18]. The first connection of the electronegativity (χ) concept with quantum mechanics within density-functional theory (DFT) is assigned to Parr et al. Furthermore, it was proposed that (μ) is the negative of electronegativity (χ), which helped to establish a direct connection with chemical reactivity. The higher the electronegativity of the species, the greater its electron-accepting power or rather the electrophilicity.

As can be seen in Table VI.4, the best electron donor is compound $HAP_2$, which has the highest HOMO energy ($E_{HOMO}$= –6.40eV) and the lowest ionization value (IP= 6.40eV), while the best electron acceptor is compound $HAP_1$, which has the lowest LUMO energy ($E_{LUMO}$ = –0.60eV), the highest electron affinity (EA = 0.60 eV), and the highest ionization value (IP=6.45eV). Furthermore, compound $HAP_2$ showed the smallest orbital energy gap (ΔE=5.79eV) among the investigated products as the consequence of the highest chemical reactivity, least kinetically stable "soft molecule", and the most polarizable. The reactivity of these compounds is the greatest based on energy gap (ΔE) parameters, which support that compound $HAP_1$ is the most stable as compared to $HAP_2$. Table VI.4, shows that the electronic chemical potential of $HAP_2$ (μ= –3.51eV) is higher than that of $HAP_1$ (–3.52eV), which indicates that the electron transfer will take place from $HAP_1$ to $HAP_2$. In addition, the electrophilicity of $HAP_1$ (ω=2.123eV) is lower than $HAP_2$ (ω=2.124eV), and therefore,

$HAP_1$ behaves like a nucleophile and $HAP_2$ behaves like an electrophile. All the other descriptors as global hardness and global softness converge to the same results. When we compare the results of the global chemical reactivity descriptors obtained in the present study of the two molecules $HAP_1$ and $HAP_2$ with other similar studies [19-22] of the same family of aminophosphonates, we see a great convergence in the results.

**Table IV. 4** Energies of HOMO, LUMO, energy gap, and global chemical reactivity indices of synthesized HAP1 and HAP2.

| **Molecular Energy(*eV*)** | **$HAP_1$** | **$HAP_2$** |
|---|---|---|
| $E_{LUMO}$ | -0.60 | -0.61 |
| $E_{HOMO}$ | -6.45 | -6.40 |
| Energy gap (Δ) | 5.85 | 5.79 |
| Ionization Potential (I) | 6.45 | 6.40 |
| Electron affinity (A) | 0.60 | 0.61 |
| Global Hardness (η) | 2.92 | 2.90 |
| Global Softness (*s*) | 126.58 | 127.78 |
| Chemical potential (μ) | -3.52 | -3.51 |
| Electrophilicity (ω) | 2.123 | 2.124 |
| Electronegativity (χ) | 3.52 | 3.51 |

### IV.2.6 Molecular Electrostatic Potential Surface (MESP)

The molecular electrostatic potential (MESP) of a molecule gives a piece of information about the net electrostatic effect produced at that point by total charge distribution (electron + nuclei) of the molecule [23-24] and correlates with the electronegativity, dipole moments, partial charges chemical reactivity of the molecule. The spatial distribution and the values of the electrostatic potential describe carefully the electrostatic interactions within the molecule by providing basic information on the physicochemical properties of the molecule, such as the molecular size and shape, in the form of color change [25,26]. It provides a visual method to understand the relative polarity of the molecule and determines the attack of an electrophilic or a nucleophilic agent as the primary event of a chemical reaction. MESP is presented in several colors. Most negative and positive potentials are presented by red and blue colors, respectively, whereas the green color indicates the neutral area. Potential increases in the order red<green<blue<pink < white. The negative (red color) regions of molecular electrostatic potential were related to electrophilic reactivity and the positive (white color) ones to nucleophilic reactivity.

In this study, MESP was mapped for the $HAP_1$ and $HAP_2$ molecules as shown in Fig.VI.4, which indicates the electrostatic potentials at the surface for the molecules which are shown by different colors. It can be seen that the negative regions, characterized by red color, are mainly over the oxygen atoms of phosphonic and hydroxyl functions (P=O, P–OH, and C–OH), represent the most negative potential region, and are permissible for electrophilic interaction. However, the hydrogen atom carries the maximum force of the positive charge (blue), while the neutral potential is localized on the carbonic chain surfaces and represented by green color. According to these results, the molecular electrostatic potential map shows that the negative potential sites are on oxygen atoms as well as positive. Potential sites are around the hydrogen atoms.

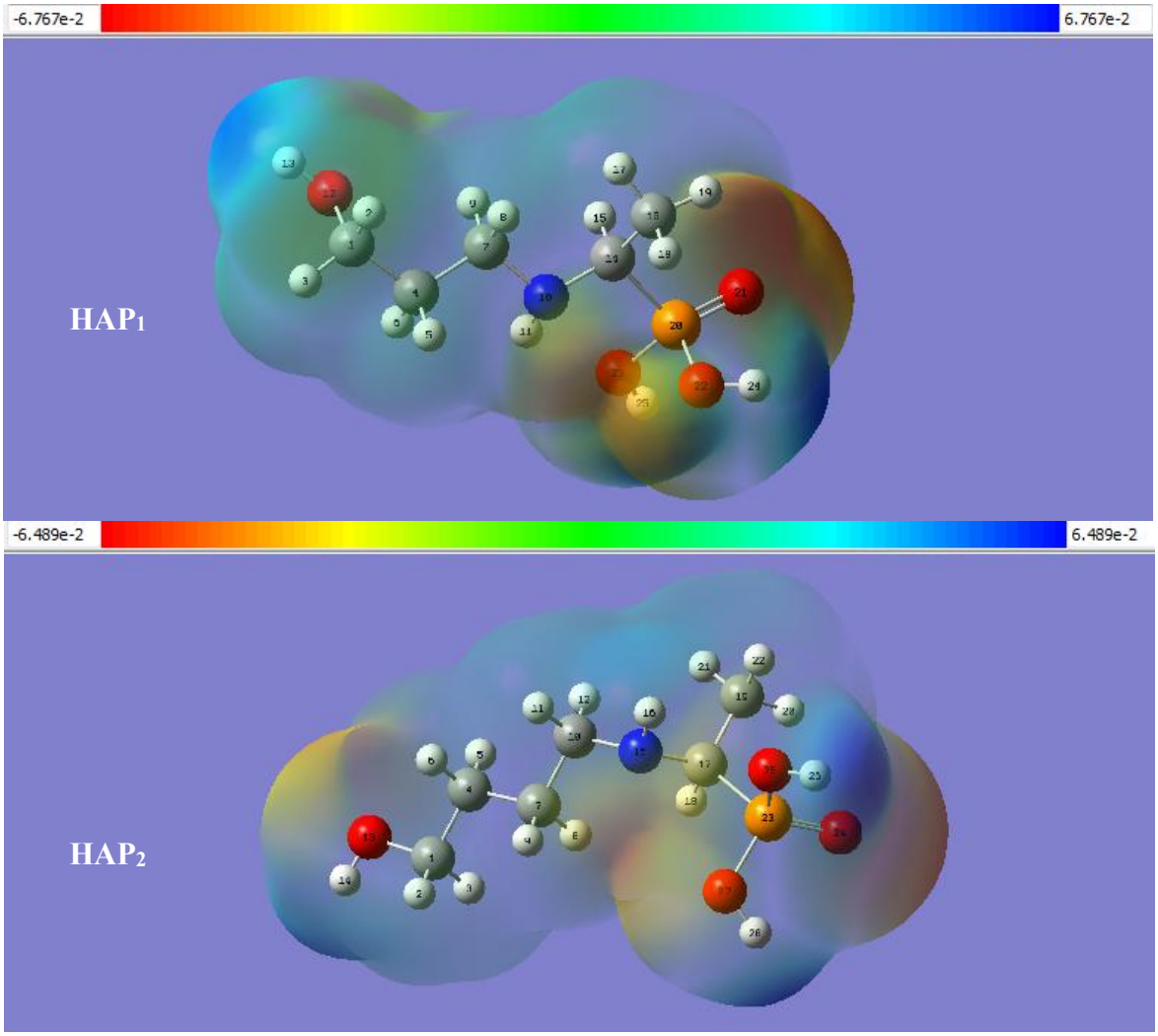


**Figure IV. 4** Molecular electrostatic potential surface (MESP) of $HAP_1$ and $HAP_2$ calculated at B3LYP/6-31G(d,p) level.

### IV.2.7 Vibrational Analysis

The target molecules $HAP_1$ and $HAP_2$ consist of 25 and 28 atoms, respectively. Hence (3N-6) gives 69 and 78 normal modes of vibrations in the range 600-4000 $cm^{-1}$ at B3LYP/6-31G++(d.p), and all are active in infrared. Out of these 69 and 78 vibrational modes. The detailed vibrational assignments of fundamental modes along with the theoretical IR intensities are reported in Table VI.5. For comparison, the observed and simulated IR spectra are presented in Fig VI.5. A few of the discrepancies are observed between the experimental and calculated data of vibrational frequencies and their assignments have also been discussed. The comparison between the theoretical IR spectrums for $HAP_1$ and $HAP_2$ using DFT at B3LYP/6-31G(d.p) basis (Black) and experimental infrared spectrums (Red color) can be seen in Fig VI.5. The discussion of assignments of the most important groups for both derivatives is presented as follows.

The phosphonic ($–P(O)(OH)_2$) groups of $HAP_1$ and $HAP_2$ give rise to several vibrational based on their ν(P=O), ν(–OH), ν(P–O), and ν(P–C) stretching. The bands that are highest in wavenumber at 3820-3804cm-1 are composed of O–H symmetric and asymmetric stretching. The bands are a broad feature in the experimental spectrum. This indicates that hydrogen bonding is rather weak in the system. The peak at 1240$cm^{-1}$ is primarily due to the P=O stretching vibrations ν(P=O), whereas the peaks at 1070 and 990$cm^{-1}$ are assigned to the symmetric and asymmetric stretching of the P–O bands. The bands located at 780–510$cm^{-1}$, are mainly due to the (P–OH) and $\delta s(C–PO_3)$ vibrations, respectively. The theoretically calculated value by the DFT method shows good agreement with the experimentally observed value.

The stretching of the N–H bands is sharp. Stretching frequencies of N–H were calculated at 3573, and 3570 $cm^{-1}$. These frequencies were similar to the experimental values 3588 and 3508 $cm^{-1}$ as shown in Table VI.5.

The contribution of the aliphatic side-chain vibrations has been widely studied. The assignments of $CH_2$ groups frequency involve 06 fundamentals namely, $CH_2$ symmetric stretch; asymmetric stretch; scissoring, and rocking which belong to in-plane and out-of-plane vibration namely $CH_2$ wagging and twisting modes. The $CH_2$ scissoring, wagging, twisting, and rocking appear in the region 1580–820 $cm^{-1}$. The aliphatic (as methyl and methylene) C-H stretching bands were normally found between 3100 and 2800 $cm^{-1}$. By considering Table VI.5 and the experimental IR spectra given in Fig VI.5, respectively, the

observed peaks at 3100-2970cm$^{-1}$ can be assigned to the C–H stretching modes. The theoretical calculations show that the observed C-H stretching vibrations calculated at the B3LYP level using 6-31G++(d,p) are in good agreement with each other and lie well within the expected range.

The C-N gives rise to medium to weak bands near 1355-1187 cm$^{-1}$ because of the C–N stretching vibration. $HAP_1$ and $HAP_2$ present peaks at 1298-872cm$^{-1}$ which are assigned to C-N stretching. The B3LYP values 1290-877 cm$^{-1}$ correspond to C–N stretching vibration. The theoretically calculated value by the DFT method shows good agreement with the experimentally observed value.

**Table IV. 5** Selected comparison of some theoretical and experimental wavenumbers (cm−1) of the HAP1 and HAP2 molecules.

| **Bonds** | **HAP1** | | **HAP2** | |
|---|---|---|---|---|
| | frequencies ($cm^{-1}$) | | | |
| Assignments | Theo. | Exp. | Theo. | Exp. |
| NsP-O-$H_{phos}$ | 3820 | 3822 | 3802 | 3791 |
| NsC-O-H | 3511 | 3512 | 3580 | 3570 |
| νsN-H | 3308 | 3350 | 3350 | 3350 |
| νasC-H, β(H-C- H), | 3144 | 3115 | 2981 | 2888 |
| νsC-H | 2852 | 2767 | 2918 | 2709 |
| ωC-H, δC-H, β(H-C-H), | 1480 | 1415 | 1433 | 1390 |
| ρ(H-C-H), d($CH_3$), νC-N | 1368 | 1341 | 1314 | 1280 |
| νCH,α C-H ,ν N-C,ρ NH | 1250 | 1254 | 1286 | 1202 |
| ν P=O | 1230 | 1200 | 1268 | 1202 |
| γ C-H ,γP-C-H | 1068 | 1062 | 1198 | 1122 |
| ωC-H, β($H_{10}$-$C_1$ -P), β(H-C-H ), β(H-O-C) | 978 | 977 | 1033 | 998 |
| γ C-H,δ C-H, β(C-N),ρ(P-O) | 856 | 839 | 1046 | 950 |
| δC-H, γ (C–P),β(H-C), β(O-P-C), β(H-O-P), ρ(O-P-C) | 780 | 769 | 741 | 687 |
| δC-H, ν (C–P), β (H-O-P), β(H-C-H), ρ(O-P-C) | 634 | 645 | 696 | 559 |

ν, stretching; δ, scissoring; wag and γ, wagging or out of plane deformation; ρ, rocking; τ, torsion, twist, twisting; a, antisymmetric; s, symmetric;

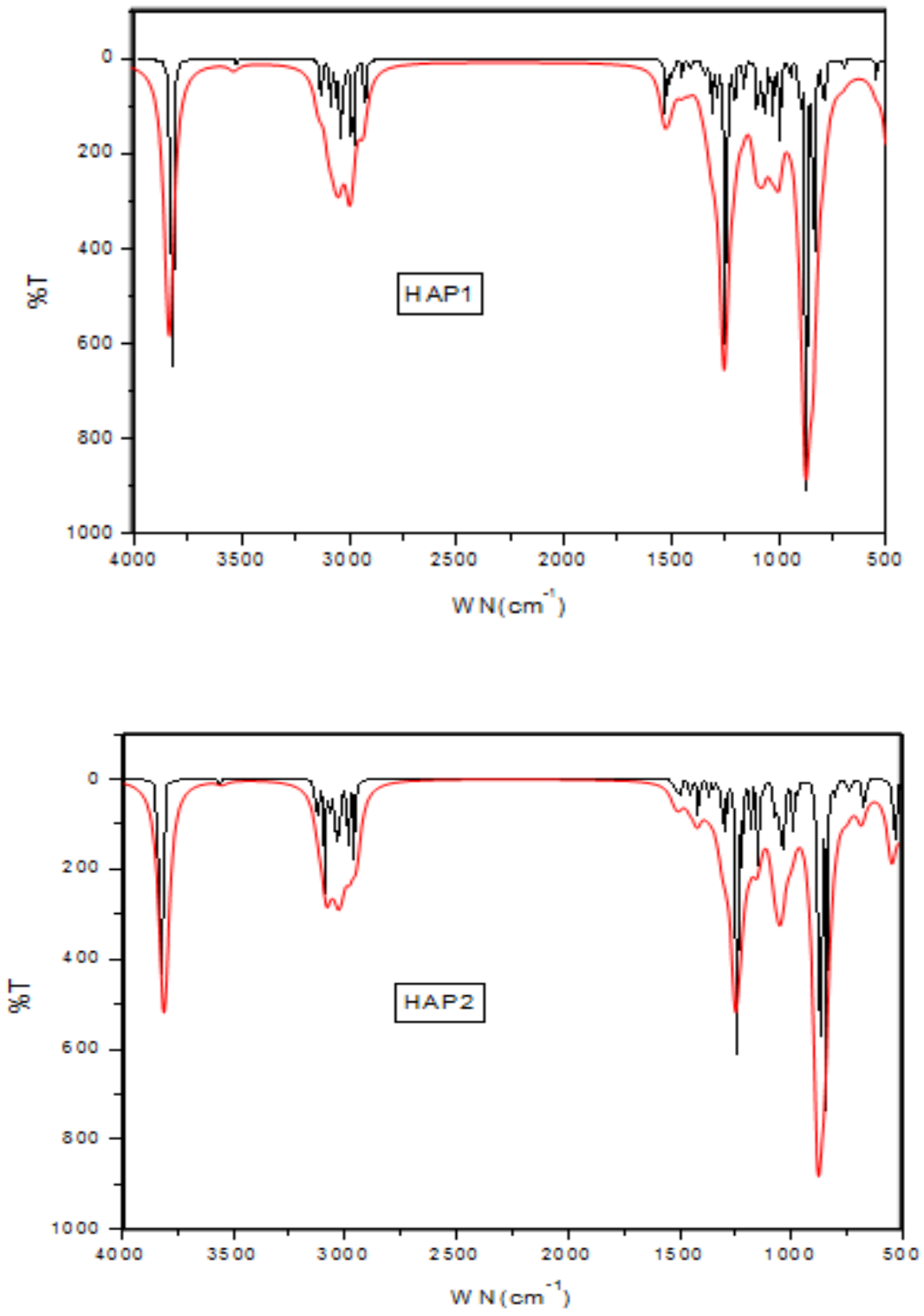


**Figure IV. 5** Experimental (Red) and Theoretical FTIR (Black) spectrums of $HAP_1$ and $HAP_2$ calculated at B3LYP/6-31G(d,p) level.

### IV.2.8 Thermodynamic characteristics

Different thermodynamic parameters like enthalpy, Gibbs free energy, entropy, zero-point vibrational energy heat capacity, thermal energy, and partition functions have been found to play crucial roles in material characterization. These thermo-molecular characteristics are used to describe the state as well as the direction of a chemical reaction. These parameters also examine the spontaneity of a reaction, and its energy profile, that is, either endothermic or exothermic, and describe temperature effects on different thermodynamic properties [27]. Based on vibration analysis, the statically thermodynamic functions: heat capacity (Cp), entropy (S), enthalpy changes (H), zero-point vibrational energy (ZPVE), thermal energy (ET), and rotational constants for the title molecules were obtained from the theoretical thermodynamic parameters of $HAP_1$ and $HAP_2$ at 298.15 K and 1.00 atm pressure in the ground state are listed in Table VI.6. These thermodynamic parameters provide helpful information for the further study on the title compounds, when these may be used as a reactant to take part in a new reaction. The zero-point vibrational energy remains constant at all temperatures because it is a characteristic property of the molecule. The biggest values of ZPVE are 147.58421kcal/mol for $HAP_2$. Whereas the smallest values of ZPVE are 130.00466Kcal/ mol for $HAP_1$. The variation in zero-point vibrational energies (ZPVEs) seems to be significant. As shown in Table VI.6, it can be seen that the Total energy (thermal), Heat capacity (Cp), and Entropy (S) of $HAP_2$ are higher than that of $HAP_1$. Therefore, the rotational constant values of $HAP_1$ are greater than that of $HAP_2$.

**Table IV. 6** Calculated thermodynamic parameters of $HAP_1$ and $HAP_2$ employing the B3LYP/6-311++G(d,p)level.

| Thermodynamic parameters | HAP1 | HAP2 |
|---|---|---|
| Total energy (thermal), E total (kcal.mol$^{-1}$) | | |
| TOTAL | 139.109 | **157.685** |
| Electronic | 0.000 | 0.000 |
| Translational | 0.889 | 0.889 |
| Rotational | 0.889 | 0.889 |
| Vibrational | 137.331 | 155.907 |
| Heat capacity at const. volume, C v (cal.mol$^{-1}$.K$^{-1}$) | | |
| TOTAL | 51.096 | **56.400** |
| Electronic | 0.000 | 0.000 |
| Translational | 2.981 | 2.981 |
| Rotational | 2.981 | 2.981 |
| Vibrational | 45.134 | 50.438 |
| Entropy, S (cal.mol$^{-1}$.K$^{-1}$) | | |
| TOTAL | 121.602 | **131.520** |
| Electronic | 0.000 | 0.000 |
| Translational | 41.520 | 41.740 |
| Rotational | 31.483 | 32.267 |
| Vibrational | 48.598 | 57.512 |
| Zero-point vibrational energy, $E_0$ (kcal.mol$^{-1}$) | 130.00466 | **147.58421** |
| Rotational constants (GHz) | | |
| A | **2.10175** | 1.68742 |
| B | **0.36024** | 0.27245 |
| C | **0.34638** | 0.25916 |

## IV.3 TD-DFT Analysis

### IV.3.1 Excited States & Transition Energies

The spectrum of UV-vis of HAP1 and HAP2 calculated by TD-DFT using the (B3LYP/6-31++G(d,p)) level was represented in fig VI.6

The TD-DFT calculation (B3LYP/6-31++G(d,p)) found four transition states for $HAP_1$ and $HAP_2$. Their excitation energies (in eV) and corresponding wavelengths (in nm) are listed below (Table VI.7) The energies correspond to UV wavelengths (220–350 nm). For that, all the transitions are in the UV range and none lie in the visible region.

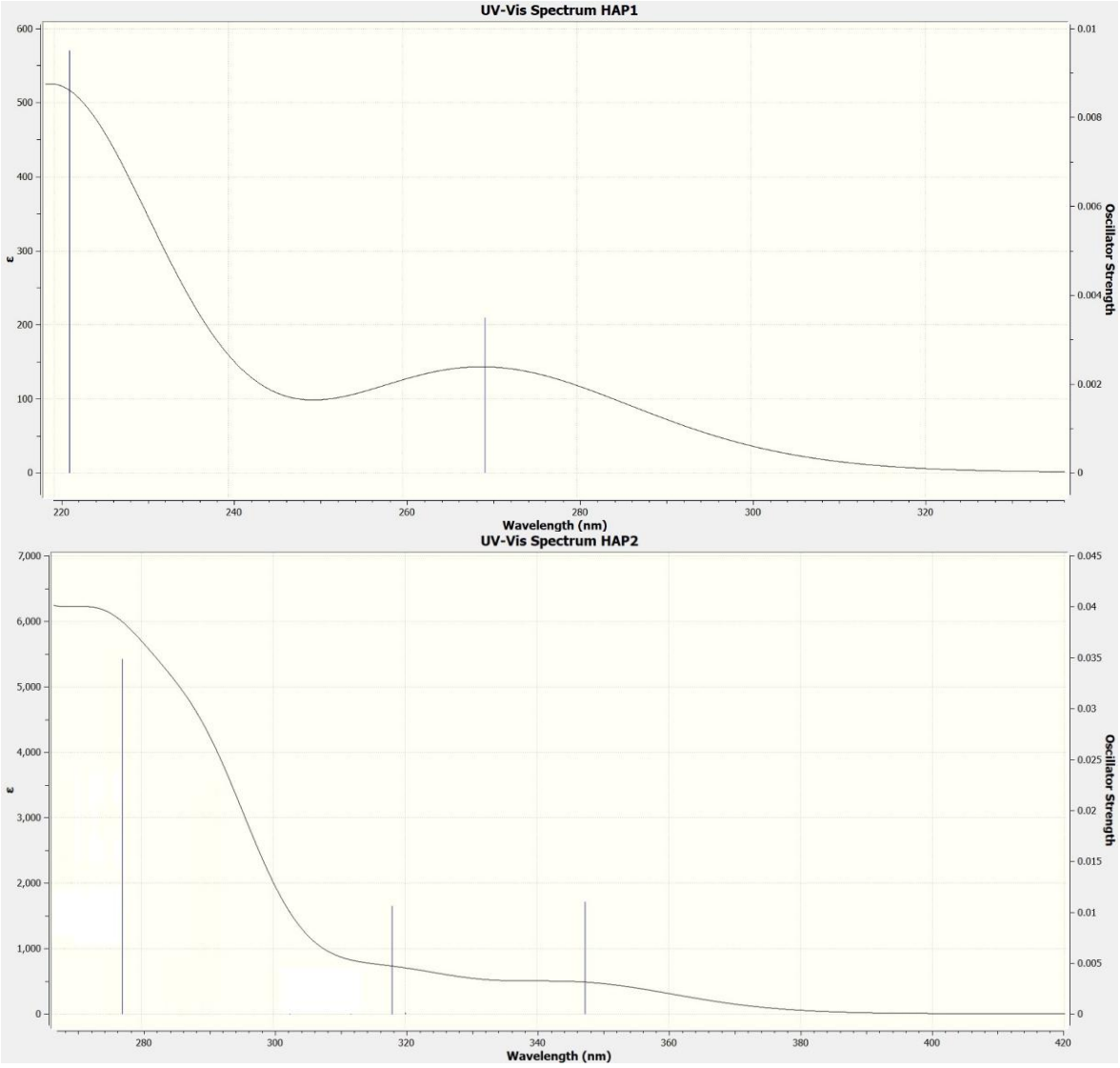


**Figure IV. 6** Calculated UV–Vis spectrum of $HAP_1$ and $HAP_2$ using TD-DFT at the B3LYP/6-31++G(d,p) level

**Table IV. 7** TD-DFT predicted Transition states energies, wavelengths, and oscillator strengths.

| Compounds | Excited State | Energy (eV) | Wavelength (nm) | Oscillator Strength (f) |
|---|---|---|---|---|
| **$HAP_1$** | Transition $states_1$ | 4.6009 eV | 269.5 nm | 0.0035 |
| | Transition $states_2$ | 5.5904 eV | 221.8 nm | 0.0095 |
| **$HAP_2$** | Transition $states_1$ | 6.9997 eV | 276.3 nm | 0.0349 |
| | Transition $states_2$ | 5.6346 eV | 347.2 nm | 0.0029 |

All computed oscillator strengths f are very small, indicating weak transitions. As seen in Table VI.7, the largest f-value is for $HAP_2$ Transition $states_1$ ($f \approx 0.0349$), For context, $\pi \rightarrow \pi^*$ transitions in conjugated molecules often have $f \gg 0.1$[28], whereas $n \rightarrow \pi^*$ transitions are much weaker. Here, the f-values ($\sim 10^{-2}$) are orders of magnitude lower than a typical allowed transition, suggesting that these excitations would be very weak in an absorption spectrum. $HAP_2$ Transition $states_1$, despite having the highest f of the four, is still a very weak transition (likely only a subtle feature in the UV spectrum).

### IV.3.2 Main Orbital Contributions to Excitations

The TD-DFT output provides the dominant molecular orbital (MO) promotions contributing to each Transition state. We can identify the MOs (by their index) involved in each transition and infer their nature (such as. HOMO, LUMO). Below are the primary orbital transitions for each state (using the MO numbering from the Gaussian output):

For $HAP_1$ HOMO → LUMO transition, denoted as MO 49 → MO 50 with a large coefficient (0.70075). This indicates the first excitation is dominated (~70% contribution) by an electron promotion from the HOMO to the LUMO. There are no significant multi-orbital admixtures for this state, implying a fairly "pure" single-orbital transition (Fig VI.7)

For the Transition $states_2$ of $HAP_1$ primarily HOMO → $LUMO_{+1}$ transition, denoted as MO48 → MO50, with coefficient 0.66871. This is the major component (~67% contribution). A secondary contribution is from $HOMO_{-2}$ → LUMO (MO 47 → MO 50) with a smaller coefficient of 0.20321 (~20%). Thus, State 2 is a mixture of two configurations, but is largely characterized by an electron from the $HOMO_{-1}$ going into the LUMO [29] (Fig VI.7).

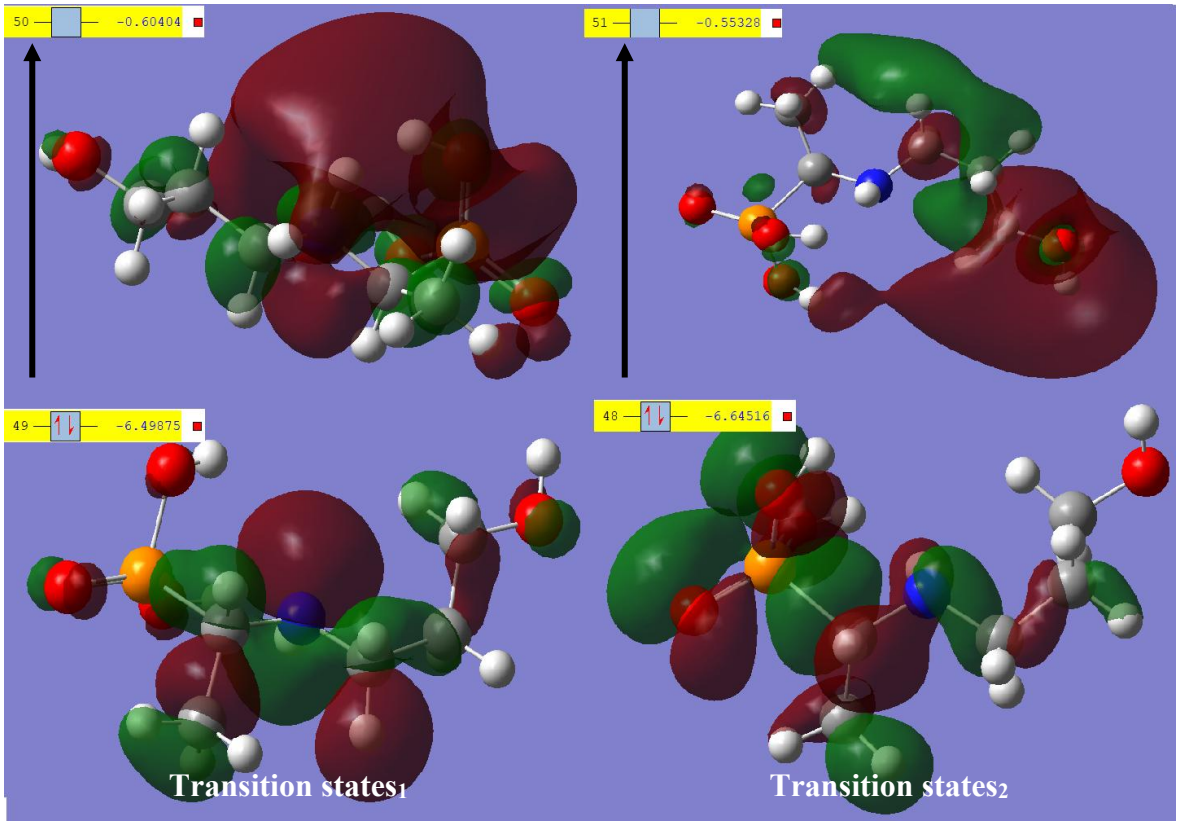


**Figure IV. 7** Molecular orbital (MO) of $HAP_1$ promotions contributing to each transition state.

The $HAP_2$ HOMO to LUMO transition is represented as MO 53 to MO 54, with a coefficient of 0.64458. This signifies that the initial excitation is mostly influenced (~65% contribution) by an electron transition from the HOMO to the LUMO. Figure VI.8

For the second transition states of $HAP_2$, the primary transition is from HOMO to $LUMO_{+1}$, specifically from MO52 to MO54, with a coefficient of 0.51869. This constitutes the primary component, contributing approximately 52%. A supplementary contribution arises from $HOMO_{-2}$ to LUMO (MO 51 → MO 54) with a coefficient of 0.37496 (about 38%). Consequently, the predominant excitation involves an electron transition from the $HOMO_{-1}$ to the LUMO (Fig VI.8).

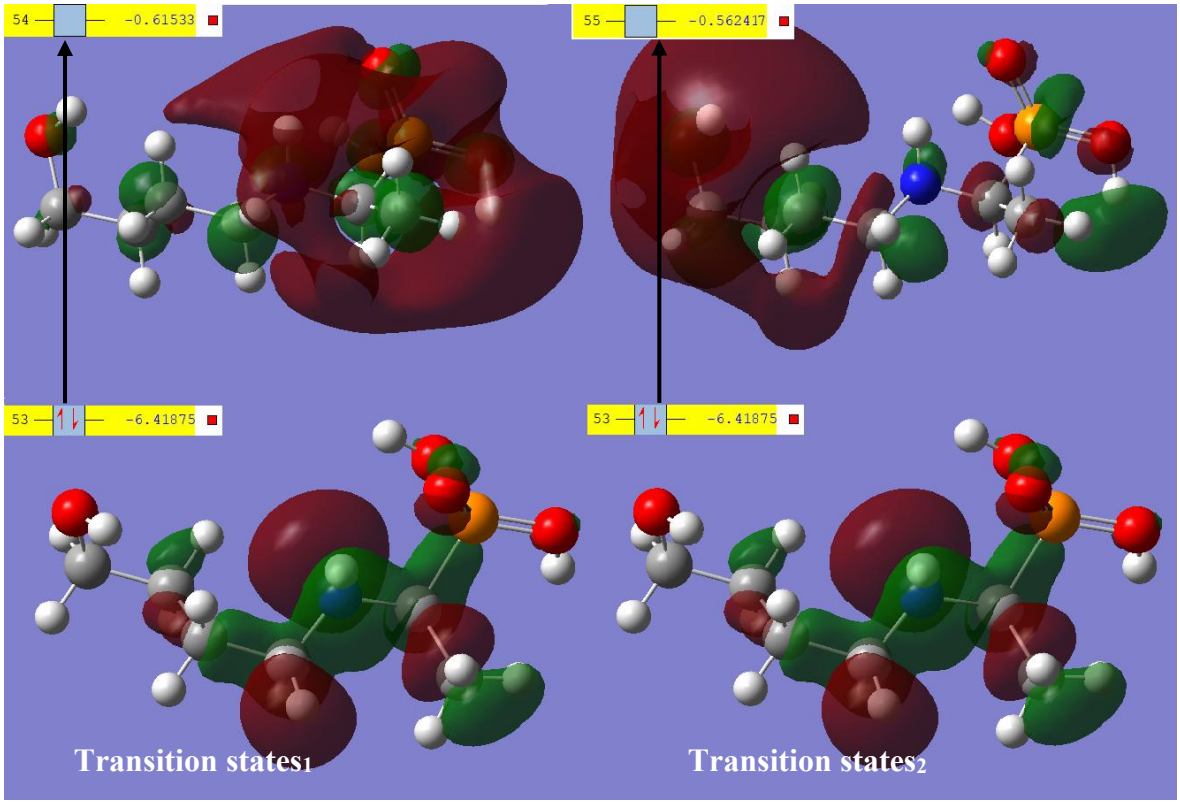


**Figure IV. 8** Molecular orbital (MO) of $HAP_2$ promotions contributing to each transition state.

The HOMO (MO 49 for $HAP_1$ and MO 53 for $HAP_2$) is probably a non-bonding orbital situated on a heteroatom, given the molecule possesses a lone pair on nitrogen and lone pairs on oxygen atoms. Considering that the lone pair of an alkyl amine frequently represents the highest-energy occupied orbital, it is reasonable to suggest that the HOMO is the nitrogen lone pair (n_N).

The LUMO (MO 50 for $HAP_1$ and MO 54 for $HAP_2$ )are probable anti-bonding orbitals. In a phosphonic acid-type structure, the π* orbital of the P=O bond is a strong candidate for the LUMO, as phosphoryl groups can accept electron density. these virtual molecular orbitals are likely localized within the phosphorus/oxygen domain (electron-deficient regions.

$LUMO_{+1}$ (MOs 41 for $HAP_1$ and MO 55 for $HAP_2$ ) are likely anti-bonding orbitals. In a phosphonic acid-type structure, a strong candidate for the LUMO is the π* orbital of the P=O bond (phosphoryl anti-bonding orbital), as phosphoryl groups can accept electron density. $LUMO_{+1}$ might be another antibonding orbital, possibly associated with σ* on the C–O In either case, these virtual MOs are probably distributed over the carbon/oxygen region (electron-deficient sites).

### IV.3.3 Characterization of Transitions

Transition $state_1$ for both compounds (HOMO→LUMO): This transition includes a lone pair (n) on the amine (or maybe oxygen) migrating to the π* orbital of the P=O group. This can be characterized as a n → π* transition. In addition, as the electron transitions from the amine area (the donor) to the phosphate group (the acceptor), the transition $state_1$ probably represents a transition in electron density from the amine's lone pair to the antibonding orbital of the phosphoryl group. n→π* transitions are generally symmetry-forbidden or only weakly permitted, aligning with the exceedingly low oscillator strength (f=0.0035). The comparatively longer wavelength (lower energy) aligns with a charge-transfer pattern, as donor-acceptor interactions often produce lower-energy transitions.

Transition $state_2$ for both compounds (HOMO→$LUMO_{+1}$) The primary component is the amine lone pair (HOMO) to a higher antibonding orbital ($LUMO_{+1}$)., LUMO+1 might be a σ* on the C–O(H) bond or even a diffuse orbital; thus we can regard as an $n \rightarrow \sigma$ transition from a lone pair. Overall, transition $state_2$ is still characterized by promotions from non-bonding orbitals to antibonding orbitals.

## IV.4 Conclusion

An integrative DFT methodology has demonstrated considerable efficacy in clarifying the structural and electronic properties of the examined molecules. Geometry optimizations validated stable conformations, while Mulliken charge analysis explained the distribution of electronic density and pinpointed areas of electrophilic and nucleophilic activity. Dipole moments and MESP surfaces elucidated the molecular polarity and possible reactive sites. Boundary Molecular Orbital and global reactivity investigations yielded significant insights into electron transfer mechanisms and predicted chemical reactivity. Vibrational analyses validated the integrity of the improved structures, and thermodynamic data corroborated their overall stability. TD-DFT calculations elucidated the characteristics of excited states, clarifying transition energies and orbital contributions. Collectively, our findings underscore the reliability and adaptability of DFT approaches in forecasting essential structural, spectroscopic, and reactive features, thereby providing a solid basis for directing experimental studies and subsequent computational inquiries.

V

# Advancing Drug Discovery Docking & ADME-T

# V Advancing Drug Discovery Docking & ADME-T

## V.1 Introduction

α-Aminophosphonic acids represent a diverse class of bioactive compounds recognized for their structural resemblance to α-amino acids and a range of biological actions [1-5]. Their distinctive phosphonate group positions them as possible inhibitors or modulators of numerous enzymes, attracting major attention in medicinal chemistry and drug discovery [6]. This study involved the evaluation of two new α-aminophosphonic acids, referred to as $HAP_1$ and $HAP_2$, against a panel of essential antioxidant enzymes: Superoxide Dismutase (SOD, PDB: 5YTO) [7], Catalase (CAT, PDB: 1DGF) [8], Glutathione Peroxidase (GPx, PDB: 2P31) [9], and Lipoxygenase (PDB: 1N8Q) [10]. These enzymes are crucial in alleviating oxidative stress, a significant factor in various diseases, including cancer [11], cardiovascular ailments [11], and neurological disorders [13]. Therefore, discovering novel small-molecule inhibitors or modulators that target these enzymes may yield significant therapeutic or preventive benefits.

Detailed molecular docking studies were conducted to clarify the binding processes of $HAP_1$ and $HAP_2$ with these enzymes. These in-silico studies elucidate the critical ligand-protein interactions, hydrogen bonding configurations, hydrophobic interactions, and overall binding affinity that may influence the inhibitory or modulatory effects of α-aminophosphonic acids.

Highlighting the essential importance of evaluating drug-likeness and potential safety issues during the initial phases of drug design, the ADME-T (Absorption, Distribution, Metabolism, Excretion, and Toxicity) characteristics of $HAP_1$ and $HAP_2$ were predicted using SwissADME [14], pkCSM [15], PROTOX [16] and STOPTOX [17]. These computational methods estimate pharmacokinetic profiles, analyze compound permeability and stability, and assess toxicological risk elements that collectively determine a chemical's viability as a lead contender. This chapter seeks to elucidate the structure-activity relationships and therapeutic potential of α-aminophosphonic acids through the integration of molecular docking, and ADME-T predictions, thereby informing the development of more effective prophylactic or therapeutic agents for oxidative stress-related disorders.

## V.2 Docking Simulations

Before conducting the molecular docking studies, all molecules ($HAP_1$, $HAP_2$, and any reference compounds) were first optimized using Gaussian at an appropriate level of theory to ensure accurate geometries and electronic properties. This step helps generate stable conformations with minimized potential energy, thereby improving the reliability of subsequent docking results. The optimized geometries were then exported in the required format (pdbqt) for further processing and docking studies.

### V.2.1 Interaction of $HAP_1$ and $HAP_2$ with Lipoxygenase (PDB: 1N8Q)

The molecular docking of $HAP_1$ into the lipoxygenase 1N8Q crystal structure resulted in a binding energy of –6.26 kcal/mol, suggesting moderate affinity. The highest-ranked posture demonstrated an RMSD of 2.167 Å, indicating a stable conformation inside the catalytic region. Table V.1 summarizes that $HAP_1$ establishes a favorable charge interaction with Ile875 and His523 via its phosphorus atom, with several hydrogen bonds with Gln514, His518, and Ile857. Additional stability is provided via a carbon-hydrogen connection between His518 and the phosphonic groups and a π–σ contact between His523 and the methyl substituent. These interactions collectively indicate a beneficial binding orientation that may affect the enzymatic activity of lipoxygenase.

**Table V. 1** Interactions Predicted for $HAP_1$ within the Lipoxygenase 1n8Q Active Site

| Interaction Type | Protein Residue(s) | Ligand Group/Atom | Notes |
|---|---|---|---|
| **Attractive charge** | Ile857, His523 | Phosphorous atom | Stabilizes ligand's aminophosphonic moiety |
| **Conventional hydrogen bond** | Gln514, His518 | Hydroxyl group of $HAP_1$ | Helps anchor ligands in the binding pocket |
| **Conventional hydrogen bond** | His518, Ile875 | Phosphonic groups of $HAP_1$ | Additional hydrogen bonding network |
| **Carbon-hydrogen bond** | His518 | Hydrogen of phosphonic groups | Minor contribution to overall stability |
| **π–σ interaction** | His523 | Methyl group of $HAP_1$ | Noncovalent contact enhancing ligand positioning |

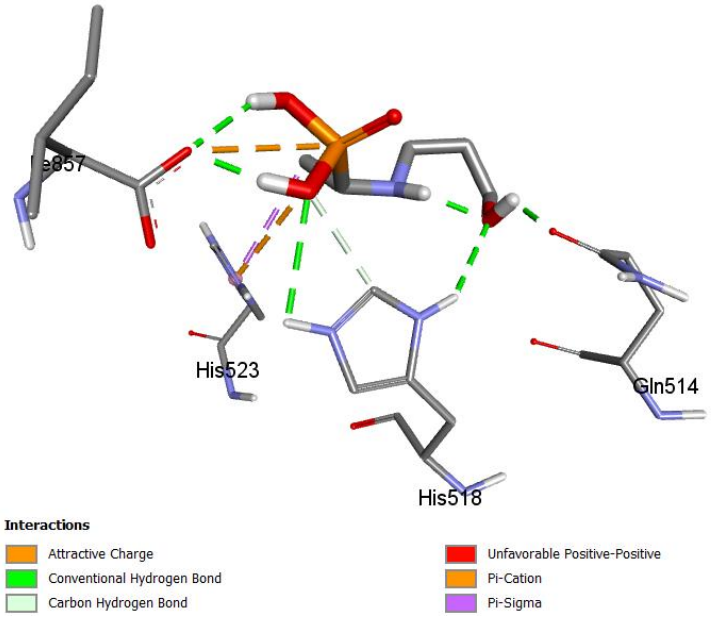


**Figure V. 1** Interactions for $HAP_1$ within the Lipoxygenase

Molecular docking of $HAP_2$ into the 1n8Q lipoxygenase structure produced a binding energy of –5.02 kcal/mol, indicative of a moderate binding affinity. The best-scoring pose exhibited an RMSD of 2.288 Å, suggesting a relatively stable conformation within the enzyme's active site. As summarized in Table V.2, the binding interactions include conventional hydrogen bonds between Ile875 and the hydroxyl group of $HAP_2$, as well as between Gln514 and the phosphonic moieties. A carbon-hydrogen bond was also observed between His518 and the hydroxyl group. Despite a lower predicted affinity than $HAP_1$, these interactions collectively stabilize $HAP_2$ within the lipoxygenase binding pocket."

**Table V. 2** Key Interactions Predicted for $HAP_2$ in the Lipoxygenase 1n8Q Active Site

| Interaction Type | Protein Residue(s) | Ligand Group/Atom | Notes |
|---|---|---|---|
| **Conventional hydrogen bond** | Ile875 | Hydrogen of the hydroxyl group | Anchors ligand via the polar hydroxyl group |
| **Conventional hydrogen bond** | Gln514 | Hydrogen of phosphonic groups | Contributes to polar stabilization in the pocket |
| **Carbon-hydrogen bond** | His518 | Hydrogen of the hydroxyl group | Provides additional noncovalent stabilization |

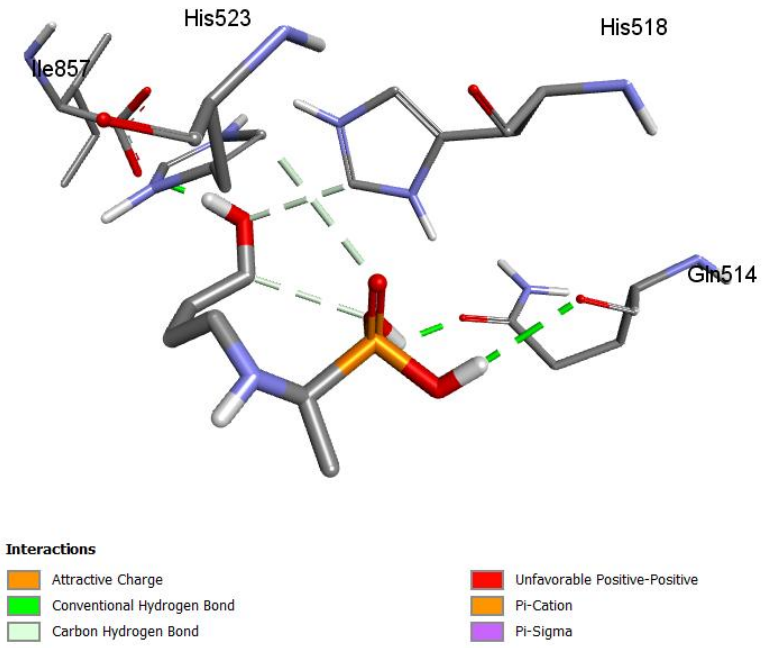


**Figure V. 2** 3D Interactions for $HAP_2$ within the Lipoxygenase

To evaluate structure–activity connections within the same scaffold, we analyzed the docking results of $HAP_1$ and $HAP_2$ in the lipoxygenase 1n8Q active site (Table V.3). $HAP_1$ demonstrated a superior projected binding energy (–6.26 kcal/mol) compared to $HAP_2$ (–5.02 kcal/mol), indicating a potentially greater affinity. This disparity is attributable to $HAP_1$'s supplementary stabilizing interactions, including the attractive charge with Ile875 and His523, as well as a π–σ contact with His523, which were not observed in $HAP_2$. Both ligands participated in standard hydrogen bonding with Gln514 and Ile875; however, $HAP_1$ established a bigger amount of hydrogen bonds, possibly enhancing its docking score. Regarding structural stability, $HAP_1$ exhibited a moderately elevated RMSD (2.288 Å) compared to HAP2 (2.167 Å), indicating a slightly less stable conformation. These findings suggest that substituents that augment electrostatic and aromatic interactions, exemplified by $HAP_1$, are essential for boosting affinity in this series.

**Table V. 3** Comparison of Docking Parameters and Key Interactions for $HAP_1$ and $HAP_2$ in Lipoxygenase 1n8Q

| Parameter | $HAP_1$ | $HAP_2$ |
|---|---|---|
| **Docking Score (kcal/mol)** | –6.26 | –5.02 |
| **RMSD (Å)** | 2.167 | 2.288 |
| **Key Residues Involved** | Ile875, His523, His518, Gln514 | Ile875, His518, Gln514 |
| **Principal Hydrogen Bonds** | Gln514 ↔ hydroxyl<br>His518, Ile875 ↔ phosphonic groups | Ile875 ↔hydroxyl<br>Gln514 ↔ phosphonic groups |
| **Additional Interactions** | Attractive charge (Ile875, His523 ↔ P atom)<br>π–σ (His523 ↔ methyl)<br>Carbon-H bond (His518 ↔ phosphonic H) | Carbon-H bond (His518 ↔ hydroxyl H) |

### V.2.2 Interaction of $HAP_1$ and $HAP_2$ with Superoxide Dismutase (SOD; PDB: 5YTO)

The molecular docking of $HAP_1$ into the superoxide dismutase (SOD; PDB: 5YTO) crystal structure resulted in a binding energy of –2.4 kcal/mol, suggesting a relatively weak affinity compared to typical drug-like ligands [18]. The highest-ranked conformation demonstrated an RMSD of 2.108 Å, indicating a modestly stable pose in the putative binding region. As summarized in Table V.4, $HAP_1$ forms several hydrogen bonds with Glu132 (including the ligand's hydroxyl, phosphonic, and amine groups) and a carbon-hydrogen bond with Val97. Additional π–cation contacts involve Glu132 and Asp96 interacting with the phosphonic moiety, although an unfavorable positive–positive interaction was also observed between the ligand's amine/hydroxyl and phosphonic groups. These interactions collectively suggest a pose in which $HAP_1$ engages key residues (Glu132 and Asp96) but may benefit from further optimization to reduce repulsive forces and enhance binding strength.

Table V. 4 **Interactions Predicted for $HAP_1$ within the SOD (5YTO) Active Site**

| Interaction Type | Protein Residue(s) | Ligand Group/Atom | Notes |
|---|---|---|---|
| **Conventional hydrogen bond** | Glu132 | Hydroxyl group of $HAP_1$ | Anchors the ligand through a strong polar interaction |
| **Conventional hydrogen bond** | Glu132 | Two hydrogens of phosphonic groups | Reinforces binding; phosphonic groups can form multiple H-bonds |
| **Conventional hydrogen bond** | Glu132 | The hydrogen of the amine group | Contributes an additional polar contact, focusing on the ligand's amine moiety |
| **Carbon–hydrogen bond** | Val97 | Carbon of hydroxyl ($HAP_1$) | Minor stabilizing interaction, often weaker than conventional H-bonds |
| **π–cation interaction** | Glu132, Asp96 | Phosphorus atom (phosphonic moiety) | Electrostatic contacts with negatively charged residues, potentially stabilizing the complex. |
| **Unfavorable positive–positive** | (Involving Glu132/asp96 environment) | H of NH (hydroxyl/amine) and OH of phosphonic | Indicates repulsive electrostatic interaction that may reduce overall binding affinity |

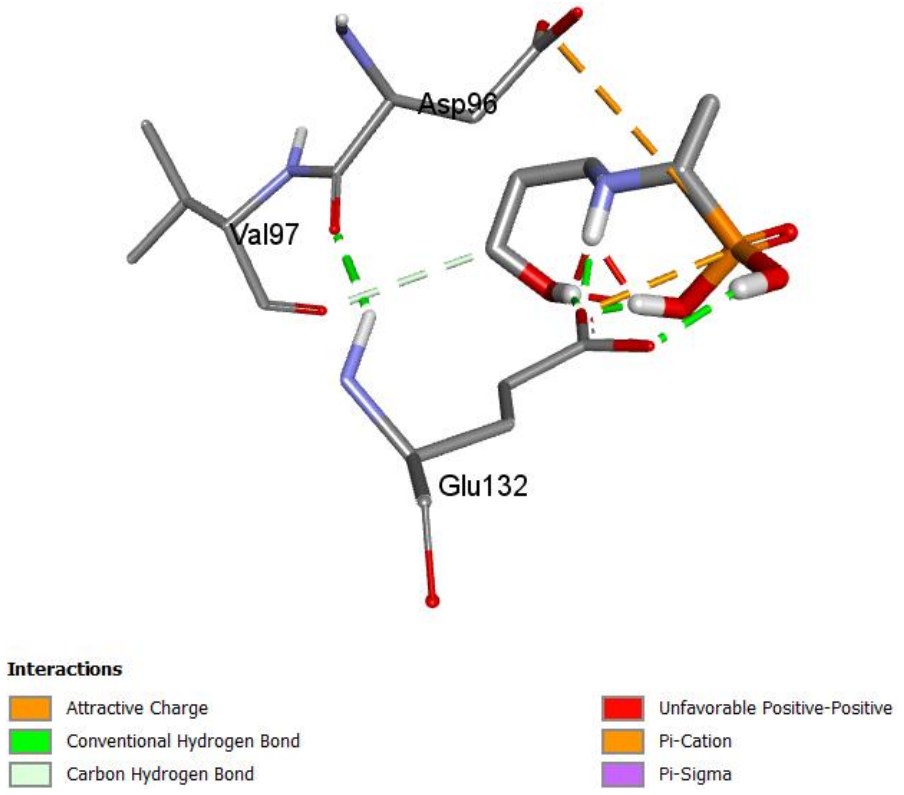


**Figure V. 3** 3D Interactions for $HAP_1$ within the Superoxide Dismutase

The molecular docking of $HAP_2$ into the superoxide dismutase (SOD; PDB: 5YTO) crystal structure showed a binding energy of –1.54 kcal/mol, signifying a comparatively poor affinity relative to conventional drug-like ligands. The optimal scoring conformation displayed an RMSD of 1.275 Å, indicating a relatively stable position within the presumed binding pocket. Table V.5 summarizes that $HAP_2$ establishes several hydrogen connections with Asn86, Glu100, Lys70, and Gly127, in addition to a carbon-hydrogen bond with Leu84. These interactions collectively stabilize $HAP_2$ in the active site.

**Table V. 5** Interactions Predicted for $HAP_2$ within the SOD (5YTO) Active Site

| Interaction Type | Protein Residue(s) | Ligand Group/Atom | Notes |
|---|---|---|---|
| **Conventional hydrogen bond** | Asn86 | Hydroxyl group of HAP2 | Anchors the ligand's hydroxyl moiety |
| **Conventional hydrogen bond** | Glu100 | Hydrogen(s) of the phosphonic group | Reinforces binding via strong polar contact |
| **Conventional hydrogen bond** | Lys70 | Hydrogen of phosphonic group | Additional polar stabilization in the binding site |
| **Conventional hydrogen bond** | Gly127 | Hydrogen of the amine group | Further strengthens the ligand's polar network |
| **Carbon–hydrogen bond** | Leu84 | Carbon of hydroxyl | Minor contribution to overall stability |

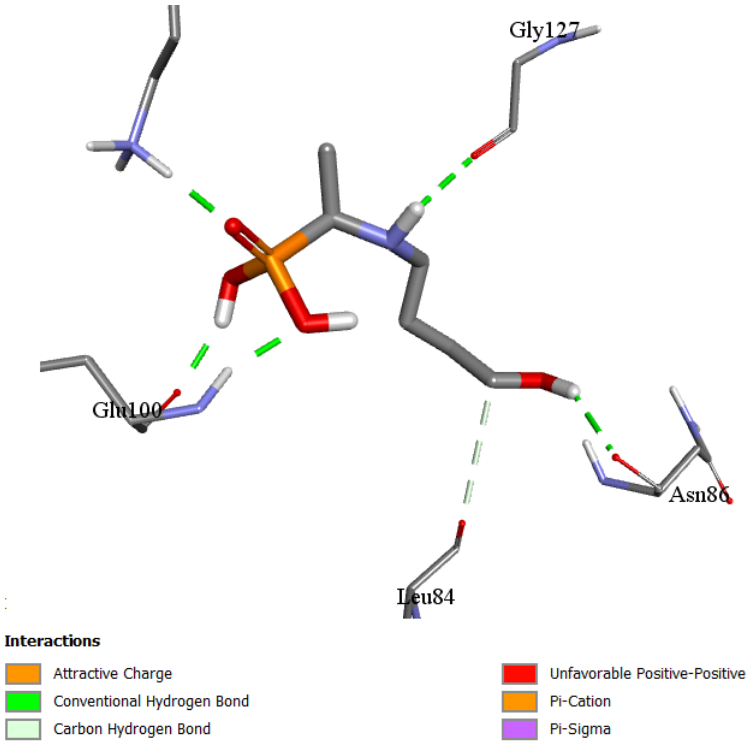


**Figure V. 4** 3D Interactions for $HAP_2$ within the Superoxide Dismutase

In summary, $HAP_1$ demonstrated a superior predicted binding affinity (–2.4 kcal/mol) compared to $HAP_2$ (–1.54 kcal/mol), likely due to $HAP_1$'s enhanced stabilizing interactions, including several conventional hydrogen bonds with Glu132 and π–cation interactions with the phosphonic group (Glu132, Asp96), which were less pronounced in $HAP_2$. Both compounds created several hydrogen bonds within the active site; however, $HAP_1$ established a greater number of polar interactions overall, possibly enhancing its docking score. In terms of structural stability, $HAP_1$ exhibited a considerably elevated RMSD of 2.108 Å in contrast to $HAP_2$'s 1.275 Å, suggesting a marginally less rigid binding conformation.

### V.2.3 Interaction of $HAP_1$ and HAP2 with Catalase (CAT, PDB: 1DGF)

The molecular docking of $HAP_1$ with Catalase (PDB: 1DGF) gave a predicted binding energy of –1.73 kcal/mol, indicating relatively weak affinity. The top-ranked pose showed an RMSD of 1.153 Å, suggesting a stable conformation in the enzyme's binding region. As summarized in Table V.4, $HAP_1$ engages in multiple conventional hydrogen bonds with Arg66, Arg363, His364, and Lys70. However, an unfavorable positive–positive electrostatic clash between the ligand's hydroxyl/amine protons and the phosphonic group was also observed, likely reducing the overall binding stability.

**Table V. 6** Interactions Predicted for $HAP_1$ with Catalase (1DGF)

| **Interaction Type** | **Protein Residue(s)** | **Ligand Group/Atom** | **Notes** |
|---|---|---|---|
| **Conventional hydrogen bond** | Arg66, Arg363 | Hydroxyl group of HAP1 | Anchors the ligand's hydroxyl functionality |
| **Conventional hydrogen bond** | His364 | Phosphonic groups | Strong polar interactions help to position the ligand |
| **Conventional hydrogen bond** | Arg363 | Hydrogen of phosphonic group | Further stabilizes HAP1 via polar contact |
| **Conventional hydrogen bond** | Lys70 | Hydrogen of phosphonic group | Contributes additional binding-site stabilization |
| **Conventional hydrogen bond** | Arg363 | The hydrogen of the amine group | Expands the hydrogen-bonding network in the active site |
| **Unfavorable positive–positive** | (Intramolecular clash) | Hydroxyl/amine protons and phosphonic OH | Electrostatic repulsion within the ligand may diminish overall binding affinity. |

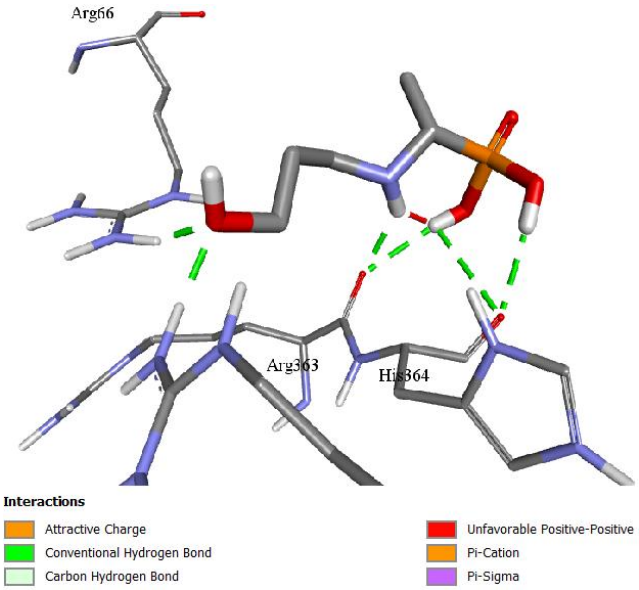


**Figure V. 5** 3D Interactions for $HAP_1$ within the Catalase

The molecular docking of HAP2 into Catalase (CAT; PDB: 1DGF) resulted in a predicted binding energy of –0.74 kcal/mol, suggesting a relatively very weak affinity. The top-scoring pose exhibited an RMSD of 1.972 Å, indicating a moderately stable orientation in the active site. As outlined in Table V.7, $HAP_2$ forms multiple hydrogen bonds with Arg66, His364, and Arg363, as well as a carbon–hydrogen bond involving Arg363. However, an unfavorable positive–positive interaction between the ligand's hydroxyl and phosphonic groups may diminish the net stability of the complex.

**Table V. 7** Interactions Predicted for HAP2 with Catalase (1DGF)

| Interaction Type | Protein Residue(s) | Ligand Group/Atom | Notes |
|---|---|---|---|
| **Conventional hydrogen bond** | Arg66, His364 | Hydroxyl group of HAP2 | Strong polar contacts anchoring the hydroxyl functionality |
| **Conventional hydrogen bond** | His364 | Hydrogen(s) of the phosphonic group | Additional polar stabilization near the enzyme's catalytic site |
| **Conventional hydrogen bond** | Arg363 | The hydrogen of the amine group | Extends the hydrogen-bonding network and enhances ligand orientation |
| **Carbon–hydrogen bond** | Arg363 | Carbon of the hydroxyl group | Minor non-covalent interaction contributing to overall ligand positioning |
| **Unfavorable positive–positive clash** | – | Hydroxyl (H) and phosphonic (OH) | Electrostatic repulsion that may reduce the overall binding affinity |

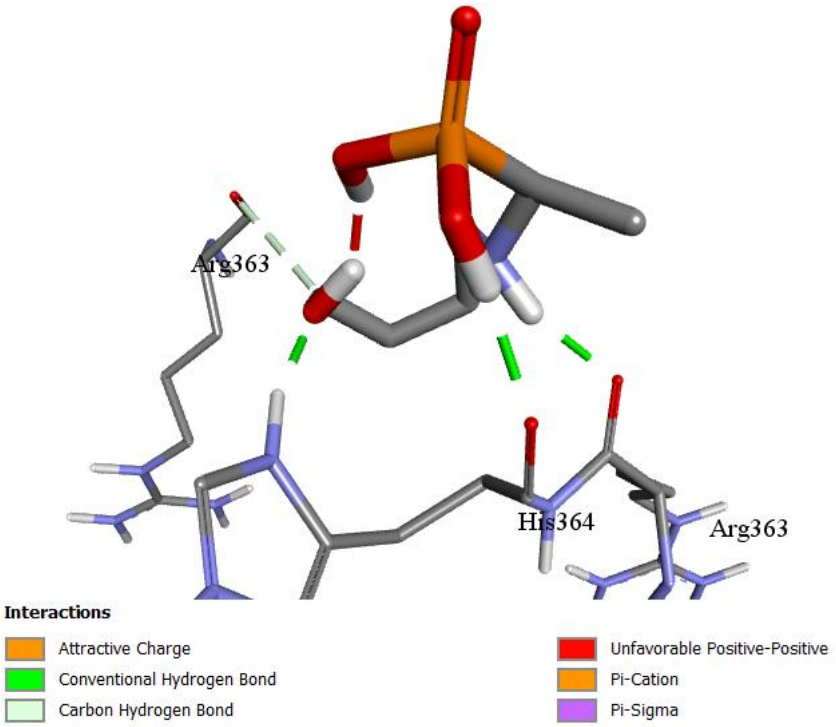


**Figure V. 6** 3D Interactions for $HAP_2$ within the Catalase

In summary, $HAP_1$ shows a stronger affinity for Catalase than $HAP_2$, as indicated by its more negative docking score and reduced RMSD value. Both ligands exhibit possibilities for additional optimization. Reducing the recognized electrostatic repulsion and maybe augmenting hydrophobic or electrostatic complementarity may enhance the binding affinities and overall stability of these ligands in forthcoming design initiatives.

### V.2.4 Interaction of $HAP_1$ and $HAP_2$ with Glutathione Peroxidase (GPx, PDB: 2P31)

The molecular docking of $HAP_1$ into Glutathione Peroxidase (GPx) predicted a binding energy of –0.22 kcal/mol, suggesting a notably weak affinity. The top-scoring conformation exhibited an RMSD of 1.679 Å, indicating moderate structural convergence within the active site. As shown in Table V.8, $HAP_1$ engages in multiple hydrogen bonds with Arg106, His364, and Ser109, along with a carbon–hydrogen bond involving Asp61. However, an unfavorable positive–positive electrostatic clash occurs between the ligand's hydroxyl group and phosphonic OH, potentially diminishing overall binding stability.

Collectively, these interactions underscore that while $HAP_1$ forms several polar contacts with key GPx residues, the weak docking score and the identified electrostatic repulsion suggest ample room for optimization perhaps through adjusting the ligand's polar functionalities or reducing intramolecular repulsion to enhance affinity and stability within the enzyme's active site.

**Table V. 8** Interactions Predicted for $HAP_1$ within Glutathione Peroxidase

| Interaction Type | Protein Residue(s) | Ligand Group/Atom | Notes |
|---|---|---|---|
| **Conventional hydrogen bond** | Arg106 | Hydrogens of phosphonic groups | Anchors the phosphonic moiety via strong polar contacts |
| **Conventional hydrogen bond** | Arg106 | The hydrogen of the amine group | Expands the hydrogen-bonding network in the active site |
| **Conventional hydrogen bond** | Ser109 | The hydrogen of the hydroxyl group | Additional polar interaction helps to position the ligand |
| **Carbon–hydrogen bond** | Asp61 | Carbon of the amine group | Minor non-covalent interaction that may aid ligand orientation |
| **Unfavorable positive–positive clash** | – | Hydroxyl (H) and phosphonic (OH) | Electrostatic repulsion likely reduces overall binding affinity |

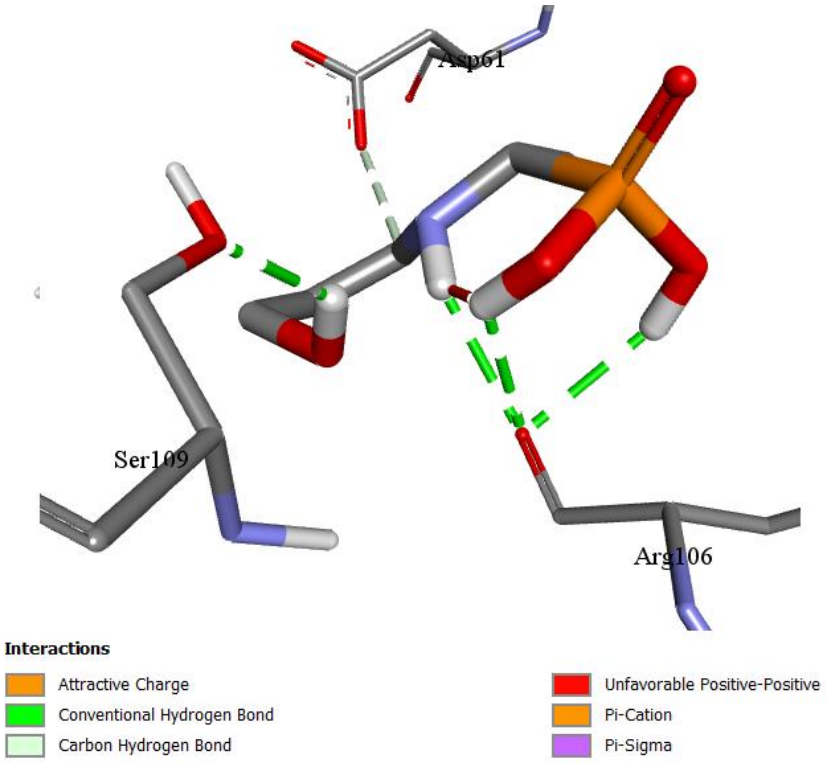


**Figure V. 7** 3D Interactions for $HAP_1$ within the Glutathione Peroxidase

The molecular docking of $HAP_2$ into the target enzyme yielded a projected binding energy of –1.97 kcal/mol, signifying a relatively poor affinity, with the optimal pose displaying an RMSD of 1.713 Å. Table V.9 indicates that HAP1 establishes many hydrogen bonds with Asp95, Glu56, and Ser55, in addition to a π–cation interaction between Glu56,

Asp95, and the phosphorus atom of the phosphonic group. A carbon–hydrogen link between Glu56 and the amine carbon also plays a minor role in ligand stability. Nonetheless, an adverse positive–positive electrostatic interaction between the ligand's amine group and phosphonic OH likely reduces the total binding affinity.

**Table V. 9** Interactions Predicted for $HAP_2$ with the Glutathione Peroxidase

| **Interaction Type** | **Protein Residue(s)** | **Ligand Group/Atom** | **Notes** |
|---|---|---|---|
| **Conventional hydrogen bond** | Asp95 | Hydrogen(s) of the phosphonic group | Strong polar contacts anchoring the phosphonic moiety |
| **Conventional hydrogen bond** | Glu56 | Hydrogen(s) of the phosphonic group | Additional polar interaction contributes to the ligand's orientation |
| **Conventional hydrogen bond** | Asp95 | The hydrogen of the amine group | Further extends the hydrogen-bonding network in the active site |
| **Conventional hydrogen bond** | Ser55 | The hydrogen of the hydroxyl group | Stabilizing polar contact with the ligand's hydroxyl functionality |
| **Carbon–hydrogen bond** | Glu56 | Carbon of the amine group | Minor non-covalent interaction that supports ligand positioning |
| **π–cation interaction** | Glu56, Asp95 | Phosphorus (phosphonic group) | Electrostatic contact with negatively charged side chains, reinforcing the ligand's binding |
| **Unfavorable positive–positive clash** | – | Amine group and phosphonic OH | Electrostatic repulsion likely reduces net binding affinity. |

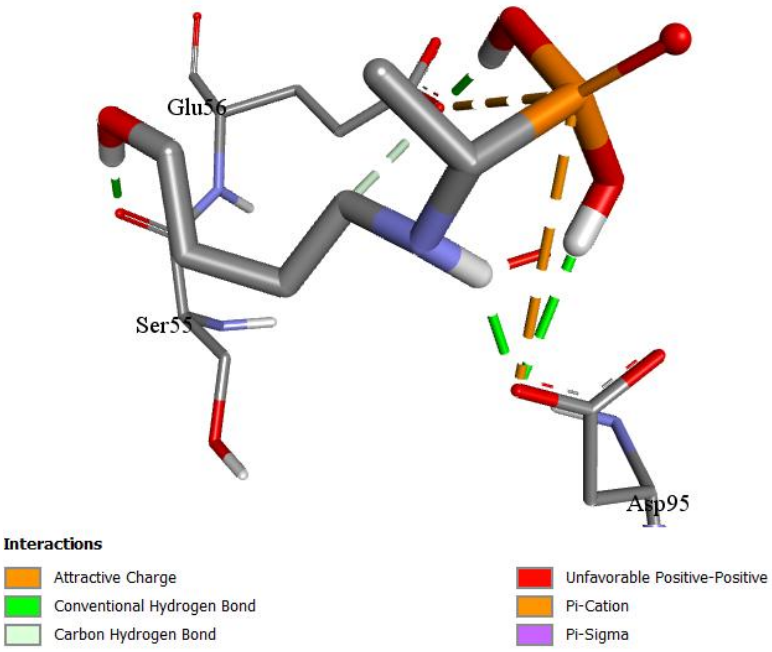


**Figure V. 8** 3D Interactions for $HAP_2$ within the Glutathione Peroxidase

After completing docking tests of $HAP_1$ and $HAP_2$ with four different proteins, Lipoxygenase (PDB: 1N8Q) was identified as the most promising target, with a docking score below –5 kcal/mol and a good RMSD, both suggesting a stable, high-affinity binding mode. Conversely, the remaining proteins evaluated (superoxide dismutase, catalase, and glutathione peroxidase) demonstrated inferior docking scores and/or elevated RMSD values, indicating fewer stable interactions. In light of the promising outcomes with Lipoxygenase, we chose the 1N8Q crystal structure for further examination, as its superior predicted affinity and sufficient pose stability render it the ideal option for following structure-based analyses.

### V.2.5 Ligand Preparation at Physiological pH for Molecular Docking

To get accurate docking results, ligands must be prepared to simulate physiological conditions. We find the predominant protonation state of each molecule at blood pH (~8) using ChemAxon, refining the geometry of that ionized form using Gaussian, and ultimately utilizing the optimized structure in docking simulations. This method guarantees that the ligands are in biologically important forms for precise interaction modeling.

### V.2.6 Determining Predominant Ionic Species (pH 8)

The protonation state of a ligand at a specific pH is crucial because it defines the dominant ionic form present under those conditions. We utilized ChemAxon's Marvin software (pKa plugin) [19] to calculate the pKa values of each compound and determine its predominant protonation state at pH ≈8 (approximately physiological blood pH) [20] Ensuring the accurate ionic form of each ligand, as it would exist in the bloodstream, presents an accurate basis for docking, as protonation may have a major impact on a molecule's interaction with a receptor.

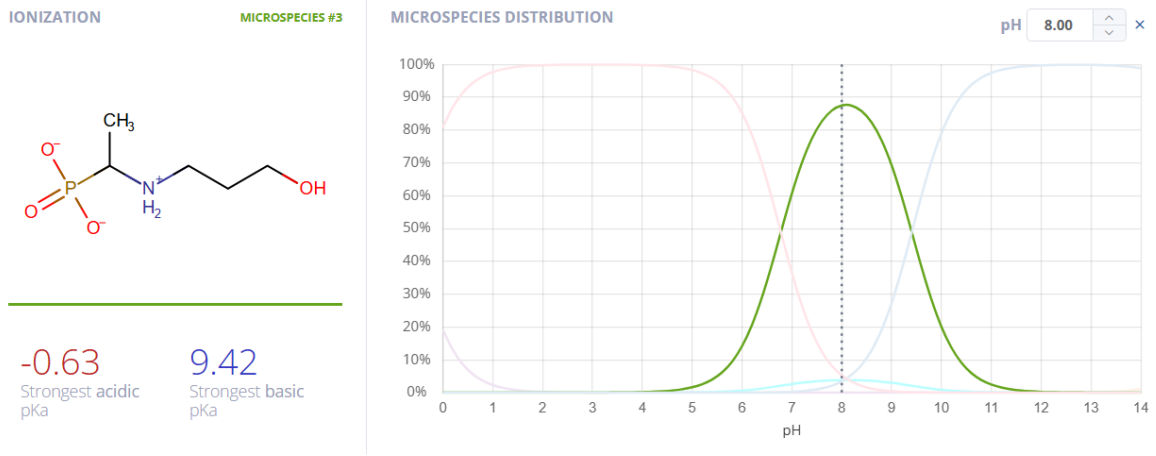


**Figure V. 10** The major microspecies output from Marvin represents the dominant protonation states of $HAP_1$ at pH 8 (physiological pH).

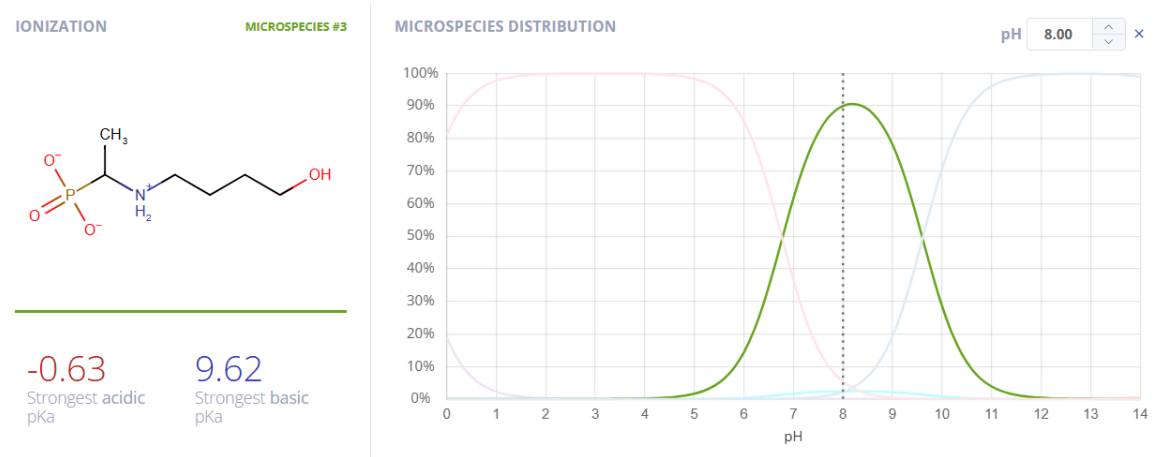


**Figure V. 9** The major microspecies output from Marvin represents the dominant protonation states of $HAP_2$ at pH 8 (physiological pH).

The protonation structures served as the input ligands for molecular docking analyses. Employing the ligands in their energy-minimized, physiological ionic state enables the docking algorithm to assess a realistic conformation and charge distribution, resulting in more biologically pertinent binding interactions. In essence, commencing with a properly

protonated and minimized structure mitigates the risk of artifacts stemming from erroneous charges or strained geometries during docking [21]. This preparatory phase enhances the reliability of docking outcomes, as shown in the literature, where optimal ligand structures at the appropriate pH are employed to augment the precision of docking simulations [22].

### V.2.7 Interaction of the major microspecies with Lipoxygenase (PDB: 1N8Q)

The molecular docking of $HAP_1$'s major microspecies at pH 8 into Lipoxygenase (PDB: 1N8Q) resulted in a predicted binding energy of –6.92 kcal/mol, indicating moderate to strong affinity. The top-scoring pose exhibited an RMSD of 2.082 Å, suggesting a relatively stable orientation within the enzyme's active site. As summarized in Table V.10, HAP1 establishes several key noncovalent contacts, including conventional hydrogen bonds with Gln514, His518, and Ile857, a carbon–hydrogen bond with His518, and a π–σ interaction involving His523. Additionally, attractive charge interactions between His518/His523 and the negatively charged oxygen, and between Ile857 and the phosphorus moiety, contribute to the ligand's overall binding stabilization.

**Table V. 10** Interactions Predicted for $HAP_1$ (pH 8) within Lipoxygenase (1N8Q)

| Interaction Type | Protein Residue(s) | Ligand Group/Atom | Notes |
|---|---|---|---|
| **Conventional hydrogen bond** | Gln514 | Hydroxyl group of HAP1 | Anchors the ligand's hydroxyl moiety in the active site |
| **Conventional hydrogen bond** | His518, Ile857 | Phosphonic groups of HAP1 | Stabilizes the phosphonic acid moiety via strong polar contacts |
| **Carbon–hydrogen bond** | His518 | Hydrogen of phosphonic groups | Minor noncovalent interaction that further supports ligand positioning |
| **π–σ interaction** | His523 | Methyl group of HAP1 | Noncovalent contact enhancing ligand orientation |
| **Attractive charge** | His518, His523 | The negative charge on phosphonic O | Electrostatic attraction further stabilizes HAP1 in the binding pocket |
| **Attractive charge** | Ile857 ↔ phosphorus of HAP1 | Phosphorus (phosphonic moiety) | Reinforces the polar network by interacting with the ligand's phosphate |

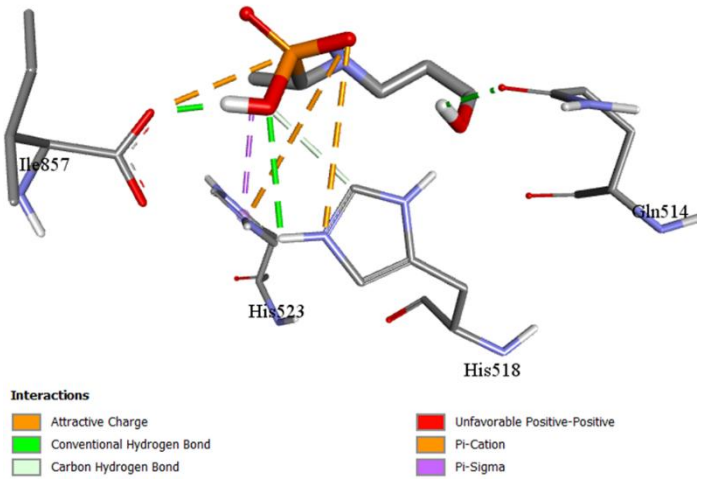


**Figure V. 12** Interactions of $HAP_1$ microspecie (pH 8) within the Lipoxygenase

The molecular docking of $HAP_2$'s primary microspecies into Lipoxygenase (PDB: 1N8Q) resulted in a binding energy of –4.25 kcal/mol, with the highest-scoring conformation exhibiting an RMSD of 1.509 Å. This conformation displays standard hydrogen bonds between Gln514 and the hydroxyl group and between Ile857 and the phosphonic groups. Carbon–hydrogen bonds are established with His518 and His523, both of which interact with the phosphonic moiety, while electrostatic interactions between His523/Ile857 and the phosphorus group further enhance the stability of $HAP_2$ in the active site. The aggregated connections indicate a moderate affinity, allowing structural optimization to improve binding strength.

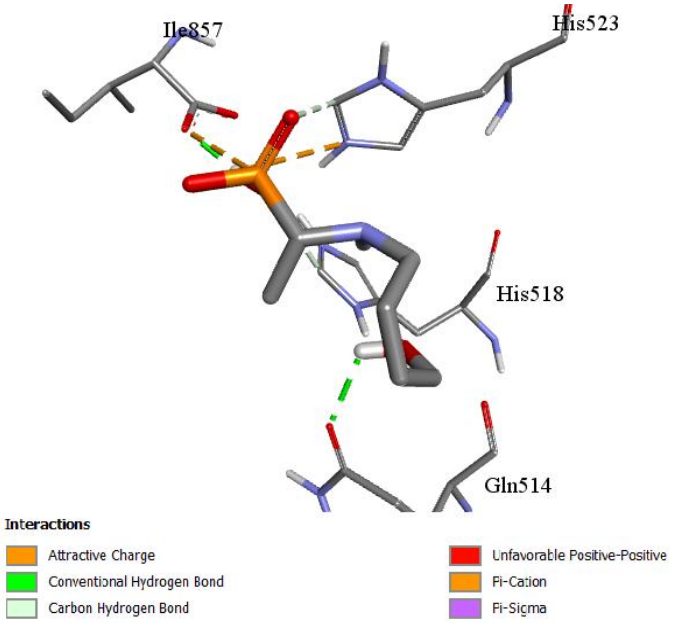


**Figure V. 11** Interactions of $HAP_2$ microspecie (pH 8) within the Lipoxygenase

**Table V. 11** Interactions Predicted for $HAP_2$ (pH 8) within Lipoxygenase (1N8Q)

| Interaction Type | Protein Residue(s) | Ligand Group/Atom | Notes |
|---|---|---|---|
| **Conventional hydrogen bond** | Gln514 | Hydroxyl group of $HAP_2$ | Anchors the ligand's polar hydroxyl moiety |
| **Conventional hydrogen bond** | Ile857 | Phosphonic groups of $HAP_2$ | Reinforces binding by stabilizing negatively charged phosphonic oxygens |
| **Carbon–hydrogen bond** | His518, His523 | Phosphonic groups of $HAP_2$ | Minor noncovalent contacts aiding ligand orientation |
| **Attractive charge** | His523, Ile857 | Phosphorus (phosphonic moiety) | Additional electrostatic stabilization via interaction with the anionic site of $HAP_2$ |

When comparing the organic (neutral) forms of $HAP_1$ and $HAP_2$ with their predominant microspecies at pH 8, distinct differences in binding affinity and position stability become evident. Both ligands were docked to lipoxygenase (PDB: 1N8Q), although their protonation states at pH 8 influence their interactions with critical residues. A deprotonated phosphonic group typically establishes more robust electrostatic interactions with positively charged or polar amino acids, however the overall impact on binding differs between $HAP_1$ and $HAP_2$.

For $HAP_1$, the natural molecule exhibited a docking score of –6.26 kcal/mol (RMSD: 2.167 Å), whereas its pH 8 microspecies demonstrated a more advantageous value of –6.92 kcal/mol (RMSD: 2.082 Å). This enhancement results from further electrostatic and aromatic interactions, particularly favorable charge interactions with histidine residues, and a π–σ contact involving His523. The reduced RMSD signifies a modestly more stable conformation, demonstrating that deprotonation can improve both binding affinity and structural convergence for $HAP_1$.

In comparison, $HAP_2$ exhibited a docking score of –5.02 kcal/mol (RMSD: 2.288 Å) in its natural configuration, but its pH 8 microspecies yielded a value of –4.25 kcal/mol (RMSD: 2.009 Å). While it assumes a more stable conformation (lower RMSD) at alkaline pH, the compound's affinity decreases, likely due to poor hydrogen-bond geometry or adverse electrostatic influences from the deprotonated phosphonic group. Collectively, these findings underscore that protonation states significantly affect the binding affinity and

structural integrity of phosphonic-containing ligands, with $HAP_1$ deriving a greater advantage from deprotonation than $HAP_2$ in this specific lipoxygenase system.

## V.3 ADME-T Predictions

In the field of integrated drug discovery, SwissADME, pkCSM, ProTox, and StopTox are vital elements of computational ADME-T profiling. SwissADME offers essential information regarding physicochemical characteristics and markers of oral bioavailability, such as lipophilicity, solubility, and anticipated gastrointestinal absorption. Similarly [23], pkCSM utilizes graph-based signatures for thorough pharmacokinetic predictions that include distribution, metabolic pathways, and interactions with cytochrome P450 enzymes [24]. ProTox enhances this framework by calculating toxicity parameters like LD50 and evaluating potential toxicological impacts, whereas [25] StopTox refines toxicity predictions using specialized modeling techniques aimed at certain toxicity endpoints [26]. These techniques, whether utilized sequentially or iteratively, facilitate the rapid discovery of drugs with advantageous ADME-T profiles, assisting in the selection and optimization of leads before the allocation of substantial resources for in vitro and in vivo testing.

### V.3.1 SwissADME Profiles of $HAP_1$ and $HAP_2$

#### V.3.1.1 Lipophilicity and Water Solubility

$HAP_1$ and $HAP_2$ exhibit predominant hydrophilic characteristics in Tables V.12, as indicated by their consensus Log Po/w values of -1.31 for $HAP_1$ and -1.06 for $HAP_2$. The negative log P values suggest that, in comparison to several therapeutic possibilities, both compounds are more polar than lipophilic. As a result, predictions regarding water solubility are consistently positive. Per the ESOL and Ali models, each molecule is classified as "Highly soluble," according to predicted solubility values ranging from $10^3$ to $10^4$ mg/ml. Even the SILICOS-IT model, which frequently produces more cautious estimates, categorizes them within the "Soluble" category. The combination of reduced lipophilicity and high water solubility indicates that both $HAP_1$ and $HAP_2$ should, theoretically, dissolve easily in gastrointestinal fluids, which is advantageous for oral administration.

**Table V. 12** Lipophilicity & Water Solubility of $HAP_1$ and $HAP_2$ predicted by SwissADME

| Property | $HAP_1$ | $HAP_2$ |
|---|---|---|
| **Log Po/w (iLOGP)** | 0.84 | 0.65 |
| **Log Po/w (XLOGP3)** | -4.11 | -3.75 |
| **Log Po/w (WLOGP)** | -0.52 | -0.13 |

| | | |
|---|---|---|
| **Log Po/w (MLOGP)** | -1.26 | -0.88 |
| **Log Po/w (SILICOS-IT)** | -1.51 | -1.17 |
| **Consensus Log Po/w** | -1.31 | -1.06 |
| **Log S (ESOL)** | 1.94 ($1.61e^{+04}$ mg/ml; $8.79e^{+01}$ mol/l) Class: Highly soluble | 1.70 ($9.79e^{+03}$ mg/ml; $4.97e^{+01}$ mol/l) Class: Highly soluble |
| **Log S (Ali)** | 2.62 ($7.67e^{+04}$ mg/ml; $4.19e^{+02}$ mol/l) Class: Highly soluble | 2.25 ($3.49e^{+04}$ mg/ml; $1.77e^{+02}$ mol/l) Class: Highly soluble |
| **Log S (SILICOS-IT)** | 0.12 ($2.44e^{+02}$ mg/ml; $1.33e^{+00}$ mol/l) Class: Soluble | -0.28 ($1.03e^{+02}$ mg/ml; $5.20e^{-01}$ mol/l) Class: Soluble |

### V.3.1.2 Pharmacokinetics

In addition to solubility, both compounds exhibit promising pharmacokinetic characteristics Table V.13. The "GI absorption" parameter of SwissADME is classified as "High" for $HAP_1$ and $HAP_2$, indicating their probable efficient absorption via the intestinal epithelium. Neither molecule is identified as a substrate for P-glycoprotein (P-gp), an efflux transporter that may diminish intracellular drug concentrations, nor are they anticipated to inhibit the principal cytochrome P450 isoforms (CYP1A2, 2C19, 2C9, 2D6, 3A4). Minimizing CYP inhibition is crucial for drug-drug interactions; the data indicate a negligible risk of metabolic interference. Regarding central nervous system exposure, both $HAP_1$ and $HAP_2$ are categorized as non-permeants of the blood-brain barrier, which could be advantageous (minimizing potential CNS side effects) or restrictive (if CNS targeting is desired). The skin penetration coefficients (Log Kp) of between -10.3 and -10.2 cm/s indicate restricted transdermal absorption, aligning with their hydrophilic characteristics.

**Table V. 13** Pharmacokinetics of $HAP_1$ and $HAP_2$ Predicted by SwissADME

| Parameter | $HAP_1$ | $HAP_2$ |
|---|---|---|
| **GI absorption** | High | High |
| **BBB permeant** | No | No |
| **P-gp substrate** | No | No |
| **CYP1A2 inhibitor** | No | No |
| **CYP2C19 inhibitor** | No | No |
| **CYP2C9 inhibitor** | No | No |
| **CYP2D6 inhibitor** | No | No |
| **CYP3A4 inhibitor** | No | No |
| **Log Kp (skin permeation)** | -10.34 cm/s | -10.17 cm/s |

### V.3.1.3 drug-likeness

From a traditional drug-likeness standpoint Table V.14, both $HAP_1$ and $HAP_2$ adhere to Lipinski's Rule of Five [28] without infractions, signifying that typical oral bioavailability

factors—molecular weight, hydrogen bond donors and acceptors, and log P—remain within permissible limits. Nonetheless, each component induces certain rule-based differences under alternative filters. $HAP_1$ contravenes the Ghose rule [29], mostly due to a WLOGP value below -0.4, while $HAP_2$ complies with the Ghose requirement. Conversely, both compounds fail Muegge [30], mostly due to their very low molecular weights (below 200 Da) and negative XLOGP3 values. Notwithstanding these violations, SwissADME allocates a bioavailability score of 0.56 to each, indicating a reasonable probability of attaining sufficient oral bioavailability in vivo.

**Table V. 14** drug-likeness of $HAP_1$ and $HAP_2$ predicted by SwissADME

| Filter | $HAP_1$ | $HAP_2$ |
|---|---|---|
| **Lipinski** | Yes; 0 violation | Yes; 0 violation |
| **Ghose** | No; 1 violation (WLOGP < -0.4) | Yes |
| **Veber** | Yes | Yes |
| **Egan** | Yes | Yes |
| **Muegge** | No; 2 violations (MW < 200) (XLOGP3 < -2) | No; 2 violations (MW < 200) (XLOGP3 < -2) |
| **Bioavailability Score** | 0.56 | 0.56 |

### V.3.1.4 Medicinal Chemistry Alerts

From a medicinal chemistry perspective, neither molecule exhibits PAINS alarms, suggesting a little probability of assay interference complications. Both activate a Brenk alarm associated with the presence of a phosphor group, which may necessitate additional scrutiny if reactivity or safety issues emerge. Lead-likeness filters identify both compounds due to their low molecular weights; yet, their reduced size may be advantageous for later structural elaboration. $HAP_2$ possesses a synthetic accessibility (SA) score of 3.27, indicating a moderate synthetic pathway; a comparable or somewhat distinct SA value can be inferred for $HAP_1$ due to its common structural classification. Moderate probability of attaining sufficient oral bioavailability in vivo.

**Table V. 15** Medicinal Chemistry Alerts of $HAP_1$ and $HAP_2$ predicted by SwissADME

| Filter / Feature | $HAP_1$ | $HAP_2$ |
|---|---|---|
| **PAINS alerts** | 0 alert | 0 alert |
| **Brenk alerts** | 1 alert: phosphor | 1 alert: phosphor |
| **Leadlikeness** | No; 1 violation (MW<250) | No; 1 violation (MW < 250) |
| **Synthetic accessibility** | 3.29 | 3.27 |

### V.3.2 pkCSM ADME-T Analysis

#### V.3.2.1 Absorption

The absorption profiles of $HAP_1$ and $HAP_2$ are useful, showing only minor differences between them Table V.16. $HAP_2$ has significantly superior performance in Caco-2 permeability (0.799 log Papp for $HAP_2$ compared to 0.689 for HAP1), indicating a slightly enhanced passive permeability across intestinal epithelial cells. Similarly, the anticipated human intestinal absorption for $HAP_2$ is 59.74%, surpassing $HAP_1$'s 56.61%, with both values beyond 50%, suggesting moderate to good oral absorption capability. Both compounds are neither substrates nor inhibitors of P-glycoprotein (P-gp), hence decreasing the potential of bioavailability concerns linked to efflux. Skin permeability, denoted as log Kp, is comparably low for both compounds (–3.386 for $HAP_1$, –3.309 for $HAP_2$), signifying limited skin absorption capacity, which is characteristic and not concerning for orally delivered pharmaceuticals. Overall, $HAP_2$ exhibits a marginally superior absorption profile; nevertheless, the discrepancies are small, and both compounds appear good for oral administration.

**Table V. 16** Absorption Profile of $HAP_1$ and $HAP_2$ predicted by pkCSM

| Parameter | $HAP_1$ | $HAP_2$ |
|---|---|---|
| **Water solubility (log mol/L)** | -0.022 | -0.028 |
| **Caco-2 permeability (log Papp)** | 0.689 | 0.799 |
| **Human intestinal absorption (%)** | 56.609 | 59.741 |
| **Skin permeability (log Kp)** | -3.386 | -3.309 |
| **P-gp substrate** | No | No |
| **P-gp I inhibitor** | No | No |
| **P-gp II inhibitor** | No | No |

#### V.3.2.2 Distribution

The distribution-related characteristics of $HAP_1$ and $HAP_2$ are also comparable in Table V.17. The steady-state volume of distribution (VDss) is minimal for both compounds [31], with log VDss values of –0.525 ($HAP_1$) and –0.534 ($HAP_2$), indicating restricted dissemination beyond plasma. Both compounds exhibit a substantial anticipated fraction unbound in plasma (Fu) [32], with $HAP_1$ at 0.85 and $HAP_2$ at 0.805. Elevated unbound fractions signify that a significant proportion of the compounds remain free and pharmacologically active, which is often advantageous. The predictions for BBB permeability (log BB) are negative for both substances, with values of –1.343 for $HAP_1$ and –1.377 for $HAP_2$, signifying inadequate BBB penetration [33]. Similarly, both exhibit low

central nervous system (CNS) permeability (log PS approximately –4.3), indicating limited brain access [34]. This may be beneficial for preventing CNS-related adverse effects unless central activity is a therapeutic objective. Both compounds exhibit restricted tissue and CNS distribution while ensuring elevated free drug availability, hence promoting effective systemic activity.

**Table V. 17** Distribution Profile of $HAP_1$ and $HAP_2$ predicted by pkCSM

| Parameter | $HAP_1$ | $HAP_2$ |
|---|---|---|
| **VDss (human, log L/kg)** | -0.525 | -0.534 |
| **Fraction unbound (human, Fu)** | 0.85 | 0.805 |
| **BBB permeability (log BB)** | -1.343 | -1.377 |
| **CNS permeability (log PS)** | -4.348 | -4.332 |

### V.3.2.3 Metabolism

The metabolic profiles of both $HAP_1$ and $HAP_2$ are notably promising Table V.18. Neither chemical is anticipated to serve as a substrate for the principal cytochrome P450 enzymes CYP2D6 or CYP3A4, indicating they could avoid notable hepatic metabolism through these routes. In addition, neither compound inhibits any of the key CYP isoforms evaluated (CYP1A2, CYP2C19, CYP2C9, CYP2D6, or CYP3A4). This absence of inhibition suggests a little possibility for metabolic drug-drug interactions, an advantageous characteristic for lead compounds. The lack of CYP-mediated liabilities in both compounds accelerates pharmacokinetic forecasts and mitigates safety doubts in drug design. In this category, $HAP_1$ and $HAP_2$ exhibit equivalent performance.

**Table V. 18** Metabolism Profile of $HAP_1$ and $HAP_2$ predicted by pkCSM

| Parameter | $HAP_1$ | $HAP_2$ |
|---|---|---|
| **CYP2D6 substrate** | No | No |
| **CYP3A4 substrate** | No | No |
| **CYP1A2 inhibitor** | No | No |
| **CYP2C19 inhibitor** | No | No |
| **CYP2C9 inhibitor** | No | No |
| **CYP2D6 inhibitor** | No | No |
| **CYP3A4 inhibitor** | No | No |

### V.3.2.4 Excretion

In terms of clearance, both compounds show moderate predicted total clearance, with $HAP_2$ having a slightly higher log clearance value (0.922 mL/min/kg) compared to $HAP_1$ (0.832 mL/min/kg). While the difference is minor, it suggests $HAP_2$ might be eliminated slightly faster. Neither compound is predicted to be a substrate for the renal organic cation transporter 2 (OCT2), which rules out active renal secretion through this specific transporter. This is generally a neutral-to-positive trait, as OCT2 substrates can sometimes face renal drug-drug interaction issues. Both compounds exhibit acceptable excretion properties, with $HAP_2$ showing marginally faster clearance.

**Table V. 19** Excretion Profile of $HAP_1$ and $HAP_2$ predicted by pkCSM

| Parameter | $HAP_1$ | $HAP_2$ |
|---|---|---|
| **Total clearance (log mL/min/kg)** | 0.832 | 0.922 |
| **Renal OCT2 substrate** | No | No |

### V.3.2.5 Toxicity

The toxicity predictions from pkCSM are important for both $HAP_1$ and $HAP_2$. Neither chemical is indicated for AMES mutagenicity, showing a minimal genotoxic risk. The anticipated maximum tolerated human dose is somewhat greater for $HAP_1$ (log 1.797 mg/kg/day) compared to $HAP_2$ (log 1.677), suggesting a potentially higher therapeutic window. Neither chemical blocks the hERG I or II potassium channels, hence reducing the risk of cardiotoxicity, including QT interval lengthening. Both compounds are anticipated to be non-hepatotoxic and non-sensitizing to the skin, alleviating worries about organ-specific toxicity or allergic reactions. The acute oral toxicity ($LD_{50}$ in rats) is substantially the same (2.237 mol/kg for $HAP_1$ compared to 2.285 mol/kg for $HAP_2$), indicating comparable tolerance to acute exposure. Predictions of chronic toxicity (LOAEL) are likewise analogous: log 3.008 for $HAP_1$ and 2.872 for $HAP_2$. Environmental toxicity endpoints, such as Tetrahymena pyriformis and minnow toxicity, indicate marginally elevated toxicity for $HAP_1$ (more negative T. pyriformis log value and increased minnow log mM), however, both remain within permissible limits. Both compounds are anticipated to be non-toxic in critical categories, with $HAP_1$ potentially exhibiting a somewhat superior safety margin for chronic exposure and acceptable dosage.

**Table V. 20** Toxicity Profile of $HAP_1$ and $HAP_2$ Predicted by pkCSM

| Parameter | $HAP_1$ | $HAP_2$ |
|---|---|---|
| **AMES toxicity** | No | No |
| **Max. tolerated dose (log mg/kg/day)** | 1.797 | 1.677 |
| **hERG I inhibitor** | No | No |
| **hERG II inhibitor** | No | No |
| **Oral Rat Acute Toxicity (LD50, mol/kg)** | 2.237 | 2.285 |
| **Oral Rat Chronic Toxicity (LOAEL, log mg/kg)** | 3.008 | 2.872 |
| **Hepatotoxicity** | No | No |
| **Skin Sensitisation** | No | No |
| **T. Pyriformis toxicity (log µg/L)** | -0.092 | -0.205 |
| **Minnow toxicity (log mM)** | 3.078 | 2.745 |

### V.3.3 StopTox Toxicological Profile Analysis

The StopTox platform evaluated the toxicological risks of $HAP_1$ and $HAP_2$ using various critical endpoints pertinent to acute systemic and local toxicity Table V.21. The findings for both substances indicate a predominantly positive toxicity profile, with just little variations noted between them.

$HAP_1$ and $HAP_2$ are both predicted to be non-toxic for acute inhalation toxicity, with confidence levels of 71.0% and 70.0%, respectively. In the same way, predictions for acute oral toxicity indicate that both substances are non-toxic, each with a confidence level of 72.0%. These results are auspicious considering that oral delivery is a prevalent method in drug discovery, and non-toxic oral profiles minimize the possibility of dose-limiting systemic toxicity.

While acute dermal toxicity, $HAP_1$ is categorized as non-toxic with a confidence level of 55.0%, whilst $HAP_2$ is similarly anticipated to be non-toxic, with a marginally elevated confidence level of 57.0%. Even becoming considerably lower than the confidence scores for oral and inhalation routes, these scores remain within a range that substantiates a non-toxic skin profile for both substances.

The only significant issue pertains to eye irritation and corrosion. $HAP_1$ and $HAP_2$ are both anticipated to be toxic in this category, with confidence levels of 60.0% and 58.0%, respectively. This indicates that both chemicals may provide a risk of ocular irritation upon

direct exposure and necessitate meticulous management during formulation and packing, especially for topical or ophthalmic uses.

Concerning skin sensitization, both compounds are anticipated to be non-sensitizers, with $HAP_2$ exhibiting a reported confidence of 60%. This forecast indicates a minimal chance of allergic dermal reactions. Similarly, both compounds are anticipated to be non-irritating and non-corrosive to the skin, suggesting that neither is likely to inflict harm or irritation under standard exposure scenarios.

The StopTox findings for both $HAP_1$ and $HAP_2$ are predominantly positive, suggesting a low chance of acute toxicity from inhalation, oral, or dermal contact, along with a negligible risk of skin sensitization or irritation. The sole persistent toxicological indicator pertains to eye discomfort, common to both compounds, necessitating formulation techniques that reduce ocular exposure. No notable disparity in safety profile exists between $HAP_1$ and $HAP_2$, rendering both chemicals equally acceptable from a toxicological perspective according to StopTox predictions.

**Table V. 21** StopTox Toxicity Predictions Summary

| Toxicity Endpoint | $HAP_1$ | $HAP_2$ |
|---|---|---|
| **Acute Inhalation Toxicity** | Non-Toxic (–), 71.0% | Non-Toxic (–), 70.0% |
| **Acute Oral Toxicity** | Non-Toxic (–), 72.0% | Non-Toxic (–), 72.0% |
| **Acute Dermal Toxicity** | Non-Toxic (–), 55.0% | Non-Toxic (–), 57.0% |
| **Eye Irritation and Corrosion** | Toxic (+), 60.0% | Toxic (+), 58.0% |
| **Skin Sensitization** | Non-Sensitizer (–) | Non-Sensitizer (–), 60% |
| **Skin Irritation and Corrosion** | Negative (–) | Negative (–), 60% |

### V.3.4 ProTox Toxicological Profile Analysis

The ProTox-3.0 predictions for $HAP_1$ and $HAP_2$ indicate in general similar toxicity profiles, with both compounds exhibiting low to moderate risk across the majority of assessed endpoints. Both are classified under Toxicity Class 5, indicating they "may be harmful if swallowed" according to the globally harmonized system (GHS) classification [35]. This classification, along with predicted $LD_{50}$ values of 2800 mg/kg for $HAP_1$ and 3000 mg/kg for $HAP_2$, suggests that both compounds exhibit relatively low acute oral toxicity and are deemed safe at therapeutic levels with a wide safety margin.

Both compounds are anticipated to exhibit non-hepatotoxic and non-neurotoxic properties across organ-specific toxicities, with a high confidence level (>0.85), which is

favorable considering the critical role of liver and CNS safety in drug discovery. Both compounds are anticipated to exhibit nephrotoxicity and respiratory toxicity, with $HAP_1$ demonstrating marginally greater confidence for nephrotoxicity (0.73 compared to 0.69) and $HAP_2$ exhibiting slightly elevated confidence for respiratory toxicity (0.79 compared to 0.78). These organ-specific projections indicate a potential risk that necessitates further examination, especially in renal and pulmonary safety pharmacology studies.

Regarding general toxicity endpoints, both compounds are anticipated to be non-carcinogenic, non-mutagenic, non-cytotoxic, and non-immunotoxic, with a high confidence level for immunotoxicity (0.99). The lack of mutagenic or carcinogenic potential is notably encouraging and reinforces their appropriateness as drug-like options. Forecasts also indicated the absence of BBB barrier breach, consistent with prior pharmacokinetic findings indicating restricted CNS entry. Moreover, neither substance presents ecotoxicological concerns nor dangers of nutritional toxicity.

In conclusion, $HAP_1$ and $HAP_2$ demonstrate acceptable ProTox toxicity profiles, with primary concerns being possible nephrotoxicity and respiratory toxicity. The anticipated concerns are comparable and equally prioritized for both compounds, necessitating validation by in vitro and in vivo safety assessments. The analogous $LD_{50}$ values and toxicity classification further substantiate that both compounds fall within a safe oral dose range, reinforcing their potential as suitable candidates for continued therapeutic development.

## V.4 Conclusion

The combined molecular docking and ADME-T evaluation of $HAP_1$ and $HAP_2$ confirm their future potential as drug-like candidates to target oxidative stress-related enzymes. Of the enzymes analyzed, lipoxygenase (1N8Q) proved to be the most promising target, with $HAP_1$ demonstrating a superior binding affinity and more stabilizing interactions compared to $HAP_2$, especially in its deprotonated microspecies at physiological pH.

ADME predictions indicated that both drugs have high water solubility, favorable gastrointestinal absorption, and limited interaction with metabolic enzymes or P-glycoprotein. However, both compounds conformed to important drug-likeness factors, and minor infractions related to low molecular weight or polarity were noted. Nevertheless, they showed satisfactory bioavailability ratings and advantageous synthetic accessibility.

Toxicity evaluations conducted with pkCSM, StopTox, and ProTox indicated little acute and chronic toxicity, absence of hepatotoxicity, and no mutagenic or cardiotoxic effects, with both chemicals categorized within toxicity class 5. The sole persistent caution was the possibility of ocular irritation and organ-specific issues associated with nephrotoxicity and respiratory toxicity.

In conclusion, $HAP_1$ emerges as the more promising candidate, exhibiting enhanced binding affinity, wider polar contacts, and a somewhat superior safety profile. $HAP_2$ continues to serve as a promising scaffold with favorable ADMET properties and may be enhanced for greater efficacy. These findings advocate for additional investigation of α-aminophosphonic acids as therapeutic agents for illnesses associated with oxidative stress.

VI

# Biological Activities

# VI Biological Activities

## VI.1 INTRODUCTION

This chapter analyzes the two synthesized α-amino phosphonic acids, $HAP_1$ and $HAP_2$, and thoroughly evaluates their antioxidant properties using different in vitro experiments. We have utilized four famous and widely acknowledged methodologies: DPPH, ABTS, FRAP, and phenanthroline [1-4], to evaluate the free radical scavenging and reduction capabilities of these compounds. Each assay offers unique insights into the behavior of $HAP_1$ and $HAP_2$ under varying oxidative conditions.

Utilizing these complementary assays, we achieve a comprehensive evaluation of the antioxidant capacity of $HAP_1$ and $HAP_2$. This multi-method approach guarantees the observation of the different strengths and mechanistic characteristics of each chemical, providing important insights into their potential as therapeutic or protective agents against oxidative stress.

The following part of this chapter examines the synergistic effects of $HAP_1$ and $HAP_2$. A review of synergy is predicated on the observation that specific bioactive substances, when combined, may demonstrate an antioxidant capability that is above the sum of their individual effects. This phenomenon, known as synergy [5], is very important in drug design and pharmaceutical development [6-7], as it enables reduced effective dosages and diminished negative effects. We employed a combinatorial matrix technique [8] and the Synergy Finder tool [9-10] to systematically assess the synergy between $HAP_1$ and $HAP_2$ in DPPH and ABTS tests. We seek to assess the combined scavenging activity of these α-amino phosphonic acids to ascertain their potency when administered jointly and to identify the best ratios for maximal antioxidant protection.

The findings in this chapter enhance the existing information regarding the biological significance of α-amino phosphonic acids and suggest possibilities for their therapeutic application. Comprehending the antioxidant characteristics and synergistic effects of innovative phosphonates $HAP_1$ and $HAP_2$ is essential for enhancing their efficacy against oxidative stress.

## VI.2 Antioxidant Activity Using Multiple Assays

### VI.2.1 Analysis of DPPH Assays

Table VI.1 presents the DPPH $IC_{50}$ values for the evaluated antioxidants. $HAP_1$ and $HAP_2$ had remarkably low $IC_{50}$ values (5.01 ± 0.36 µg/mL and 4.86 ± 0.40 µg/mL, respectively), signifying superior efficacy in free-radical scavenging relative to the conventional antioxidants BHT (10.57 ± 0.22 µg/mL) and BHA (13.23 ± 0.56 µg/mL).

**Table VI. 1** DPPH $IC_{50}$ Values of Antioxidant Compounds

| **Compound** | **DPPH $IC_{50}$ (*µg/mL*)** |
|---|---|
| **$HAP_1$** | 5.01±0.36 |
| **$HAP_2$** | 4.86±0.40 |
| **BHT** | 10.57±0.22 |
| **BHA** | 13.23±0.56 |

Figure VI.1 demonstrates that the percentage inhibition of DPPH escalates with concentration for all drugs; yet, $HAP_1$ and $HAP_2$ attain the 50% inhibition benchmark at markedly lower concentrations, highlighting their enhanced efficacy. The dose-response curves indicate that although BHT and BHA ultimately reach comparable maximal inhibition, they necessitate significantly greater dosages, aligning with their elevated $IC_{50}$ values.

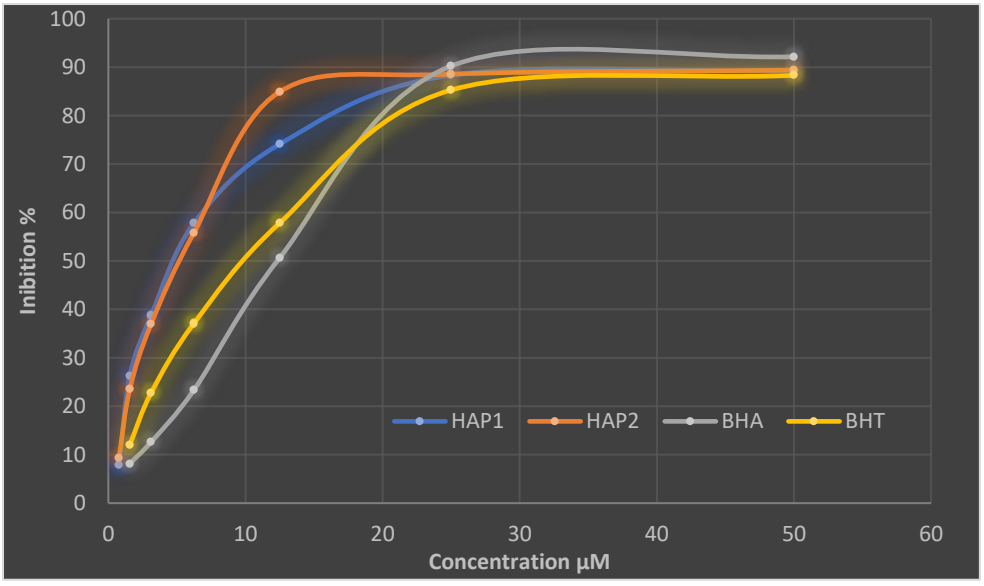


**Figure VI. 1** DPPH Antioxidant activity of selected single antioxidant compounds ($HAP_1$, $HAP_2$, BAH, and BHT in methanol 100 %) (n = 3).

### VI.2.1.1 Dose-Response Patterns

Low doses: At around 0.8–1.6 µg/mL, all drugs showed little inhibition (8–12%). At around 3 µg/mL, HAP1 and HAP2 achieve an inhibition rate of approximately 37–39%, but BHT and BHA maintain an inhibition rate of only 12–23% even at 6 µg/mL. This indicates that HAP1 and HAP2 are efficacious at reduced dosages [11].

50% Inhibition ($IC_{50}$ Range): HAP1 and HAP2 attain approximately 50% inhibition at concentrations of 5–6 µg/mL, aligning with their $IC_{50}$ of approximately 5 µg/mL. BHT and BHA achieve approximately 50–60% inhibition at around 12.5 µg/mL, indicative of their elevated $IC_{50}$ values (approximately 10–13 µg/mL).

High Doses: HAP1 and HAP2 plateau at ~88–89% inhibition by 25 µg/mL, whereas BHT and BHA require higher concentrations (up to 100 µg/mL) to approach similar levels. Thus, HAP compounds achieve maximal antioxidant effects with much less material.

### VI.2.1.2 $IC_{50}$ Values and Antioxidant Potency

The $IC_{50}$ indicates the amount of antioxidant needed to neutralize 50% of DPPH radicals; a lower $IC_{50}$ means a stronger antioxidant.

$HAP_2$ and $HAP_1$ have very low $IC_{50}$ values (4.86 ± 0.40 and 5.01 ± 0.36 µg/mL, respectively). Their dose-response curves show that even at ~5 µg/mL, they achieve about 50% inhibition, with higher doses quickly pushing inhibition toward 80–90%. These values fall well below the 50 µg/mL threshold that distinguishes “powerful” antioxidants, highlighting their high potency.

BHT has an $IC_{50}$ of 10.57 ± 0.22 µg/mL, roughly double that of $HAP_{1/2}$. Its % inhibition rises more slowly, requiring 10–15 µg/mL to pass 50% inhibition and up to 100 µg/mL to reach nearly maximum effect.

BHA is the least potent, with an $IC_{50}$ of 13.23 ± 0.56 µg/mL. Its curve indicates that significant inhibition (around 50%) is only achieved at approximately 12.5 µg/mL, and it takes 25 µg/mL to approach ~90% inhibition.

### VI.2.1.3 Comparative Antioxidant Performance

$HAP_1$ and $HAP_2$: Both novel compounds exhibit outstanding potency. They achieve significant DPPH inhibition at low doses and nearly max out (≈88–89% inhibition) by 25–

50 µg/mL. Their very low $IC_{50}$ values (~5 µg/mL) place them among the most potent antioxidants. Although $HAP_2$ is marginally more potent than $HAP_1$ (e.g., reaching ~85% inhibition at 12.5 µg/mL versus ~74% for $HAP_1$), they are essentially equivalent within experimental error. Overall, they outperform the standards on a per-dose basis.

BHT displays strong, dose-dependent antioxidant activity with an $IC_{50}$ of approximately 10.6 µg/mL—about double that of $HAP_1$/$HAP_2$. It requires a higher dose to reach 50% inhibition, and by 25 µg/mL, it approaches ~85% inhibition, eventually maxing out near 90% at 50–100 µg/mL. Although effective, its potency is notably lower compared to $HAP_1$/$HAP_2$.

BHA is the least potent of the four, with an $IC_{50}$ of ~13.2 µg/mL. Its % inhibition increases more slowly, reaching ~50% inhibition only at about 12.5 µg/mL. Even though it can eventually achieve ~92–93% inhibition at higher doses (50–100 µg/mL), BHA requires significantly more compound to achieve similar effects to the other antioxidants.

In summary, the data confirm that $HAP_1$ and $HAP_2$ are the most efficient DPPH scavengers, requiring lower concentrations to achieve similar or superior inhibition compared to the standards. The overall ranking of antioxidant strength is:

$$HAP_2 \approx HAP_1 > BHT > BHA$$

This means that for equivalent radical neutralization, the HAP compounds need roughly half the dose of BHT and significantly less than BHA, underscoring their superior free-radical scavenging capability.

### VI.2.2 ABTS Radical Scavenging Activity

Table VI.2 summarizes the ABTS $IC_{50}$ values for the tested antioxidants. Notably, $HAP_1$ exhibited an exceptionally low $IC_{50}$ (2.78 ± 0.02 µg/mL), indicating very high potency in scavenging ABTS radicals. In contrast, $HAP_2$ required a higher concentration (8.44 ± 0.09 µg/mL) to achieve 50% inhibition. The standard antioxidants BHT (10.83 ± 0.06 µg/mL) and BHA (13.62 ± 0.20 µg/mL) showed even higher $IC_{50}$ values, which suggests that they are less efficient than the novel compounds.

**Table VI. 2** ABTS $IC_{50}$ Values of Antioxidant Compounds

| Compound | ABTS $IC_{50}$ (µg/mL) ± SD |
|---|---|
| **$HAP_1$** | 2.78 ± 0.02 |
| **$HAP_2$** | 8.44 ± 0.09 |
| **BHT** | 10.83 ± 0.06 |
| **BHA** | 13.62 ± 0.20 |

As illustrated in Figure VI.2, the % inhibition of ABTS increases with concentration for all compounds; however, $HAP_1$ reaches the 50% inhibition threshold at significantly lower doses, underscoring its superior efficacy. The dose-response curves further indicate that although $HAP_2$, BHT, and BHA eventually achieve high levels of inhibition, they require markedly higher concentrations compared to $HAP_1$.

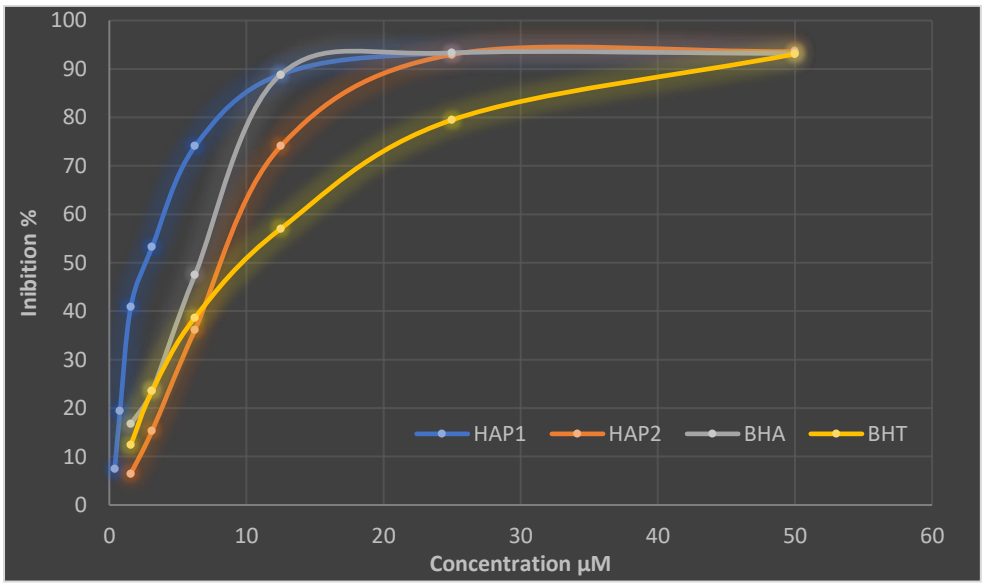


**Figure VI. 2** ABTS Antioxidant activity of selected single antioxidant compounds ($HAP_1$, $HAP_2$, BAH, and BHT in methanol 100 %) (n = 3).

### VI.2.2.1 ABTS Dose-Response Analysis

With an $IC_{50}$ of 2.78 µg/mL, $HAP_1$ demonstrates exceptional ABTS radical scavenging activity. Its steep dose-response curve shows that even at very low concentrations, $HAP_1$ rapidly reduces ABTS^•+ radicals. This indicates that $HAP_1$ is highly effective at neutralizing radicals in both hydrophilic and lipophilic environments, and $HAP_2$ has an $IC_{50}$ of 8.44 µg/mL, indicating good antioxidant potency but lower than $HAP_1$.

Although HAP2 still exhibits a concentration-dependent increase in % inhibition, it requires roughly three times the concentration of $HAP_1$ to achieve 50% inhibition.

BHT and BHA show higher $IC_{50}$ values (10.83 and 13.62 µg/mL, respectively), meaning they are less potent than $HAP_1$ and $HAP_2$ in the ABTS assay. BHT is moderately potent, whereas BHA requires the highest concentration to reach the same level of ABTS scavenging, aligning with its profile from the DPPH assay.

### VI.2.2.2 Comparative Antioxidant Performance (ABTS)

The ABTS assay demonstrates that $HAP_1$ is the most effective antioxidant among the evaluated chemicals in the ABTS system, exhibiting the lowest $IC_{50}$ of 2.78 µg/mL. $HAP_2$, although effective, exhibits lower potency than HAP1, with an $IC_{50}$ of 8.44 µg/mL. The standard antioxidants BHT and BHA exhibit markedly reduced efficacy in this assay, with $IC_{50}$ values of 10.83 µg/mL and 13.62 µg/mL, respectively. Consequently, in the comparison of both DPPH and ABTS assays, $HAP_1$ consistently demonstrates enhanced free radical scavenging capacity. The reduced $IC_{50}$ values for $HAP_1$ in both systems underscore its potential as a potent antioxidant. $HAP_2$ has remarkable potency, albeit with more variability in performance across the two experiments.

### VI.2.3 Phenanthroline Assay

In the phenanthroline assay data for $HAP_1$, $HAP_2$, BHA, and BHT, we determined the A50 for each molecule. $A_{50}$ is the concentration necessary to achieve 50% of the compound's maximum absorbance [12], comparable to an $IC_{50}$ in inhibition experiments. A reduced half-maximal concentration signifies enhanced potency in antioxidant activity, indicating a more robust chelating or lowering action. BHA and BHT are recognized synthetic antioxidants commonly utilized as reference standards in these experiments; hence, evaluating the novel compounds ($HAP_1$ and $HAP_2$) against them underscores their relative efficacy. The table below encapsulates the $A_{50}$ values acquired for each compound:

**Table VI. 3** $A_{50}$ Values of Antioxidant Compounds in the Phenanthroline Assay

| | Absorbances in the phenanthroline assay | | | | | | | |
|---|---|---|---|---|---|---|---|---|
| | 0.78µg | 1.56µg | 3.125 µg | 6.25 µg | 12.5 µg | 25 µg | 50 µg | $A_{0.5}$ µg/mL |
| **HAP1** | 0.50±0 .01 | 0.61±0 .02 | 0.90±0 .04 | 1.30±0 .08 | 2.17±0 .13 | 3.21±0 .07 | 3.68±0 .08 | 0.38±0, 01 |
| **HAP2** | 0.46±0 .02 | 0.53±0 .02 | 0.68±0 .01 | 0.99±0 .03 | 1.47±0 .02 | 2.57±0 .10 | 3.57±0 .12 | 0.40±0, 02 |
| **BHA** | 0,49±0 ,01 | 0,59±0 ,01 | 0,73±0 ,02 | 0,93±0 ,01 | 1,25±0 ,04 | 2,10±0 ,05 | 4,89±0 ,06 | 0,93±0, 07 |
| **BHT** | 0,47±0 ,01 | 0,47±0 ,01 | 0,53±0 ,03 | 1,23±0 ,02 | 1,84±0 ,01 | 3,48±0 ,03 | 4,84±0 ,01 | 2,24±0, 17 |

### VI.2.3.1 Dose-Response Curves and Comparative Effectiveness

All four compounds show a dose-dependent increase in absorbance, confirming their antioxidant/chelating activity, but the shapes of the curves differ significantly (Fig. VI.3):

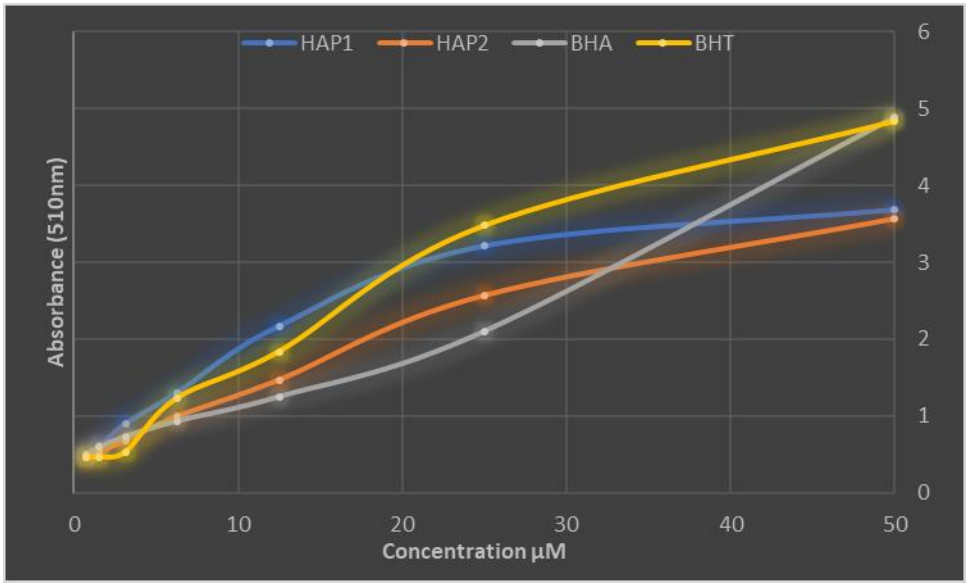


**Figure VI. 3** Absorbance vs. concentration dose-response curves for $HAP_1$, $HAP_2$, BHA, and BHT in the phenanthroline assay.

$HAP_1$ and $HAP_2$. These compounds demonstrate a rapid rise in absorbance even at the lowest doses. By around 6–12 µg/mL, they are already near the upper portion of their curve. $HAP_1$'s absorbance climbs from ~0.5 at 0.78 µg/mL to ~2.2 at 12.5 µg/mL, eventually reaching ~3.7 at 50 µg/mL. $HAP_2$ follows a similar pattern (0.46 at 0.78 µg/mL to ~3.6 at 50 µg/mL). The curve for each compound starts high and tapers off, indicating an early saturation of effect. This means small doses of $HAP_{1/2}$ are very effective, and increasing the dose beyond a certain point yields diminishing returns (a plateau as the maximum

chelation/reduction is approached). $HAP_1$ and $HAP_2$ achieve 50% of their maximal absorbance at well below 1 µg/mL, reflecting their high potency.

The BHA curve shows a more gradual increase at low–mid concentrations, then a dramatic jump at the highest dose. For instance, BHA's absorbance rises modestly from ~0.49 at 0.78 µg/mL to ~1.25 at 12.5 µg/mL, then increases to 2.10 at 25 µg/mL and surges up to ~4.89 at 50 µg/mL. This suggests that BHA requires a higher concentration to unlock its full antioxidant effect; the dose-response is somewhat delayed, with a steep phase occurring later (between 25 and 50 µg/mL). BHA's $A_{50}$ (~0.93 µg/mL) is higher than that of $HAP_{1/2}$, indicating lower potency than these compounds, but once at sufficiently high concentration, BHA is capable of achieving a high absorbance (in fact slightly exceeding the maximal absorbance reached by $HAP_{1/2}$). This high maximum absorbance for BHA at 50 µg/mL implies that BHA can ultimately reduce or chelate a large amount of iron (strong total effect), but it needs a larger dose to reach that level.

BHT is the slowest to take off. Notably, between 0.78 and 1.56 µg/mL, BHT's absorbance remains nearly unchanged (~0.47), indicating a minimal effect at very low doses (a lag phase). Only after about 3–6 µg/mL does the absorbance start to climb substantially (1.23 at 6.25 µg/mL, 1.84 at 12.5 µg/mL). By 25 µg/mL, BHT reaches ~3.48, and at 50 µg/mL, it reaches ~4.84. The curve is shifted furthest to the right, consistent with BHT's high $A_{50}$ (≈2.24 µg/mL) – it is the least potent of the four. BHT requires significantly higher concentrations to achieve the same fraction of effect that $HAP_1$, $HAP_2$, or even BHA achieve at lower doses. Like BHA, at sufficiently high concentration, BHT can produce a large absorbance (indicating a strong overall antioxidant effect when enough is used), nearly matching BHA's absorbance at 50 µg/mL. However, its slow start means half of its max effect comes much later (at a higher dose).

In summary, $HAP_1$ and $HAP_2$ are the most effective antioxidants of the group on a per concentration basis, as evidenced by their low $A_{50}$ values and steep early dose-response. BHA is somewhat less potent but can achieve a high maximum effect at sufficient dosage, and BHT is the least effective, with the highest $A_{50}$ and a delayed dose-response. The lower the $A_{50}$, the stronger the antioxidant potency, so these results indicate that $HAP_1 \approx$ , $HAP_2 >$ BHA > BHT in terms of iron-chelating antioxidant strength. Such insights are important for comparing antioxidant compounds: a compound that acts at a lower concentration is

considered more powerful or efficient as an antioxidant, which in this case positions these compounds as promising strong antioxidants relative to the classic standards BHA and BHT.

### VI.2.4 FRAP Assay

#### VI.2.4.1 Antioxidant Potency

The A0.5 value is the concentration required to reach 50% of a compound's maximal FRAP absorbance (half of its maximum reducing effect). A lower A0.5 indicates higher potency, meaning the compound achieves half of its total reducing power at a lower dose [13]. The table below summarizes the maximum absorbance observed (at 50 µg/mL) and the calculated A0.5 for each compound:

**Table VI. 4** $A_{0.5}$ Values of Antioxidant Compounds in the FRAP Assay

| | Absorbances in FRAP assay | | | | | | | |
|---|---|---|---|---|---|---|---|---|
| | 0.78µg | 1.5625 | 3.12 µg | 6.25 µg | 12.5 µg | 25 µg | 50 µg | $A_{0.5\ µg/mL}$ |
| **HAP1** | 0.19±0.03 | 0.28±0.02 | 0.45±0.03 | 0.56±0.03 | 0.82±0.01 | 0.92±0.02 | 1.11±0.08 | 4.55±0.22 |
| **HAP2** | 0.12±0.02 | 0.21±0.02 | 0.28±0.03 | 0.36±0.01 | 0.66±0.02 | 0.95±0.04 | 1.24±0.03 | 8.97±0.36 |
| **Asc Acid** | 0.09±0.02 | 0.11±0.01 | 0.16±0.01 | 0.33±0.04 | 0.76±0.16 | 2.02±0.23 | 3.87±0.27 | 9.01±1.46 |

#### VI.2.4.2 Dose-Response

All three compounds exhibit increasing FRAP absorbance with concentration, indicating greater ferric reducing power at higher doses. Notable trends from Fig. VI.4:

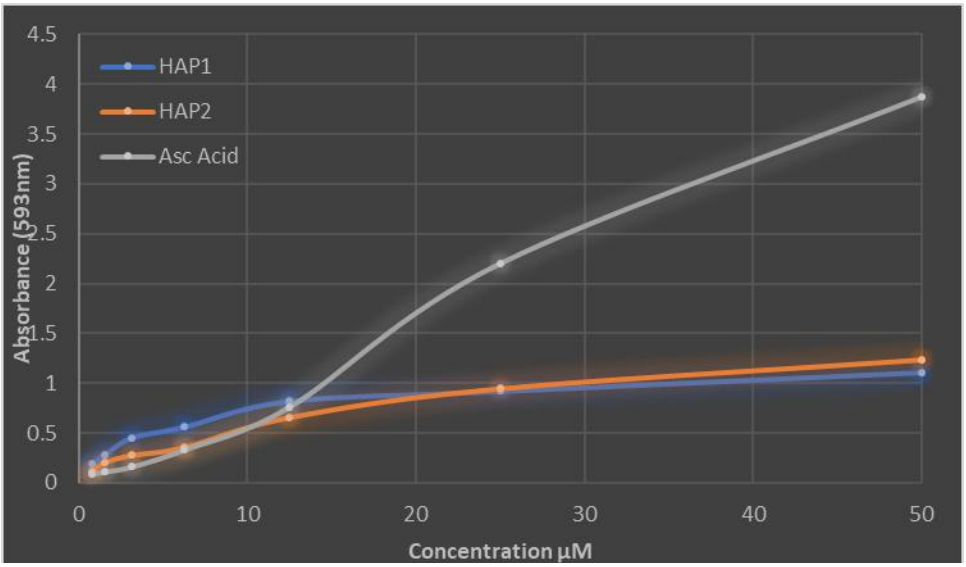


**Figure VI. 4** FRAP dose-response curves for $HAP_1$, $HAP_2$, and ascorbic acid (absorbance at 593 nm vs. concentration)

$HAP_1$ rises quickly at low concentrations and begins to plateau, reaching an absorbance of ~1.11 by 50 µg/mL (indicating a limited maximum reducing capacity). HAP2 shows a steadier increase, reaching ~1.24 at 50 µg/mL—slightly higher maximum absorbance than $HAP_1$. Finely Ascorbic Acid starts with a slower increase but then climbs sharply at higher doses, attaining ~3.87 absorbance at 50 µg/mL, by far the highest reducing capacity among the three.

In summary, $HAP_1$ is the strongest antioxidant on a per-concentration basis (needing the smallest dose for a significant effect), while ascorbic acid has the greatest overall reducing power at high concentration (reaching the highest absorbance). A compound with a lower A0.5 is considered a more potent antioxidant because it achieves 50% of its maximal activity at a lower dose.

## VI.3 Synergy Analysis of Antioxidant Combinations

### VI.3.1 Comparison of Synergy in DPPH and ABTS Assays

The combination studies in the DPPH and ABTS radical scavenging assays produced similar results. In the DPPH assay, the $HAP_1$ and $HAP_2$ combination demonstrated positive synergy scores in all models (ZIP, HSA, Loewe, Bliss), Fig. VI.6, signifying a synergistic interaction. The BHA and BHT combination had negative synergy scores, indicating antagonism Fig.VI.5. The ABTS assay confirmed the same trend: $HAP_1$ and $HAP_2$ showed synergy (Fig. VI.9), while BHA and BHT showed antagonism Fig.VI.9. The extent of the synergy varied among experiments. The DPPH test demonstrated more significant effects; for instance, the average ZIP synergy score for $HAP_1$ and $HAP_2$ was around 9.4 in DPPH compared to about 5.9 in ABTS, while for BHA and BHT, it was -36.7 in DPPH vs -20.4 in ABTS. However, with differences in quantity, both assays concur on the interaction direction (synergy or antagonism), indicating that the results are adaptable to the method of measuring antioxidant activity. This consistency suggests that the identified drug interactions are true and not an effect of a specific assay method. Minor variations in synergy magnitude may result from variances in test sensitivity or radical species. Nevertheless, both methodologies provide a consistent understanding of the interactions between these antioxidant pairs.

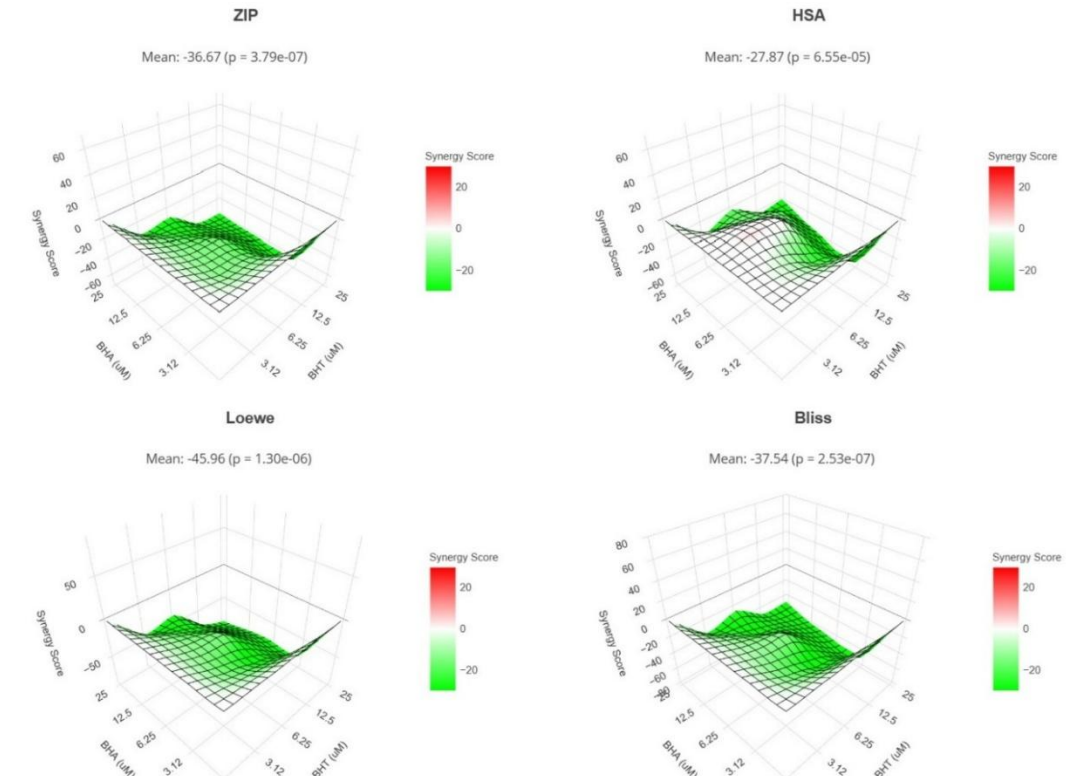


**Figure VI. 5** DPPH Antioxidant activity synergy scores models of selected single antioxidant compounds (BHA,BHT) by Synergie Finder

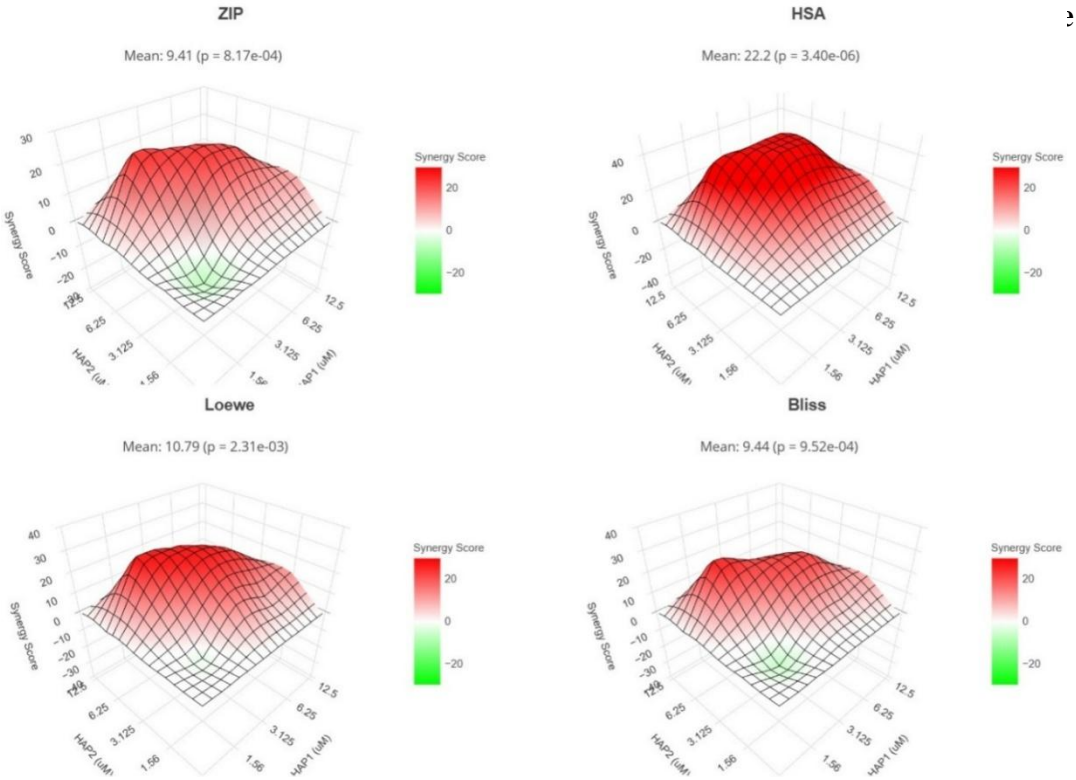


**Figure VI. 6** DPPH Antioxidant activity synergy scores models of selected single antioxidant compounds ($HAP_1$, $HAP_2$) by Synergie Finder

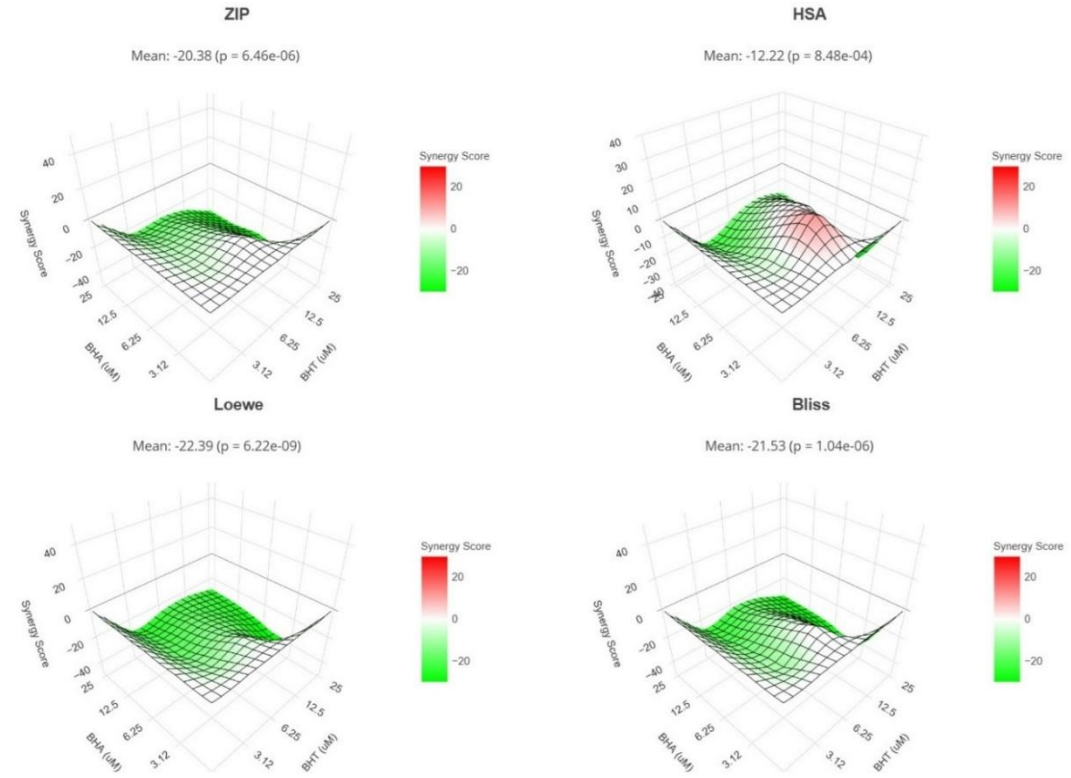


**Figure VI. 8** ABTS Antioxidant activity synergy scores models of selected single antioxidant compounds (BHA, BHT) by Synergie Finder

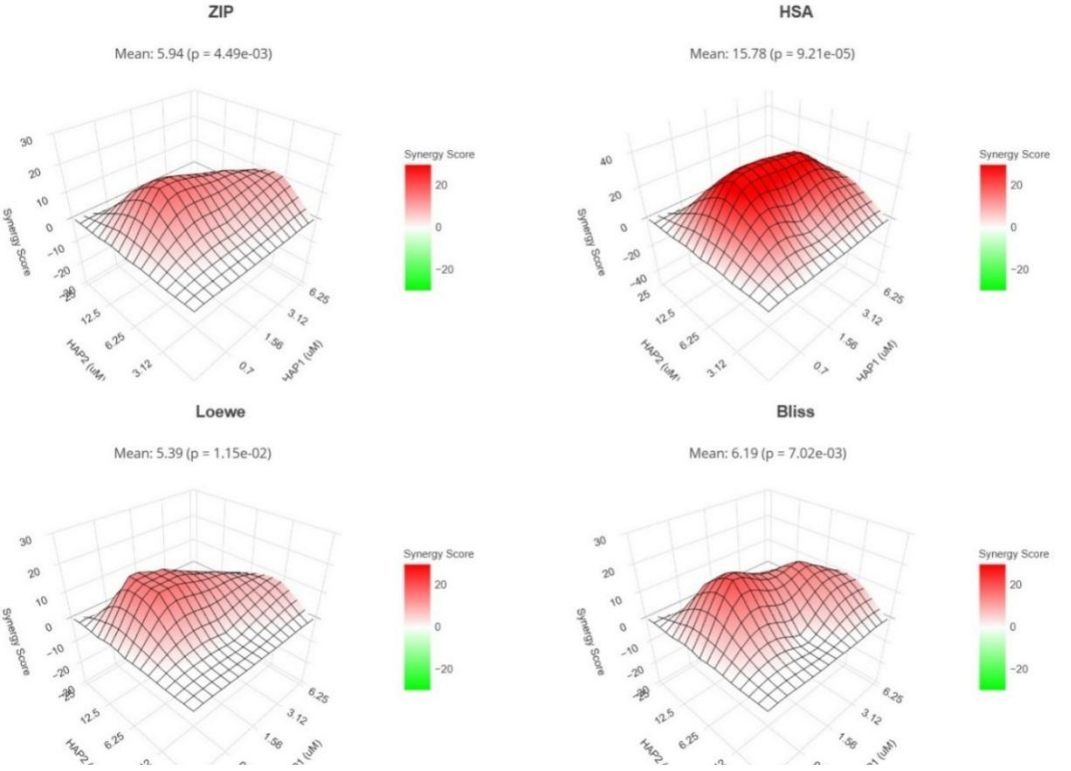


**Figure VI. 7** ABTS Antioxidant activity synergy scores models of selected single antioxidant compounds ($HAP_1$,$HAP_2$) by Synergie Finder

### VI.3.2 Interaction Effects: Synergy vs. Antagonism for Each Combination

The two synthesized α-aminophosphonic acids, $HAP_1$ and $HAP_2$, showed synergistic interactions in both tests. All four synergy models showed positive scores, with many exceeding the typical limit of 10, which indicates probable synergy [14-15]. In the DPPH assay, $HAP_1$ and $HAP_2$ exhibited a ZIP synergy score of approximately 9.4 and an HSA synergy score of approximately 22.2 (Table VI.5). The Bliss independence and Loewe additivity models showed comparable positive ratings of approximately 9.4 and 10.8, respectively. In the ABTS assay, the synergy was significantly reduced; however, still apparent: ZIP approximately 5.9, HSA about 15.8, Bliss approximately 6.2, and Loewe approximately 5.4. All these values are positive, signifying that the combination's effect surpassed the expected additive effect of the two antioxidants. Although several scores (for example, approximately 5–9) fall within a moderate range, the HSA model, specifically, demonstrated strong synergy (15 to 22). All models indicated that $HAP_1$ and $HAP_2$ have a synergistic interaction, since none presented a negative or near-zero score, therefore confirming the stability of this synergy independent of the model employed. This indicates that $HAP_1$ and $HAP_2$ directly augment each other's radical-scavenging activity, resulting in a larger suppression of DPPH/ABTS radicals collectively than anticipated from their actions.

**Table VI. 5** Synergy Scores for HAP1 and HAP2 Combination (α-amino phosphonic acids) in DPPH and ABTS assays.

| **Model** | **DPPH: HAP1, HAP2 (Synergy Score, p)** | **ABTS: HAP1, HAP2 (Synergy Score, p)** |
|---|---|---|
| **ZIP (Zero Interaction Potency)** | 9.41 ($p = 8.17\times10^{-4}$) | 5.94 ($p = 4.49\times10^{-3}$) |
| **HSA (Highest Single Agent)** | 22.20 ($p = 3.0\times10^{-6}$) | 15.78 ($p = 9.2\times10^{-5}$) |
| **Loewe Additivity** | 10.79 ($p = 2.31\times10^{-3}$) | 5.39 ($p = 1.15\times10^{-2}$) |
| **Bliss Independence** | 9.44 ($p = 9.52\times10^{-4}$) | 6.19 ($p = 7.02\times10^{-3}$) |
| **Interpretation** | Synergistic | Synergistic |

Values are the synergy scores calculated by the synergy finder of four reference models, with p-values in parentheses indicating the significance of deviation from additivity. Positive scores for synergy and negative scores denote antagonism. All p-values are <0.01, confirming statistically significant synergy in both assays.

The interaction between BHA and BHT was antagonistic in both experiments. Each model showed an extensive negative synergy score (Table VI.6), much beneath the -10 threshold indicative of probable antagonism [16]. For DPPH, the ZIP score was around -36.7, and the Loewe synergy was much lower (~46), showing that the combination's effect was significantly less than additive. The Bliss and HSA ratings, around -37.5 and -27.9, respectively, were very low. In the ABTS assay, the antagonism of BHA and BHT continued, but to a lesser degree (ZIP ~-20.4, Loewe ~-22.4, Bliss ~-21.5, HSA ~12.2). The negative values indicate that the two antioxidants block each other's efficacy, resulting in a mixture that scavenges fewer radicals than the sum of their activities would suggest. All four models agreed on antagonism (no positive scores), signifying a distinct hostile interaction.

Consequently, BHA and BHT are ineffective in combination under these conditions; rather than enhancing each other's efficacy, one drug likely diminishes the radical-scavenging capacity of the other, presumably through competitive or quenching interactions. The persistent antagonism noted in both DPPH and ABTS assays indicates that the impact is not specific to a single assay. The consensus among models and tests indicates a high level of confidence that BHA and BHT constitute a genuinely antagonistic duo.

**Table VI. 6** Synergy Scores for BHA and BHT Combination in DPPH and ABTS Assays

| **Model** | **DPPH: BHA, BHT (Synergy Score, p)** | **ABTS: BHA, BHT (Synergy Score, p)** |
|---|---|---|
| **ZIP** | -36.67 ($p = 3.79\times10^{-7}$) | -20.38 ($p = 6.46\times10^{-6}$) |
| **HSA** | -27.87 ($p = 6.6\times10^{-5}$) | -12.22 ($p = 8.48\times10^{-4}$) |
| **Loewe Additivity** | -45.96 ($p = 1.30\times10^{-6}$) | -22.39 ($p = 6.22\times10^{-9}$) |
| **Bliss Independence** | -37.54 ($p = 2.53\times10^{-7}$) | -21.53 ($p = 1.04\times10^{-6}$) |
| **Interpretation** | Antagonistic | Antagonistic |

Negative values in all models indicate antagonism. All interactions are statistically significant ($p < 0.001$), confirming true antagonistic effects.

### VI.3.3 Dose-Dependence of Synergy Effects

The type of synergy or antagonism was dependent on the dose, varying across the concentration matrix for every compound combination. The analysis of the synergy score heatmaps (2D synergy heatmaps) identifies particular areas where the interaction is strong.

In the $HAP_1$ and $HAP_2$ combination, synergy reached its peak at moderate

concentrations of both drugs. In the DPPH experiment, dosages of approximately 1.6–6.3 µM of $HAP_1$ coupled with about 3–6 µM of $HAP_2$ produced the highest synergy scores (ZIP synergy around 20–24 and HSA synergy reaching almost 42% beyond expectation at these levels) Fig.VI.9. At those mid-range concentrations, the synergistic scavenging action was practically total (about 90–94% inhibition of DPPH), while each compound yielded only mild inhibition. This signifies an optimal point where both components synergistically boost the reaction towards near saturation, above additive predictions. Notably, at elevated doses of $HAP_1$ and $HAP_2$, the synergy decreased; the efficacy reached a plateau, and the observed effect approximated the predictions of additivity. At the highest doses (e.g., 12.5 µM of each), the synergy scores approached zero or became slightly negative in certain models, indicating no additional benefit, since the combination only maximized the assay result. This pattern synergy peaking at mid-range and then declining at the plateau is prevalent in combination dose-response landscapes. Once each drug alone approaches its maximal effect, there is a diminished capacity for additional interaction effects.

In the ABTS assay, doses between 0.7 and 6.25 µM of $HAP_1$ combined with 6 µM of $HAP_2$ produced the highest synergy scores (ZIP synergy approximately 16–19 and HSA synergy reaching around 35% beyond expectation at these doses). Fig.VI.10.

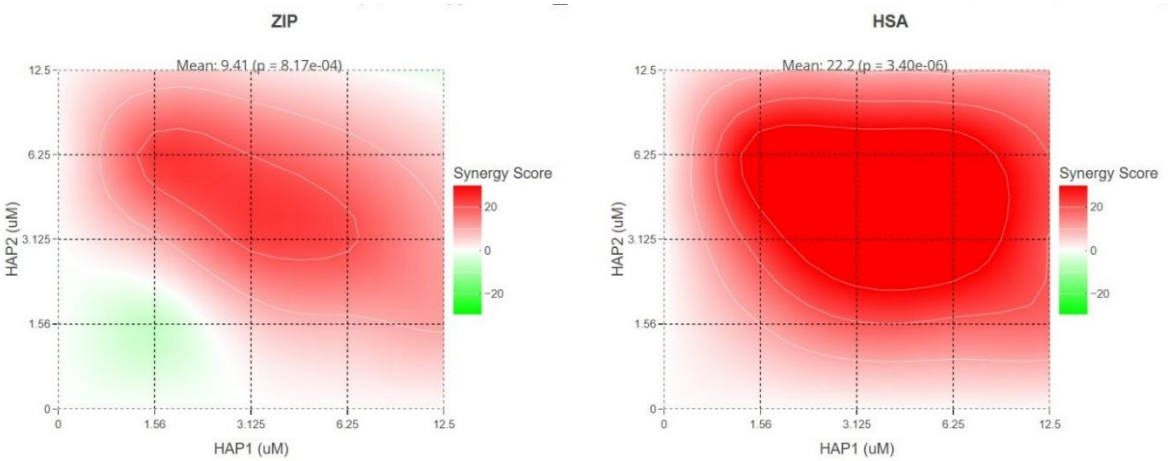


**Figure VI. 9** 2D synergy heatmaps of DPPH antioxidant assay combination $HAP_1$ and $HAP_2$ using ZIP and HAS model generated by SynergyFinder

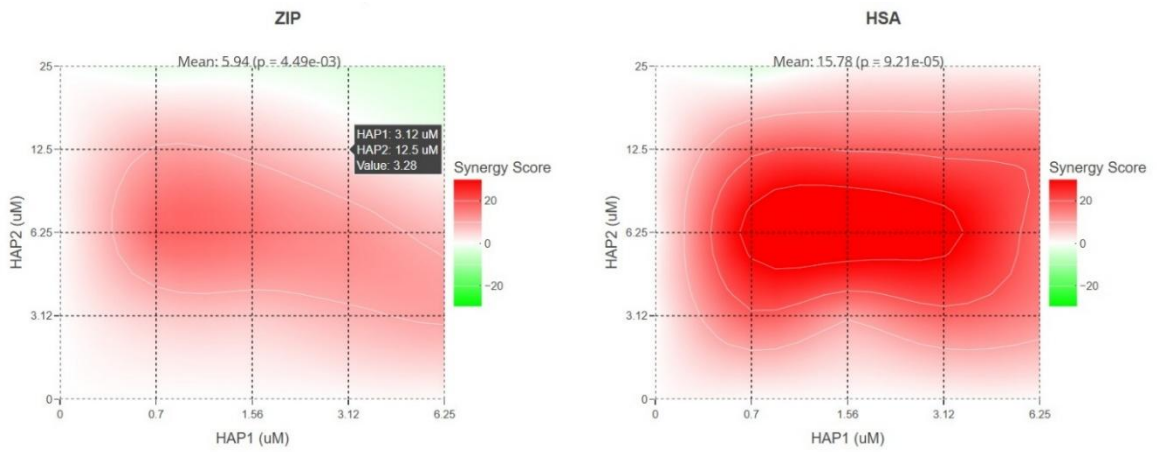


**Figure VI. 10** 2D synergy heatmaps of ABTS antioxidant assay combination HAP1 and HAP2 using ZIP and HAS model generated by SynergyFinder

For the BHA and BHT pair, the strongest antagonism emerged at high doses. In both assays, combinations where one or both antioxidants were at the upper end of the tested concentration range (e.g., 12.5–25 µM) showed the most pronounced negative interactions.

In the DPPH matrix, for instance, when BHT was 25 µM combined with BHA in the 3–12 µM range, the measured radical scavenging was dramatically lower than expected, yielding large negative ZIP synergy (around -60) and Loewe synergy scores as low as -72 to -84 in those regions. This indicates that at high BHT levels, adding BHA suppressed the activity (the mixture was far less effective than BHT alone at 25 µM). The heatmap shows a broad zone of green (antagonism) in the high-BHT quadrant [17]. By contrast, at lower concentrations of BHA and BHT (e.g., both 3.1 µM), the interaction was much closer to additive (synergy scores around -5 to -15, a light color on the map), Fig. VI.11.

In the ABTS assay, a similar trend was observed: antagonism was most acute at the highest BHT and BHA concentrations tested (though not as extreme as in DPPH) Fig.VI.12. At mid-to-low doses in ABTS, the combination's effect nearly matched additivity (synergy scores hovered closer to 0, indicating neither strong synergy nor antagonism). These results suggest that the dose ratio and absolute concentrations are critical in determining the interaction outcome.

For BHA and BHT, low doses do not markedly interfere with each other (each can work partially), but at high doses one antioxidant likely regenerates or reduces the other, leading to net loss of efficacy – a phenomenon reported in other studies of phenolic antioxidant mixtures (e.g., one compound may reduce the radical form of the other, thereby blunting overall radical scavenging).

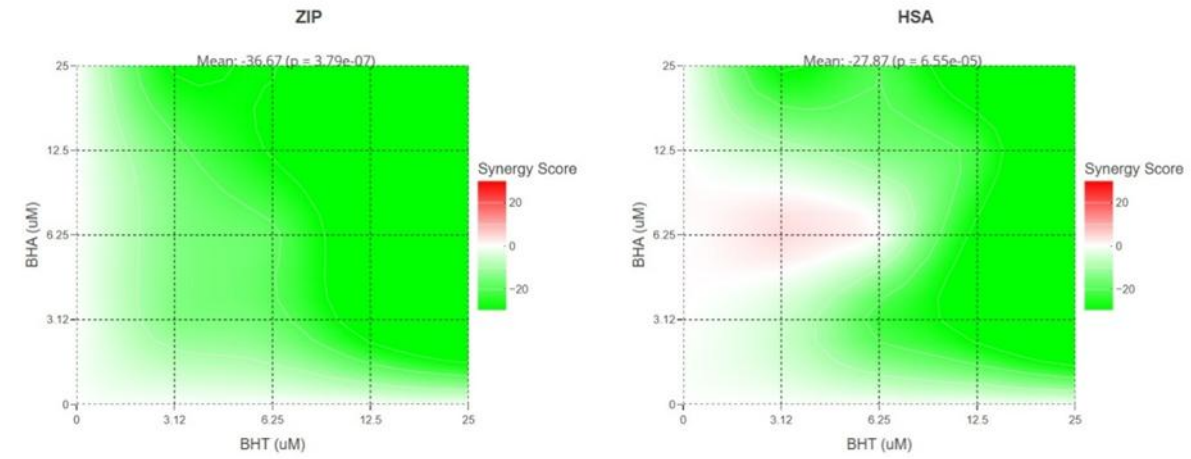


**Figure VI. 11** synergy heatmaps of DPPH antioxidant assay combination to standard BHA and BHT using the ZIP and HAS model generated by SynergyFinder

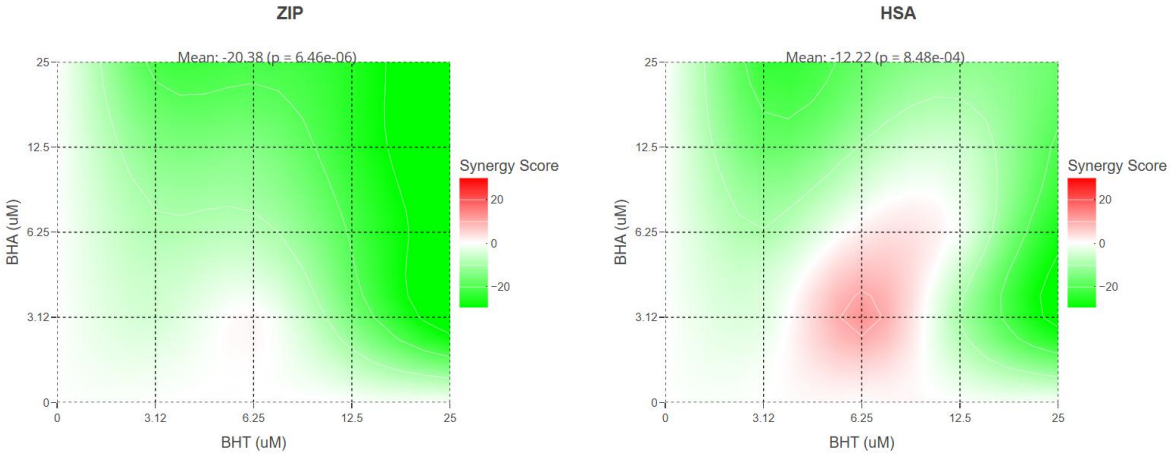


**Figure VI. 12** 2D synergy heatmaps of ABTS antioxidant assay combination to standard BHA and BHT using the ZIP and HAS model generated by SynergyFinder

### VI.3.4 Statistical Significance of Synergy Scores

Each synergy score was accompanied by a statistical significance analysis (per the SynergyFinder output). The p-values (Tables VI.5–VI.6) indicate whether the observed synergy or antagonism is significantly different from zero (no interaction). For all combinations and models in this dataset, the p-values were very low (generally $p < 0.01$, and

often much lower), denoting high confidence in the interaction effects. For example, the synergistic $HAP_1$ and $HAP_2$ combination in DPPH had $p = 8.17\times10^{-4}$for the ZIP score and $p = 3\times10^{-6}$For the HSA score, confirming that the positive synergy scores are statistically significant (the probability of seeing such an excess effect by chance is <0.1%). Similarly, the antagonism of BHA and BHT was highly significant; in the worst case (DPPH), p-values on the order of $10^{-6}$to $10^{-7}$Indicate an extremely low likelihood that the large negative deviations are due to random variability. Even in the ABTS assay, where the magnitude was somewhat less, p-values for BHA and BHT were $\sim10^{-6}$Or smaller, reinforcing that antagonism is real. In summary, the statistical analysis strongly supports that $HAP_1$ and $HAP_2$ interact synergistically and BHA and BHT interact antagonistically, rather than the combinations behaving as merely additive. The consistency of low p-values across multiple synergy models (ZIP, Loewe, Bliss, HSA) further strengthens this conclusion since all models reach significance; we can be confident the finding is not an artifact of one particular reference model assumption.

### VI.3.5 Synergy-Sensitivity Analysis of Antioxidant Combinations

To further evaluate the relationship between synergy and drug sensitivity, a Synergy-Sensitivity (SS) plot was generated, integrating synergy scores with Combination Sensitivity Scores (CSS) derived from IC50 values.

The results indicate a clear distinction between the two syntheses of α-amino phosphonic acids. The $HAP_1$ and $HAP_2$ combination exhibited both high synergy and high sensitivity, with CSS values exceeding 88 for ABTS and 94 for DPPH, positioning it in the upper-right quadrant of the SS plot. This suggests that the combination is not only highly effective in radical scavenging but also exceeds the expected additive effect, making it a promising antioxidant formulation. Conversely, the BHT and BHA combination demonstrated strong antagonism (ZIP synergy scores < -30) and lower sensitivity (CSS around 44–52), placing it in the bottom-left quadrant of the SS plot. This pattern suggests that these two compounds interfere with each other's antioxidant activity, leading to reduced efficacy compared to their individual effects. The consistency of these findings across multiple synergy models (ZIP, HSA) and two independent assays (DPPH, ABTS) reinforces the robustness of the $HAP_1$ and $HAP_2$ synergy while highlighting the ineffectiveness of BHT and BHA. These results provide a strong rationale for further development of $HAP_1$ and

$HAP_2$ as a superior antioxidant combination for potential therapeutic or industrial applications.

## VI.4 antibacterial activity

The antibacterial activity of the synthesized compounds was examined against two Gram-positive and two Gram-negative bacteria by measuring the inhibition zone in terms of (mm)via the paper disc diffusion technique. The antibiotic Penicillin at 50µg/ml was used as a positive control against all tested bacteria. Table VI.7 summarizes the findings of the antibacterial evaluation. According to the observations, both tested compounds ($HAP_1$ and $HAP_2$) show positive activities against all bacterial species. $HAP_2$ aminophosphonic acid showed weak potential against both the Gram-positive and Gram-negative organisms. Although $HAP_1$ presents high antibacterial activity against Gram-positive bacteria than Gram-negative pathogens, overall, the activities are weaker than the standard antibiotic.

$HAP_1$ demonstrated the highest activity against two kinds of bacteria in comparison with Penicillin and $HAP_2$ molecules, respectively. The higher antimicrobial activity of $HAP_1$ may be because of the impact of the dipole moment. The order of the dipole moment is: $\mu HAP_1$(3.0869D)>µpenic(1.98D)[18]> $\mu HAP_2$(1.0948D). The highest dipole moment was obtained for the $HAP_1$, which then appears as the most polar of the three molecules. Improved dipole moment enhances the polar nature of a molecule and promotes the binding affinity, hydrogen bonding, and nonbonding interaction with the receptor protein [19]. The dipole moment of compound $HAP_1$ was 3.0869 Debye, and for compound Penicillin was 1.98 Debye[19], which were slightly higher than that of $HAP_2$ (1.0948 Debye), resulting in their better binding affinity and interactions with the amino acid residues of receptor protein, which enabled improved intracellular penetrability of the molecule. By comparing the antibacterial activity of the $HAP_1$ and $HAP_2$ α-aminophophonic acids and some synthesized α-aminophosphonate esters [20] (Table 8), the results show that the acids gave more significant antibacterial activity than the esters. These acidic compounds are active on Gram-positive and Gram-negative bacteria by interacting with their cell membranes. The antimicrobial potential of α-aminophophonic acids is related to the number of -OH groups present in the structure [21]. Thanks to their character of acids, they can diffuse through the bacterial membrane and acidify the cytoplasm, leading to cell death [22]. The antibacterial

information provided here may indeed be a good approach for further antimicrobial agent research.

**Table VI. 7** The $HAP_1$ and $HAP_2$ antibacterial activity was evaluated by the disc diffusion method (Mean ± SD, n=3).

| | ***S. pyogenes*** | | ***S. aureus*** | | ***E. coli*** | | ***P. aeruginosa*** | |
|---|---|---|---|---|---|---|---|---|
| **Concentration** | 50 µg/ml | 100 µg/ml | 50 µg/ml | 100 µg/ml | 50 µg/ml | 100 µg/ml | 50 µg/ml | 100 µg/ml |
| **$HAP_1$** | 14±0.2 | 19±0.2 | 15±0.2 | 20±0.2 | 23±0.3 | 26±0.6 | 17±0.6 | 27±0.1 |
| **$HAP_2$** | 11±0.1 | 13±0.3 | 12±0.4 | 14±0.2 | 13±0.3 | 16±0.7 | 12±0.4 | 19±0.2 |
| **Penc.** | 13±0.2 | 16±0.2 | 16±0.1 | 18±0.1 | 17±0.4 | 23±0.2 | 16±0.1 | 24±0.8 |
| 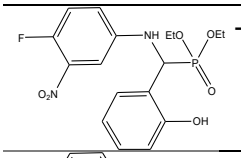 | - | - | - | 12.19±0.96 [23] | | 14.18±0.62 [23] | | 13.84±0.16 [23] |
| 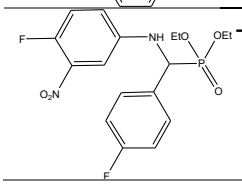 | - | - | - | 11.24±1.76 [23] | | 13.54±0.46 [23] | | 12.68±1.32 [23] |

Zones are presented in (mm) as (Mean±SD) (SD = standard deviation)

## VI.5 Conclusion

This chapter showed that the two synthesized α-amino phosphonic acids, $HAP_1$ and $HAP_2$, have remarkably powerful antioxidant activities in several in vitro tests. In DPPH and ABTS radical scavenging assays, both compounds exhibited notably lower $IC_{50}$ values compared to the conventional antioxidants BHT, BHA, indicating that they need considerably fewer dosages to neutralize 50% of the free radicals. These low $IC_{50}$ values correspond to increased efficacy; notably, $HAP_1$ and $HAP_2$ surpassed established antioxidants in these experiments. Similarly, in the FRAP experiment and the phenanthroline assay, $HAP_1$ and $HAP_2$ demonstrated enhanced reducing power and metal-chelating capacity, highlighting their extensive antioxidant effectiveness. The data combined demonstrate that $HAP_1$ and $HAP_2$ are superior free-radical scavengers and reducing agents compared to the benchmark antioxidants evaluated.

In addition to their antioxidant properties, both compounds were evaluated for antibacterial activity against Gram-positive and Gram-negative bacteria using the disc diffusion method, with Penicillin as a positive control. Although both $HAP_1$ and $HAP_2$ showed antibacterial effects, $HAP_1$ demonstrated higher activity, particularly against Gram-

positive bacteria, likely due to its higher dipole moment, which enhances its binding affinity and cellular penetration. Overall, while the antibacterial activity of $HAP_1$ and $HAP_2$ was lower than that of Penicillin, their performance indicates potential for further development as antimicrobial agents.

Moreover, synergy analysis with the SynergyFinder program demonstrated a significant synergistic interaction between $HAP_1$ and $HAP_2$. In the DPPH and ABTS assays, the two compounds collaboratively exhibited antioxidant effects that were much larger than the mere sum of their individual effects, underscoring a pronounced synergistic effect. Conversely, a mixture of the traditional antioxidants BHT and BHA did not produce any enhancement; rather, the BHT–BHA combination demonstrated antagonism, resulting in a combined effect that was inferior to the anticipated outcome based on their separate efficacy. This pronounced disparity indicates that $HAP_1$ and $HAP_2$ possess complementary mechanisms that augment one another's efficacy when utilized concurrently, whereas BHT and BHA may obstruct one another. The observed synergy between $HAP_1$ and $HAP_2$ enhances their overall antioxidant capacity and suggests that their combined use may yield desired benefits at reduced dosages.

Overall, the superior potency of $HAP_1$ and $HAP_2$ surpassing that of standard antioxidants, combined with their cooperative (synergistic) behavior, highlights their significant therapeutic potential as next-generation antioxidant agents. Their outstanding performance across all assays suggests that these α-amino phosphonic acids could be valuable in developing novel interventions against oxidative stress. Given the pressing need for effective antioxidant interventions to combat oxidative stress-related diseases [24], $HAP_1$ and $HAP_2$ emerge as promising candidates for further research and development. In conclusion, they could serve as potent therapeutic antioxidants or as safer, more effective alternatives to current synthetic antioxidants, offering great promise for mitigating oxidative damage in biological and possibly industrial applications.

VII

# Nanodrug Delivery and Emerging Challenges

# VII Nanodrug Delivery and Emerging Challenges

## VII.1 Introduction

In this chapter, the dynamic field of nanodrug delivery is explored, building on the foundational work established in the preceding chapters, which include the full bibliographic review (Chapter I), materials, synthesis, computational analysis, docking studies, and biological evaluations (Chapters II–VI). To improve targeted therapy, first of all looks at contemporary methods of nanodrug delivery, including creative approaches that use our synthesized organophosphonates, computer predictions, and known biological activities. This section illustrates how drug solubility, stability, and specificity can be enhanced by nanotechnology [1], resulting in more potent therapeutic outcomes [2].

A thorough analysis of the present limitations of these distribution techniques is provided in the second section. Despite significant progress, challenges, such as the production of organophosphonates [3], clinical scalability [4], potential toxicity [5], and complex regulatory limitations [6], still exist. This section examines several possible avenues for further study, such as improved in vivo models, adaptable regulatory frameworks, and developments in drug design. The goal is to develop a path that not only overcomes present challenges but also fosters creativity in the next generation of drug design.

This chapter aims to support future research that could link experimental advancement with clinical application by thoroughly analyzing the successes and difficulties of drug design, emphasizing its current impact and potential future developments [7].

## VII.2 Nanocarriers for Organophosphonate Drug Delivery

### VII.2.1 Drug Loading

Both compounds demonstrate robust performance, though $HAP_1$ consistently exhibits superior encapsulation efficiency (EE%) and drug loading (DL%) compared to $HAP_2$. For $HAP_1$, EE% values are 98%, 95%, and 92% at initial drug loadings of 1, 1.5, and 2 mg, respectively, whereas HAP2 shows lower EE% values of 96%, 91%, and 88% over the same range (Fig. VII.1). This gradual decline in EE% with increased drug quantity is indicative of saturation effects within the hydrogel network, where available binding sites become occupied, reducing the proportion of drug that can be encapsulated at higher concentrations [8].

In parallel, DL% for $HAP_1$ rises significantly from 35.4±1.1% at 1 mg to 52.7±2.4% at 1.5 mg and reaches 66.6±2.2% at 2 mg, correlating to NHs drug concentrations of 354, 527, and 666 µg/mL. $HAP_2$, on the other hand, shows DL% values of 34.7±0.9%, 49.4±1.7%, and 63.7±3.1% at the corresponding loadings, with NHs drug concentrations of 347, 494, and 637 µg/mL.

The consistently higher DL% and drug concentrations in $HAP_1$ suggest that its hydrogel matrix likely possesses a denser network structure or more effective chemical functionalities that enhance drug-polymer interactions, thereby improving drug binding and retention [9].

These insights underscore the critical importance of optimizing formulation parameters such as crosslinking density, network topology, and chemical interactions to achieve a delicate balance between high encapsulation efficiency and enhanced drug loading capacity, all while maintaining the physical stability and therapeutic functionality of the delivery system. Capacity, while preserving the stability and functionality of the delivery system [10].

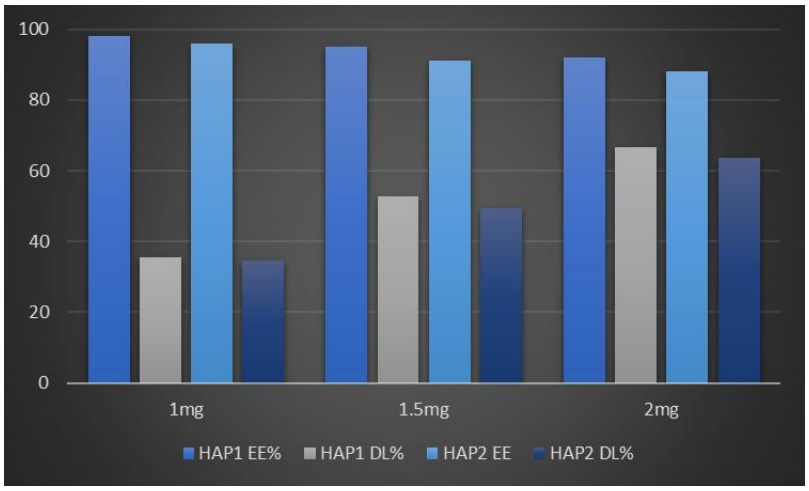


**Figure VII. 1** Comparative Encapsulation Efficiency and Drug Loading of HAP1 and HAP2 at Different Drug Amounts

### VII.2.2 Nanohydrogel Characterization:

Both $HAP_1$ and $HAP_2$ compounds demonstrate a strong and stable nanohydrogel system characterized by uniform particle sizes and low polydispersity indices across different drug loadings Fig. VII.2, indicating that drug incorporation does not appreciably disturb the hydrogel network structure. In $HAP_1$, the vacant nanohydrogel shows a particle size of 190nm with a PDI of 0.24, which remains stable at 190 nm for a 1 mg loading, coupled with a reduced PDI of 0.20, signifying a more uniform size distribution at this concentration.

At 1.5 mg, the particle size minimally reduces to 188 nm, followed by a little increase in PDI to 0.22, while preserving a tight distribution. At a dosage of 2 mg, the size returns to 190 nm, but the PDI increases to 0.29, indicating an appearance of modest heterogeneity, possibly due to the hydrogel nearing its maximal drug incorporation capacity, which may cause slight combination or variability in particle production.

In contrast, $HAP_2$ begins with a size of 190 nm and a PDI of 0.24, but exhibits a slight rise in size to 196 nm at 1 mg loading, alongside a reduced PDI of 0.18, suggesting a very uniform dispersion, maybe resulting from initial swelling or improved drug-hydrogel interactions. At loadings of 1.5 and 2 mg, the particle sizes in $HAP_2$ stabilize at approximately 192 nm, with polydispersity indices of 0.23 and 0.27, respectively. This indicates a modest increase in size relative to $HAP_1$, however, the system maintains a narrow size distribution overall.

The nuanced distinctions in particle size and PDI between $HAP_1$ and $HAP_2$ may arise from intrinsic variances in their internal network architectures or chemical properties, which affect the hydrogel's interaction with and incorporation of the medication.

The low PDI values among the formulations highlight the repeatability and predictability of the nanohydrogel technology, essential for maintaining constant biodistribution and therapeutic efficacy in drug delivery applications [11].

Moreover, $HAP_1$ and $HAP_2$ demonstrate consistent zeta potential values, suggesting that the addition of the compounds does not substantially modify the surface charge properties of the nanohydrogels. The zeta potential of the drug-loaded NHs for $HAP_1$ is measured at $-36.5 \pm 4.2$ mV, similar to that of the empty NHs at $-38.1 \pm 1.4$ mV. In the same way, $HAP_2$ has a zeta potential of $-34.2 \pm 4.2$ mV for drug-loaded nanocarriers, in contrast to $-38.1 \pm 1.4$ mV for empty NHs.

The proximity of these values indicates that the loading procedure protects the negative surface charge of the nanohydrogel particles, which is essential for their colloidal stability and potential contact with biological membranes [12]. Preserving a stable zeta potential during drug loading indicates that the hydrogels' structural integrity and surface chemistry are maintained, which is advantageous for ensuring predictable behavior in biological systems and reducing aggregation during storage and delivery [13].

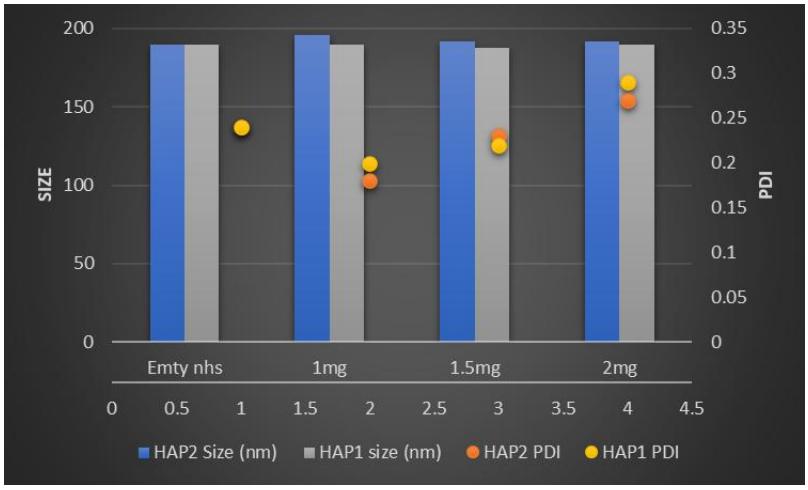


**Figure VII. 2** Distribution of Nanohydrogel Particle Size in Hap1 and Hap2 with Different Drug Loadings

### VII.2.3 *In Vitro* Drug-Release Analysis

#### VII.2.3.1 Release Profiles and $t_{50}$ Values

The time to 50% cumulative release ($t_{50}$) for $HAP_1$ is 54.6±5.2 minutes, and for $HAP_2$ it is 98.4±8.3 minutes (Fig. VII.3). This implies that $HAP_1$ demonstrates a faster release profile, achieving half of its pharmacological payload in under an hour, but $HAP_2$ releases its payload more gradually. The disparity in $t_{50}$ values may arise from differences in matrix composition, porosity, and drug–carrier interactions: $HAP_1$ may exhibit weaker drug-binding sites or a more porous structure facilitating rapid diffusion, while $HAP_2$'s formulation might possess stronger intermolecular bonds or diminished porosity, hindering release. These contrasts are essential for customizing drug delivery to particular treatment requirements. Faster-release formulations can quickly attain effective drug concentrations, while slow-release systems can sustain levels over an extended duration without repeated dosing [14].

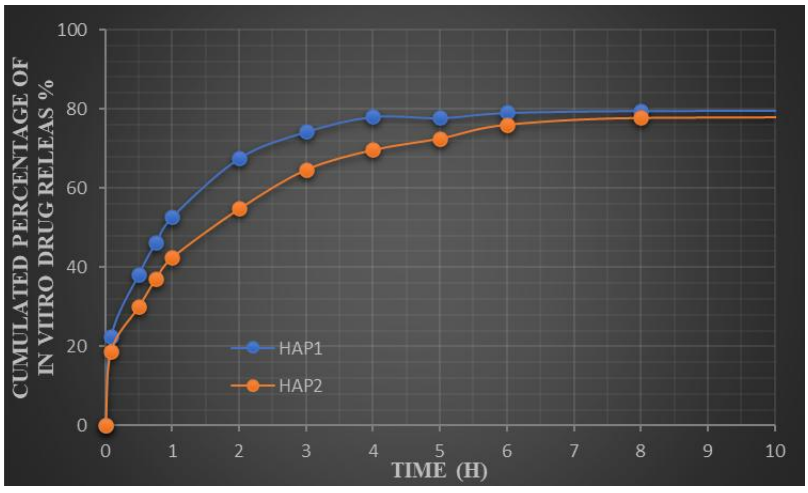


**Figure VII. 3** In-vitro drug release profile of $HAP_1$ and $HAP_2$ at PH = 7.5

### VII.2.3.2 Kinetic Models and Equations

**Higuchi Model:** Describes drug release as a diffusion process from a homogeneous matrix. Cumulative release is proportional to the square root of time [15].

$$Q_t = k_H\sqrt{t} \ldots\ldots\ldots\ldots (4)$$

Where $k_H$ is the Higuchi constant. This model assumes a diffusion-controlled mechanism with a uniform initial drug distribution and negligible matrix swelling or dissolution.

**Korsmeyer–Peppas Model:** A semi-empirical model for the initial 60% of release, useful for identifying the mechanism [16]. It is given by:

$$\frac{M_t}{M_\infty} = k_{KP}t^n \ldots\ldots\ldots\ldots (5)$$

Where $M_t/M_\infty$ is the fraction released at time t, $k_{KP}$ is the KP rate constant, and n is the release exponent indicative of the mechanism. A log plot of released fraction yields a line of slope n and intercept log($k_{KP}$). The value of n helps classify the release mechanism. For example, $n \leq 0.5$ indicates Fickian diffusion (Case I), $0.5 < n < 0.89$ indicates anomalous (non-Fickian) transport, and $n = 1$ suggests (Case II) transport (erosion-controlled or zero-order)

### VII.2.3.3 Kinetic Model Results

Both $HAP_1$ and $HAP_2$ exhibited a biphasic drug release profile consisting of an initial burst phase (0–4 h) followed by a slower sustained release phase (4–28 h). The release data in each phase, as well as over the full 0–28 h period, were fitted to the Higuchi diffusion model and the Korsmeyer–Peppas (K–P) power-law model to elucidate the kinetics and mechanisms. The goodness-of-fit ($R^2$) and fitted parameters for each model are summarized in Tables 1 and 2. In general, the K–P model provided excellent fits in the early and late stages (higher $R^2$), while the Higuchi model was only valid for the initial diffusion-dominated period and failed to describe the full release curve (negative $R^2$ in some cases). These trends reflect the changing release mechanism: predominantly diffusion-controlled in the early phase and essentially depletion-controlled in the late phase.

- **Early Phase Release (0–4h) :**

In the first 4 hours, both compounds showed a significant release of their payloads in a diffusion-driven burst. $HAP_1$ released approximately 78% of its total concentration within 4 hours, while $HAP_2$ released about 70% throughout the same timeframe, as seen by the upward shift of Figure VII.4 . The early-phase Higuchi diffusion constant, $k_H$, of $HAP_1$ was greater ($\approx 44.7 \frac{\%}{\sqrt{h}}\cdot$) than that of $HAP_2$ ($\approx 38.0 \frac{\%}{\sqrt{h}}\cdot$) indicating a more rapid initial diffusion rate in $HAP_1$ (Table VII.1 and Table VII.2). The Higuchi model adequately described the early release ($R^2$ = 0.83 for $HAP_1$, 0.93 for $HAP_2$), indicating a diffusion-controlled mechanism during this period [17]. However, the $K_P$ model provided a superior representation of the early release ($R^2$ = 0.99 for both), accurately reflecting the subtle curve in the $HAP_1$ profile, which the linear √t Higuchi model fails to capture. The fitted $K_P$ release exponents (n) for the (0–4h) data ranged from 0.33 to 0.35 for both $HAP_1$ and $HAP_2$ (Table VII.1 and Table VII.2), indicating n < 0.5, which suggests Fickian diffusion-controlled release [18]. This shows that in the preliminary stage, drug release from both compounds is primarily controlled by concentration-driven diffusion (Case I transport).

The only notable difference is that $HAP_1$ has a higher $K_P$ rate constant ($K \approx 0.64\ h^{-n}$ compared to $0.53\ h^{-n}$ for $HAP_2$) and a greater initial burst, suggesting a more accessible drug concentration at or near the surface, resulting in an accelerated release rate. Following this, $HAP_1$ exhibits a more pronounced increase in cumulative release during the initial hour (about 54% in 2 hours) relative to $HAP_2$ (approximately 45% in 2 hours), as illustrated in Figure VII.3. Mechanistically, $HAP_1$ and $HAP_2$ function as diffusion-controlled systems in the initial phase; however, $HAP_1$'s formulation facilitates a more rapid diffusion of a greater proportion of the drug, while $HAP_2$ retains a larger quantity of the drug for subsequent release.

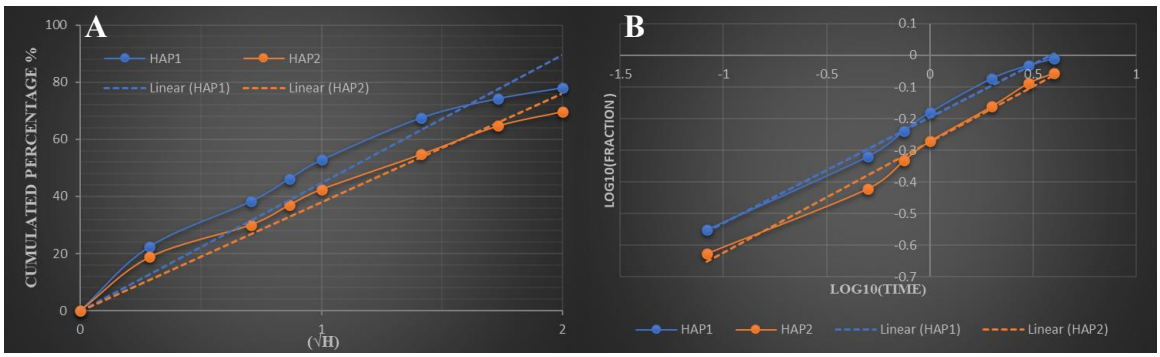


**Figure VII. 4 Early-phase (0–4h) release kinetics of HAP1 (blue) and HAP2 (orange), showing experimental model fits (Higuchi – A; Korsmeyer–Peppas – B**

- **Late-Phase Release (4–28h)**

During the 4–28-hour interval, the release rates significantly decreased, particularly for $HAP_1$. $HAP_2$ released an additional around 9–10% of the compound between 4 and 28 hours (a rise from 70 % to 79.3%), while $HAP_1$ released just about 2% more over this period, effectively plateauing at around 80% by 6 to 8 hours. The experimental findings in this late phase indicate that $HAP_2$'s cumulative release gradually increases with time, but $HAP_1$'s curve almost levels off. This disparity is seen in the model fits. The Higuchi model is no longer applicable in the late phase; analyzing the post 4-hour release as a basic √t process yields a suboptimal fit ($R^2 \approx 0.01$ for $HAP_2$ and negative for $HAP_1$, Tables 1–2), since the assumptions of the Higuchi model fail when a significant portion of the medication has been exhausted. Conversely, the $K_P$ model adequately characterized the gradual tail of the release for both formulations. The late-phase $K_P$ exponent for $HAP_2$ (n = 0.29) consistently stayed below 0.45, further suggesting a diffusion-controlled mechanism throughout this phase. For $HAP_1$, the exponent n in the late phase was approximately 0.20, indicating an exceedingly low value that characterizes a "pseudo-Fickian" diffusion, suggestive of a nearly static release regime[19]. The $K_P$ fits indicate that $HAP_2$ continues to release the medication, albeit at a sluggish rate, throughout 28 hours, but $HAP_1$'s release has nearly stopped by approximately 8 hours (Figure VII.5). In the late diffusion phase, $HAP_2$ has a modest yet quantifiable release rate, indicative of ongoing diffusion from less accessible interior drug sites, whereas $HAP_1$ attains an early equilibrium with no substantial further release. This dichotomy illustrates that $HAP_1$ had fully depleted its accessible drug in the early phase, but $HAP_2$ maintained a residual drug fraction that diffused over a longer duration.

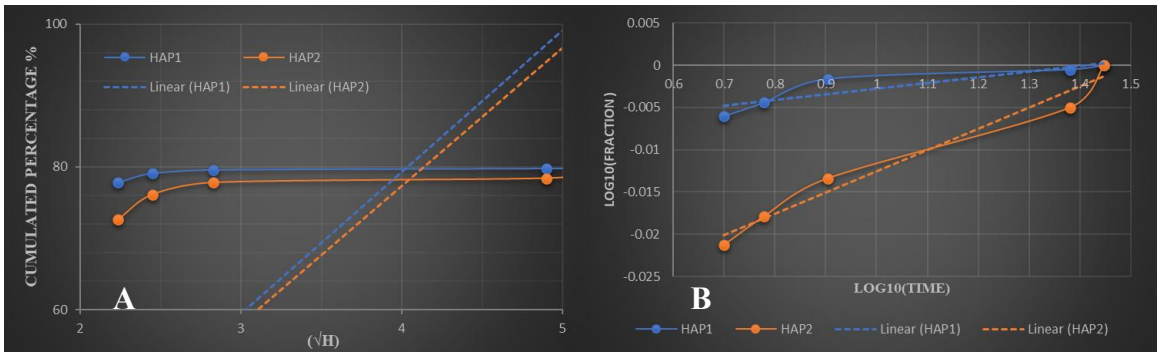


**Figure VII. 5 Late-phase (4–28h) release kinetics of HAP1 (blue) and HAP2 (orange), showing experimental model fits (Higuchi – A; Korsmeyer–Peppas – B).**

**Table VII. 1** Kinetic parameters for $HAP_1$ drug release derived from model fitting.

| Interval | $k_H$(Higuchi) | $R^2$ (Higuchi) | K (K–P) | n (K–P) | $R^2$ (K–P) |
|---|---|---|---|---|---|
| **Early (0–4 h)** | 44.72 | 0.83 | 0.64 | 0.33 | 0.99 |
| **Late (4–28 h)** | 0.42 | –0.84 | 0.54 | 0.20 | 0.83 |

**Table VII. 2** Kinetic parameters for $HAP_2$ drug release derived from model fitting.

| Interval | $k_H$(Higuchi) | $R^2$ (Higuchi) | K (K–P) | n (K–P) | $R^2$ (K–P) |
|---|---|---|---|---|---|
| **Early (0–4 h)** | 37.96 | 0.93 | 0.53 | 0.35 | 0.99 |
| **Late (4–28 h)** | 2.24 | 0.01 | 0.43 | 0.29 | 0.68 |

In summary, the release kinetics of $HAP_1$ and $HAP_2$ are diffusion-controlled for both early and late phases, with $HAP_1$ demonstrating a significantly faster release due to its structural configuration. $HAP_2$ delivers a quick high amount (high burst), achieving nearly for release in the initial hours, but $HAP_2$ facilitates a gradual and sustained drug release, allowing continuous delivery. The linker length, along with associated structural variations, is the pivotal element influencing this behavior: shortening the linker (as observed in $HAP_1$) facilitates rapid diffusion and swift drug depletion; inversely, lengthening it (as seen in $HAP_2$) prolongs the diffusion pathway, leading to a slowed release and better drug retention.

This discovery is crucial for the design of controlled release systems; by adjusting structural characteristics such as linker length, one can control the balance between an initial burst effect and prolonged sustained release to meet certain therapeutic needs. The Higuchi and Korsmeyer–Peppas models confirm these findings: $HAP_1$'s elevated $k_H$ and nearly negligible late-phase release highlight its burst-release characteristics, whereas $HAP_2$'s nonzero late-phase $k_H$ and sustained diffusion (n ~0.3 in late phase) illustrate its ability for prolonged release. Ultimately, both systems achieve approximately 80% complete release; however, the release profile, fast versus sustained, is determined by the molecular architecture. By comprehending and regulating this design, one can anticipate and customize the drug release kinetics from HAP-based delivery systems, utilizing diffusion as the primary mechanism for drug delivery.

## VII.3 Emerging Challenges

### VII.3.1 Novel Synthetic Methods

#### VII.3.1.1 Novel Functionalization Techniques and Future Outlook

The functionalization of organophosphonates, which involves incorporating the phosphonate group into intricate molecules or adjusting phosphonate-containing compounds, is a field of active advancement. Conventional techniques for incorporating a phosphonate moiety frequently show restricted functional group tolerance and may prove incompatible with late-stage modifications of sensitive drug candidates. Chemists are employing cross-coupling strategies similar to those utilized for C–C bonds to tackle this issue. The Hirao reaction exemplifies the use of palladium catalysis to couple dialkyl phosphites with aryl halides, resulting in the formation of aryl phosphonates under mild circumstances [20]. Recent advancements in Hirao-type reactions feature novel ligand or catalyst complexes that operate at reduced temperatures and support a wider array of substrates, including heterocycles prevalent in medicines [20]. Likewise, nickel-catalyzed C($sp^2$)–P and C($sp^3$)–P couplings have been established, broadening the range of phosphonate functionalization to include alkyl halides and more [21]. These metal-catalyzed techniques facilitate the late-stage incorporation of phosphonate groups into intricate structures, which is highly advantageous for medicinal chemistry endeavors, particularly when rapidly investigating a phosphonate analog of a lead chemical is desired.

Another novel technique is C–H activation to form C–P bonds [22]. Pioneering studies have shown that certain directing groups can allow for direct phosphorylation of aromatic C–H bonds (using a phosphite source and a transition metal catalyst), installing a phosphonate without pre-functionalization of the aryl ring [23]. This approach could allow one to take an existing drug scaffold and add a phosphonate at a specific position in a single step. While still under exploration, such methods point to a future where phosphonate medicinal chemistry is as flexible as modern C–H functionalization for other groups.

#### VII.3.1.2 Automation And Machine Learning

From a global trends perspective, the intersection of synthetic chemistry with automation and machine learning may also influence organophosphonate development [23]. Computational retrosynthesis tools can suggest creative routes for complex phosphonates, and automated flow platforms can rapidly test these routes in the lab [24]. We might envision an AI-driven system proposing a synthetic pathway for a new phosphonate prodrug, which

is then executed in a miniaturized continuous reactor, optimizing each step for yield and purity in real-time [25]. Embracing such technologies will be crucial for keeping organophosphonate synthesis innovative and efficient.

### VII.3.2 Computational Modeling

Computational modeling has become an indispensable tool in organophosphonate research, aiding in the design of new molecules, the prediction of their properties, and the understanding of reaction mechanisms. Techniques range from quantum chemical calculations (DFT) to molecular docking and machine learning predictions of biological activity. However, these in silico approaches face their own limitations when applied to organophosphonates.

#### VII.3.2.1 Accuracy of DFT and Molecular Simulations

Although computational chemistry provides profound insights, users must recognize its limitations. Validation using experimental data, such as the comparison of calculated and observed NMR shifts, crystallographic geometries, reaction energetics, UV or IR spectra, or other characteristics, is crucial for confirming the reliability of the models. Addressing existing deficiencies may necessitate the development of enhanced computational methods for phosphonate modeling, including standardized basis sets for phosphorus and suggested functionals, or even AI-enhanced density functional theory (utilizing machine learning to rectify systematic DFT inaccuracies). These enhancements would significantly increase our capacity to anticipate and elucidate organophosphonate behavior in silico.

#### VII.3.2.2 Integration of AI and Machine Learning

The integration of artificial intelligence (AI) and machine learning (ML) into chemical research is a defining trend of the past decade, and organophosphonate research is no exception. AI/ML techniques are being applied to various facets: virtual screening of phosphonate libraries, de novo design of phosphonate analogs, retrosynthetic planning, and property prediction (such as activity or toxicity). ML promises that it can recognize complex, non-linear patterns in data that might be difficult to capture with human-designed models. For instance, an ML model could be trained on known phosphonate drug candidates to predict new structures that balance potency and bioavailability.

However, effectively using AI for organophosphonates comes with challenges. One major issue is the availability of data. Machine learning models, especially deep learning, typically require large datasets to learn from. Organophosphonates represent a relatively

specialized chemical space; there are far fewer known phosphonates (with experimental activity/ADMET data) compared to, say, drug-like molecules at large. This means ML models might struggle due to limited training examples and a lack of representation of organophosphonate-like compounds in public datasets [26]. A recent analysis noted that existing ADMET benchmark sets have limited utility because of small dataset sizes and under-representation of certain compound classes used in drug discovery.

### VII.3.2.3 Challenges in Molecular Docking Simulations

Molecular docking is a computational technique heavily used to predict how a small molecule (ligand) might bind to a protein target. For organophosphonate drug candidates, docking is often employed in the early stages of drug design to screen compounds for likely binding to enzymes or receptors of interest. While docking tools have become quite sophisticated, phosphonate ligands pose special challenges that can limit the reliability of predictions.

Organophosphonates are difficult to dock due to their charge and tautomeric state. At physiological pH, a phosphonic acid moiety is typically dianionic or monoanionic. Docking algorithms often require specifying the protonation state of the ligand, which can lead to misassignment of protonation state and incorrect docking. High charge can cause strong interactions with metal ions or residues in the binding site, which are difficult to model with simple scoring functions. Standard docking scoring functions may not accurately capture these coordination interactions or desolvation penalties associated with binding a charged ligand. Additionally, scoring and ranking can be challenging, as traditional scoring functions use oversimplified energy terms and cannot learn from corner cases like atypical functional groups or bridging bidentate interactions. This can result in false negatives or false positives, as well as not properly accounting for the requirement of a specific water molecule mediating interactions between a phosphonate and the protein.

Different approaches are being implemented to solve these challenges. Covalent docking is employed when organophosphonates function as irreversible inhibitors, as certain phosphonates permanently change enzymes by establishing a covalent P-enzyme link, akin to specific enzyme assay "suicide substrates." Specialized docking procedures can incorporate covalent bond formation as a component of the binding event [27]. In non-covalent scenarios, induced-fit docking or molecular dynamics (MD) refinement may be utilized to accommodate protein flexibility and re-evaluate binding conformations using

more sophisticated force fields. This frequently enhances precision for ligands such as phosphonates that prompt the rearrangement of binding site residues or water molecules.

Additionally, machine learning-based scoring algorithms are being implemented to augment or supplant traditional ones [28]. These systems analyze extensive datasets of ligand–protein complexes, potentially enhancing the identification of accurate poses and significant interactions. Deep learning models can be trained to accept a protein-ligand configuration and produce a binding affinity, having implicitly acquired knowledge of interaction patterns, including those involving charged groups and metals. Nevertheless, as previously stated, these models require exposure to pertinent examples; if the training dataset includes a limited number of complexes with phosphonate ligands, their efficacy with such ligands may remain inadequate [29].

#### VII.3.2.4 ADMET Prediction and In Silico Screening

Recent advancements in ADMET modeling could alleviate some issues. Multi-task learning models can predict multiple properties simultaneously, which sometimes enhances performance by leveraging correlations between properties. Graph-based deep learning models can inherently consider the presence of ionizable groups and larger molecular size. There are web platforms and tools ( ADMETlab 2.0/3.0) that incorporate huge datasets and can predict properties with confidence intervals, alerting when a compound lies outside the chemical domain of the training data [30]. If an organophosphonate is flagged as out-of-domain, researchers know to take that prediction with caution. Additionally, specialized models for phosphonate prodrugs have been developed in academia: these attempt to predict the activation and distribution of prodrugs like bis-alkoxycarbonyloxymethyl (bis-POM) esters of phosphonates, which are used to improve cell permeability [31]. Incorporating such sub-models into larger ADMET frameworks is a future direction.

ADMET prediction for organophosphonates is challenging but improving. It is crucial to keep models updated with relevant data – as more phosphonate drugs are developed and characterized, feeding this information back into ML models will make them more accurate for future compounds. Also, adopting a consensus approach (averaging or considering results from multiple different models) can offset the bias of any single predictive method. The main research gaps involve representation (ensuring phosphonate-like structures are well-represented in training data) and mechanism awareness (models that understand unique aspects like prodrug activation or active transport). By addressing these

gaps, future ADMET prediction tools are expected to provide more confident guidance, helping chemists design organophosphonates with potent activity and acceptable pharmacokinetic and safety profiles.

### VII.3.3 Biological Testing: Translational and Analytical Challenges

Organophosphonates present some distinctive challenges in biological testing due to their chemical properties and mechanisms of action. Key issues include the translation of in vitro potency to in vivo effectiveness, the sensitivity and specificity of assays used to detect their activity, and the need for regulatory validation of new or unconventional assays that might be developed for these compounds.

#### VII.3.3.1 In Vitro–In Vivo Translation:

One of the perennial problems in drug development is that compounds showing promising activity *in vitro* often underperform *in vivo*. This problem is especially pronounced for organophosphonates, which are often highly potent at their molecular target but struggle to reach it in a living organism [32]. The root causes are typically pharmacokinetic: poor absorption from the gut, inability to cross cell membranes, rapid clearance from circulation, or sequestration in unintended sites. For instance, many phosphonate drugs are not orally bioavailable because they cannot efficiently traverse the intestinal epithelium (their polar nature prevents passive diffusion, and they may lack specific uptake transporters) [31]. If given intravenously, they may largely remain in the bloodstream and be filtered out by the kidneys, with minimal distribution to tissues like the brain (BBB penetration is extremely low for most organophosphonates, as we see in the preceding chapters) or even to intracellular sites of infection.

A clear illustration is provided by the case of antiviral acyclic nucleoside phosphonates such as adefovir and tenofovir. These molecules are very effective at inhibiting viral polymerases in vitro, but the parent drugs have almost no oral activity. To solve this, prodrug forms (adefovir dipivoxil, tenofovir disoproxil fumarate, see chapter I) were developed, masking the phosphonate with lipophilic groups to enable absorption; once inside the body, these prodrugs are metabolized to release the active phosphonate [33]. Even then, delivering them to the target tissue (such as the liver for hepatitis, or lymphocytes for HIV) is not trivial. In general, formulation strategies or chemical modification (prodrugs) are essential to translate the in vitro potency of phosphonates to in vivo efficacy [34].

Organophosphonates can exhibit differences in behavior between in vitro systems and biological environments. For instance, a potent enzyme inhibitor might be less effective in a cell if active transport is unavailable. In a cell-based assay, some phosphonates may appear inactive if the assay doesn't provide the necessary metabolic activation. Additionally, translational gaps can occur with target engagement, as organophosphonates might inhibit an enzyme in a cell-free system but not in an organism [35].

Overall, narrowing the *in vitro in vivo* gap for organophosphonates requires an integrated approach: designing compounds with some drug-like properties, using predictive ADME assays, and employing surrogate markers of efficacy in vivo. As technology progresses, non-invasive imaging techniques (like PET scans using radiolabeled phosphonates [36]) could provide real-time data on distribution in vivo, helping validate whether the in vitro promise is being realized. Bridging this translational gap is crucial: it's often said that "phosphonates don't fail to bind the target; they fail to reach the target." Future research must continue to focus on methods to ensure that potent phosphonate inhibitors discovered in vitro are effectively delivered and active in the relevant biological context.

#### VII.3.3.2 Assay Sensitivity and Specificity

Accurate biological evaluation of organophosphonates requires assays that are both sensitive and specific. Sensitivity challenges arise due to the need for testing at very low concentrations in biological samples, especially if they are potent. Analytical sensitivity becomes an issue when measuring the concentration of a phosphonate in plasma or tissue, as many phosphonates lack UV absorbance or fluorescence [37]. Researchers rely on techniques like liquid chromatography-tandem mass spectrometry (LC-MS/MS) to offer the necessary sensitivity and selectivity.

Specificity challenges arise from the structure of organophosphonates, which can introduce artifacts in assays. For example, assays that rely on measuring phosphate release may introduce false signals or quench detection reagents. To ensure specificity, alternate assay formats may be used, such as radiolabeled substrates or $^{31}$P NMR to monitor phosphate vs phosphonate [38].

Specialty concerns include off-target effects, as phosphonates often chelate metal ions, leading to unintended consequences. To control for this, assays might include supplemental cofactors or use cell media formulations that account for chelation [39]. On the other hand, it is essential to ensure the assay captures the intended mechanism. If an

organophosphonate is a prodrug, an in vitro assay with isolated enzyme might show no activity, and a more specific assay system would be to use a cell line that overexpresses the relevant transporter or permeabilize cells in the assay to allow compound entry [40].

Regulatory validation is also crucial for new assays, as they must be validated for accuracy, precision, and specificity under guidelines such as Good Laboratory Practice (GLP) for regulatory submissions. Modern analytical science offers solutions to improve sensitivity and specificity, such as ultra-sensitive detection methods like time-resolved fluorescence resonance energy transfer (TR-FRET) [41] assays or digital PCR[41]. Stability-indicating assays can differentiate a parent phosphonate from any breakdown products, and sometimes, combining multiple readouts provides confidence.

#### VII.3.3.3 Novel Assays

Innovations in biological testing (such as a new surrogate endpoint assay[42] or a microphysiological system for testing drug efficacy) are scientifically exciting, but before they can be broadly adopted – especially in drug development pipelines that feed into regulatory decisions – they must undergo rigorous validation. This becomes particularly relevant for organophosphonates if researchers develop specialized assays to evaluate them (for instance, a custom in vitro model of bone uptake for phosphonates, or a novel biomarker assay for phosphonate action in vivo).

### VII.3.4 Nano-Drug Delivery :

Nano-drug delivery systems have garnered significant attention as a means to overcome the delivery challenges of problematic molecules like organophosphonates. By encapsulating or conjugating a drug to a nanoscale carrier (such as liposomes, polymeric nanoparticles, dendrimers, or inorganic nanomaterials), one can potentially improve the solubility, stability, biodistribution, and targeting of the drug. For organophosphonates, which are typically hydrophilic and rapidly excreted, nano-delivery offers hope to prolong circulation, enhance cellular uptake, and direct the drug to specific tissues (for instance, tumors or bones) while sparing others. However, the field of nanomedicine faces its own set of challenges that must be addressed for successful translation. These include formulation stability and manufacturability, achieving precise targeting to the desired site, mitigating the toxicity of the nanomaterials, and navigating a complex regulatory landscape for approval.

## VII.4 Conclusion

This chapter underscores both the promise and the complexity of nanodrug delivery strategies for organophosphonates. Experimental results with HAP1 and HAP2 demonstrate how subtle differences in hydrogel architecture and linker length can tune encapsulation efficiency, particle size, and release kinetics—ranging from rapid "burst" profiles to sustained diffusion. These findings emphasize the potential of nanoscale formulations to address longstanding obstacles in organophosphonate therapy, notably poor solubility and rapid renal clearance. At the same time, the chapter highlights critical barriers to broader clinical adoption: achieving reproducible large-scale synthesis and formulation, mitigating toxicity, and managing increasingly stringent regulatory requirements.

Emerging synthetic methods are poised to expand chemical space for organophosphonates, including improved functionalization protocols and catalytic systems. Likewise, computational modeling, particularly with AI and machine learning, offers powerful tools for virtual screening, structure prediction, and property estimation; however, their reliable application to organophosphonates hinges on better data availability and refined algorithms that capture the unique chemistry of phosphorus. From a biological testing perspective, bridging in vitro efficacy to in vivo performance remains challenging, as phosphonate-based drugs often struggle with membrane permeability and complex pharmacokinetics. This chapter thus emphasizes a holistic approach—combining prodrug strategies, advanced assays, and carefully tailored nanocarriers to enhance uptake, targeting, and controlled release.

Ultimately, the success of nanodrug delivery for organophosphonates will depend on seamless integration of synthetic innovation, computational insights, and biological validation. By capitalizing on these converging technologies, future research can move beyond proof-of-concept studies toward genuine clinical solutions, making phosphonate drugs more accessible, potent, and safe for a range of therapeutic applications.

# General Conclusion

# General Conclusion

In this work, two α-aminophosphonic acids, HAP1 and HAP2, were successfully synthesized and extensively studied via in silico (computational) and in vitro methods. A direct comparative evaluation of HAP1 and HAP2 has been conducted, encompassing their synthesis efficiency, structural characterization, theoretical DFT descriptors, enzyme docking affinities, ADME-T profiles, antioxidant activities, antibacterial effects, and performance in a nanohydrogel drug-delivery system. The findings indicate that subtle structural differences between HAP1 and HAP2 result in notable variations in their properties and biological activities, with HAP1 often outperforming HAP2 in key assays. Table 1 summarizes the key comparative data between HAP1 and HAP2:

**Table 1.** comparative data for HAP1 vs. HAP2. HAP1 generally shows higher performance in antioxidant and antibacterial assays and greater polarity, whereas HAP2 is slightly more reactive (higher HOMO) and exhibits a more sustained release profile in nanohydrogels. Data are from experimental measurements or calculations as indicated

| Property | HAP1 | HAP2 |
|---|---|---|
| **Synthesis Yield (Conventional / Microwave)** | 44% / 90% | 66% / 92% |
| **UV–Vis λ_max (n→σ*, n→π* transitions)** | 236.5 nm; 275.1 nm *(shorter conjugation)* | 265.3 nm; 345.8 nm *(bathochromic shift due to extended conjugation)* |
| **FT-IR Key Bands (P=O stretch)** | 1244 $cm^{-1}$ | 1234–1240 $cm^{-1}$ |
| **$^{1}H/^{13}C$ NMR (structural highlights)** | –OH, –NH, P–OH protons and five distinct carbons; chemical shifts indicate slightly more shielded environment. | –OH, –NH, P–OH protons and six distinct carbons; downfield shifts (e.g. $CH_2$–NH) indicate more deshielding. |

| | | |
|---|---|---|
| **Dipole Moment (Debye)** | 3.09 D (higher polarity) | 1.09 D (lower polarity) |
| **HOMO–LUMO Gap (eV, B3LYP/6-31++G**)** | 5.85 eV (slightly larger gap; more kinetically stable) | 5.79 eV (slightly smaller gap; more reactive/"softer") |
| **HOMO Energy (eV)** | –6.45 eV (lower EHOMO) | –6.40 eV (higher EHOMO → better $e^-$ donor) |
| **LUMO Energy (eV)** | –0.60 eV (lower ELUMO → better $e^-$ acceptor) | –0.61 eV |
| **Docking: Lipoxygenase Binding ΔG (kcal/mol)** | –6.26 kcal/mol (stronger binding) | –5.02 kcal/mol |
| **Docking: Superoxide Dismutase** | –2.40 kcal/mol | –1.54 kcal/mol |
| **Docking: Catalase** | –1.73 kcal/mol | –0.74 kcal/mol |
| **Docking: Glutathione Peroxidase** | –0.22 kcal/mol | –1.97 kcal/mol *(HAP2 binds slightly better)* |
| **DPPH Radical Scavenging $IC_{50}$ (µg/mL)** | 5.01 ± 0.36 | 4.86 ± 0.40 |
| **ABTS Radical Scavenging $IC_{50}$ (µg/mL)** | 2.78 ± 0.02 | 8.44 ± 0.09 |
| **FRAP (Reducing Power) A0.5 (µg/mL)** | 4.55 ± 0.22 | 8.97 ± 0.36 |
| **Phenanthroline ($Fe^{2+}$ chelation) A50 (µg/mL)** | 0.38 ± 0.01 | 0.40 ± 0.02 |
| **Antibacterial (S. aureus) Inhibition zone (100 µg)** | 20 ± 0.2 mm | 14 ± 0.2 mm |

| | | |
|---|---|---|
| **Encapsulation Efficiency in nanohydrogel (EE%)** | ~92% (at 2 mg loading) *(98% at 1 mg)* | ~88% (at 2 mg loading) *(96% at 1 mg)* |
| **Nanohydrogel Particle Size (DLS, ~2 mg load)** | ~190 nm, PDI ~0.29 | ~192 nm, PDI ~0.27 |
| **Initial Drug Release (first 4 h, % of payload)** | ~78% released (pronounced burst) | ~70% released (more gradual) |

**Synthesis and Characterization**

Both compounds were synthesized via a modified Kabachnik–Fields (Moedritzer-Irani) one-pot reaction, using conventional heating and microwave-assisted conditions. The microwave-assisted method was markedly superior, yielding ~90% of each product in minutes, versus modest yields under conventional reflux (~44% for HAP1 and 66% for HAP2 over 5–8 hours) in general both methods produced high-purity HAP1 and HAP2 in excellent yield under microwave conditions.

The new compounds were thoroughly characterized to confirm their structures. FT-IR spectra for HAP1 and HAP2 showed the expected phosphonate functional group vibrations, including a broad O–H stretch (~3800–3820 $cm^{-1}$) and strong P=O stretching bands (around 1240 $cm^{-1}$). Notably, HAP2's P=O band appeared at a slightly lower frequency (1234–1240 $cm^{-1}$ vs. 1244 $cm^{-1}$ in HAP1)

UV–Vis spectrophotometry further highlighted the electronic differences: HAP1 displayed absorption peaks at ~236 nm ($n\rightarrow\sigma^*$) and 275 nm ($n\rightarrow\pi^*$), whereas HAP2's corresponding bands were significantly red-shifted to ~265 nm and 345.8 nm. This pronounced bathochromic shift for HAP2 indicates greater conjugation or polarizability in HAP2's structure

The NMR spectra of both compounds in D_2O showed exchangeable –OH and –NH protons and expected aliphatic protons, with slight shifts between them. HAP2's protons were slightly more downfield, reflecting the electron-withdrawing effect of its substituent. HAP1 exhibited 5 distinct carbon signals, while HAP2 showed 6 distinct carbons, including a similar P-coupled carbon at ~47 ppm. Both spectra indicated common structural motifs, but HAP2's carbons were slightly more deshielded on average. These small shifts support that HAP2's substituent exerts a different electronic influence than HAP1's. Overall, the

spectroscopic characterization confirms that both HAP1 and HAP2 were obtained in high purity and that HAP2 possesses a more extended electronic system than HAP1, as evident in its NMR and UV-Vis signatures.

**Molecular Docking with Antioxidant Enzymes**

HAP1 demonstrated a consistently higher (or equal) binding affinity to the antioxidant enzymes LOX, SOD, and CAT compared to HAP2, aligning with its higher polarity and ability to form hydrogen bonds. HAP1's better docking scores suggest it might modulate these enzymes slightly more effectively (e.g. as a weak inhibitor or ligand), though the binding energies are in a range that may not translate to strong in vivo inhibition. HAP2's only advantage was in GPx binding, but even there its affinity was low. The docking results reinforce the experimental findings that HAP1 is generally the more biologically active compound, and they also highlight that both compounds likely exert their antioxidant effects predominantly through direct radical scavenging (discussed next) rather than through enzyme inhibition.

**ADME-T Profiles and Drug-Likeness**

Physicochemical & Absorption: HAP1 and HAP2 are small molecules (MW ≈ 173–187) and highly polar. Both were predicted to be highly water-soluble. Their lipophilicity is very low (consensus Log $P_{o/w}$ ≈ –1.3 for HAP1 and –1.1 for HAP2), reflecting the presence of polar phosphonate and amino groups. Consequently, both compounds are predicted to have high gastrointestinal (GI) absorption They also satisfy Lipinski's Rule of Five with zero violations, indicating good oral drug-likeness (e.g., MW <500, LogP <5, H-bond donors/acceptors within limits). They share a moderate predicted oral bioavailability score of ~0.56

Distribution: Both compounds are expected to distribute primarily in plasma rather than deep into tissues. Predicted steady-state volume of distribution (Vd_ss) values (log L/kg) were low (approximately –0.48 for HAP1 and –0.53 for HAP2, corresponding to Vd on the order of 0.3 L/kg) they have a high fraction unbound in plasma (fu ≈ 0.85 for HAP1, 0.80 for HAP2), meaning most of the drug remains free rather than protein-bound. This is advantageous pharmacodynamically (more free drug available to act)

Metabolism: Neither HAP1 nor HAP2 is expected to inhibit major cytochrome P450 enzymes (CYP1A2, 2C19, 2C9, 2D6, 3A4)

Excretion: pkCSM predicted moderate clearance for both. The total clearance was estimated to be slightly faster for HAP2 (log Clearance ~0.92 mL/min/kg) than HAP1 (0.83 mL/min/kg)

**In Vitro Antioxidant Activity**

HAP1 emerged as the superior antioxidant overall, especially in the radical scavenging assays (ABTS, FRAP). HAP2 did show equal (phenanthroline) or slightly better (DPPH) performance in certain aspects, but across the spectrum of assays HAP1 was more consistently potent. HAP1's higher polarity and its electronic characteristics (higher dipole, lower LUMO) likely enhance its ability to stabilize radicals or transition states during electron transfer. Meanwhile, HAP2's extended conjugation and electron-donating benzyl-like substituent aided it in the DPPH assay (which might favor electron donation), but apparently that same trait did not help – and perhaps hindered – its efficacy in aqueous-phase ABTS scavenging (possibly due to steric or solvation differences). It is important to note that both compounds outperformed classic antioxidants in most tests, indicating that the α-aminophosphonic acid framework is highly effective for antioxidant activity. The presence of multiple functional groups (amine, phosphonic acid) may allow multiple modes of action: direct radical quenching (through H-atom or $e^-$ donation), reductive capacity, and metal chelation, as demonstrated.

A particularly intriguing outcome was observed when HAP1 and HAP2 were used in combination. We explored whether the mixture of the two could produce synergistic effects (since they have slightly different antioxidant strengths, a combination might cover a broader range of radical types). Using synergy analysis models (Bliss, Loewe, HSA, ZIP), we found that HAP1 + HAP2 together interact synergistically in both DPPH and ABTS assays, meaning the combined effect is greater than the sum of their individual effects.

**Antibacterial Activity**

We also screened HAP1 and HAP2 for antibacterial effects, since some organophosphonates are known to have antimicrobial properties and oxidative stress is linked to bacterial killing mechanisms. The compounds were tested against a panel of two Gram-positive bacteria (Streptococcus pyogenes and Staphylococcus aureus) and two Gram-negatives (Escherichia coli and Pseudomonas aeruginosa), using a disk diffusion method (with penicillin as a reference standard). Both HAP1 and HAP2 showed measurable

antibacterial activity against all tested strains, but HAP1 exhibited significantly larger zones of inhibition than HAP2

**Nanohydrogel Formulation and Drug Release**

Encapsulation was highly successful for both compounds, but HAP1 consistently showed a slightly higher encapsulation efficiency (EE) and drug loading than HAP2.

The nanoparticle size was measured by DLS and found to be in the ~180–200 nm range for both formulations, and the polydispersity indices (PDI) were low (~0.2–0.3) for both, signifying uniform particles.

Both release profiles had their advantages: HAP1's burst could be useful for acute scavenging of radicals (such as immediately after an ischemia-reperfusion injury), whereas HAP2's sustained release could maintain antioxidant levels over time to prevent chronic oxidative damage.

**Future Directions**

Future research directions stemming from this thesis include: (1) In vivo evaluation of HAP1 and HAP2 (and their combination) in animal models of oxidative stress (such as ischemia-reperfusion injury, neurodegeneration, or chronic inflammation) to assess their protective effects and bioavailability. (2) Mechanistic studies on the synergy of HAP1/HAP2 – investigating whether they target different radical species or regeneration pathways, which could provide insight for designing synergistic antioxidant cocktails. (3) Optimization of antibacterial activity, possibly by modifying the phosphonate or amino substituents (e.g., introducing alkyl chains to increase membrane penetration for Gram-negatives, or conjugating a known antibiotic to the phosphonate to create a dual-action prodrug). (4) Exploration of prodrug forms – since phosphonic acids are highly polar, making prodrugs (e.g. cyclic phosphonate esters) that convert to HAP1/HAP2 in vivo could enhance cell permeability; our ADME data show good oral absorption, but prodrugs might further improve tissue penetration or targeting. (5) Advanced drug delivery systems, such as targeting ligands on the nanohydrogels to direct HAP1/2 to mitochondria (where antioxidant action is often needed most) or inflamed tissues. Additionally, one could explore other nanocarriers (liposomes, dendrimers) to see if the burst vs sustained release difference persists or if those can be tuned differently.

In conclusion, the thesis successfully met its objectives of synthesizing two α-aminophosphonic acids and evaluating their antioxidant activities in silico and in vitro. HAP1 and HAP2 have been shown to be highly potent antioxidants, with HAP1 generally providing greater efficacy, likely due to its unique electronic and polarity characteristics. The slight differences in their behavior provided valuable insights – for example, HAP2's higher HOMO made it a better electron donor but did not translate to overall better antioxidant performance, reminding us that antioxidant efficacy is multifaceted (involving not just electron donation but also solubility, stability of the resulting radical, etc.). The comprehensive data collected – from quantum chemical descriptors to biological assays – paints a coherent picture where HAP1's overall profile is superior for potential therapeutic use (combining strong efficacy with safety), whereas HAP2 might still have niche advantages and serves as a proof of concept for tuning molecular properties. This work lays a strong foundation for the development of phosphonate-based therapeutics, whether as standalone antioxidant agents or as synergistic adjuncts in oxidative stress-related diseases. By advancing our understanding of how these compounds interact with biological systems and how formulation can modulate their delivery, this research paves the way for translating these promising molecules from the bench towards clinical consideration. Future studies building on these findings are well-positioned to make impactful contributions to drug discovery and the management of diseases where oxidative damage is a central concern.

# References

# References

## General Introduction

[1] Zhang, P., Wang, Y., Deng, Z., & Gao, J. (2025). Synthetic versatility: the C–P bond odyssey. Organic & Biomolecular Chemistry.

[2] Furtak, A., Szafranek-Nakonieczna, A., Furtak, K., & Pytlak, A. (2024). A review of organophosphonates, their natural and anthropogenic sources, environmental fate and impact on microbial greenhouse gases emissions–Identifying knowledge gaps. Journal of Environmental Management, 355, 120453.

[3] Drake, G. L., & Calamari, T. A. (2018). Industrial uses of phosphonates. In The role of phosphonates in living systems (pp. 171-194). CRC press.

[4] Demkowicz, S., Rachon, J., Daśko, M., & Kozak, W. (2016). Selected organophosphorus compounds with biological activity. Applications in medicine. RSC advances, 6(9), 7101-7112.

[5] Malik, J., Barry, G., & Kishore, G. (1989). The herbicide glyphosate. BioFactors (Oxford, England), 2(1), 17-25.

[6] Engel, R. (1977). Phosphonates as analogues of natural phosphates. Chemical Reviews, 77(3), 349-367.

[7] Tichý, T., Andrei, G., Dračínský, M., Holý, A., Balzarini, J., Snoeck, R., & Krečmerová, M. (2011). New prodrugs of Adefovir and Cidofovir. Bioorganic & medicinal chemistry, 19(11), 3527-3539.

[8] Ouahrouch, A., Taourirte, M., Schols, D., Snoeck, R., Andrei, G., Engels, J. W., & Lazrek, H. B. (2016). Design, synthesis, and antiviral activity of novel ribonucleosides of 1, 2, 3-triazolylbenzyl-aminophosphonates. Archiv der Pharmazie, 349(1), 30-41.

[9] Azaam, M. M., Kenawy, E. R., El-din, A. S. B., Khamis, A. A., & El-Magd, M. A. (2018). Antioxidant and anticancer activities of α-aminophosphonates containing thiadiazole moiety. Journal of Saudi Chemical Society, 22(1), 34-41.

[10] Kenawy, E. R. S., Azaam, M. M., & Saad-Allah, K. M. (2015). Synthesis and antimicrobial activity of α-aminophosphonates containing chitosan moiety. Arabian Journal of Chemistry, 8(3), 427-432.

## References


[11] Arbuzov, B. A., & hgovkin, B. P. (1951). Chemical Abstracts, 45, 7002.

[12] Garner, A. Y., Chapin, E. C., & Scanlon, P. M. (1959). Mechanism of the Michaelis–Arbuzov reaction: Olefin formation. The Journal of Organic Chemistry, 24(4), 532–536.

[13] Horner, L., & Hoffman, H. (1958). Wippel, HG Chem. Ber, 91, 61.

[14] Wadsworth, W. S., & Emmons, W. D. (1961). The utility of phosphonate carbanions in olefin synthesis. Journal of the American Chemical Society, 83(7), 1733-1738.

[15] Kabachnik, M. I., & Medved, T. Y. (1952). New synthesis of aminophosphonic acids. Dokl. Akad. Nauk SSSR, 83, 689–692

[16] Fields, E. K. (1952). The synthesis of esters of substituted amino phosphonic acids. Journal of the American Chemical Society, 74, 1528–1531.

[17] Moedritzer, K., & Irani, R. R. (1966). The direct synthesis of α-aminophosphonic acids: Mannich-type reactions with orthophosphorous acid. Journal of Organic Chemistry, 31, 1603–1607.

[18] Kalek, M., Ziadi, A., & Stawinski, J. (2008). Microwave-assisted palladium-catalyzed cross-coupling of aryl and vinyl halides with H-phosphonate diesters. Organic letters, 10(20), 4637-4640.

[19] Aluri, B. R., Kindermann, M. K., Jones, P. G., Dix, I., & Heinicke, J. (2008). Bulky N-Substituted 1, 3-Benzazaphospholes: Access via Pd-Catalyzed C− N and C− P Cross Coupling, Lithiation, and Conversion to Novel P • C− P t Bu2 Hybrid Ligands. Inorganic chemistry, 47(15), 6900-6912.

[20] Liu, J., Xiao, H. Z., Fu, Q., & Yu, D. G. (2021). Advances in radical phosphorylation from 2016 to 2021. Chemical Synthesis, 1(1), N-A.

[21] Vashistha, V. K., Sethi, S., Mittal, A., Das, D. K., Pullabhotla, R. V., Bala, R., & Yadav, S. (2024). Stereoselective analysis of chiral pesticides: a review. Environmental Monitoring and Assessment, 196(2), 153.

[22] Han, J., Kiss, L., Mei, H., Remete, A. M., Ponikvar-Svet, M., Sedgwick, D. M., ... & Soloshonok, V. A. (2021). Chemical aspects of human and environmental overload with fluorine. Chemical Reviews, 121(8), 4678-4742.

[23] Dash, R. P., Tichý, T., Veeravalli, V., Lam, J., Alt, J., Wu, Y., ... & Rais, R. (2019). Enhanced oral bioavailability of 2-(phosphonomethyl)-pentanedioic acid (2-PMPA) from its

(5-methyl-2-oxo-1, 3-dioxol-4-yl) methyl (ODOL)-based prodrugs. Molecular pharmaceutics, 16(10), 4292-4301.

**Chapter I**

[1] Quin, L. D. (2000). *A guide to organophosphorus chemistry*. John Wiley & Sons.

[2] Kukhar, V. P., & Hudson, H. R. (Eds.). (2000). *Aminophosphonic and aminophosphinic acids: Chemistry and biological activity*. Wiley.

[3] Corbridge, D. E. C. (2013). *Phosphorus: Chemistry, biochemistry, and technology*. CRC Press.

[4] Iremonger, S. S., Liang, J., Vaidhyanathan, R., Martens, I., Shimizu, G. K., Daff, T. D., ... & Woo, T. K. (2011). Phosphonate monoesters as carboxylate-like linkers for metal-organic frameworks. *Journal of the American Chemical Society*, *133*(50), 20048-20051.

[5] Ma, T. Y., & Yuan, Z. Y. (2011). Metal phosphonate hybrid mesostructures: environmentally friendly multifunctional materials for clean energy and other applications. *ChemSusChem*, *4*(10), 1407-1419.

[6] Hilderbrand, R. L. (1983). *The role of phosphonates in living systems*. CRC Press.

[7] Cowley, A. H. (1965). The chemistry of the phosphorus-phosphorus bond. *Chemical Reviews*, *65*(6), 617-634.

[8] Kosolapoff, G. M. (1948). Synthesis of aromatic phosphonic acids and their derivatives. II. Some halobenzene derivatives. *Journal of the American Chemical Society*, *70*(10), 3465-3467.

[9] Drake, L. R. (1937). *The preparation of phosphonic acids and their alkyl esters*. University of Illinois at Urbana-Champaign.

[10] Kabachnik, M. I., & Medved, T. Y. (1952). New synthesis of aminophosphonic acids. *Dokl. Akad. Nauk SSSR, 83*, 689–692

[11] Fields, E. K. (1952). The synthesis of esters of substituted amino phosphonic acids. Journal of the American Chemical Society, 74, 1528–1531.

[12] Cowley, A. H. (1965). The chemistry of the phosphorus-phosphorus bond. *Chemical Reviews*, *65*(6), 617-634.

[13] Edmundson, R. (Ed.). (1987). *Dictionary of organophosphorus compounds*. CRC Press.

[14] Sawamura, M., Ito, Y., & Hayashi, T. (1989). Asymmetric synthesis of (1-aminoalkyl) phosphonic acids via asymmetric aldol reaction of (isocyanomethyl) phosphonates catalyzed by a chiral ferrocenylphosphine-gold (I) complex. *Tetrahedron Letters*, *30*(17), 2247-2250.

[15] Kobayashi, S., & Ishitani, H. (1999). Catalytic enantioselective addition to imines. *Chemical Reviews*, *99*, 1069-1094.

[16] Lawrence, N. J. (1998). Aldehydes and ketones. *Journal of the Chemical Society, Perkin Transactions 1*, (10), 1739-1750.

[17] Merino, P., Marqués-López, E., & Herrera, R. P. (2008). Catalytic enantioselective hydrophosphonylation of aldehydes and imines. *Advanced Synthesis & Catalysis*, *350*(9), 1195-1208.

[18] Horváth, I. T., & Anastas, P. T. (2007). Introduction: green chemistry. *Chemical Reviews*, *107*(6), 2167-2168.

[19] Rueping, M., Dufour, J., & Schoepke, F. R. (2011). Advances in catalytic metal-free reductions: from bio-inspired concepts to applications in the organocatalytic synthesis of pharmaceuticals and natural products. *Green Chemistry*, *13*(5), 1084-1105.

[20] Zhu, Y. P., Yin, J., Abou-Hamad, E., Liu, X., Chen, W., Yao, T., ... & Alshareef, H. N. (2020). Highly stable phosphonate-based MOFs with engineered bandgaps for efficient photocatalytic hydrogen production. *Advanced Materials*, *32*(16), 1906368.

[21] Mady, M. F., Warsame, M. T., Pires, A. A., Abdelhay, A. H., Kelland, M. A., Hussein, I. A., & Demadis, K. D. (2024). Exploring Trends in Scale Control with Homologous, Structurally Expanded, Phosphonate Functionalized Linear Amino Acids as Environmentally Acceptable Scale Inhibitors. *ACS ES&T Water*.

[22] Demadis, K. D., Adla, S. K., Timonen, J., & Turhanen, P. A. (2025). Green phosphonate chemistry–Does it exist? Green Chemistry.

[23] Russell, R. G. G., & Rogers, M. J. (1999). Bisphosphonates: from the laboratory to the clinic and back again. *Bone*, *25*(1), 97-106.

[24] Rodan, G. A., & Fleisch, H. A. (1996). Bisphosphonates: mechanisms of action. *The Journal of Clinical Investigation*, *97*(12), 2692-2696.

[25] Fleisch, H., Reszka, A., Rodan, G., & Rogers, M. (2002). Bisphosphonates: mechanisms of action. *Principles of bone biology*, 1361-XLIII.

## References


[26] Chen, L., Liu, X. Y., & Zou, Y. X. (2020). Recent Advances in the Construction of Phosphorus-Substituted Heterocycles, 2009–2019. *Advanced Synthesis & Catalysis*, *362*(9), 1724-1818.

[27] Han, B. X., Jiang, Y. F., Sun, X. R., Li, Z. F., & Li, G. (2021). Proton conductive N-heterocyclic metal-organic frameworks. *Coordination Chemistry Reviews*, *432*, 213754.

[28] Arbuzov, B. A., & hgovkin, B. P. (1951). *Chemical Abstracts*, 45, 7002.

[29] Garner, A. Y., Chapin, E. C., & Scanlon, P. M. (1959). Mechanism of the Michaelis–Arbuzov reaction: Olefin formation. *The Journal of Organic Chemistry, 24*(4), 532–536.

[30] Michaelis, A., & Kaehne, R. (1898). *Berichte der deutschen chemischen Gesellschaft*, 31, 1048–1055.

[31] Moedritzer, K., & Irani, R. R. (1966). The direct synthesis of α-aminophosphonic acids: Mannich-type reactions with orthophosphorous acid. *Journal of Organic Chemistry, 31*, 1603–1607.

[32] Kukhar, V. P., & Hudson, H. R. (Eds.). (2000). *Aminophosphonic and aminophosphinic acids: Chemistry and biological activity*. Wiley-VCH.

[33] Pudovik, A. N. (1950). *Doklady Akademii Nauk SSSR, 73*, 499–502.

[34] Pudovik, A. N. (1952). *Doklady Akademii Nauk SSSR, 83*, 865–868.

[35] Engel, R. (2003). *Synthesis of carbon-phosphorus bonds*. CRC press.

[36] Semenzin, D., Etemad-Moghadam, G., Albouy, D., Diallo, O., & Koenig, M. (1997). Dual radical/polar Pudovik reaction: application field of new activation methods. *The Journal of Organic Chemistry*, *62*(8), 2414-2422.

[37] Rostamnia, S., & Amini, M. (2014). Ultrasonic and Lewis acid ionic liquid catalytic system for Kabachnik–Fields reaction. *Chemical Papers, 68*, 834–837.

[38] Kafarski, P., & Lejczak, B. (1991). Kabachnik–Fields reaction under green conditions – A critical overview. *Pure and Applied Chemistry, 63*, 163–168.

[39] Mucha, A., Kafarski, P., & Berlicki, Ł. (2021). Lewis acid catalysts in Kabachnik–Fields reaction. *Molecules, 26*(9), 2511.

(a) Abdeen, M. M., Hamed, M. A., Abdel Aleem, H. A., Nassar, I. F., & El-Sayed, I. E. T. (2021). A comparative study of metal-catalyzed three-component synthesis of α-aminophosphonates. *Journal of the Iranian Chemical Society*. 54.1680-1688

(b) Rezaei, Z., Khabnadideh, S., Ghasemi, Y., Fadaei, M., & Karimi, Z. (2011). Design and one-pot synthesis of new α-aminophosphonates and antimicrobial activity. *Journal of Pharmacy Negative Results, 2*(2), 53–58.

(c) Reddy, Y. T., Reddy, P. N., Kumar, B. S., Rajput, P., Sreenivasulu, N., & Rajitha, B. (2007). $TiCl_4$-catalyzed efficient one-pot synthesis of α-aminophosphonates. *Phosphorus, Sulfur, and Silicon and the Related Elements, 182*(1), 161–165.

(d) Baylis, E. K., Campbell, C. D., & Dingwall, J. G. (1984). 1-Aminoalkylphosphonous acids. Part 1. Isosteres of the protein amino acids. *Journal of the Chemical Society, Perkin Transactions 1*, 2845–2853.

(e) Xu, F., Luo, Y., Wu, J., Shen, Q., & Chen, H. (2006). Facile one-pot synthesis of α-aminophosphonates using lanthanide chloride as catalyst. *Heteroatom Chemistry, 17*(5), 389–392.

[40] For regarding the recent reviews of microwave use,

(a) Kappe, C. O., Pieber, B., & Dallinger, D. (2013). *Angewandte Chemie International Edition, 52*, 1088.

(b) Kappe, C. O. (2013). *Accounts of Chemical Research, 46*, 1579.

(c) Kirouani, I., Hellal, A., Madani, A., Layaida, H., Haddadi, I., Bouchama, A., & Chafai, N. (2023). Phosphorylated p-aminophenol derivatives: Microwave-assisted synthesis, density functional theory study, and biological activities evaluation. *Journal of Molecular Structure, 1290*, 135916.

(d) Haddadi, I., Hellal, A., Kirouani, I., Layaida, H., & Bensouici, C. (2022). Microwave-assisted synthesis, DFT theoretical study, and biological activities evaluation of two phosphorylated m-toluidine derivatives. *Journal of Molecular Structure, 1251*, 131948.

[41] Dar, B. A., Singh, A., Sahu, A. K., Patidar, P., Chakraborty, A., Sharma, M., & Singh, B. (2012). Catalyst and solvent-free ultrasound promoted rapid protocol for the one-pot synthesis of α-amino phosphonates at room temperature. *Tetrahedron Letters, 53*, 5497–5502.

[42] Wang, L., Cui, S., Meng, W., & et al. (2010). Asymmetric synthesis of α-aminophosphonates by means of direct organocatalytic three-component hydrophosphonylation. *Chinese Science Bulletin, 55*, 1729–1731.

[43] Xu, W., Zhang, S., Yang, S., Jin, L.-H., Bhadury, P. S., Hu, D.-Y., & Zhang, Y. (2010). Asymmetric synthesis of α-aminophosphonates using the inexpensive chiral catalyst 1,1'-binaphthol phosphate. *Molecules, 15*, 5782–5796.

[44] Maestro, A., del Corte, X., López-Francés, A., Martínez de Marigorta, E., Palacios, F., & Vicario, J. (2021). Asymmetric synthesis of tetrasubstituted α-aminophosphonic acid derivatives. *Molecules, 26*, 3202.

[45] Walęcka-Kurczyk, A., Walczak, K., Kuźnik, A., Stecko, S., & Październiok-Holewa, A. (2020). The synthesis of α-amino phosphonates via enantioselective organocatalytic reaction of 1-(N-acylamino) alkyl phosphonium salts with dimethyl phosphite. *Molecules, 25*, 405.

[46] Koszelewski, D., Kowalczyk, P., Śmigielski, P., Samsonowicz-Górski, J., Kramkowski, K., Wypych, A., Szymczak, M., & Ostaszewski, R. (2022). Relationship between structure and antibacterial activity of α-aminophosphonate derivatives obtained via lipase-catalyzed Kabachnik–Fields reaction. *Materials*.15(10), 1234–1245

[47] Mavel, G. (1974). NMR Studies of Phosphorus Compounds (1965–1969). *Annual reports on NMR spectroscopy*, *5*, 1-305.

[48] Kim, H., & Lipscomb, W. N. (1991). Comparison of the structures of three carboxypeptidase A-phosphonate complexes determined by X-ray crystallography. *Biochemistry*, *30*(33), 8171-8180.

[49] Zapf, P. J., Rose, D. J., Haushalter, R. C., & Zubieta, J. (1996). Synthesis and Structural Characterization of Solid Phases of the Sn (II)–Organophosphonate System: The 1-Dimensional [Sn (HO3PCH2PO3H)] · H2O and the 3-Dimensional [Sn2 {O3PC (OH)(CH3) PO3}]. *Journal of Solid-State Chemistry*, *125*(2), 182-185.

[50] Copeland, R. A. (2005). *Evaluation of enzyme inhibitors*. Wiley.

[51] Singh, P., & Gupta, R. (2015). Design of phosphonate-based enzyme inhibitors for AD therapy. *Journal of Medicinal Chemistry, 58*, 7653–7662.

[52] Asante-Appiah, E., & Kennedy, B. P. (2003). Protein tyrosine phosphatases: the quest for negative regulators of insulin action. *American Journal of Physiology-Endocrinology and Metabolism*, *284*(4), E663-E670.

[53] Mucha, A., Kafarski, P., & Berlicki, Ł. (2011). Remarkable potential of the α-aminophosphonate/phosphinate structural motif in medicinal chemistry. *Journal of Medicinal Chemistry, 54*, 5955–5980.

[54] Neiber, R. R., Samak, N. A., Xing, J., Elmongy, E. I., Galhoum, A. A., El Sayed, I. E.-T., Guibal, E., Xin, J., & Lu, X. (2024). Synthesis and molecular docking study of α-aminophosphonates as potential multi-targeting antibacterial agents. *Journal of Hazardous Materials, 465*, 133203.

[55] Bahadi, R., Berredjem, M., Benzaid, C., Bouchareb, F., Dekir, A., Djendi, M. L., Ibrahim-Ouali, M., Boussaker, M., Bouacida, S., Bhat, A. R., Ahmed, S., Bachari, K., & Redjemia, R. (2023). Efficient synthesis, crystallography study, antibacterial/antifungal activities, DFT/ADMET studies, and molecular docking of novel α-amino phosphonates. *Journal of Molecular Structure, 1289*, 135849.

[56] Falagas, M. E., Vouloumanou, E. K., Samonis, G., & Vardakas, K. Z. (2016). Fosfomycin. *Clinical microbiology reviews*, *29*(2), 321-347.

[57] Silver, L. L. (2017). Fosfomycin: mechanism and resistance. *Cold Spring Harbor perspectives in medicine*, *7*(2), a025262.

[58] Horsman, G. P., & Zechel, D. L. (2017). Phosphonate biochemistry. *Chemical Reviews*, *117*(8), 5704-5783.

[59] Yang, X. C., Zeng, C. M., Avula, S. R., Peng, X. M., Geng, R. X., & Zhou, C. H. (2023). Novel coumarin aminophosphonates as potential multitargeting antibacterial agents against Staphylococcus aureus. *European Journal of Medicinal Chemistry*, *245*, 114891.

[60] Fox, E. M., & Mendz, G. L. (2006). Phosphonate degradation in microorganisms. *Enzyme and microbial technology*, *40*(1), 145-150.

[61] Ohtake, H., Wu, H., Imazu, K., Anbe, Y., Kato, J., & Kuroda, A. (1996). Bacterial phosphonate degradation, phosphite oxidation, and polyphosphate accumulation. *Resources, conservation, and recycling*, *18*(1-4), 125-134.

(a) Hellal, A., Chafaa, S., Chafai, N., & Touafri, L. (2017). Synthesis, antibacterial screening, and DFT studies of a series of α-aminophosphonate derivatives from aminophenols. *Journal of Molecular Structure, 1134*, 217–225.

(b) Poola, S., Nagaripati, S., Tellamekala, S., Chintha, V., Kotha, P., Yagani, J. R., & Cirandur, S. R. (2020). Green synthesis, antibacterial, antiviral, and molecular docking studies of α-aminophosphonates. *Synthetic Communications, 50*(15), 2259–2276.

(c) Reddy, S. S., Rao, V. K., Krishna, B. S., Reddy, C. S., Rao, P. V., & Raju, C. N. (2011). Synthesis, antimicrobial, and antioxidant activity of new α-aminophosphonates. *Phosphorus, Sulfur, and Silicon and the Related Elements, 186*(7), 1411–1421.

(d) Rezaei, Z., Khabnadideh, S., Zomorodian, K., Pakshir, K., Nadali, S., Mohtashami, N., & Faghih Mirzaei, E. (2011). Design, synthesis, and antifungal activity of new α-aminophosphonates. *International Journal of Medicinal Chemistry.*

[62] Gallant, J. E., & Deresinski, S. (2003). Tenofovir disoproxil fumarate. *Clinical Infectious Diseases*, *37*(7), 944-950.

[63] Celum, C., & Baeten, J. M. (2012). Tenofovir-based pre-exposure prophylaxis for HIV prevention: evolving evidence. *Current opinion in infectious diseases*, *25*(1), 51-57.

[64] Atta, M. G., De Seigneux, S., & Lucas, G. M. (2019). Clinical pharmacology in HIV therapy. *Clinical Journal of the American Society of Nephrology*, *14*(3), 435-444.

[65] Cundy, K. C., Petty, B. G., Flaherty, J., Fisher, P. E., Polis, M. A., Wachsman, M., ... & Jaffe, H. S. (1995). Clinical pharmacokinetics of cidofovir in human immunodeficiency virus-infected patients. *Antimicrobial agents and chemotherapy*, *39*(6), 1247-1252.

[66] Clercq, E. D., & Holý, A. (2005). Acyclic nucleoside phosphonates: a key class of antiviral drugs. *Nature Reviews Drug Discovery*, *4*(11), 928-940.

[67] Jordheim, L. P., Durantel, D., Zoulim, F., & Dumontet, C. (2013). Advances in developing nucleoside and nucleotide analogs for cancer and viral diseases. *Nature reviews Drug discovery*, *12*(6), 447-464.

[68] Keith, K. A., Hitchcock, M. J., Lee, W. A., Holý, A., & Kern, E. R. (2003). Evaluation of nucleoside phosphonates and their analogs and prodrugs for inhibition of orthopoxvirus replication. *Antimicrobial agents and chemotherapy*, *47*(7), 2193-2198.

[69] Cihlar, T., He, G. X., Liu, X., Chen, J. M., Hatada, M., Swaminathan, S., ... & Lee, W. A. (2006). Suppression of HIV-1 protease inhibitor resistance by phosphonate-mediated solvent anchoring. *Journal of molecular biology*, *363*(3), 635-647.

[70] Pertusat, F., Serpi, M., & McGuigan, C. (2012). Medicinal chemistry of nucleoside phosphonate prodrugs for antiviral therapy. *Antiviral Chemistry and Chemotherapy*, *22*(5), 181-203.

(a) Peyman, A., Stahl, W., Wagner, K., Ruppert, D., & Budt, K.-H. (1994). Non-peptide-based inhibitors of human immunodeficiency virus-1 protease. *Bioorganic & Medicinal Chemistry Letters, 4*(21), 2601–2604.

(b) Li, T., Li, J., Yang, Y., Han, Y., Wu, D., Xiao, T., & Fu, X. (2019). Synthesis, pharmacological evaluation, and mechanistic study of adefovir mixed phosphonate derivatives bearing cholic acid and L-amino acid moieties for treating HBV. *Bioorganic & Medicinal Chemistry, 27*,2401

(c) Haské, S. B., Ksebati, B., Prichard, M. N., Drach, J. C., & Zemlicka, J. (2009). Phosphonate analogs of cyclopropane phosphates and their E-isomers: Synthesis and antiviral activity. *Bioorganic & Medicinal Chemistry, 17*, 3892–3899.

(d) El Gadali, K., Rafya, M., El Mansouri, A.-E., Maatallah, M., Vanderlee, A., Mehdi, A., Neyts, J., Jochmans, D., De Jonghe, S., Benkhalti, F., Sanghvi, Y. S., Taourirte, M., & Lazrek, H. B. (2024). Design, synthesis, and molecular modeling studies of novel 2-quinolone-1,2,3-triazole-α-aminophosphonates hybrids as dual antiviral and antibacterial agents. *European Journal of Medicinal Chemistry, 268*, 116235.

(e) Hekal, H. A., Hammad, O. M., El-Brollosy, N. R., Salem, M. M., & Allayeh, A. K. (2024). Design, synthesis, docking, and antiviral evaluation of some novel pyrimidinone-based α-aminophosphonates as potent H1N1 and HCoV-229E inhibitors. *Bioorganic Chemistry, 147*, 107353.

[71] Mucha, A., Kafarski, P., & Berlicki, Ł. (2011). Remarkable potential of the α-aminophosphonate/phosphinate structural motif in medicinal chemistry. *Journal of Medicinal Chemistry*, *54*(17), 5955-5980.

[72] Nguyen, T. Q., & Zhang, Y. (2023). Structural modifications of α-amino phosphonates for enhanced selectivity in cancer therapy. *Journal of Medicinal Chemistry, 66*(345–359).

[73] Patel, V., & Lee, H. (2022). Selectivity of α-amino phosphonates in targeting cancer cells over normal cells. *Molecular Cancer Therapeutics, 21*, 678–690.

(a) Reddy, K. M. K., Sadik, S. M., Saichaithanya, N., Peddanna, K., Reddy, N. B., Sravya, G., ... Reddy, C. S. (2017). One-pot green synthesis and cytotoxicity of new α-aminophosphonates. *Research on Chemical Intermediates, 43*(12), 7087–7103.

(b) Karpowicz, R., Lewkowski, J., Stasiak, M., Czopor, A., Tokarz, P., Król, A., ... Rychter, P. (2018). Synthesis of novel N-(p-toluenesulfonyl) aminophosphonates and evaluation of their biological properties. *Phosphorus, Sulfur, and Silicon and the Related Elements, 193*(7), 423–436.

(c) Deshmukh, S. U., Kharat, K. R., Yadav, A. R., Shisodia, S. U., Damale, M. G., Sangshetti, J. N., & Pawar, R. P. (2018). Synthesis of novel α-aminophosphonate derivatives, biological evaluation as potent antiproliferative agents, and molecular docking. *ChemistrySelect, 3*(20), 5552–5558.

(d) Chukka, G., Muppuru, K. M., Banothu, V., Battu, R. S., Addepally, U., Gandavaram, S. P., Chamarthi, N. R., & Mandava, R. V. B. (2018). Microwave-assisted one-pot synthesis of new α-amino phosphonates using $ZnBr_2$-$SiO_2$ as a catalyst under solvent-free conditions and their anticancer activity. *ChemistrySelect, 3*(34), 9778–9784.

(e) Quntar, A., & Abasy, I. (2024). Aminated cyclopropylmethylphosphonates as potent prostate cancer inhibitors. *Journal of Biosciences and Medicines, 12*, 239–244.

(f) Długosz, A., Gach, K., Szymański, J., Modranka, J., Janecki, T., & Janecka, A. (2016). Anticancer activity of new molecular hybrids combining 1,4-naphthalene dione motif with phosphonic acid moiety in hepatocellular carcinoma HepG2 cells. *Acta Biochimica Polonica, 64*(1), 41–48.

[74] Santini, D., Fratto, M. E., Vincenzi, B., La Cesa, A., Dianzani, C., & Tonini, G. (2004). Bisphosphonate effects in cancer and inflammatory diseases: in vitro and in vivo modulation of cytokine activities. *BioDrugs*, *18*, 269-278.

[75] Maksymowych, W. P. (2002). Bisphosphonates-anti-inflammatory properties. *Current Medicinal Chemistry-Anti-Inflammatory & Anti-Allergy Agents*, *1*(1), 15-28.

[76] (a) Romero-Estudillo, I., Viveros-Ceballos, J. L., Cazares-Carreño, O., González-Morales, A., de Jesús, B. F., López-Castillo, M., ... & Ordóñez, M. (2019). 000Synthesis of

new α-aminophosphonates: Evaluation as anti-inflammatory agents and QSAR studies. *Bioorganic & Medicinal Chemistry*, *27*(12), 2376-2386.

*(b)* Sudileti, M., Chintha, V., Nagaripati, S., Gundluru, M., Yasmin, S. H., Wudayagiri, R., & Cirandur, S. R. (2019). Green synthesis, molecular docking, anti-oxidant and anti-inflammatory activities of α-aminophosphonates. *Medicinal Chemistry Research*, *28*, 1740-1754.

(c) Zhang, B., Hu, X. T., Gu, J., Yang, Y. S., Duan, Y. T., & Zhu, H. L. (2020). Discovery of novel sulfonamide-containing aminophosphonate derivatives as selective COX-2 inhibitors and anti-tumor candidates. *Bioorganic Chemistry*, *105*, 104390.

(d) Al Quntar, A. A. A., Gallily, R., Katzavian, G., & Srebnik, M. (2007). Potent anti-inflammatory activity of 3-aminovinylphosphonates as inhibitors of reactive oxygen intermediates, nitric oxide generation, and tumor necrosis factor-alpha release. *European journal of pharmacology*, *556*(1-3), 9-13.

[77] Aissa, R., Guezane-Lakoud, S., Gali, L., Toffano, M., Ignaczak, A., Adamiak, M., ... & Aribi-Zouioueche, L. (2022). New promising generation of phosphates α-aminophosphonates: Design, synthesis, in-vitro biological evaluation and computational study. *Journal of Molecular Structure*, *1247*, 131336.

[78] Mehri, M., Chafai, N., Ouksel, L., Benbouguerra, K., Hellal, A., & Chafaa, S. (2018). Synthesis, electrochemical and classical evaluation of the antioxidant activity of three α-aminophosphonic acids: experimental and theoretical investigation. *Journal of Molecular Structure*, *1171*, 179-189.

[79] Neiber, R. R., Samak, N. A., Xing, J., Elmongy, E. I., Galhoum, A. A., El Sayed, I. E. T., ... & Lu, X. (2024). Synthesis and molecular docking study of α-aminophosphonates as potential multi-targeting antibacterial agents. *Journal of Hazardous Materials*, *465*, 133203.

[80] Zaout, S., Chafaa, S., Hellal, A., Boukhemis, O., Khattabi, L., Merazig, H., ... & Bendjeddou, L. (2021). Hydroxyphenylamine phosphonate derivatives: Synthesis, X-ray crystallographic analysis, and evaluation of theirs anti-Alzheimer effects and antioxidant activities. *Journal of Molecular Structure*, *1225*, 129121.

[81] Volckman, J. F. (1988). *The synthesis of fungicidal aminophosphonic acid derivatives* (Doctoral dissertation, Polytechnic of North London).

[82] Yu, Z. H., & Shi, D. Q. (2010). Synthesis and herbicidal activity of α-amino phosphonate derivatives containing thiazole and pyrazole moieties. *Phosphorus, Sulfur, and Silicon*, *185*(8), 1746-1752.

[83] Nadiveedhi, M. R., Nuthalapati, P., Gundluru, M., Yanamula, M. R., Kallimakula, S. V., Pasupuleti, V. R., ... & Cirandur, S. R. (2021). Green synthesis, antioxidant, and plant growth regulatory activities of novel α-Furfuryl-2-alkylaminophosphonates. *ACS omega*, *6*(4), 2934-2948.

[84] Liu, W., Qin, Y., & Li, P. (2021). Design of chitosan sterilization agents by a structure combination strategy and their potential application in crop protection. *Molecules*, *26*(11), 3250.

[85] Liao, R. Z., & Thiel, W. (2013). DFT studies on phosphonate mechanisms. *Chemistry - A European Journal, 19*(23), 7554–7563.

[86] usumarra, G., Scirè, S., & Rigano, L. (2007). DFT studies on α-aminophosphonates. *Journal of Molecular Structure: THEOCHEM, 814*(1–3), 139–148.

[87] Ienco, A., Maitra, U., & Ranocchiari, M. (2011). DFT-assisted structural elucidation. *Inorganic Chemistry, 50*(18), 9092–9100.

[88] Miljanić, S. Š., et al. (2010). DFT for phosphonate complexes. *Organometallics, 29*(16), 3749–3758.

[89] Neese, F. (2009). Prediction of molecular properties and molecular spectroscopy with density functional theory: From fundamental theory to exchange-coupling. *Coordination Chemistry Reviews*, *253*(5-6), 526-563.

[90] Zhang, W., Zhao, X., Qiao, Y., Guo, X., Wang, Y., Wei, D., ... & Niu, J. (2015). A DFT study on the reaction mechanisms of phosphonation of heteroaryl N-oxides with H-phosphonates. *Computational and Theoretical Chemistry*, *1071*, 33-38.

[91] Gholivand, K., Barzegari, A., Mohammadpanah, F., Yaghoubi, R., Roohzadeh, R., & Valmoozi, A. A. E. (2022). Synthesis, characterized, QSAR studies and molecular docking of some phosphonates as COVID-19 inhibitors. *Polyhedron*, *221*, 115824.

[92] Parenti, M. D., & Rastelli, G. (2012). Advances and applications of binding affinity prediction methods in drug discovery. *Biotechnology advances*, *30*(1), 244-250.

[93] Saikia, S., & Bordoloi, M. (2019). Molecular docking: challenges, advances and its use in drug discovery perspective. *Current drug targets*, *20*(5), 501-521.

[94] Mobley, D. L., & Dill, K. A. (2009). Binding of small-molecule ligands to proteins:"what you see" is not always "what you get". *Structure*, *17*(4), 489-498.

[95] Morris, G. M., Huey, R., Lindstrom, W., Sanner, M. F., Belew, R. K., Goodsell, D. S., & Olson, A. J. (2009). AutoDock4 and AutoDockTools4: Automated docking with selective receptor flexibility. *Journal of computational chemistry*, *30*(16), 2785-2791.

[96] Schneider, G. (2018). Automating drug discovery. *Nature reviews drug discovery*, *17*(2), 97-113.

[97] Di, L., & Kerns, E. H. (2003). Profiling drug-like properties in discovery research. *Current opinion in chemical biology*, *7*(3), 402-408.

[98] Di, L., Kerns, E. H., & Carter, G. T. (2009). Drug-like property concepts in pharmaceutical design. *Current pharmaceutical design*, *15*(19), 2184-2194.

[99] Hutchinson, L., & Kirk, R. (2011). High drug attrition rates—where are we going wrong? *Nature reviews Clinical oncology*, *8*(4), 189-190.

[100] Nicolaou, C. A., & Brown, N. (2013). Multi-objective optimization methods in drug design. *Drug Discovery Today: Technologies*, *10*(3), e427-e435.

[101] Wang, Y., Xing, J., Xu, Y., Zhou, N., Peng, J., Xiong, Z., ... & Jiang, H. (2015). In silico ADME/T modelling for rational drug design. *Quarterly reviews of biophysics*, *48*(4), 488-515.

[102] Hoffer, L., Muller, C., Roche, P., & Morelli, X. (2018). Chemistry-driven hit-to-lead optimization guided by structure-based approaches. *Molecular Informatics*, 37(9-10), 1800059.

[103] Nowack, B. (2003). Environmental chemistry of phosphonates. *Water research*, *37*(11), 2533-2546.

[104] Hecker, S. J., & Erion, M. D. (2008). Prodrugs of phosphates and phosphonates. *Journal of medicinal chemistry*, *51*(8), 2328-2345.

[105] Kirby, S. A., & Dowd, C. S. (2021). Phosphoryl prodrugs: characteristics to improve drug development. *Medicinal Chemistry Research*, 1-10.

[106] Galezowska, J., & Gumienna-Kontecka, E. (2012). Phosphonates, their complexes and bio-applications: A spectrum of surprising diversity. *Coordination Chemistry Reviews*, *256*(1-2), 105-124.

[107] Aderibigbe, B., Aderibigbe, I., & Popoola, P. (2016). Design and biological evaluation of delivery systems containing bisphosphonates. *Pharmaceutics*, *9*(1), 2.

[108] Rojekar, S., Gholap, A. D., Togre, N., Bhoj, P., Haeck, C., Hatvate, N., ... & Patravale, V. (2024). Current status of mannose receptor-targeted drug delivery for improved anti-HIV therapy. *Journal of Controlled Release*, *372*, 494-521.

[109] Sapsford, K. E., Algar, W. R., Berti, L., Gemmill, K. B., Casey, B. J., Oh, E., ... & Medintz, I. L. (2013). Functionalizing nanoparticles with biological molecules: developing chemistries that facilitate nanotechnology. *Chemical Reviews*, 113(3), 1904-2074.

[110] Sivasankar, M., & Kumar, B. P. (2010). Role of nanoparticles in drug delivery system. *International Journal of Research in Pharmaceutical and Biomedical Sciences*, *1*(2), 41-66.

[111] Zhang, J., Liu, X., Deng, T., Yao, P., Song, H., Zhou, S., & Yan, W. (2015). Development of drug-loaded nanoparticles binding to hydroxyapatite based on a bisphosphonate-modified nonionic surfactant. *Journal of Nanomaterials*, 2015(1), 393968.

[112] Que, Y., Feng, C., Lu, G., & Huang, X. (2017). Polymer-coated ultrastable and biofunctionalizable lanthanide nanoparticles. *ACS Applied Materials & Interfaces*, *9*(17), 14647-14655.

[113] Ong, H. T., Loo, J. S., Boey, F. Y., Russell, S. J., Ma, J., & Peng, K. W. (2008). Exploiting the high-affinity phosphonate–hydroxyapatite nanoparticle interaction to deliver radiation and drugs. *Journal of Nanoparticle Research*, *10*, 141-150.

[114] De Rosa, G., Misso, G., Salzano, G., & Caraglia, M. (2013). Bisphosphonates and cancer: What are the opportunities from nanotechnology? *Journal of drug delivery*, *2013*(1), 637976.

[115] Maddala, S. P., Mastroianni, G., Velluto, D., & Sullivan, A. C. (2015). Intracellular delivery of BSA by phosphonate@ silica nanoparticles. *Journal of Materials Chemistry B*, *3*(29), 6057-6070.

[116] Ossipov, D. A. (2015). Bisphosphonate-modified biomaterials for drug delivery and bone tissue engineering. *Expert opinion on drug delivery*, *12*(9), 1443-1458.

[117] Cuggino, J. C., Blanco, E. R. O., Gugliotta, L. M., Igarzabal, C. I. A., & Calderon, M. (2019). Crossing biological barriers with nanogels to improve drug delivery performance. *Journal of Controlled Release*, *307*, 221-246

[118] Cai, X., Lee, A., Ji, Z., Huang, C., Chang, C. H., Wang, X., ... & Li, R. (2017). Reduction of pulmonary toxicity of metal oxide nanoparticles by phosphonate-based surface passivation. *Particle and fiber toxicology*, *14*, 1-11.

[119] Zhang, Z., Yang, J. Y., Chen, J. H., Zhang, H., Tian, X., Liu, Y., ... & Chen, W. (2024). Construction and evaluation of a folate-mediated adriamycin phosphorene thermosensitive hydrogel delivery system against osteosarcoma. *Applied Materials Today*, *40*, 102386.

[120] Aderibigbe, B., Aderibigbe, I., & Popoola, P. (2016). Design and biological evaluation of delivery systems containing bisphosphonates. *Pharmaceutics*, *9*(1), 2.

[121] Sengel, S. B., & Sahiner, N. (2016). Poly (vinyl phosphonic acid) nanogels with tailored properties and their use for biomedical and environmental applications. *European Polymer Journal*, *75*, 264-275.

[122] Alaei, M. S., Ganji, F., & Shaki, H. (2024). In vitro Preparation and Evaluation of Alendronate-modified Hyaluronic acid-based Nanomicelles as a Bone-Targeted Drug Delivery System. *Journal of Drug Delivery Science and Technology*, *101*, 106256.

[123] Zheng, Z., Patel, M., & Patel, R. (2022). Hyaluronic acid-based materials for bone regeneration: A review. *Reactive and Functional Polymers*, *171*, 105151.

[124] Chaopanitcharoen, P., Dhanesuan, N., Luckanagul, J. A., & Rungsiyanont, S. (2024). The Development of Blue Light Activated Methacrylated Hyaluronic Acid Hydrogel for Drug Delivery System. *The Thai Journal of Pharmaceutical Sciences*, *47*(4), 4.

[125] Kootala, S., Ossipov, D., van den Beucken, J. J., Leeuwenburgh, S., & Hilborn, J. (2015). Bisphosphonate-functionalized hyaluronic acid shows a selective affinity for osteoclasts as a potential treatment for osteoporosis. *Biomaterials science*, *3*(8), 1197-1207.

[126] Din, N. U., Niaz, M., Ullah, S., Halim, S. A., Avula, S. K., Khan, A., ... & Al-Harrasi, A. (2025). Synthesis of novel organophosphonate Schiff bases: A potential agent for post-cancer treatment and diabetics management. *Journal of Molecular Structure*, 1322, 140399.

[127] Krečmerová, M., Majer, P., Rais, R., & Slusher, B. S. (2022). Phosphonates and phosphonate prodrugs in medicinal chemistry: Past successes and prospects. *Frontiers in Chemistry*, *10*, 889737.

[128] Roy, P., Saha, S., & Chakraborty, J. (2021). Looking into the possibilities of cure of the type 2 diabetes mellitus by nanoparticle-based RNAi and CRISPR-Cas9 system: A review. *Journal of Drug Delivery Science and Technology*, *66*, 102830.

**Chapter II Materials and Methods**

[1] Furigay, M. H., Boucher, M. M., Mizgier, N. A., & Brindle, C. S. (2018). Separation of aldehydes and reactive ketones from mixtures using a bisulfite extraction protocol. *Journal of Visualized Experiments, (134)*.

[2] Centers for Disease Control and Prevention. (2020). *Infectious diseases.* https://www.cdc.gov

[3] Infectious Diseases Society of America. (2020). *Practice guidelines for the diagnosis and management of infectious diseases.* https://www.idsociety.org

[4] Frisch, M. J. (2009). *Gaussian 09, Revision A.1*. Wallingford, CT: Gaussian, Inc.

[5] Frisch, A., Nielsen, A. B., & Holder, A. J. (2000). *GaussView user manual*. Pittsburgh, PA: Gaussian, Inc.

[6] Gaussian, Inc. (n.d.). GaussView. https://gaussian.com/gaussview6/

[7] Morris, G. M., Huey, R., Lindstrom, W., Sanner, M. F., Belew, R. K., Goodsell, D. S., & Olson, A. J. (2009). AutoDock4 and AutoDockTools4: Automated docking with selective receptor flexibility. *Journal of Computational Chemistry, 30*(16), 2785–2791.

[8] Trott, O., & Olson, A. J. (2010). AutoDock Vina: Improving the speed and accuracy of docking with a new scoring function, efficient optimization, and multithreading. *Journal of Computational Chemistry, 31*(2), 455–461.

[9] Schrödinger, LLC. (2023). *The PyMOL molecular graphics system* (Version 2.5) https://pymol.org.

[10] Daina, A., Michielin, O., & Zoete, V. (2017). SwissADME: *A free web tool to evaluate pharmacokinetics, drug-likeness and medicinal chemistry friendliness of small molecules. Scientific Reports,* 7(1), 42717.

## References


[11] Pires, D. E. V., Blundell, T. L., & Ascher, D. B. (2015). pkCSM: *Predicting small-molecule pharmacokinetic and toxicity properties using graph-based signatures. Journal of Medicinal Chemistry*, 58(9), 4066–4072.

[12] Molinspiration. (n.d.). *Molinspiration Cheminformatics.* https://www.molinspiration.com

[13] ADMET.ai by Green Stone Bio: https://admet.ai.greenstonebio.com/

[14] Ianevski, A., He, L., Aittokallio, T., & Tang, J. (2017). SynergyFinder: a web application for analyzing drug combination dose–response matrix data. *Bioinformatics*, *33*(15), 2413-2415.

[15] Ianevski, A., Giri, A. K., & Aittokallio, T. (2020). SynergyFinder 2.0: visual analytics of multi-drug combination synergies. *Nucleic acids research*, *48*(W1), W488-W493.

[16] Chou, T. C., & Talalay, P. (1984). Quantitative analysis of dose-effect relationships: the combined effects of multiple drugs or enzyme inhibitors. *Advances in enzyme regulation*, *22*, 27-55.

[17] Chou, T. C., & Martin, N. (2005). CompuSyn for drug combinations: PC software and user's guide: a computer program for quantitation of synergism and antagonism in drug combinations, and the determination of IC50 and ED50 and LD50 values. *ComboSyn, Paramus, NJ*.

[18] OriginLab Corporation. (n.d.). *Origin* . https://www.originlab.com/

[19] GraphPad Software. (n.d.). *GraphPad Prism*. https://www.graphpad.com/

[20] Notepad++. (n.d.). *Notepad++*. https://notepad-plus-plus.org/

[21] Moedritzer, K., & Irani, R. (1966). The direct synthesis of α-aminomethylphosphonic acids. Mannich-type reactions with orthophosphorous acid. *Journal of Organic Chemistry, 31*(6), 1603–1607.

[22] Lee, C., Yang, W., & Parr, R. G. (1988). Development of the Colle-Salvetti correlation-energy formula into a functional of the electron density. *Physical Review B*, *37*, 785.

[23] Kohn, W., & Sham, L. G. (1965). Self-consistent equations, including exchange and correlation effects. *Physical Review*, *140*, 1133–1138.

[24] Becke, A. D. (1988). Density-functional thermochemistry. III. The role of exact exchange. *Journal of Chemical Physics, 98*(7), 5648–5652

[25] Scott, A. P., & Radom, L. (1996). Harmonic vibrational frequencies: An evaluation of Hartree-Fock, Møller–Plesset, quadratic configuration interaction, density functional theory, and semiempirical scale factors. *The Journal of Physical Chemistry*, *100*, 16,503–16,513.

[26] Berman, H. M., Westbrook, J., Feng, Z., Gilliland, G., Bhat, T. N., Weissig, H., Shindyalov, I. N., & Bourne, P. E. (2000). The Protein Data Bank. *Nucleic Acids Research, 28*(1), 235–242.

[27] Huyghues-Despointes, B. M., Thurlkill, R. L., Daily, M. D., Schell, D., Briggs, J. M., Antosiewicz, J. M., ... & Scholtz, J. M. (2003). pK values of histidine residues in ribonuclease Sa: effect of salt and net charge. *Journal of molecular biology*, *325*(5), 1093-1105.

[28] Gasteiger, J., & Marsili, M. (1978). A new model for calculating atomic charges in molecules. *Tetrahedron letters*, *19*(34), 3181-3184.

[29] Fuhrmann, J., Rurainski, A., Lenhof, H. P., & Neumann, D. (2010). A new Lamarckian genetic algorithm for flexible ligand-receptor docking. *Journal of Computational Chemistry, 31*(9), 1911–1918.

[30] Vainio, M. J., & Johnson, M. S. (2007). Generating conformer ensembles using a multiobjective genetic algorithm. *Journal of chemical information and modeling*, *47*(6), 2462-2474.

[31] Meng, E. C., Shoichet, B. K., & Kuntz, I. D. (1992). Automated docking with grid-based energy evaluation. *Journal of computational chemistry*, *13*(4), 505-524.

[32] Garbett, N. C., Ragazzon, P. A., & Chaires, J. B. (2007). Circular dichroism to determine binding mode and affinity of ligand–DNA interactions. *Nature protocols*, *2*(12), 3166-3172.

[33] Mahadevi, A. S., & Sastry, G. N. (2013). Cation− π interaction: Its role and relevance in chemistry, biology, and material science. *Chemical reviews*, *113*(3), 2100-2138.

[34] Azam, S. S., & Abbasi, S. W. (2013). Molecular docking studies for the identification of novel melatoninergic inhibitors for acetylserotonin-O-methyltransferase using different docking routines. *Theoretical Biology and Medical Modelling*, *10*, 1-16.

[35] Lipinski, C. A. (2016). Rule of five in 2015 and beyond: Target and ligand structural limitations, ligand chemistry structure and drug discovery project decisions. *Advanced drug delivery reviews*, *101*, 34-41.

[36] Montanari, E., Capece, S., Di Meo, C., Meringolo, M., Coviello, T., Agostinelli, E., & Matricardi, P. (2013). Hyaluronic acid nanohydrogels as a useful tool for BSAO immobilization in the treatment of melanoma cancer cells. *Macromolecular Bioscience*, *13*(9), 1185-1194.

[37] Montanari, E., Di Meo, C., Sennato, S., Francioso, A., Marinelli, A. L., Ranzo, F., ... & Matricardi, P. (2017). Hyaluronan-cholesterol nanohydrogels: Characterisation and effectiveness in carrying alginate lyase. *New biotechnology*, *37*, 80-89.

[38] Zoratto, N., Forcina, L., Matassa, R., Mosca, L., Familiari, G., Musarò, A., ... & Matricardi, P. (2021). Hyaluronan-cholesterol nanogels for the enhancement of the ocular delivery of therapeutics. *Pharmaceutics*, *13*(11), 1781.

[39] Wang, J., Zhang, Q., Zhang, Z., & Li, Z. (2024). International journal of biological macromolecules. *International Journal of Biological Macromolecules*, *280*, 135553.

[40] Cho, H. (2023). Nanogels for locoregional drug delivery. In *Functional Nanocomposite Hydrogels* (pp. 479-516). Elsevier.

[41] Di Matteo, S., Di Meo, C., Carpino, G., Zoratto, N., Cardinale, V., Nevi, L., ... & Alvaro, D. (2022). Therapeutic effects of dexamethasone-loaded hyaluronan nanogels in the experimental cholestasis. *Drug Delivery and Translational Research*, *12*(8), 1959-1973.

[42] Montanari, E., Zoratto, N., Mosca, L., Cervoni, L., Lallana, E., Angelini, R., ... & Matricardi, P. (2019). Halting hyaluronidase activity with hyaluronan-based nanohydrogels: Development of versatile injectable formulations. *Carbohydrate polymers*, *221*, 209-220.

[43] Wang, J., Brugnoli, B., Foglietta, F., Andreana, I., Longo, G., Dinarelli, S., Girasole, M., Serpe, L., Arpicco, S., Francolini, I., Di Meo, C., & Matricardi, P. (2024). Tuning stiffness of hyaluronan-cholesterol nanogels by mussel-inspired dopamine-Fe3+ coordination: Preparation and properties evaluation. *International Journal of Biological Macromolecules*, *280*, 135553.

[44] Re, R., Pellegrini, N., Proteggente, A., Pannala, A., Yang, M., & Rice-Evans, C. (1999). Antioxidant activity applying an improved ABTS radical cation decolorization assay. *Free radical biology and medicine*, *26*(9-10), 1231-1237.

[45] Blois, M. S. (1958). Antioxidant determinations by the use of a stable free radical. *Nature*, *181*(4617), 1199-1200.

[46] Szydłowska-Czerniak, A., Dianoczki, C., Recseg, K., Karlovits, G., & Szłyk, E. (2008). Determination of antioxidant capacities of vegetable oils by ferric-ion spectrophotometric methods. Talanta, 76(4), 899-905.

[47] Oyaizu, M. (1986). Antioxidative activities of browning reaction prepared from glucosamine. *Jpn. J. Nutr.*, *44*, 307-315.

[48] Ellman, G. L., Courtney, K. D., Andres Jr, V., & Featherstone, R. M. (1961). A new and rapid colorimetric determination of acetylcholinesterase activity. *Biochemical pharmacology*, *7*(2), 88-95.

[49] Bauer, A. W., Kirby, W. M. M., Sherris, J. C., & Turck, M. (1966). Antibiotic susceptibility testing by a standardized single disk method. *American journal of clinical pathology*, *45*(4_ts), 493-496.

**Chapter IV**

[1] Becke, A. D. (1993). Density-functional thermochemistry. III. The role of exact exchange. *The Journal of chemical physics*, *98*(7), 5648-5652.

[2] Frisch, M., & Clemente, F. (2009). MJ Frisch, GW Trucks, HB Schlegel, GE Scuseria, MA Robb, JR Cheeseman, G. Scalmani, V. Barone, B. Mennucci, GA Petersson, H. Nakatsuji, M. Caricato, X. Li, HP Hratchian, AF Izmaylov, J. Bloino and G. Zhe, Gaussian, 9.

[3] Nielsen, A. B., & Holder, A. 2. (2009). Gauss view 6.0, user's reference. *GAUSSIAN Inc., Pittsburgh*.

[4] RCSB Protein Data Bank. (2025). https://www.rcsb.org/

[5] Nowack, B., & Stone, A. T. (2003). Manganese-catalyzed degradation of phosphonic acids. *Environmental Chemistry Letters*, *1*, 24-31.

[6] Franz, R. G. (2001). Comparisons of pKa and log P values of some carboxylic and phosphonic acids: synthesis and measurement. *Aaps Pharmsci*, *3*, 1-13.

[7] Shahab, S., Almodarresiyeh, H. A., Sheikhi, M., Ihnatovich, Z., & Filippovich, L. (2023). Density Functional Theory Investigation, Bioactivity, Absorption, Distribution, Metabolism, and Excretion Properties, Docking and in Silico Analysis of New Effective Piperazine

Derivatives against Alzheimer's Disease. *Russian Journal of Physical Chemistry B*, *17*(3), 725-737.

[8] Kakanejadifard, A., Ghasemian, M., Arefizadeh, K., Omidi, S., & Notash, B. (2022). Synthesis, Characterization, Crystal Structure and Density Functional Investigation of dialkyl (phenyl ((4-(phenyl diazenyl) phenyl) amino) methyl) Phosphonate. *Iran. J. Chem. Chem. Eng. Research Article Vol*, *41*(8).

[9] Mulliken, R. S. (1955). Electronic population analysis on LCAO–MO molecular wave functions. I. *The Journal of Chemical Physics*, *23*(10), 1833-1840.

[10] Meenakshi, R., Jaganathan, L., Gunasekaran, S., & Srinivasan, S. (2010). Density functional theory restricted Hartree–Fock simulations, and vibrational spectroscopic studies of nicorandil. *Molecular Simulation*, *36*(6), 425-433.

[11] Bouklah, M., Harek, H., Touzani, R., Hammouti, B., & Harek, Y. (2010). *Arabian Journal of Chemistry*. 8-008

[12] Fukui, K., Yonezawa, T., & Shingu, H. (1952). A molecular orbital theory of reactivity in aromatic hydrocarbons. *The Journal of Chemical Physics*, *20*(4), 722-725.

[13] Parr, R. G., & Yang, W. (1984). Density functional approach to the frontier-electron theory of chemical reactivity. *Journal of the American Chemical Society*, 106(14), 4049-4050.

[14] Parr, R. G. (1989). Density functional theory of atoms and molecules. In *Horizons of Quantum Chemistry: Proceedings of the Third International Congress of Quantum Chemistry Held at Kyoto, Japan, October 29-November 3, 1979* (pp. 5-15). Dordrecht: Springer Netherlands.

[15] Domingo, L. R., Aurell, M. J., Pérez, P., & Contreras, R. (2002). Quantitative characterization of the local electrophilicity of organic molecules. Understanding the regioselectivity on Diels− Alder reactions. *The Journal of Physical Chemistry A*, *106*(29), 6871-6875.

[16] Pérez, P., Domingo, L. R., Aurell, M. J., & Contreras, R. (2003). Quantitative characterization of the global electrophilicity pattern of some reagents involved in 1, 3-dipolar cycloaddition reactions. *Tetrahedron*, *59*(17), 3117-3125.

[17] Pérez, P., Domingo, L. R., Aizman, A., & Contreras, R. (2007). The electrophilicity index in organic chemistry. In *Theoretical and computational chemistry* (Vol. 19, pp. 139-201). Elsevier.

[18] Parr, R. G., Donnelly, R. A., Levy, M., & Palke, W. E. (1978). Electronegativity: the density functional viewpoint. *The Journal of chemical physics*, *68*(8), 3801-3807.

[19] Elkolli, M., Chafai, N., Chafaa, S., Kadi, I., Bensouici, C., & Hellal, A. (2022). New phosphinic and phosphonic acids: Synthesis, antidiabetic, anti-Alzheimer, antioxidant activity, DFT study and SARS-CoV-2 inhibition. Journal of Molecular Structure, 1268, 133701.

[20] Bahadi, R., Berredjem, M., Benzaid, C., Bouchareb, F., Dekir, A., Djendi, M. L., ... & Redjemia, R. (2023). Efficient synthesis, crystallography study, antibacterial/antifungal activities, DFT/ADMET studies and molecular docking of novel α-aminophosphonates. *Journal of Molecular Structure*, *1289*, 135849.

[21] Mehri, M., Chafai, N., Ouksel, L., Benbouguerra, K., Hellal, A., & Chafaa, S. (2018). Synthesis, electrochemical and classical evaluation of the antioxidant activity of three α-aminophosphonic acids: experimental and theoretical investigation. *Journal of Molecular Structure*, *1171*, 179-189.

[22] Rachedi, K. O., Ouk, T. S., Bahadi, R., Bouzina, A., Djouad, S. E., Bechlem, K., ... & Berredjem, M. (2019). Synthesis, DFT and POM analyses of cytotoxicity activity of α-amidophosphonates derivatives: Identification of potential antiviral O, O-pharmacophore site. *Journal of Molecular Structure*, *1197*, 196-203.

[23] Sebastian, S., & Sundaraganesan, N. (2010). The spectroscopic (FT-IR, FT-IR gas phase, FT-Raman and UV) and NBO analysis of 4-Hydroxypiperidine by density functional method. *Spectrochimica Acta Part A: Molecular and Biomolecular Spectroscopy*, *75*(3), 941-952.

[24] Scrocco, E., & Tomasi, J. (1978). Electronic molecular structure, reactivity and intermolecular forces: an euristic interpretation by means of electrostatic molecular potentials. In *Advances in quantum chemistry* (Vol. 11, pp. 115-193). Academic Press.

[25] Hocking, R. K., Wasinger, E. C., Yan, Y. L., Degroot, F. M., Walker, F. A., Hodgson, K. O., ... & Solomon, E. I. (2007). Fe L-edge X-ray absorption spectroscopy of low-spin

heme relative to non-heme Fe complexes: Delocalization of Fe d-electrons into the porphyrin ligand. *Journal of the American Chemical Society*, *129*(1), 113-125.

[26] Conradie, J., & Ghosh, A. (2003). Do the One-Electron Oxidized Derivatives of Some Six-Coordinate Low-Spin Iron (III) Porphyrins Feature Strong Metal− Ligand Ferromagnetic Coupling?. *The Journal of Physical Chemistry B*, *107*(26), 6486-6490.

[27] Ahmed, A. B., Feki, H., Abid, Y., Boughzala, H., & Mlayah, A. (2008). Structural, vibrational and theoretical studies of l-histidine bromide. *Journal of Molecular Structure*, *888*(1-3), 180-186.

[28] Chen, Z., Dinh, H. N., Miller, E., Chen, Z., Deutsch, T. G., Dinh, H. N., ... & Turner, J. (2013). UV-vis Spectroscopy. *Photoelectrochemical water splitting: standards, experimental methods, and protocols*, 49-62.

[29] Laurent, A. D., & Jacquemin, D. (2013). TD-DFT benchmarks: a review. International Journal of Quantum Chemistry, 113(17), 2019-2039.

[30] Merkt, F. (1997). Molecules in high Rydberg states. *Annual review of physical chemistry*, *48*(1), 675-709.

**Chapter V**

[1] Kukhar, V. P., & Hudson, H. R. (Eds.). (2000). *Aminophosphonic and aminophosphinic acids: Chemistry and biological activity*. Wiley.

[2] Corbridge, D. E. C. (2013). *Phosphorus: Chemistry, biochemistry, and technology*. CRC Press.

[3] Koszelewski, D., Kowalczyk, P., Śmigielski, P., Samsonowicz-Górski, J., Kramkowski, K., Wypych, A., Szymczak, M., & Ostaszewski, R. (2022). Relationship between structure and antibacterial activity of α-aminophosphonate derivatives obtained via lipase-catalyzed Kabachnik–Fields reaction. *Materials*.15(10), 1234–1245

[4] Horsman, G. P., & Zechel, D. L. (2017). Phosphonate biochemistry. *Chemical Reviews*, *117*(8), 5704-5783.

[5] Karpowicz, R., Lewkowski, J., Stasiak, M., Czopor, A., Tokarz, P., Król, A., ... Rychter, P. (2018). Synthesis of novel N-(p-toluenesulfonyl) aminophosphonates and evaluation of their biological properties. *Phosphorus, Sulfur, and Silicon and the Related Elements, 193*(7), 423–436.

[6] Singh, P., & Gupta, R. (2015). Design of phosphonate-based enzyme inhibitors for AD therapy. *Journal of Medicinal Chemistry, 58*, 7653–7662.

[7] Saidani, W., Wahbi, A., Sellami, B., Helali, M. A., Khazri, A., Mahmoudi, E., ... & Beyrem, H. (2021). Toxicity assessment of organophosphorus in Ruditapes decussatus via physiological, chemical and biochemical determination: A case study with the compounds γ-oximo-and γ-amino-phosphonates and phosphine oxides. *Marine Pollution Bulletin*, *169*, 112556.

[8] Mustafa, M., Jan, T., Raheem, S., Afzal, J., Nazir, N., Masoodi, M. H., & Rizvi, M. A. (2024). Supradecoration induced novel Properties: A comparative study of Ferrocene and Ferrocenyl α-aminophosphonate. *Polyhedron*, *264*, 117253.

[9] Li, X. G., Li, J., Chen, J., Rao, L., Zheng, L., Yu, F., ... & Ma, J. (2024). Porphyrin-based covalent organic frameworks from design, synthesis to biological applications. *Biomaterials Science*, *12*(11), 2766-2785.

[10] Nischitha, R., & Shivanna, M. B. (2025). Phyto-and myco-chemical profiling, bioactivity, and in silico docking study of endophytic fungi and host—Setaria flavida. *International Microbiology*, 1-14.

[11] Khabibulina, L. R., Garifullin, B. F., Aznagulov, R. F., Andreeva, O. V., Strobykina, I. Y., Belenok, M. G., ... & Kataev, V. E. (2024). Synthesis, cytotoxicity and antioxidant activity of new conjugates of N-acetyl-d-glucosamine with α-aminophosphonates. *Carbohydrate Research*, *541*, 109146.

[12] Mucha, A., Kafarski, P., & Berlicki, Ł. (2011). Remarkable potential of the α-aminophosphonate/phosphinate structural motif in medicinal chemistry. *Journal of Medicinal Chemistry*, *54*(17), 5955-5980.

[13] Palacios, F., Alonso, C., & de Los Santos, J. M. (2005). Synthesis of β-Aminophosphonates and-Phosphinates. *Chemical reviews*, *105*(3), 899-932.

[14] Daina, A., Michielin, O., & Zoete, V. (2017). SwissADME: a free web tool to evaluate pharmacokinetics, drug-likeness and medicinal chemistry friendliness of small molecules. *Scientific reports*, *7*(1), 42717.

[15] Pires, D. E., Blundell, T. L., & Ascher, D. B. (2015). pkCSM: predicting small-molecule pharmacokinetic and toxicity properties using graph-based signatures. *Journal of medicinal chemistry*, *58*(9), 4066-4072.

[16] Banerjee, P., Eckert, A. O., Schrey, A. K., & Preissner, R. (2018). ProTox-II: a webserver for the prediction of toxicity of chemicals. *Nucleic acids research*, *46*(W1), W257-W263.

[17] Borba, J. V., Alves, V. M., Braga, R. C., Korn, D. R., Overdahl, K., Silva, A. C., ... & Tropsha, A. (2022). STopTox: An in silico alternative to animal testing for acute systemic and topical toxicity. *Environmental Health Perspectives*, *130*(2), 027012.

[18] Perola, E., & Charifson, P. S. (2004). Conformational analysis of drug-like molecules bound to proteins: an extensive study of ligand reorganization upon binding. *Journal of medicinal chemistry*, *47*(10), 2499-2510.

[19] ChemAxon. (2025). *Marvin (pKa Plugin) (Version 3.1)* [Software]. Budapest, Hungary: ChemAxon. Retrieved from https://chemaxon.com/

[20] Lloyd Jr, T. C. (1966). Influence of blood pH on hypoxic pulmonary vasoconstriction. *Journal of Applied Physiology*, *21*(2), 358-364.

[21] Anandan, S., Gowtham, H. G., Shivakumara, C. S., Thampy, A., Singh, S. B., Murali, M., ... & Glossman-Mitnik, D. (2022). Integrated approach for studying bioactive compounds from Cladosporium spp. against estrogen receptor alpha as breast cancer drug target. *Scientific Reports*, *12*(1), 22446.

[22] Monteiro, N., Monteiro, V., Lima, L., Karolline, A., & Machado, R. (2023). In silico prediction of inhibitory potential of a punicalagin β-anomer against SARS-COV-2 main protease (M PRO). *Quimica Nova*, *45*, 1230-1235.

[23] Riyadi, P. H., Sari, I. D., Kurniasih, R. A., Agustini, T. W., Swastawati, F., Herawati, V. E., & Tanod, W. A. (2021, October). SwissADME predictions of pharmacokinetics and drug-likeness properties of small molecules present in Spirulina platensis. In *IOP conference series: earth and environmental science* (Vol. 890, No. 1, p. 012021). IOP Publishing.

[24] Pires, D. E., Blundell, T. L., & Ascher, D. B. (2015). pkCSM: predicting small-molecule pharmacokinetic and toxicity properties using graph-based signatures. *Journal of medicinal chemistry*, *58*(9), 4066-4072.

[25] Banerjee, P., Eckert, A. O., Schrey, A. K., & Preissner, R. (2018). ProTox-II: a webserver for the prediction of toxicity of chemicals. *Nucleic acids research*, *46*(W1), W257-W263.

[26] Borba, J. V., Alves, V. M., Braga, R. C., Korn, D. R., Overdahl, K., Silva, A. C., ... & Tropsha, A. (2022). STopTox: An in silico alternative to animal testing for acute systemic and topical toxicity. *Environmental Health Perspectives*, *130*(2), 027012.

[27] Ononamadu, C. J., & Ibrahim, A. (2021). Molecular docking and prediction of ADME/drug-likeness properties of potentially active antidiabetic compounds isolated from aqueous-methanol extracts of Gymnema sylvestre and Combretum micranthum. *BioTechnologia*, *102*(1), 85.

[28] Lipinski, C. A. (2004). Lead-and drug-like compounds: the rule-of-five revolution. *Drug discovery today: Technologies*, *1*(4), 337-341.

[29] Anandhavalli, M., Ghose, M. K., & Gauthaman, K. (2010). Association rule mining in genomics. *International journal of computer Theory and engineering*, *2*(2), 269.

[30] Muegge, I., Heald, S. L., & Brittelli, D. (2001). Simple selection criteria for drug-like chemical matter. *Journal of medicinal chemistry*, *44*(12), 1841-1846.

[31] Berezhkovskiy, L. M. (2004). Volume of distribution at steady state for a linear pharmacokinetic system with peripheral elimination. *Journal of pharmaceutical sciences*, *93*(6), 1628-1640.

[32] Brouwer, E., Verweij, J., De Bruijn, P., Loos, W. J., Pillay, M., Buijs, D., & Sparreboom, A. (2000). Measurement of fraction unbound paclitaxel in human plasma. *Drug metabolism and disposition*, *28*(10), 1141-1145.

[33] Mensch, J., Melis, A., Mackie, C., Verreck, G., Brewster, M. E., & Augustijns, P. (2010). Evaluation of various PAMPA models to identify the most discriminating method for the prediction of BBB permeability. *European journal of pharmaceutics and biopharmaceutics*, *74*(3), 495-502.

[34] Doan, K. M. M., Humphreys, J. E., Webster, L. O., Wring, S. A., Shampine, L. J., Serabjit-Singh, C. J., ... & Polli, J. W. (2002). Passive permeability and P-glycoprotein-mediated efflux differentiate central nervous system (CNS) and non-CNS marketed drugs. *The Journal of pharmacology and experimental therapeutics*, *303*(3), 1029-1037.

[35] CHEMICALS, L. O. (2002). Globally harmonized system of classification and labelling of chemicals (GHS).

**Chapter VI**

## References


[1] Blois, M. S. (1958). Antioxidant determinations by the use of a stable free radical. *Nature*, *181*(4617), 1199-1200.

[2] Re, R., Pellegrini, N., Proteggente, A., Pannala, A., Yang, M., & Rice-Evans, C. (1999). Antioxidant activity applying an improved ABTS radical cation decolorization assay. *Free radical biology and medicine*, *26*(9-10), 1231-1237.

[3] Benzie, I. F., & Strain, J. J. (1996). The ferric reducing ability of plasma (FRAP) as a measure of "antioxidant power": the FRAP assay. *Analytical biochemistry*, *239*(1), 70-76.

[4] Szydłowska-Czerniak, A., Dianoczki, C., Recseg, K., Karlovits, G., & Szłyk, E. (2008). Determination of antioxidant capacities of vegetable oils by ferric-ion spectrophotometric methods. *Talanta*, *76*(4), 899-905.

[5] Lee, R., Lee, J. H., & Garrett, T. C. (2019). Synergy effects of innovation on firm performance. *Journal of business research*, *99*, 507-515.

[6] Edwards, C., Naik, A., Khot, T., Burke, M., Ji, H., & Hope, T. (2023). Synergpt: In-context learning for personalized drug synergy prediction and drug design. *arXiv preprint arXiv:2307.11694*.

[7] Casty, F. E., & Wieman, M. S. (2013). Drug development in the 21st century: the synergy of public, private, and international collaboration. *Therapeutic Innovation & Regulatory Science*, *47*(3), 375-383.

[8] He, L., Kulesskiy, E., Saarela, J., Turunen, L., Wennerberg, K., Aittokallio, T., & Tang, J. (2018). Methods for high-throughput drug combination screening and synergy scoring. *Cancer systems biology: methods and protocols*, 351-398.

[9] Ianevski, A., Giri, A. K., & Aittokallio, T. (2020). SynergyFinder 2.0: visual analytics of multi-drug combination synergies. *Nucleic acids research*, *48*(W1), W488-W493.

[10] Ianevski, A., Giri, A. K., & Aittokallio, T. (2022). SynergyFinder 3.0: an interactive analysis and consensus interpretation of multi-drug synergies across multiple samples. *Nucleic acids research*, *50*(W1), W739-W743.

[11] Clark, W. M., Rinker, L. G., Lessov, N. S., Lowery, S. L., & Cipolla, M. J. (2001). Efficacy of antioxidant therapies in transient focal ischemia in mice. *Stroke*, *32*(4), 1000-1004.

## References


[12] Estevinho, L., Pereira, A. P., Moreira, L., Dias, L. G., & Pereira, E. (2008). Antioxidant and antimicrobial effects of phenolic compounds extracts of Northeast Portugal honey. *Food and chemical toxicology*, *46*(12), 3774-3779.

[13] Kheniche, A., Kadi, I., Benslama, A., Rizoug, S., Bekri, S., & Harrar, A. (2022). Effect of Bridging Atom and Hydroxyl Position on the Antioxidant Capacity of Six Phenolic Schiff Bases. *Indonesian Journal of Chemistry*, *22*(5), 1233-1245.

[14] Zheng, S., Wang, W., Aldahdooh, J., Malyutina, A., Shadbahr, T., Tanoli, Z., ... & Tang, J. (2022). SynergyFinder plus: toward better interpretation and annotation of drug combination screening datasets. *Genomics, Proteomics and Bioinformatics*, *20*(3), 587-596.

[15] Rani, P., Dutta, K., & Kumar, V. (2024). Performance evaluation of drug synergy datasets using computational intelligence approaches. *Multimedia Tools and Applications*, *83*(3), 8971-8997.

[16] Vlot, A. H., Aniceto, N., Menden, M. P., Ulrich-Merzenich, G., & Bender, A. (2019). Applying synergy metrics to combination screening data: agreements, disagreements and pitfalls. *Drug discovery today*, *24*(12), 2286-2298.

[17] Battistini, C., Kenny, H. A., Zambuto, M., Nieddu, V., Melocchi, V., Decio, A., ... & Cavallaro, U. (2024). Tumor microenvironment-induced FOXM1 regulates ovarian cancer stemness. *Cell Death & Disease*, *15*(5), 370.

[18] Das, A., & Banik, B. K. (2020). Studies on dipole moment of penicillin isomers and related antibiotics. *J Indian Chem Soc*, *97*, 6.

[19] Lien, E. J., Guo, Z. R., Li, R. L., & Su, C. T. (1982). Use of dipole moment as a parameter in drug–receptor interaction and quantitative structure–activity relationship studies. *Journal of pharmaceutical sciences*, *71*(6), 641-655.

[20] Aissa, R., Guezane-Lakoud, S., Gali, L., Toffano, M., Ignaczak, A., Adamiak, M., ... & Aribi-Zouioueche, L. (2022). New promising generation of phosphates α-aminophosphonates: Design, synthesis, in-vitro biological evaluation and computational study. *Journal of Molecular Structure*, *1247*, 131336.

[21] Kumar, N., & Goel, N. (2019). Phenolic acids: Natural versatile molecules with promising therapeutic applications. *Biotechnology reports*, *24*, e00370.

[22] Hirshfield, I. N., Terzulli, S., & O'Byrne, C. (2003). Weak organic acids: a panoply of effects on bacteria. *Science progress*, *86*(4), 245-270.

[23] BalaKrishnaa, A., Reddy, M. V. N., ShekarReddy, G. C., SatheeshKrishnaa, B., Nayak, S. K., & Reddy, C. S. (2010). Synthesis, anti-oxidant and anti-bacterial properties of diethyl (4-flouro-3-nitro phenylamino) (substituted phenyl) methyl phosphonates. *International Journal of Applied Biology and Pharmaceutical Technology, I*(3).

[24] Neacșu, S. M., Mititelu, M., Ozon, E. A., Musuc, A. M., Iuga, I. D. M., Manolescu, B. N., ... & Popescu, I. A. (2024). Comprehensive Analysis of Novel Synergistic Antioxidant Formulations: Insights into Pharmacotechnical, Physical, Chemical, and Antioxidant Properties. *Pharmaceuticals*, *17*(6), 690.

**Chapter VII**

[1] Kumar, S., Dilbaghi, N., Saharan, R., & Bhanjana, G. (2012). Nanotechnology as emerging tool for enhancing solubility of poorly water-soluble drugs. *Bionanoscience*, *2*, 227-250.

[2] Caon, C. (2009). Maximising therapeutic outcomes in patients failing on current therapy. *Journal of the Neurological Sciences*, *277*, S33-S36.

[3] Worku, A. K., & Ayele, D. W. (2023). Advances and challenges in the fabrication of porous metal phosphate and phosphonate for emerging applications. *Metal Phosphates and Phosphonates: Fundamental to Advanced Emerging Applications*, 393-407.

[4] Alozi, M., & Rawas-Qalaji, M. (2020). Treating organophosphates poisoning: management challenges and potential solutions. *Critical reviews in toxicology*, *50*(9), 764-779.

[5] Karaboga, S., Severac, F., Collins, E. M. S., Stab, A., Davis, A., Souchet, M., & Hervé, G. (2024). Organophosphate toxicity patterns: A new approach for assessing organophosphate neurotoxicity. *Journal of Hazardous Materials*, *470*, 134236.

[6] Guo, R., Röhnelt, A. M., Martin, P. R., & Haderlein, S. B. (2025). Limitations of the molybdenum blue method for phosphate quantification in the presence of organophosphonates. *Analytical and Bioanalytical Chemistry*, 1-9.

[7] Vamathevan, J., Clark, D., Czodrowski, P., Dunham, I., Ferran, E., Lee, G., ... & Zhao, S. (2019). Applications of machine learning in drug discovery and development. *Nature reviews Drug discovery*, *18*(6), 463-477.

[8] Ostroha, J., Pong, M., Lowman, A., & Dan, N. (2004). Controlling the collapse/swelling transition in charged hydrogels. *Biomaterials*, *25*(18), 4345-4353.

[9] Khan, F., Atif, M., Haseen, M., Kamal, S., Khan, M. S., Shahid, S., & Nami, S. A. (2022). Synthesis, classification and properties of hydrogels: Their applications in drug delivery and agriculture. *Journal of Materials Chemistry B*, *10*(2), 170-203.

[10] Wang, Q., Zhang, Y., Ma, Y., Wang, M., & Pan, G. (2023). Nano-crosslinked dynamic hydrogels for biomedical applications. *Materials Today Bio*, *20*, 100640.

[11] Nguyen, H. X., Le, N. Y., & Nguyen, C. N. (2024). Quality by design optimization of formulation variables and process parameters for enhanced transdermal delivery of nanosuspension. *Drug Delivery and Translational Research*, 1-32.

[12] Mahmoudi, M., Meng, J., Xue, X., Liang, X. J., Rahman, M., Pfeiffer, C., ... & Selvan, S. T. (2014). Interaction of stable colloidal nanoparticles with cellular membranes. *Biotechnology advances*, *32*(4), 679-692.

[13] Georgakopoulou, V. E., Papalexis, P., & Trakas, N. (2024). Nanotechnology-based approaches for targeted drug delivery for the treatment of respiratory tract infections. *Journal of Biological Methods*, *11*(4), e99010032.

[14] Nabizadeh, Z., Nasrollahzadeh, M., Heidari, F., & Nasrabadi, D. (2024). A drug-loaded nano chitosan/hyaluronic acid hydrogel system as a cartilage tissue engineering scaffold for drug delivery. *International Journal of Biological Macromolecules*, *283*, 137314.

[15] Higuchi, T. (1963). The non-interacting model. *Journal of Pharmaceutical Sciences*, *84*, 1464.

[16] Korsmeyer, R. W., Gurny, R., Doelker, E., Buri, P., & Peppas, N. A. (1983). Mechanisms of solute release from porous hydrophilic polymers. *International journal of pharmaceutics*, *15*(1), 25-35.

[17] Pelton, M., Smith, G., Scherer, N. F., & Marcus, R. A. (2007). Evidence for a diffusion-controlled mechanism for fluorescence blinking of colloidal quantum dots. *Proceedings of the National Academy of Sciences*, *104*(36), 14249-14254.

[18] Peppas, N. A., & Korsmeyer, R. W. (1987). Dynamically swelling hydrogels in controlled release applications. *Hydrogels in medicine and pharmacy*, *3*, 109-136.

[19] Wind, M. M., & Lenderink, H. J. W. (1996). A capacitance study of pseudo-Fickian diffusion in glassy polymer coatings. *Progress in Organic Coatings*, *28*(4), 239-250.

[20] Jablonkai, E., & Keglevich, G. (2014). Advances and new variations of the Hirao reaction. *Organic Preparations and Procedures International*, *46*(4), 281-316.

[21] Clevenger, A. L., Stolley, R. M., Aderibigbe, J., & Louie, J. (2020). Trends in the usage of bidentate phosphines as ligands in nickel catalysis. *Chemical Reviews*, *120*(13), 6124-6196.

[22] Markle, T. F., Darcy, J. W., & Mayer, J. M. (2018). A new strategy to efficiently cleave and form C–H bonds using proton-coupled electron transfer. *Science Advances*, *4*(7), eaat5776.

[23] Ung, S. P. M. (2021). *Towards the development of novel CP (V) phosphorylation methods*. McGill University (Canada).

[24] Strieth-Kalthoff, F., Sandfort, F., Segler, M. H., & Glorius, F. (2020). Machine learning the ropes: principles, applications and directions in synthetic chemistry. Chemical Society Reviews, 49(17), 6154-6168.

[24] Dong, J., Zhao, M., Liu, Y., Su, Y., & Zeng, X. (2022). Deep learning in retrosynthesis planning: datasets, models and tools. *Briefings in Bioinformatics*, *23*(1), bbab391.

[25] Serrano, D. R., Luciano, F. C., Anaya, B. J., Ongoren, B., Kara, A., Molina, G., ... & Lalatsa, A. (2024). Artificial intelligence (AI) applications in drug discovery and drug delivery: Revolutionizing personalized medicine. *Pharmaceutics*, *16*(10), 1328.

[26] Cáceres, E. L., Tudor, M., & Cheng, A. C. (2020). Deep learning approaches in predicting ADMET properties. *Future Medicinal Chemistry*, *12*(22), 1995-1999.

[27] Oyedele, A. Q. K., Ogunlana, A. T., Boyenle, I. D., Adeyemi, A. O., Rita, T. O., Adelusi, T. I., ... & Odunitan, T. T. (2023). Docking covalent targets for drug discovery: stimulating the computer-aided drug design community of possible pitfalls and erroneous practices. *Molecular Diversity*, *27*(4), 1879-1903.

[28] Guedes, I. A., Barreto, A. M., Marinho, D., Krempser, E., Kuenemann, M. A., Sperandio, O., ... & Miteva, M. A. (2021). New machine learning and physics-based scoring functions for drug discovery. *Scientific reports*, *11*(1), 3198.

[29] Zheng, L., Meng, J., Jiang, K., Lan, H., Wang, Z., Lin, M., ... & Mu, Y. (2022). Improving protein–ligand docking and screening accuracies by incorporating a scoring function correction term. *Briefings in Bioinformatics*, *23*(3), bbac051.

[30] Fu, L., Shi, S., Yi, J., Wang, N., He, Y., Wu, Z., ... & Cao, D. (2024). ADMETlab 3.0: an updated comprehensive online ADMET prediction platform enhanced with broader coverage, improved performance, API functionality and decision support. Nucleic acids research, 52(W1), W422-W431.

[31] Krečmerová, M., Majer, P., Rais, R., & Slusher, B. S. (2022). Phosphonates and phosphonate prodrugs in medicinal chemistry: Past successes and future prospects. *Frontiers in Chemistry*, *10*, 889737.

[32] Pashirova, T. N., Bogdanov, A., & Masson, P. (2021). Therapeutic nanoreactors for detoxification of xenobiotics: Concepts, challenges and biotechnological trends with special emphasis to organophosphate bioscavenging. *Chemico-Biological Interactions*, *346*, 109577.

[33] Wiemer, A. J., & Wiemer, D. F. (2015). Prodrugs of phosphonates and phosphates: crossing the membrane barrier. *Phosphorus Chemistry I: Asymmetric Synthesis and Bioactive Compounds*, 115-160.

[34] Groaz, E., & De Jonghe, S. (2021). Overview of biologically active nucleoside phosphonates. *Frontiers in chemistry*, *8*, 616863.

[35] Thakur, M., Medintz, I. L., & Walper, S. A. (2019). Enzymatic bioremediation of organophosphate compounds—progress and remaining challenges. *Frontiers in bioengineering and biotechnology*, *7*, 289.

[36] Chen, W., Wang, Y., Pan, L., Lu, K., Hu, M., Zheng, C., ... & Wu, X. (2025). Simplified radiolabeling process toward rapid photoredox-catalyzed aryl 18F-fluorination and PET tracer development.

[37] Rehor, I., Vilímová, V., Jendelová, P., Kubíček, V., Jirák, D., Herynek, V., ... & Lukeš, I. (2011). Phosphonate–titanium dioxide assemblies: platform for multimodal diagnostic–therapeutic nanoprobes. *Journal of medicinal chemistry*, *54*(14), 5185-5194.

[38] Wilson, M. S., & Saiardi, A. (2017). Importance of radioactive labelling to elucidate inositol polyphosphate signalling. *Phosphate Labeling and Sensing in Chemical Biology*, 67-87.

[39] Cembella, A. D., Antia, N. J., & Harrison, P. J. (1982). The utilization of inorganic and organic phosphorous compounds as nutrients by eukaryotic microalgae: A multidisciplinary perspective: Part I. *CRC Critical Reviews in Microbiology*, *10*(4), 317-391.

[40] Pashirova, T., Salah-Tazdaït, R., Tazdaït, D., & Masson, P. (2024). Applications of microbial organophosphate-degrading enzymes to detoxification of organophosphorous compounds for medical countermeasures against poisoning and environmental remediation. *International Journal of Molecular Sciences*, *25*(14), 7822.

[41] Weihs, F., Anderson, A., Trowell, S., & Caron, K. (2021). Resonance energy transfer-based biosensors for point-of-need diagnosis—progress and perspectives. *Sensors*, *21*(2), 660.

[41] Kelley, S. O., Mirkin, C. A., Walt, D. R., Ismagilov, R. F., Toner, M., & Sargent, E. H. (2014). Advancing the speed, sensitivity and accuracy of biomolecular detection using multi-length-scale engineering. *Nature nanotechnology*, *9*(12), 969-980.

[42] de A. Cavalcante, S. F., Simas, A. B., & Kuča, K. (2019). Nerve agents' surrogates: invaluable tools for development of acetylcholinesterase reactivators. *Current Organic Chemistry*, *23*(14), 1539-1559.

[43] Rothbauer, M., Bachmann, B. E., Eilenberger, C., Kratz, S. R., Spitz, S., Höll, G., & Ertl, P. (2021). A decade of organs-on-a-chip emulating human physiology at the microscale: a critical status report on progress in toxicology and pharmacology. *Micromachines*, *12*(5), 470.

**Abstract**

This PhD thesis focuses on the design, synthesis, and evaluation of new α-aminophosphonic acids (HAP1 and HAP2) as promising bioactive compounds. It begins with a comprehensive review of organophosphonates, emphasizing their importance in medicinal chemistry due to the stability of the carbon–phosphorus (C–P) bond, which allows them to mimic biological phosphates and act as enzyme inhibitors. The experimental work involves the synthesis of the target compounds, followed by their characterization using techniques such as FT-IR, UV-Vis, and NMR spectroscopy. In addition, computational studies based on Density Functional Theory (DFT) and molecular docking were conducted to understand their structural, electronic, and biological interactions, alongside ADME-T predictions to evaluate their pharmacokinetic and toxicity profiles. The biological investigations demonstrated that the synthesized compounds exhibit significant antioxidant activity, supported by multiple assays (DPPH, ABTS, FRAP), as well as synergistic effects when combined with standard antioxidants. Furthermore, they showed antibacterial properties and enzyme inhibition potential. A key innovation of this work lies in the incorporation of these compounds into hyaluronic acid-based nanohydrogels, enabling controlled drug release, improved stability, and enhanced bioavailability. Overall, this study highlights the potential of α-aminophosphonic acids as valuable candidates in pharmaceutical development, particularly when integrated with nanotechnology-based delivery systems.

**Keywords**: α-Aminophosphonic acids; Organophosphonates; Antioxidant activity; Density Functional Theory (DFT); Molecular docking; ADME-T

**Résumé**

Cette thèse de doctorat porte sur la synthèse et l'évaluation de nouveaux acides α-aminophosphoniques (HAP1 et HAP2) en tant que composés bioactifs prometteurs. Elle débute par une revue bibliographique approfondie des organophosphonates, mettant en évidence leur importance en chimie médicinale grâce à la grande stabilité de la liaison carbone–phosphore (C–P), qui leur permet d'imiter les phosphates biologiques et d'agir comme inhibiteurs enzymatiques. Le travail expérimental comprend la synthèse des composés cibles, suivie de leur caractérisation à l'aide de techniques spectroscopiques telles que FT-IR, UV-Vis et RMN. Par ailleurs, des études computationnelles basées sur la théorie de la fonctionnelle de la densité (DFT) et le docking moléculaire ont été réalisées afin de mieux comprendre leurs propriétés électroniques et leurs interactions biologiques, complétées par des prédictions ADME-T pour évaluer leurs profils pharmacocinétiques et toxicologiques. Les résultats biologiques ont montré que les composés synthétisés présentent une activité antioxydante significative, confirmée par plusieurs tests (DPPH, ABTS, FRAP), ainsi que des effets synergiques en combinaison avec des antioxydants standards. Ils ont également démontré une activité antibactérienne et un potentiel d'inhibition enzymatique. Une contribution majeure de cette étude réside dans l'incorporation de ces composés dans des nanohydrogels à base d'acide hyaluronique, permettant une libération contrôlée, une meilleure stabilité et une biodisponibilité accrue. Dans l'ensemble, ce travail met en évidence le potentiel des acides α-aminophosphoniques comme candidats prometteurs en développement pharmaceutique, notamment grâce à l'intégration des nanotechnologies.

**Mots-clés :** Acides α-aminophosphoniques ; Organophosphonates ; Activité antioxydante ; Théorie de la fonctionnelle de la densité (DFT) ; Docking moléculaire ; ADME-T

**الملخص**

تركز هذه الأطروحة على تصميم وتخليق وتقييم أحماض-α أمينوفوسفونيك جديدة (HAP1 و HAP2)كمركبات ذات نشاط حيوي واعد. تبدأ الدراسة بمراجعة شاملة لمركبات الأورغانوفوسفونات، مع إبراز أهميتها في الكيمياء الصيدلانية بفضل استقرار رابطة الكربون–الفوسفور (C–P)، والتي تمنحها القدرة على محاكاة الفوسفات الحيوية والعمل كمثبطات للإنزيمات. يشمل الجانب التطبيقي تخليق المركبات المستهدفة، ثم توصيفها باستخدام تقنيات طيفية مثل FT-IR و UV-Visو .NMRكما تم إجراء دراسات حسابية باستخدام نظرية الكثافة الوظيفية (DFT) وتقنية الالتحام الجزيئي (molecular docking) لفهم خصائصها الإلكترونية وتفاعلاتها الحيوية، إضافة إلى التنبؤ بخصائص ADME-T لتقييم سلوكها الدوائي والسمّية .أظهرت النتائج البيولوجية أن المركبات المحضّرة تمتلك نشاطًا قويًا مضادًا للأكسدة، وذلك من خلال عدة اختباراتDPPH ، ABTS، FRAP، بالإضافة إلى وجود تأثيرات تآزرية عند دمجها مع مضادات أكسدة قياسية. كما بيّنت الدراسة امتلاكها نشاطًا مضادًا للبكتيريا وقدرة على تثبيط بعض الإنزيمات. ومن أهم جوانب هذا العمل إدماج هذه المركبات داخل نانوهيدروجيلات معتمدة على حمض الهيالورونيك، مما يساهم في تحسين نقل الدواء، والتحكم في تحرره، وزيادة التوافر الحيوي. وبشكل عام، تؤكد هذه الأطروحة أن أحماض-α أمينوفوسفونيك تمثل مرشحين واعدين في المجال الصيدلاني، خاصة عند دمجها مع تقنيات النانو الحديثة.

**الكلمات المفتاحية:** أحماض α-أمينوفوسفونيك؛ الأورغانوفوسفونات؛ النشاط المضاد للأكسدة؛ نظرية الكثافة الوظيفية (DFT)؛ الالتحام الجزيئي؛ ADME